A Study of Proton-Induced Pion Production on ^{12}C at Intermediate Energies via Recoil Detection

Erik Richard Jacobsen

A Dissertation
Presented to the Faculty
of Princeton University
in Candidacy for the Degree
of Doctor of Philosophy

Recommended for Acceptance
by the Department of Physics

June 1994

Typeset using TEX 3.1415 (D. Knuth),
with Adobe New Century, Adobe Palatino,
Adobe Helvetica, and Computer Modern fonts.
Printed at 600 × 600 dpi on 9/4/2007
using dvips 5.521 (T. Rokicki).

for my parents

Abstract

This work describes a study of proton-induced pion production from ^{12}C, for proton energies in the range E_p = 166–350 MeV. The (p,π) reaction is particularly useful as a means by which the π-N interaction mechanism within a bound nuclear system can be sampled. Of further interest, double-pion production processes $(p,\pi\pi)$ near threshold in nuclei may be sensitive to any breaking of the underlying chiral symmetry. A full description of the pion-production process in nuclei is a key step toward understanding the long-range part of the nuclear strong force.

The experiment for this study was carried out at the Indiana University Cyclotron Facility Cooler ring, a high-resolution, electron-cooled, proton beam storage device. Recoil detection techniques, in which the heavy, highly-ionizing recoil nuclei are detected rather than the light, outgoing particles, were used for this experiment. The advantages of the recoil method include: the capability of simultaneous study of several processes such as (p,π) for different pion charge states; large center-of-mass acceptance fractions close to the reaction thresholds; and, the obviation of high-energy, neutral-particle detection.

A kinematically complete and unique reconstruction of the two-body reaction parameters was carried out through the use of raytracing code developed for both online analysis and offline calculations. Differential cross-sections for $^{12}C(p,\pi^+)^{13}C$ leading to strongly-bound final nuclear states are presented for proton energies of 166 MeV, 294 MeV, and 330 MeV, corresponding in particular to extreme forward and backward pion angles in the center-of-mass frame. Angular distributions for $^{12}C(p,\pi^0)^{13}N_{g.s.}$ have also been obtained at 166 MeV and 294 MeV. The total cross-section for this process at 166 MeV is found to be $\sigma(\pi^0) = 374\pm46$ nb, leading to a pion charge state ratio of $R \equiv \sigma(\pi^+)/\sigma(\pi^0) = 2.0\pm0.3$, in good agreement with the value $R = 2$ expected from isospin invariance arguments.

At E_p = 330 MeV, a search for events corresponding to $^{12}C(p,\pi^+\pi^0)^{13}C$ was performed, leading to an upper limit (at the 2σ confidence level) of $\sigma_{\pi\pi} < 17$ nb. This limit corresponds to less than 1% of the single positive-pion production strength.

Acknowledgements

This work was possible only through the efforts and support of many people, without whom the project could not have been completed. I am grateful to all of them; however, I would specifically like to thank:

Jeremy Brown, for his assistance, guidance, and patience throughout the project as my advisor;

The other members of my committee: Bruce Vogelaar, Cem Girit, and Ed Groth, for allowing me to take that final step;

All of my collaborators, for their hard work in seeing the CE-06 experiment through to its conclusion;

Vladimir Derenchuk, Bill Lozowski, and Keith Solberg, for their much needed and gladly given technical support at IUCF during the CE-06 project;

Bob Bent and Peter Heimberg, for making my stays at IUCF tennis-filled and a more enjoyable experience overall;

The Princeton Cyclotron staff: Fred Loeser and Steve Kidner, for getting the most out of what we had, and especially Amir Razzaghi, for being so hard to beat on the links;

Yitzhak Sharon, whose friendship and guidance were invaluable almost from the start of the project, and Danny Deptuck, my officemate and friend, from whom I learned most of my chemistry;

Gregg Berman, a true friend from the very first day of our graduate school careers, for his sense of humor and perspective on life, and for being part of so many of the good memories I have from the past seven years; and, finally,

My family, especially my parents, whose love and support endured through good times and bad, and without whom I surely could not have made it this far.

Table of Contents

Abstract iv

Acknowledgements v

Chapter 1 Introduction 1

Chapter 2 Theory and Experiment: The Scientific Motivation 5

2.1 Theoretical Concepts, Models, and Predictions 5
2.1.1 Elementary Pion Production Processes: NN $\rightarrow$ NNπ 5
2.1.2 Single-Pion Production in Light Nuclei: A(p, π)A+1 7
2.1.3 Double-Pion Production in Light Nuclei: A(p, $\pi\pi$)A+1 12
2.2 Experimental Motivations: Data, Anomalies, and Resonances . . . 14
2.2.1 Single-Pion Production 14
2.2.2 Double-Pion Production 17
2.2.3 CE-06: ^{12}C(p, π) and ^{12}C(p, $\pi\pi$) via the Recoil Method 18

Chapter 3 The CE-06 Experimental Apparatus 22

3.1 The Cooler Ring 22
3.2 Targets 28
3.3 The T-Site Magnet 34
3.4 The Detector Stack 38
3.4.1 Overall Setup 38
3.4.2 The Parallel Grid Avalanche Counter 42
3.4.3 The Proportional Counter 45
3.4.4 The Silicon Array 51

3.4.5 The Luminosity Monitor 60
3.5 Electronics 62

Chapter 4 Data Analysis and Results **65**

4.1 The Analysis Method: An Overview 65
4.2 Calibration of the Detector Stack 70
4.2.1 Silicon Energy Measurement 70
4.2.2 The PC Calibration 72
4.2.3 The PGAC and Si Position Calibration 74
4.2.4 The Absolute Timing Calibration 77
4.3 First-Level Analysis: Z, M, Q, p/Q, and θ 79
4.3.1 Atomic Number (Z) 79
4.3.2 Nuclear Mass (M) and Atomic Charge (Q) 81
4.3.3 Reaction Parameters: Momentum (p) and Angle (θ, ϕ) 87
4.4 Second-Level Analysis: $L_{\rm int}$ and $d\sigma/d\Omega$ 92
4.4.1 Multiple Scattering Effects 92
4.4.2 The Calculation of $d\sigma/d\Omega$ 94
4.4.3 Determination of the Luminosity 97
4.5 Results: 166 MeV, 294 MeV, and 330 MeV 100
4.5.1 Single-Pion Production at $E_p = 166$ MeV 100
4.5.2 Single-Pion Production at 294 and 330 MeV 103
4.5.3 Double-Pion Production at $E_p = 330$ MeV 106

Chapter 5 Conclusion **109**

Appendix A: Gas Detector Operation **112**

A.1 General Principles 112
A.2 Low-Pressure Detectors 117

Appendix B: Semiconductor Detectors **119**

B.1 General Principles 119
B.2 Passivated, Ion-Implanted Silicon Detectors 123

Appendix C: Software **125**

C.1 The T-Site Magnet Map 125
C.2 Forward Raytracing Simulations 127
C.3 Backward Raytracing 130

References **134**

Index **141**

1

Introduction

Single-pion production and meson-nucleon interaction studies have been an active area of physics research ever since artificial production of mesons was achieved in the laboratory more than 40 years ago. This activity is indicative not only of the amount of knowledge already gained, but also of that yet to be learned. The work described herein is, in all generality, an attempt primarily to improve our understanding of the nuclear strong force via the study of pion-nucleon interactions in light nuclei.

Meson-nucleon studies and the research leading up to this work originated with Yukawa's extension [Yk35] of the exchange force concept to describe the nucleon-nucleon (N-N) interaction. Although firm evidence did not yet exist[1] to support the exchange character of the interaction, Yukawa postulated that the force experienced by two nucleons in close proximity is the result of emission of a massive boson from one nucleon with subsequent absorption by the other. Mathematically, a scalar potential for this force satisfies the Klein-Gordon equation for a boson of mass m,

$$\left(\nabla^2 - \frac{1}{c^2}\frac{\partial}{\partial t^2}\right)\phi = \frac{m^2c^2}{\hbar^2}\phi.$$

A static solution is

$$\phi(r) = \frac{g}{4\pi r}e^{-r/r_0},$$

[1] The charge exchange process $\mathrm{p} \rightarrow \mathrm{n} + \pi^+$ was discovered in n-p scattering more than 15 years later.

where $r_0 \equiv \hbar/mc$ and g is a constant. In the limit $m \to 0$, this solution is analogous to a Coulomb potential for a point charge of strength g.

The key characteristic of Yukawa's potential is the range of the interaction as specified by the parameter r_0: a boson mass of $m \approx 200$ MeV corresponds to a typical nuclear dimension of 1 fm. The particles in this mass range are today known as *pions*, and form an isospin $T = 1$ triplet: π^+, π^0, and π^-. Pions, as strongly-interacting particles with integral spin ($S_\pi = 0$), are part of the meson family (see Table 1.1). Since the total number of mesons is not necessarily conserved in an interaction, these particles are composed of quark-antiquark pairs, the lightest examples of which are $u\bar{d}$ (π^+) and $\bar{u}d$ (π^-).

Particle	Quarks	Mass (MeV)	τ or Γ	$T(J^P)$	Decay
$\pi^\pm$	$u\bar{d}$, $\bar{u}d$	$139.5675 \pm .0004$	2.6×10^{-8} sec	$1(0^-)$	$\pi \to \mu\nu$
π^0	$u\bar{u}$, $d\bar{d}$	$134.9739 \pm .0006$	8×10^{-17} sec	$1(0^-)$	$\pi^0 \to 2\gamma$
η	$u\bar{u}$, $d\bar{d}$, $s\bar{s}$	$548.8 \pm .6$	1.2 keV	$0(0^-)$	$\eta \to 2\gamma, 3\pi$
σ (?)	(?)	~ 560	broad	$0(0^+)$	(?)
$\rho^\pm$	$u\bar{d}$, $\bar{u}d$	$768.3 \pm .5$	~ 150 MeV	$1(1^-)$	$\rho^\pm \to 2\pi$
ρ^0	$u\bar{u}$, $d\bar{d}$, $s\bar{s}$	~ 768	~ 150 MeV	$1(1^-)$	$\rho^0 \to 2\pi$
ω	$u\bar{u}$, $d\bar{d}$, $s\bar{s}$	$781.95 \pm .14$	8 MeV	$0(1^-)$	$\omega \to 3\pi$

Table 1.1 A summary [Pd90] of the mesons most important to the nucleon-nucleon interaction at low and medium energies. The existence of the σ meson as a true resonance has not yet been verified. Only the primary modes of decay are listed in the rightmost column.

Although the exchange of pions is only part of a complete N-N interaction scenario, this mechanism is responsible for the "long-range" ($r \gtrsim 1.5$ fm) component of the nuclear binding force. In a modern picture, this force is a consequence of gluon exchange between the quarks of which mesons (see Table 1.1) and nucleons are comprised, and in principle can be described via low-energy QCD theory. Some success has been achieved, for example, by treating the meson-nucleon interaction as an overlapping collision of quark "bags" (e.g., see [Ln87]). These and other calculations can at least qualitatively reproduce the important features of the short- and medium-range N-N interaction. However, no QCD-motivated model to date can even qualitatively describe the long-range (pion-exchange dominated) part of the interaction. In the absence of a complete QCD calculation, a full description of the long-range nuclear force via the study of the π-N interaction is clearly an important step toward understanding the strong force.

Proton-induced pion production from light nuclei is a particularly important means of exploring the π-N mechanism in the nuclear medium. With the existence of a pion in the final state, the (p,π) production channel is indicative of the possibility of directly sampling the π-N interactions as they occur inside a bound nuclear system. By comparison with data obtained from the study of elementary pion production channels such as $pp \rightarrow pn\pi^+$, the analysis of (p,π) reactions in nuclei may reveal information about differences between the free and bound nucleon-nucleon interactions.

High-resolution studies of the (p,π) reaction began [Da71] in Uppsala, Sweden, more than 20 years ago, and many of the original motivations for this spectroscopic research remain today. One primary interest in reactions of this type stems from the large momentum transfers that are available. For example, in $^{12}C(p,\pi^+)^{13}C$, the minimum momentum transfer[2] is $\Delta p \approx 500$ MeV/c (or $\Delta k \approx 2.5$ fm^{-1}) for $E_p = 200$ MeV. Since the wavelengths of incident protons in this energy range are less than 2 fm, only a few target nucleons are available to participate in the reaction. In this way, the (p,π) reaction should be sensitive to the high-momentum components of single-particle nuclear wave functions.

Although the nuclear structure emphasis on these motivational considerations has changed somewhat since Uppsala, (p,π^+) studies continue to be an important focus of intermediate-energy nuclear physics. The proton-induced production of *two* pions from light nuclei is of more recent interest: the study of these reactions may yield valuable information on the medium-range (0.8 fm $< r < 1.5$ fm), higher-order π-N interactions. Relatively little is known about $(p,\pi\pi)$ from light nuclei, however, due not only to the theoretical complexity in describing such reactions (to which many elementary production channels can contribute), but also to the experimental difficulties in obtaining cross-section data. Even so, a comparison of the relative population of different ion species via $(p,\pi\pi)$ reactions may reveal key information about the importance of specific, high-order π-N diagrams to the nuclear strong force.

This work reports on a study of proton-induced single- and double-pion production in ^{12}C, at proton energies ranging from 166 MeV to 350 MeV. The study is comprised of the IUCF Cooler ring experiment designated [Se87] CE-06. Chapter 2 details the theoretical and experimental interests in pion production from light nuclei. The Cooler ring, detection apparatus, and other scientific equipment associated with the CE-06 experiment are dis-

[2] Other reactions such as $^{12}C(p,p')^{12}C$ can achieve similar momentum transfers but only for large-angle scattering of the light exit particle.

cussed in Chapter 3. Techniques used in the analysis of the data are presented in Chapter 4 along with subsequent results, and this work concludes with a summary in Chapter 5.

2

Theory and Experiment: The Scientific Motivation

Proton-induced pion production, in "elementary" pN $\rightarrow$ NNπ processes and in light nuclei, has been an intensely active area of study in intermediate energy nuclear physics over recent years. Pions, being the least massive mesons, are fundamental to the most successful, modern descriptions [Ma87] of the nucleon-nucleon interaction. A full understanding of proton-induced pion production is an important component of a complete description of the nuclear strong force. This chapter describes the theoretical and experimental motivations for the study of A(p, π)A+1 and A(p, $\pi\pi$)A+1 in general and for the CE-06 experiment in particular.

2.1 Theoretical Concepts, Models, and Predictions

2.1.1 Elementary Pion Production Processes: NN $\rightarrow$ NNπ

Pions are specific examples of *mesons*: that collection of strongly interacting particles which are also bosons, and are comprised solely of quark-antiquark pairs. As such, any number of pions can be created or absorbed in collisions between two nucleons. Table 2.1 shows the seven possible NN $\rightarrow$ NNπ reactions for which at least one of the nucleons in the incident channel is a proton. For protons with energies $E_p \approx 300$ MeV, the probe size is $\lambda_p \approx 1.5$ fm, so that for (p, π) reactions, even in heavy nuclei, the channels listed would be expected [Ma79] to play an important role in the production process.[1] Since the Q-value

[1] A truly complete calculation of A(p, π)A+1 would, in fact, predict the elementary reaction cross-

for these inelastic N-N reactions is $Q \approx -m_\pi$, the threshold proton kinetic energies are $E_{p,\mathrm{thr}} \approx 2m_\pi \approx 280$ MeV.

pN $\rightarrow$ NNπ Reaction	Isospin Decomposition
$\mathrm{p+p \rightarrow d+\pi^+}$	$\sigma_{10}(\mathrm{d})$
$\mathrm{p+p \rightarrow p+n+\pi^+}$	$\sigma_{10}(\mathrm{np}) + \sigma_{11}$
$\mathrm{p+n \rightarrow n+n+\pi^+}$	$\frac{1}{2}(\sigma_{01} + \sigma_{11})$
$\mathrm{p+n \rightarrow d+\pi^0}$	$\frac{1}{2}\sigma_{10}(\mathrm{d})$
$\mathrm{p+p \rightarrow p+p+\pi^0}$	σ_{11}
$\mathrm{p+n \rightarrow p+n+\pi^0}$	$\frac{1}{2}(\sigma_{10}(\mathrm{np}) + \sigma_{01})$
$\mathrm{p+n \rightarrow p+p+\pi^-}$	$\frac{1}{2}(\sigma_{01} + \sigma_{11})$

Table 2.1 The elementary pN $\rightarrow$ NNπ reactions and corresponding total cross-section isospin decompositions, labelled by $\sigma_{T_i T_f}$, where T_i and T_f are the isospin states of the initial and final nucleon pairs, respectively. The factors of 1/2 appear since the incident p + n state can be both $T = 0$ or $T = 1$.

To the extent that electromagnetic effects can be ignored (early measurements [Wi71] of pn $\rightarrow$ dπ^0, for example, showed that isospin-violating contributions are at the 1% level), the total reaction cross-sections can be decomposed in terms of the isospin of the initial and final nucleon pairs, as shown in Table 2.1. With this decomposition, several interesting points can be made. Since the pion is a $T = 1$ state, there can be no contribution from the isospin singlet-singlet channel σ_{00} for the pn $\rightarrow$ dπ^0 and pn $\rightarrow$ pnπ^0 reactions. For the latter, furthermore, there is no contribution from σ_{11}, since the appropriate Clebsch-Gordan coefficient, $\langle T = 1,\, M = 0 \,|\, m_{\mathrm{NN}} = 0,\, m_\pi = 0\rangle$, vanishes. These seven reactions can therefore be described by the four parameters σ_{10}(d), σ_{10}(np), σ_{11}, and σ_{01}. Finally, the table shows that whereas π^+ and π^0 production are equally represented by three channels, π^- production is possible only via pn $\rightarrow$ ppπ^-.

Probably the simplest mechanism through which elementary pion production can occur at intermediate energies is via NN $\rightarrow$ NΔ $\rightarrow$ NNπ, where Δ is the $T = 3/2$, $J = 3/2$ resonance with $m_\Delta \approx 1232$ MeV. This mechanism has in fact long been known [Lm70] to dominate pp $\rightarrow$ dπ^+: a very strong, broad peak is evident in $\sigma(E_p)$, for $\sqrt{s} \approx m_p + m_\Delta$, where s is the square of the total four-momentum. More recently, non-phenomenological models of NN $\rightarrow$ NNπ [Du87] have confirmed the Δ^{++} dominance in this reaction. For

sections of Table 2.1 in a few-nucleon simplification of the model.

such a process to occur, the initial isospin channel must be $T = 1$ since $T(\mathrm{N}\Delta) \geq 1$. The σ_{01} amplitude of Table 2.1 should therefore be small, and experimental data [Ma79] suggests that this is so. For proton energies in the 500 MeV range, in particular, $\sigma_{10}(\mathrm{d}) > \sigma_{10}(\mathrm{pn}) > \sigma_{11} > \sigma_{01}$, so that $\sigma(\mathrm{pp} \rightarrow \mathrm{d}\pi^+)$ and $\sigma(\mathrm{pn} \rightarrow \mathrm{d}\pi^0)$ $(= \sigma(\mathrm{pp} \rightarrow \mathrm{d}\pi^+)/2)$ are the dominating cross-sections.

Despite long-term efforts to model theoretically the excitation functions and angular distributions of these reactions[2], problems in the calculations remain, especially near threshold [Bl90] where the Δ resonance is not as important. For example, only the Ss, Sp, Ps, and Pp states (using the standard spectroscopic notation $L_{NN}l_\pi$ for the exit channel partial waves) should contribute significantly for $E_p \lesssim 400$ MeV. For the $\mathrm{pp} \rightarrow \mathrm{pp}\pi^0$ reaction in particular, only the Ss state is important close to the reaction threshold. Nonetheless, not until recently [Le93] have theoretical predictions been successful in describing the total cross-section for this reaction.[3]

2.1.2 Single-Pion Production in Light Nuclei: A(p, π)A+1

Although the reactions listed in Table 2.1 can be expected to contribute significantly to pion production in nuclei, there are several new considerations involved in studies of (p, π^+) on more complex $(A \geq 3)$ systems:

a) "sub-threshold" pion production (i.e., at proton energies below the threshold for elementary production) can occur, due in part to the Fermi motion of the nucleons in a bound nuclear state;

b) multiple interactions, such as internal charge exchange ($\pi^0\mathrm{p} \rightarrow \pi^-\mathrm{n}$), or absorption on a nucleon pair ($\pi^0\mathrm{np} \rightarrow \mathrm{np}$) may take place (reducing exclusive (p, π) cross-sections for heavy nuclei compared to light systems);

c) the Pauli principle and spin considerations can forbid or simplify some reaction processes: the population of a ground state nucleus, for example, may eliminate underlying contributions from some of the processes in Table 2.1;

d) collective nuclear effects can be important: the nucleus may act as a whole in $\mathrm{A}(\mathrm{p}, \pi)\mathrm{A}{+}1$ processes.

Much theoretical work has been carried out [Fe81] since the early 1970's to develop models of $\mathrm{A}(\mathrm{p}, \pi)\mathrm{A}{+}1$, instigated (at least initially) by the motivations of Ch. 1. All

[2] Phenomenological models for $\mathrm{NN} \rightarrow \mathrm{NN}\pi$ were first described [Ge54] in 1954.

[3] This is indicative, in fact, of the lack of knowledge concerning the very short-range part of the N-N interaction.

of these models incorporate some or all of the components diagrammed schematically in Fig. 2.1. Multi-nucleon effects are included through nuclear bound-state wave functions and initial and final state distortions. The wave functions directly incorporate the system's nuclear structure in the model; in fact, the use of A(p, π)A+1 as a structure probe was a primary motivation in these studies. However, the complexities involved in understanding the reaction mechanism have turned the problem around. For example, more recent model calculations ([Be92], [Co82]) tend to incorporate tractable nuclear wave functions (or those which are well-defined in terms of the shell model) to achieve insight into the fundamental production processes.

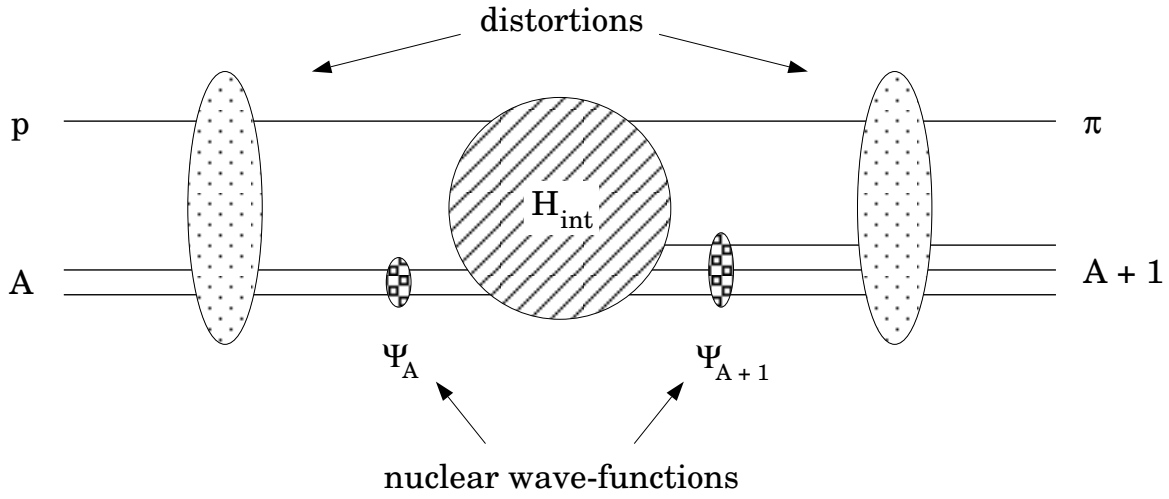

Figure 2.1 The primary components involved in modern model calculations of A(p, π)A+1: a) proton-nucleus and pion-nucleus distortions; b) nuclear wave-functions; and c) the fundamental pion production process $H_{\rm int}$.

The distortions included in the models account for the *average* effect of the initial and final nuclear states on the incident proton and outgoing pion, respectively. For the incident distortions, proton elastic scattering data (for the target nucleus in question) are typically used to generate phenomenological potentials of the proton-nucleus interaction. Similarly, the pion-nucleus distortions are usually incorporated by the calculation of optical-model parameters to describe pion-nucleus elastic scattering (for the final state nucleus in question). Both the proton and pion distortion potentials include Coulomb effects and, in fact, typically describe low-energy elastic scattering [Ks84]; however, more recent calculations [Be90] allow the inclusion of both resonant (Δ formation) and non-resonant pion-nucleus scattering potentials.

Although the nuclear wave functions and distortions are an important component of

all current models, much of the modern interest in (p,π) reactions lies in determining the structure of the complex pion-production interaction labelled by $H_{\rm int}$ in Fig. 2.1. Models are conventionally classified according to whether $H_{\rm int}$ explicitly includes a single nucleon (the "one-nucleon mechanism" or ONM) or two nucleons (TNM).[4] Conceptually, the ONM and TNM models can be described as $N \rightarrow N\pi$ and $NN \rightarrow NN\pi$ processes, respectively, within the nuclear medium.

The $N \rightarrow N\pi$ process is the simplest means by which a pion can be produced, although conservation of momentum and energy forbid the free $N \rightarrow N\pi$ reaction (unlike the elementary $NN \rightarrow NN\pi$ processes of Sec. 2.1.1). For a proton projectile, the ONM production processes are: $p \rightarrow n\pi^+$, $p \rightarrow p\pi^0$, and $p\pi^- \rightarrow n$. These reactions are possible in the nuclear medium since spectator nucleons are available to provide the needed momentum conservation.

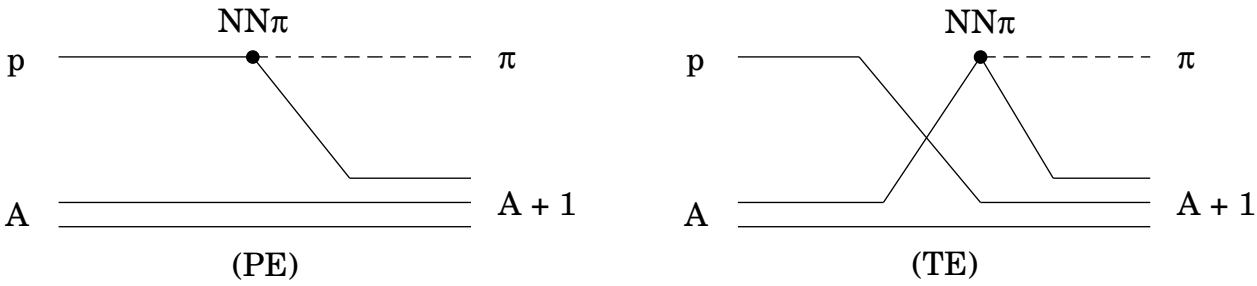

Figure 2.2 Schematic diagrams underlying the $H_{\rm int}$ part of the ONM models. The two contributions are the projectile-emission (PE) diagram (left) and the target-emission (TE) diagram (right).

Figure 2.2 schematically shows the diagrams involved in the ONM calculations, which are often referred to as "pionic stripping" models from the similarity to (d,p) and (d,n) reactions. The ONM is further categorized by the left and right diagrams in the figure, corresponding respectively to projectile emission (PE) and target emission (TE) of the pion. Most current calculations (e.g., [Al88]) that involve the ONM include only the PE diagram, although some authors [Ks84] have argued that the TE diagram tends to cancel the PE contribution. Since the TE diagrams need to be summed over all target nucleons, however, it seems likely [Al88] that the TE contribution in itself is negligible.

In the simplest ONM scenario, such as a plane-wave Born approximation (PWBA), all of the (large) momentum transfer occurs via the single captured nucleon, so that the

[4] The ONM and TNM models are both multi-nucleon calculations, however, due to the inclusion of distortions and nuclear wave functions.

process directly samples the high-momentum components of the (single-particle) bound-state wave function. Since the momentum transfer in (p, π) reactions is typically much larger than the average Fermi momentum for a light nucleus, the PWBA picture tends to greatly underestimate [Fe81] the measured cross-sections. The inclusion of distortions in a more sophisticated calculation, however, removes this problem by allowing a further means of momentum sharing. Full, relativistic ONM treatments [Co82], in fact, reproduce differential cross-sections for (p, π^+) reactions leading to doubly-magic nuclei (in both strength and shape) with reasonable success. All ONM calculations to date are, however, quite sensitive[5] to the number (e.g., pion, proton, or both) and form (calculational method or approximation) of the distortions used.

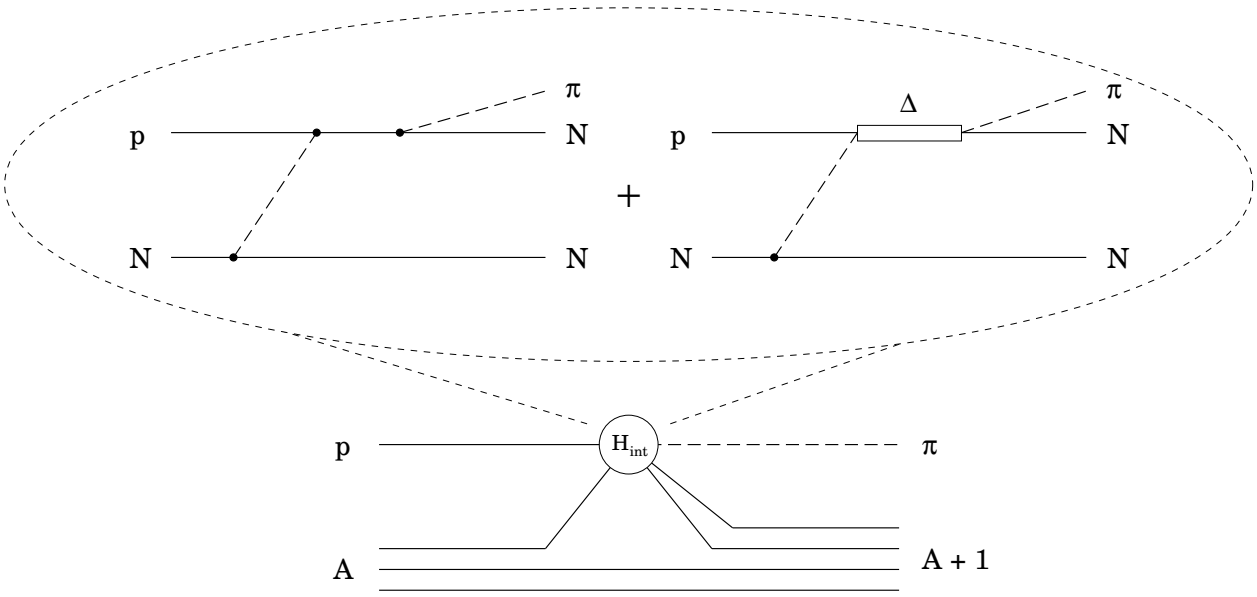

Figure 2.3 Diagrams involved in the TNM calculation of the fundamental production process $H_{\rm int}$. Only the "post-emission", TE diagrams for resonant and non-resonant pion production are shown; in general, the corresponding PE diagrams and "pre-emission" contributions (where the outgoing pion is emitted before the virtual pion is absorbed) must also be included.

Figure 2.3 shows the diagrams involved in the TNM calculations, the next level of complexity in terms of $H_{\rm int}$. This model can address specific deficiencies of the ONM calculations: π^- production (not allowed via PE ONM diagrams) can occur through the last process in Table 2.1; two-particle, one-hole (2p-1h) states in the final nucleus can be

[5] The resulting cross-sections may easily vary [Co82] by an order of magnitude or more for different types of distortions.

directly populated (the ONM can directly "reach" only single-particle states); and, the TNM does not rely as heavily on distortions for the needed momentum sharing, since the second nucleon is available to absorb some of the momentum transfer.

Another important aspect of the TNM is the capability for direct inclusion of the Δ resonance, the excitation of which can actually simplify [Ks84] the TNM calculations. For (p,π^+) reactions with $E_p \gtrsim 200$ MeV, in particular, the non-resonant diagrams of Fig. 2.3 are negligible [Iq85] in comparison to the resonant contributions. As discussed in Sec. 2.1.1, the Δ resonance dominates elementary NN $\rightarrow$ NNπ processes at intermediate energies, hence the large contribution of resonant TNM diagrams to $\mathrm{A}(\mathrm{p},\pi)\mathrm{A}{+}1$ is not unexpected.

The flexibility associated with TNM models does, however, imply considerable complexity in practical, microscopic calculations. For example, both PE and TE diagrams can contribute to the TNM, and the intermediate virtual boson can not only be a pion but also a (vector-isovector) ρ meson, even at near-threshold energies ($E_p \approx 200$ MeV). Nonetheless, an extensive, microscopic description (the "ABCD" model) has recently been developed ([Al88], [Al89], [Be90]) which incorporates both ONM and resonant TNM diagrams. Although these calculations were primarily concerned with $^3\mathrm{He}(\mathrm{p},\pi^+)^4\mathrm{He}$, several generally applicable conclusions can be drawn from this work. First, the ONM and TNM diagrams can, in general, both contribute significantly (and interfere) for a given reaction. In this way, it is not appropriate to state whether the ONM or the TNM is the "correct" production process; rather, the dominance (if any) of a particular mechanism over another for the particular reaction, proton energy, and final-state nucleus should be considered.

Second, the best results are often achieved when the nuclear states involved have well-defined shell model configurations. The application of the ABCD model to 2p-1h states [Be92] has shown considerable sensitivity to configuration mixing, as have other models [Co82] in calculations for (expected) single-particle states in carbon. Today, these sensitivities play a dual role as the *raison d'être* for (p,π) studies (for example, as a probe ([Ja85], [Vi82]) of high-spin excitations in nuclei) and as a complication in determining the fundamental production mechanism.

Finally, current calculations remain sensitive to initial and final state distortions. Although TNM calculations tend to demonstrate a weaker dependence [Iq85] on distortions than ONM models, higher-order TNM effects which are as yet not possible to include microscopically are not necessarily negligible [Di82]. A modern goal for these calculations

is the shifting of the sensitivity from distortion potentials to details of the pion production mechanism.

In summary, much progress has been made in the last two decades toward the development of fully microscopic models of pion production in nuclei. Although the most complete calculations are still sensitive to various "external" inputs such as nuclear wave functions or pion distortions, it is reasonable to hope that comparison between these models and (as yet non-existent) quark/gluon models will shed light on the form of the nuclear strong force. Through extensive comparison with (p,π) data (the primary test, of course, of $\mathrm{A}(\mathrm{p},\pi)\mathrm{A}{+}1$ models), questions of the differences between the free and bound N-N interaction may well be answered.

2.1.3 Double-Pion Production in Light Nuclei: A(p, $\pi\pi$)A+1

For proton energies greater than $E_p \approx 600$ MeV, the production of *two* pions in free NN collisions becomes kinematically feasible. The possible pN→NN$\pi\pi$ reactions are listed in Table 2.2, along with the corresponding reactions for proton bombardment on ^{12}C leading to strongly-bound final-state nuclei. Relatively little theoretical work has been applied to understanding the elementary processes, compared to their single-pion counterparts in Table 2.1. This is at least partly due to the difficulty in obtaining exclusive cross-section data for these reactions out of the single-pion background.

pN → NN$\pi\pi$ Reaction	^{12}C(p, $\pi\pi$) Reaction
$\mathrm{p}+\mathrm{p}\rightarrow\mathrm{n}+\mathrm{n}+\pi^+\pi^+$	$\mathrm{p}+{}^{12}\mathrm{C}\rightarrow{}^{13}\mathrm{B}+\pi^+\pi^+$
$\mathrm{p}+\mathrm{p}\rightarrow\mathrm{p}+\mathrm{n}+\pi^+\pi^0$ $\mathrm{p}+\mathrm{n}\rightarrow\mathrm{n}+\mathrm{n}+\pi^+\pi^0$	$\mathrm{p}+{}^{12}\mathrm{C}\rightarrow{}^{13}\mathrm{C}+\pi^+\pi^0$
$\mathrm{p}+\mathrm{p}\rightarrow\mathrm{p}+\mathrm{p}+\pi^0\pi^0$ $\mathrm{p}+\mathrm{n}\rightarrow\mathrm{p}+\mathrm{n}+\pi^0\pi^0$	$\mathrm{p}+{}^{12}\mathrm{C}\rightarrow{}^{13}\mathrm{N}+\pi^0\pi^0$
$\mathrm{p}+\mathrm{p}\rightarrow\mathrm{p}+\mathrm{p}+\pi^+\pi^-$ $\mathrm{p}+\mathrm{n}\rightarrow\mathrm{p}+\mathrm{n}+\pi^+\pi^-$	$\mathrm{p}+{}^{12}\mathrm{C}\rightarrow{}^{13}\mathrm{N}+\pi^+\pi^-$
$\mathrm{p}+\mathrm{p}\rightarrow\mathrm{p}+\mathrm{n}+\pi^0\pi^-$	$\mathrm{p}+{}^{12}\mathrm{C}\rightarrow{}^{13}\mathrm{O}+\pi^0\pi^-$

Table 2.2 The elementary pN → NN$\pi\pi$ reactions and corresponding double-pion production reactions from ^{12}C. Reactions leading to final-state pn pairs also have deuteron counterparts (not shown). The $\pi^-\pi^-$ elementary reaction (also not shown) leads to the unbound nucleus ^{13}F.

The charge-exchange reactions $(\pi^\pm,\pi^\mp)$ and $(\pi,\pi\pi)$ processes, however, have been studied fairly extensively in recent years. Fig. 2.4 demonstrates the intimate connection

between the $(\pi, \pi\pi)$ and $(\mathrm{p}, \pi\pi)$ reactions for two particular diagrams (called the "pion-pole" and "contact" terms). A complete model for $(\pi, \pi\pi)$ must consider [Os85] many more diagrams: for example, those with intermediate Δ states[6] or two and three pion vertices for each nucleon line. Although these diagrams can primarily contribute only as higher-order effects in single-pion production (and are "included" in the $\mathrm{A}(\mathrm{p}, \pi)\mathrm{A}{+}1$ models via distortions), the neglect of such non-linear terms in microscopic double-pion production calculations results [Os85] in significant underprediction of measured $(\pi, \pi\pi)$ cross-sections.

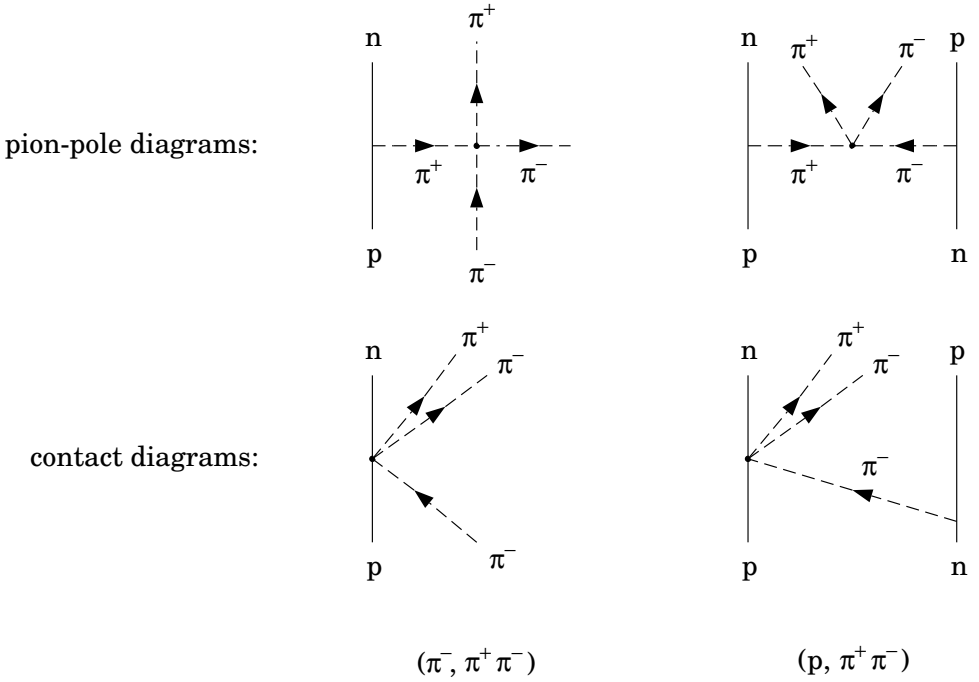

Figure 2.4 A comparison between the $(\pi, \pi\pi)$ (left) and $(\mathrm{p}, \pi\pi)$ (right) reactions for two important contributing diagrams: the pion-pole (top) and contact (bottom) terms (as specific examples, $(\pi^-, \pi^+\pi^-)$ and $(\mathrm{p}, \pi^+\pi^-)$ are shown). The diagrams are highly non-linear: three- and four-pion vertices are involved.

This complicated situation is greatly simplified ([Os85], [Jk90]) near the threshold of the $(\pi, \pi\pi)$ reaction (and correspondingly for $(\mathrm{p}, \pi\pi)$). In particular, only four diagrams can contribute, two of which are the pion-pole and contact terms shown in Fig. 2.4 for both $(\pi, \pi\pi)$ and $(\mathrm{p}, \pi\pi)$. As third- and fourth-order pion diagrams, respectively, the contact and pion-pole diagram strengths directly reflect any possible underlying symmetry breaking in the chiral πN interaction. The contributions of the other two diagrams that do not vanish

[6] At $E_p \approx 1.5$ GeV, for example, $\mathrm{NN} \rightarrow \Delta\Delta \rightarrow \mathrm{NN}\pi\pi$ should [Lm70] be important.

near-threshold are not well-defined[7]. Nonetheless, the behavior of the very near-threshold cross-section for $(\pi, \pi\pi)$ (and for $(\mathrm{p}, \pi\pi)$) as a function of incident pion (proton) energy is sensitive [Os85] to this symmetry breaking (if it exists). No data for $(\pi, \pi\pi)$ as yet exists for $E_\pi < 200$ MeV, and similarly for elementary $(\mathrm{p}, \pi\pi)$ with $E_p \lesssim 700$ MeV [Dh83].

A related interest in these reactions is the possible formation of quasi-bound ($\Gamma \approx 30$ MeV), multiple-pion states within the nuclear medium. These states could, for example, consist [Sk88] of $(\pi\pi)^{T=0}_{J=0}$ pairs, analogous to electron Cooper pairs. Other authors [Ei80] suggest that double-pion production reactions would be sensitive to effects indicative of Bose condensed pion groups; however, the $(\pi, \pi\pi)$ sensitivity to such "pre-cursor" phenomena has recently been questioned [Os86].

Although the similarity of $(\mathrm{p}, \pi\pi)$ and $(\pi, \pi\pi)$ is evident from Fig. 2.4, one can infer from the discussion in Sec. 2.1.2 that proton-induced double-pion production in light nuclei will in general be more complicated than the elementary $(\pi, \pi\pi)$ processes. Near threshold, however, it may at least be possible [Wa52] to distinguish the production mechanism from $\pi\pi$ interaction effects. Furthermore, as with single-pion production, isospin constraints can simplify the picture somewhat.

For example, the contact term of Fig. 2.4 does not [Di89] contribute, near threshold, to the ^{13}B reaction in Table 2.2, whereas both diagrams can contribute to the ^{13}C reaction. Determination of the ratio $\sigma(^{13}\mathrm{B})/\sigma(^{13}\mathrm{C})$ near threshold, therefore, directly measures the relative strengths of these two diagrams. Similarly to (p, π) studies, it is hoped that cross-section data for $\mathrm{A}(\mathrm{p}, \pi\pi)\mathrm{A}{+}1$, perhaps near threshold, may reveal much about the NN interaction within the nucleus.

2.2 Experimental Motivations: Data, Anomalies, and Resonances

The theoretical motivations of Sec. 2.1 can hardly be considered to be independent of the experimental data for pion production in light systems. In this sense, the need for high-quality data as a basis of comparison for models of single- and double-pion production is an important experimental motivation ([Fe81], [Ma79]) for these studies. Rather than reviewing the complete body of existing pion-production data, however, this section considers specific, recent experimental developments in pion production which the CE-06 experiment hopes to address in particular.

---

[7] The strengths of these diagrams depend indirectly [Os85] on the characteristics of the σ "resonance" of Table 1.1.

2.2.1 Single-Pion Production

Cross-section data for several of the proton-induced, elementary pion production reactions in Table 2.1 have been available [Jo82] for more than a decade, and in particular for proton energies in the realm of the Δ resonance ($E_p \approx 600$ MeV). More recently, very near-threshold measurements ($E_p \lesssim 320$ MeV) of $pp \rightarrow pp\pi^0$ ([Me90], [Me92]), $pp \rightarrow pn\pi^+$ [Ha93], and $pp \rightarrow d\pi^+$ [He93] cross-sections have added significantly to the data base for $NN \rightarrow NN\pi$ reactions.

The situation for (p, π^+) data in light nuclei is now, however, somewhat different: Due in part to the possibility of sub-threshold pion production, a fair amount of high-resolution (p, π^+) data exists ([Gr83], [So81], [Hd80]) near threshold ($E_p \lesssim 200$ MeV), but not in the realm of the Δ (200 MeV $\lesssim E_p \lesssim 400$ MeV). This lack of data is the case in particular for positive-pion production on carbon via $^{12}C(p, \pi^+)^{13}C_{g.s.}$ (see Fig. 2.5), for which differential cross-sections have been measured at only three proton energies greater than $E_p = 250$ MeV.

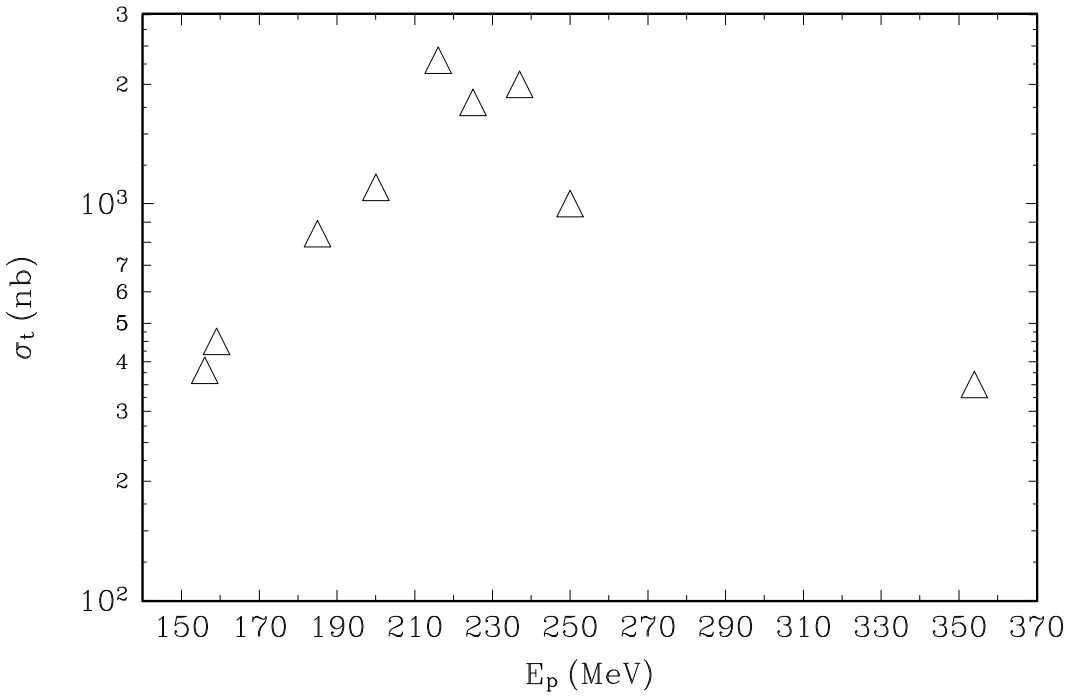

Figure 2.5 Total cross-section data for $^{12}C(p, \pi^+)^{13}C_{g.s.}$ as a function of the incident proton energy. The data are from a variety of sources ([Hu87] and references therein).

The target ^{12}C has received more attention in *near-threshold* pion production studies than other, light ($A \lesssim 20$) nuclei for several reasons. Experimentally, ^{12}C targets are

advantageous in that pure samples are readily available and easily constructed [Lz92] into solid targets of varying thicknesses. Also, ^{12}C is the lightest nucleus (other than ^{4}He) which is stable and spinless in its ground state, simplifying experimental and theoretical treatments. Finally, the nuclei in the $A = 12 - 14$ mass region, including the (p, π) reaction products from ^{12}C targets, have been studied [Ko89] fairly extensively in other, high-momentum transfer reactions. Consequently, the nuclear structure in this mass region has been reasonably well-determined ([Aj90], [Aj91]).

Measurements of cross-sections for $^{12}\mathrm{C}(\mathrm{p}, \pi^+)^{13}\mathrm{C}$ and $^{12}\mathrm{C}(\mathrm{p}, \pi^-)^{13}\mathrm{O}$ in the Δ resonance region are needed to fully map out the energy dependence of the total cross-section, as has been suggested before [Lo84]. Although the dominant role of the $\Delta(1232)$ baryon in $\mathrm{A}(\mathrm{p}, \pi^+)\mathrm{A}{+}1$ seems to be on firm ground [Be92], the shift of the maximum of the excitation function [Hu87] below the Δ invariant mass is somewhat surprising. Furthermore, data for $^{12}\mathrm{C}(\mathrm{p}, \pi^-)^{13}\mathrm{O}$ cross-sections with 205 MeV $< E_p <$ 600 MeV are non-existent and necessary to elucidate the role of non-resonant contributions that are important [Be92] at lower energies, compared to (p, π^+).

The above considerations for studying pion production from ^{12}C in the resonance region also apply to $^{12}\mathrm{C}(\mathrm{p}, \pi^0)^{13}\mathrm{N}$. Even compared to $^{12}\mathrm{C}(\mathrm{p}, \pi^-)^{13}\mathrm{O}$, the neutral pion reaction has received little attention, and to date there are only two studies ([Pi93], [Ho92]). In part, this lack of data is due to the experimental difficulty in measuring exclusive cross-sections for reactions with a neutral particle in the exit channel. Furthermore, one could argue that no fundamentally different information is available from (p, π^0): the isospin amplitudes for the contributing two-nucleon elementary processes (see Table 2.1) are the same for π^+ and π^0. The reactions $^{12}\mathrm{C}(\mathrm{p}, \pi^+)^{13}\mathrm{C}_{\mathrm{g.s.}}$ and $^{12}\mathrm{C}(\mathrm{p}, \pi^0)^{13}\mathrm{N}_{\mathrm{g.s.}}$ are, in particular, closely related due to the simple isospin structure of the target ($T = 0$) and final-state ($T = 1/2$) nuclei. After Coulomb corrections, the total cross-sections for these reactions are related by a simple ratio of Clebsch-Gordan coefficients:

$$R = \frac{\sigma(\pi^+)}{\sigma(\pi^0)} = \left(\sqrt{\frac{2}{3}} \Big/ \sqrt{\frac{1}{3}} \right)^2 = 2. \tag{2.1}$$

Nonetheless, an apparent discrepancy in this simple picture has itself provided motivation for further study of the $^{12}\mathrm{C}(\mathrm{p}, \pi^0)^{13}\mathrm{N}$ process in the threshold region. Fig. 2.6 shows a comparison between the total cross-sections for $^{12}\mathrm{C}(\mathrm{p}, \pi^+)^{13}\mathrm{C}_{\mathrm{g.s.}}$ and $^{12}\mathrm{C}(\mathrm{p}, \pi^0)^{13}\mathrm{N}_{\mathrm{g.s.}}$, for $E_p \lesssim 200$ MeV. For proton energies of 154 MeV ($\eta \approx 0.34$) and 186 MeV ($\eta \approx 0.78$), the measured ratio of the cross-sections is in good agreement with Eq. (2.1). However, at

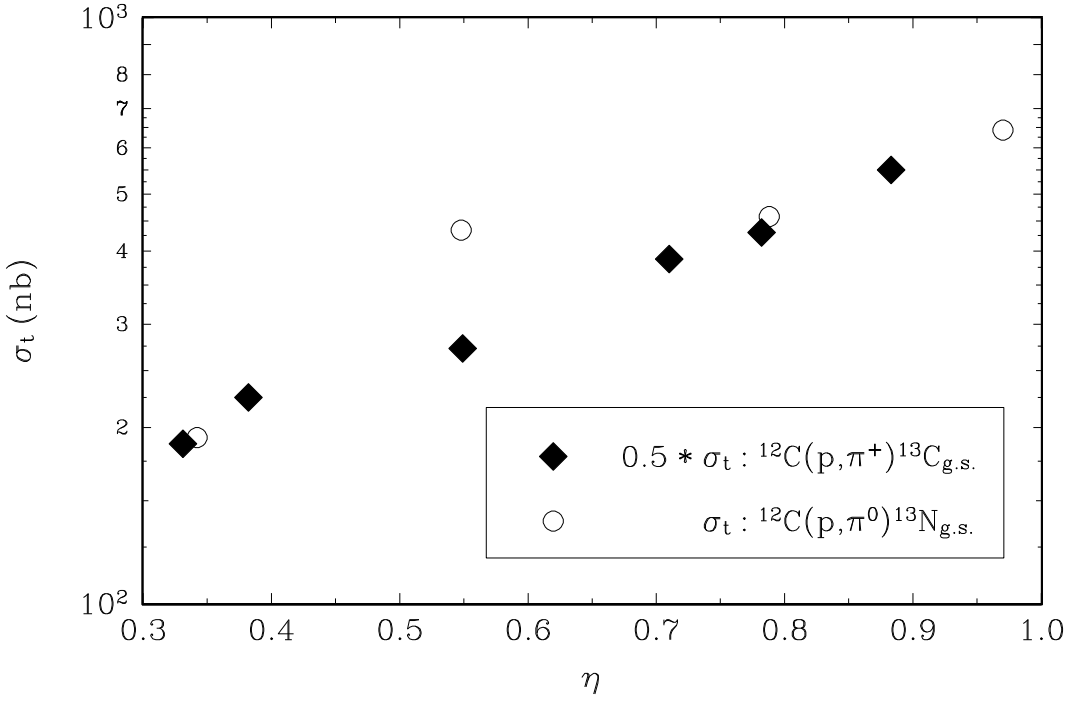

Figure 2.6 Comparison of the total cross-sections for $^{12}\mathrm{C}(\mathrm{p},\pi^+)^{13}\mathrm{C}_{\mathrm{g.s.}}$ and $^{12}\mathrm{C}(\mathrm{p},\pi^0)^{13}\mathrm{N}_{\mathrm{g.s.}}$ (adapted from [Ho92]), as a function of the center-of-mass reduced momentum $\eta \equiv p_\pi/m_\pi c$. The (p,π^+) cross-sections have been multiplied by a factor of 1/2 to account for Eq. (2.1).

$E_p = 166$ MeV ($\eta \approx 0.55$), the ratio falls [Ho92] to $R = 1.27 \pm .05$. Pickar *et al.* [Pi93] have argued that Coulomb suppression of the low-energy π^+ production can explain the 166 MeV discrepancy, although this analysis produces a similar but "opposite" anomaly ($R = 2.8 \pm 0.4$) at 186 MeV, using the data of [Ho92] (π^0) and [So81] (π^+). In any case, there is clear need for confirmation of the anomaly (if it exists) via further measurements of $^{12}\mathrm{C}(\mathrm{p},\pi^0)^{13}\mathrm{N}_{\mathrm{g.s.}}$ for $E_p < 200$ MeV.

2.2.2 Double-Pion Production

In contrast to the modern availability of $\mathrm{A}(\mathrm{p},\pi)\mathrm{A}{+}1$ data, there are to date no exclusive studies of $\mathrm{A}(\mathrm{p},\pi\pi)\mathrm{A}{+}1$ within 400 MeV of the threshold ($E_p \approx 2m_\pi c^2$). Extrapolating from measured elementary $\mathrm{NN} \rightarrow \mathrm{NN}\pi\pi$ cross-sections [Dh83] near $E_p \approx 800$ MeV, the expected cross-sections would indeed be small: from approximately 1 to 100 nb. However, the corresponding $\pi\pi$ production cross-sections may [Gn87] be significantly larger in nuclei. The only existing experimental study [Fn90] of $\mathrm{A}(\mathrm{p},\pi\pi)\mathrm{A}{+}1$ ($E_p = 800$ MeV) suggests that a cross-section measurement is feasible (i.e., 1 nb $\lesssim \sigma \lesssim$ 100 nb) even within 250 MeV of the threshold energy. Hence, the biggest *a priori* challenge in studies of $\mathrm{A}(\mathrm{p},\pi\pi)\mathrm{A}{+}1$

may rest in the exclusivity of the measurement; as mentioned before, the background from single-pion production would be significant for intermediate energy protons.

Inclusive measurements of proton-induced pion production in nuclei *do* exist, however, and recent studies ([Kr82], [Ju84], [Ak92]) report an excessive production of low-energy pions (compared to that for high-energy pions) near $E_p = 350$ MeV, which would seem to suggest an enhanced double-pion production. Although the possibility of the formation of $(\pi\pi)$ bound states in nuclei has been suggested theoretically [Sk88] and experimentally [Ca93] in this energy range, the apparent width ($\Gamma < 10$ MeV) of the resonance at $E_p = 350$ MeV is much too narrow to be explained in this way. The enhancement may, however, be the result [Ku90] of the double-pion decay of a $\Delta\Delta$ state in nuclear matter. Exclusive double-pion production data for $E_p \approx 350$ MeV is clearly needed to confirm the existence of this structure.

2.2.3 CE-06: ^{12}C(p, π) and ^{12}C(p, $\pi\pi$) via the Recoil Method

Nearly all of the experimental studies of pion production in nuclei referred to in this section were accomplished via detection of the pion (or, one of the pions, in the case of the inclusive $\pi\pi$ production experiments). Several very successful studies for $E_p \lesssim 200$ MeV were completed using high-resolution spectrometers: notably, the Indiana QDDM and QQSP devices [Gr82]. However, the need for a large momentum bite (due to the large range in p_π possible even near threshold), large solid angle ((p, π) total cross-sections in light nuclei are typically less than 1 microbarn), and short pion flight paths (to reduce decay losses) greatly complicates the construction of the spectrometers. At higher energies (300 MeV $\lesssim E_p \lesssim$ 500 MeV), the emitted pions are magnetically very stiff ($B\rho \approx 1$ T-m) and other detection methods [Fa86] must be employed. Furthermore, none of these techniques is applicable for studies of (p, π^0) or any exclusive measurements of systems with three-body final states.

The CE-06 experiment addresses these difficulties for the study of pion production from ^{12}C by detection of the (heavy) recoil ion.[8] The method of recoil detection has several immediately apparent advantages for measurements of (p, π) in light nuclei. First, the determination of cross-sections for (p, π^+), (p, π^0), (p, π^-), and $(\mathrm{p}, \pi\pi)$ can be accomplished simultaneously. Table 2.3 shows the possible recoil ions for the different charge states of the pion(s) emitted in $^{12}\mathrm{C} + \mathrm{p} \rightarrow \pi(\pi) + \mathrm{X}$. Here, the detection of a mass-13 recoil ion uniquely specifies the reaction via conservation of baryon number. This ability to use

[8] The reaction nomenclature used in this work, however, always lists the recoil ion *last*.

$Q_{\pi(\pi)}$	$A = 13$ Ion	Possible Final States
$+2$	^{13}B	ground state only
$+1$	^{13}C	0.0, 3.09, 3.68, 3.85
$+0$	^{13}N	ground state only
-1	^{13}O	ground state only

Table 2.3 Recoil ions obtained in pion production from proton bombardment of ^{12}C, as specified by the total charge of the outgoing pion(s). Also given are the final-state nuclear excitation levels (MeV) that are accessible via the recoil method.

the same integrated beam, target, and detection system for several reaction measurements is clearly well-suited for studies of branching ratios into the different isospin channels.

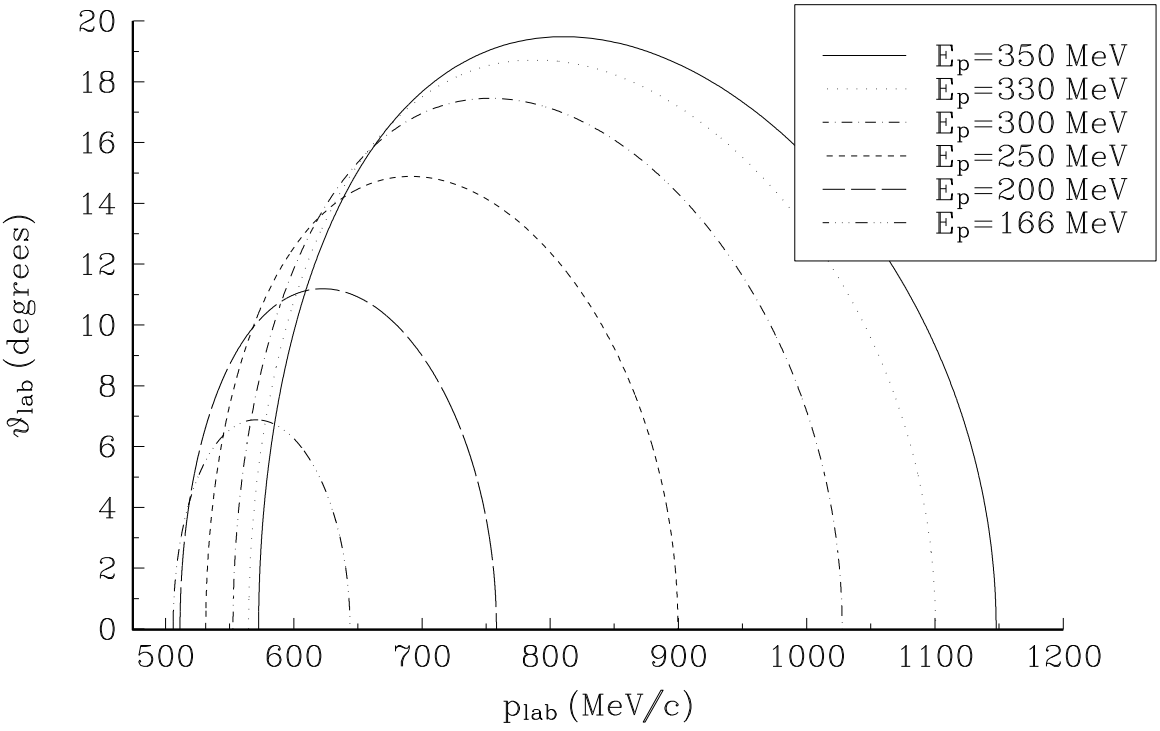

Figure 2.7 Laboratory (target-at-rest) kinematics for $^{12}\mathrm{C}(\mathrm{p},\pi^+)^{13}\mathrm{C}_{\mathrm{g.s.}}$, for several incident proton energies within 200 MeV of the reaction threshold. The ^{13}C recoil polar angle θ is plotted vs. the ion momentum.

Another motivation for the recoil method is kinematical in nature: in the laboratory, the heavy particle is emitted in a limited range of angles with respect to the beam direction. Fig. 2.7 describes the kinematics of $^{12}\mathrm{C}(\mathrm{p},\pi^+)^{13}\mathrm{C}_{\mathrm{g.s.}}$ for proton beam energies in the range covered by the CE-06 experiment. Close to threshold ($E_p < 170$ MeV), the ^{13}C

recoils are emitted in a narrow forward cone with $\theta_{\max} \lesssim 7°$. Even 200 MeV above the reaction threshold, the maximum recoil emission angle is less than 20° with respect to the incident beam direction. This kinematical "compression" from the center-of-mass system to the laboratory frame allows solid angles which are reasonably achieved in the lab (e.g., $\Omega \approx 10$ msr) to correspond to nearly 4π acceptance in the c.m.s., near threshold. Other authors ([Sc86], [Ho87]) have demonstrated the feasibility of studies of near-threshold π^+ production in light nuclei, using recoil detection techniques.

A third reason to use the recoil method is the ability to measure neutral-pion reactions along with the corresponding charged-pion states via the same experimental apparatus. By detection of the recoil, the difficulties involved in the coincident measurement of high-energy γ rays (from $\pi^0 \rightarrow \gamma\gamma$) are avoided. With the exception of a single, very near-threshold measurement [Pi93], the only reported A(p, π^0)A+1 work (with $A > 4$) has used the recoil method [Ho92] (the data from which is shown in Fig. 2.6).

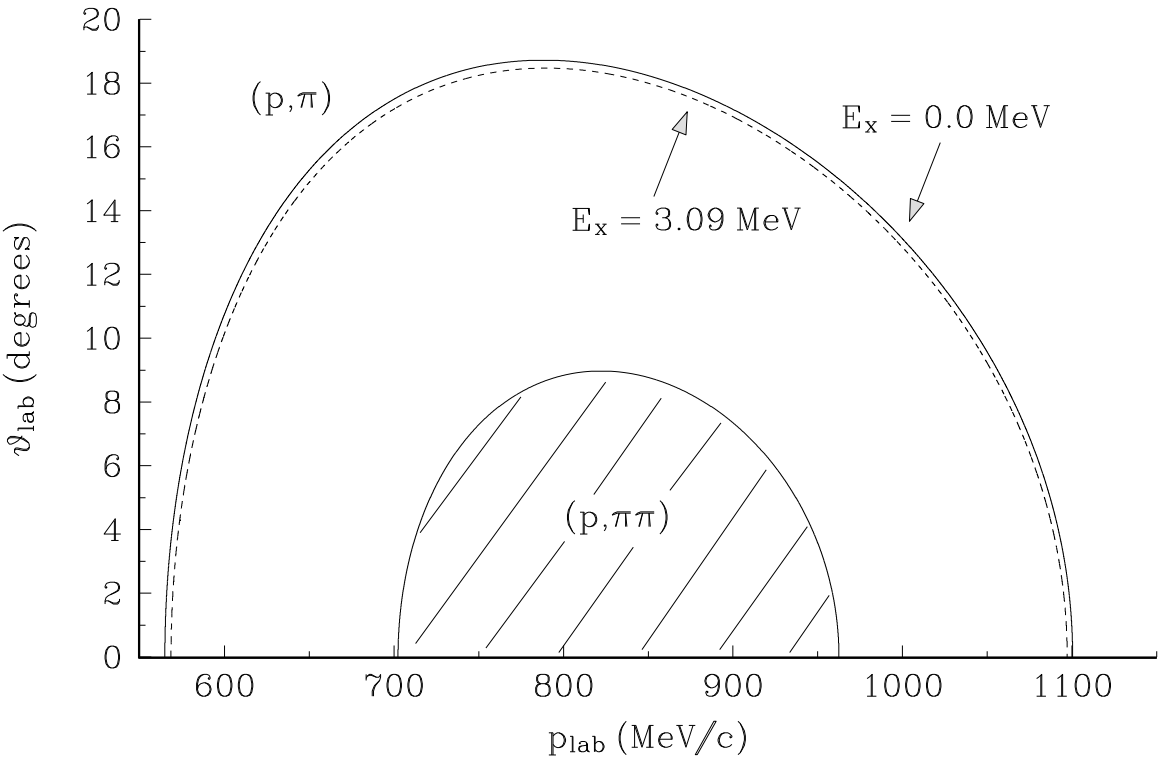

Figure 2.8 The recoil ion kinematics ($E_p = 330$ MeV) of ^{12}C(p, π^+)^{13}C (two-body final state) compared to ^{12}C(p, $\pi^+\pi^0$)^{13}C (three-body final state). The locus of single-pion events lies only along the curves shown (^{13}C ground state and first excited state), and so is well-separated from the two-pion locus.

Finally, the recoil method can greatly simplify the measurements of reactions which

lead to three-body final states, such as $^{12}\mathrm{C}(\mathrm{p},\pi\pi)$. Although two-pion final states with the same charge as corresponding single-pion emissions lead to identical types of recoil ions, the single- and double-pion production kinematics are well-separated, as shown in Fig. 2.8. The complete identification of an $M = 13$ nucleus within the shaded area of the figure corresponds uniquely to a double-pion production reaction.

The remainder of this work details the study of proton-induced, single- and double-pion production from $^{12}\mathrm{C}$ as realized in the CE-06 experiment, which was developed and carried out at the Indiana University Cyclotron Facility in 1991–93. Since much near-threshold $^{12}\mathrm{C}(\mathrm{p},\pi^+)^{13}\mathrm{C}$ work has already been done, the primary goals of CE-06 are to study the $^{12}\mathrm{C}(\mathrm{p},\pi^0)^{13}\mathrm{N}$ reaction (addressing in particular the anomaly of Fig. 2.6) and to attempt the first measurements of double-pion production in light nuclei near threshold.

3

The CE-06 Experimental Apparatus

The subject of this work, the Cooler ring experiment CE-06, involved the development and construction of equipment designed specifically to take advantage of the physics opportunities afforded by the new accelerator. CE-06 was the first experiment to measure exclusive pion production using a solid target in a storage ring, and represented the first use of heavy recoil ($A > 4$) detection techniques in such a facility. To achieve these goals, a number of experimental challenges had to be met. This chapter describes the Cooler ring facility and the detection apparatus specific to the CE-06 experiment.

3.1 The Cooler Ring

The Indiana University Cyclotron Facility (IUCF) synchotron-storage ring, known in short as the "Cooler," was completed in March, 1988, and the first proton beams were stored a month later. The Cooler represented a new and unique opportunity for nuclear physics: the use of medium-energy light-ion beams of unprecedented brightness and quality. Now, after only a few years of operation, new physics measurements have been made, with an improvement in precision by an order of magnitude in some cases. The elementary pion-production process $pp \rightarrow pp\pi^0$ has been studied in detail [Me90] near threshold to great success, inspiring new theoretical calculations to explain the data [Le93]. A study of s-wave processes in near-threshold $pp \rightarrow pn\pi^+$[Ha93] yielded data closer to threshold (within 2 MeV) than previously accomplished by a factor of 50. The CE-06 experiment

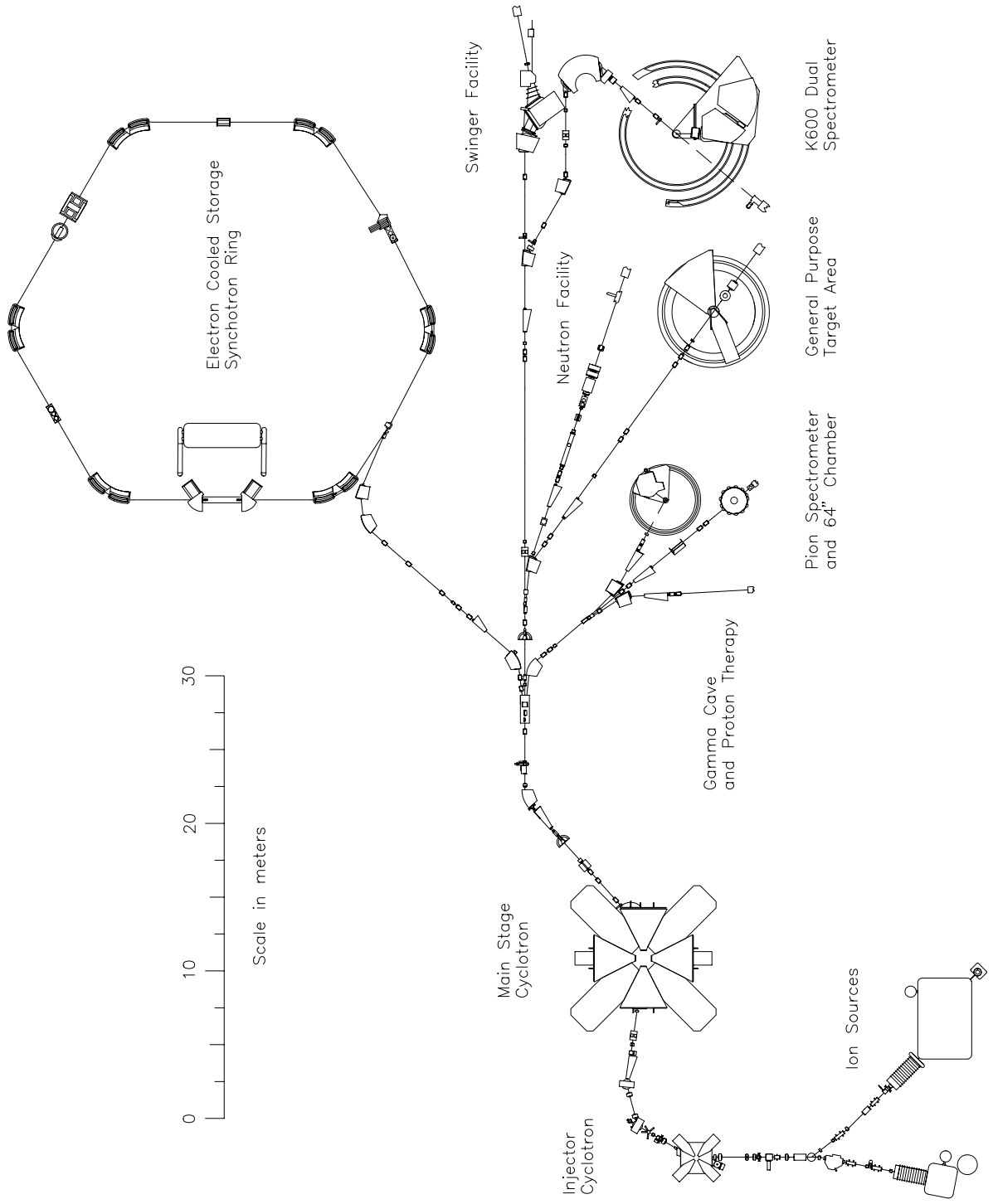

Figure 3.1 Simplified schematic of IUCF, including the injection and main cyclotrons, experimental areas, and Cooler ring. Not shown is the high-intensity polarized ion source to be commissioned in 1993.

was ideally suited to the Cooler, primarily because of the high luminosities possible even with ultra-thin targets.

Figures 3.1 and 3.2 show the Cyclotron Facility and Cooler Ring, respectively, at Indiana University, Bloomington, Indiana. The ion sources can provide both polarized and unpolarized beams of several light-ion species, including H_2^+, He^+, and Li^+. The two-stage accelerator produces proton beams with energies of up to 200 MeV, and services the variety of experimental areas shown in Fig. 3.1. For the CE-06 experiment, the cyclotron facility served as the injection device to the Cooler ring, which can accelerate proton beams to nearly 500 MeV.

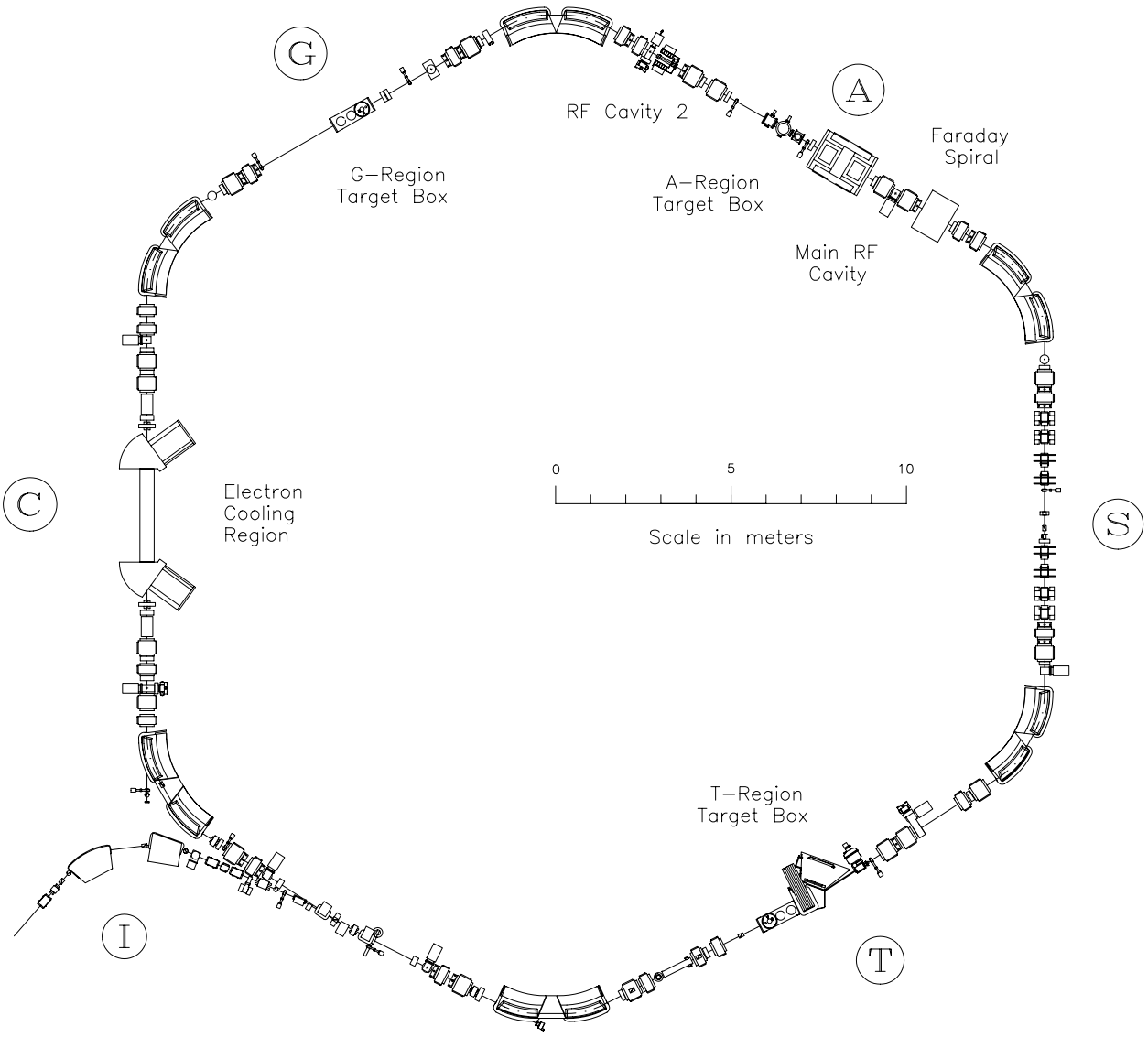

Figure 3.2 The IUCF Cooler ring, with the electron cooling system at the left and the CE-06 location (T-site) at the lower right.

Unlike the main cyclotron and the associated experimental areas, the Cooler is a

storage ring designed for multi-pass experiments using internal targets. Figure 3.2 shows a more detailed drawing of the Cooler. The unusual hexagonal design makes possible a larger number of experimentally accessible straight-sections than in the more typical four-sided "ring." Of the six possible areas, only the cooling system (C) and injection (I) sections are devoted solely to machine operation. The tagged beam (T) and general (G) regions are exclusively for experimental use, whereas the acceleration section (A) not only contains the RF synchotron cavity but has recently been the site of several polarized target experiments [Fr93]. Some important ring parameters are listed in Table 3.1.

General	E_p	30–480 MeV
	ΔE_p (300 MeV)	± 100 keV (sys.) ± 20 keV (stat.)
	$(\beta\rho)_{\max}$	3.6 Tesla-meters
	$L_{\rm ring}$	$86.78 \pm .01$ m
	A_x ($\approx A_y$)	30π mm-mrad
	$\Delta p/p$	$\pm 0.2\%$
	Ramp rate	1 Tesla-meter/sec
Cooling System	kT_e	0.1–0.2 eV
	I_e	0.5–4 amps
	e^- beam diameter	2.5 cm
	$\tau_{\rm cool}$ (300 MeV)	0.5 sec
	longitudinal B field	0.15 Tesla

Table 3.1 Some characteristic cooler ring parameters.

The centerpiece of the Cooler is its namesake, the electron cooling system. The term "cooling" is used here to describe the increase in phase space density of the circulating ion beam. Equivalently, in a reference frame moving at the beam's average velocity, the cooling can be viewed as a decrease in the width of the ions' velocity distribution, i.e., a reduction of its "temperature." Beam cooling is often very beneficial to experiments for a variety of reasons. First and foremost is the quality of the beam: the small transverse emittance resulting from cooling implies an extremely localized beam profile on target with small halo, and subsequent reduction of background. The compressed longitudinal momentum phase space results in excellent beam energy definition, making possible measurements at closely spaced energies, which is especially important near the threshold of a particular reaction. For example, in the T-region, where the CE-06 experiment was located, a 150 MeV proton

beam on a 100 ng/cm^2 ^{12}C target, typically has [Me88] a diameter of 2 mm, a divergence of less than 1 mrad, and an energy spread (FWHM) of less than 10 keV.[1] In comparison, a 150 MeV proton beam generated by the cyclotron is characterized [Gr83], after momentum selection and collimation in an analyzing magnet, by an energy spread (FWHM) of 160 keV.

Another benefit of cooling is the possibility of running luminosity-limited experiments, for example, measurements of near-threshold and nanobarn-scale cross-sections. A storage ring requires very thin targets ($d_{\rm tgt} < 100$ ng/cm^2) since the beam is not constantly being replenished as in a single-pass facility. Normally, this would imply luminosities much smaller than that in typical cyclotron experiments. However, the use of cooling enables the storage of very intense beams, yielding large luminosities even with the necessarily thin targets. More than 1 mA of protons have been stored in the Cooler, and luminosities greater than 10^{30} cm^{-2} sec^{-2} have been achieved with both gaseous [Dr91] and solid [this work] targets.

Finally, cooling can greatly increase the storage lifetime of ion beams by counteracting "heating" due to residual beam-line gases or targets, and other destabilizing effects.[2] In the original electron cooling studies [Bu76], the beam lifetime was increased by nearly a factor of 6 compared to a non-cooled beam. Storage times of almost two hours [Po90] have been achieved at the Cooler, with a typical ring vacuum of better than 10^{-8} torr H_2 equivalent.

At IUCF, the cooling process is accomplished by accelerating a "cold," intense ($I_e \approx$ 1 A) electron beam parallel to the circulating ion beam for a short distance (about 3 meters) in the cooling section (C). The electron energy is tuned to match the ions' average velocity to better than one part in 10^3. In this situation, the cooling process has a quantitative analog in the passage of ions through matter, where the particles lose energy via collisions with atomic electrons, eventually coming to rest in the material. The cooling mechanism is essentially the same process, when viewed from the electrons' rest frame, as long as the electron temperature is much lower than that of the ions.

Equilibrium between the electrons and ions is typically reached in a few hundred msec. This can be accelerated by the strong longitudinal magnetic field commonly used to contain the intense electron beam against its own space charge build-up. The field can also allow the ion beam to be cooled to temperatures well below that of the electrons [Pa84].

---

[1] The accuracy of the absolute value of the beam energy is, however, typically an order of magnitude worse than this (see Table 3.1), due primarily to the uncertainty in the ring circumference $L_{\rm ring}$.

[2] Here, the lifetime is defined as $1/\tau \equiv (-1/N)dN/dt$, where N is the number of stored ions.

Parameters characteristic of the cooling system at IUCF are shown in the lower half of Table 3.1.

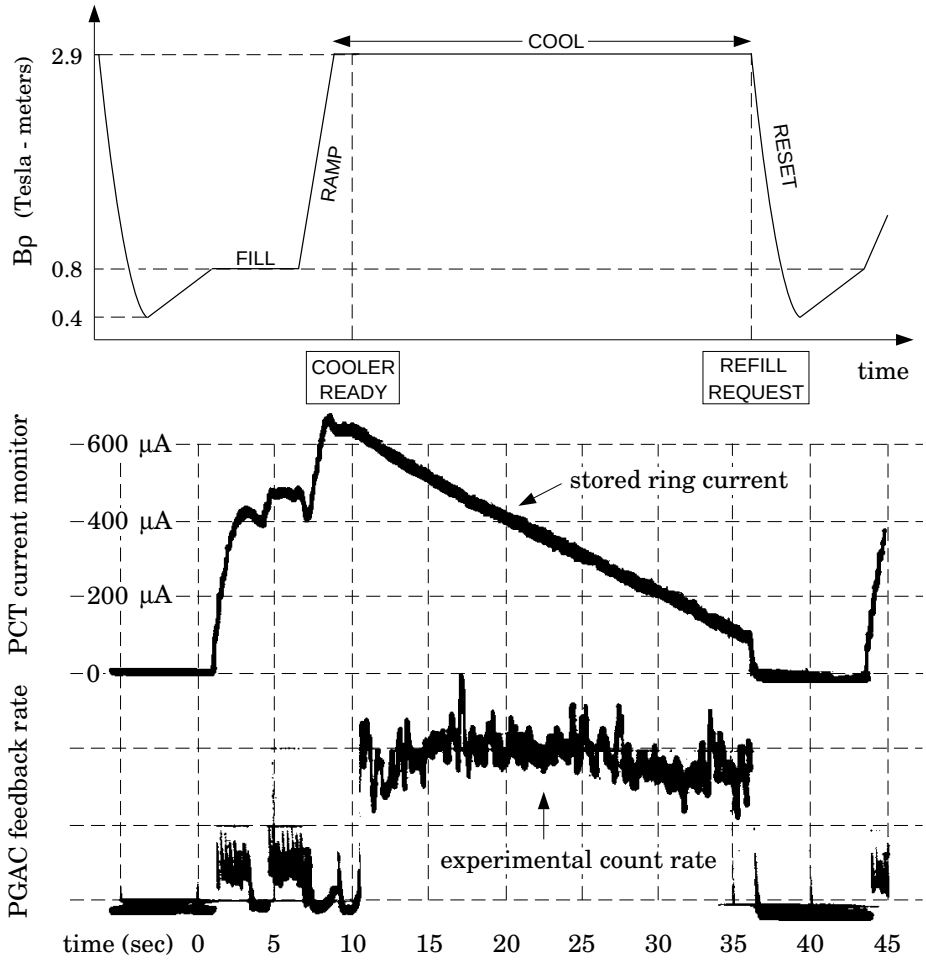

Figure 3.3 A Cooler cycle typical to the CE-06 experiment. The upper half shows the time dependence of the ring rigidity for $E_p = 330$ MeV. The lower half displays the stored current and experimental data rate on the same time scale, taken from an actual scope display. The apparent increase in current during the ramp is artificial.

The operation of the Cooler is executed in cycles, since the experimental target depletes the beam and new particles must be injected periodically. Fig. 3.3 shows the time structure of a ring cycle characteristic to this work. The first part of the cycle is the beam injection from the main cyclotron into the ring. For an unpolarized proton beam, as needed for the CE-06 experiment, "stripping injection" is used. Using molecular hydrogen ions from the ion source, a 90 MeV H_2^+ beam is produced by the cyclotron, and stripped by a thin carbon foil in the I-region, resulting in a 45 MeV proton beam in the ring. Beam

is injected at the edge of the ring's transverse acceptance until the rate of particles gained equals the rate lost (usually after a few hundred msec).[3] The new beam is then moved away from the foil via bumper magnets and cooled so that the beam can be brought back again close to the foil for further injections. Typically, five to ten injection pulses are used per cycle. Cooling of the ions during the injection is critical to obtaining a highly intense stored beam: the circulating protons must be brought close to the (fixed) foil, which is located near the edge of the ring acceptance.

After injection is completed, often in a few seconds for unpolarized beam, a cool–ramp–cool sequence occurs. The cooling before acceleration increases the ramping efficiency by making the beam less susceptible to magnetic distortions or other effects which could normally bring some beam particles outside the ring acceptance. At the ramp top (defined by the ring dipole magnetic fields being constant), the beam is again cooled, at which time it is ready for experimental use.

The target is placed in the beam at this point, and cooling continues as particles are removed from the beam by the target. Given a total cycle time T, and a fill–ramp overhead time $t_{\rm oh}$, the average luminosity over the cycle is

$$L_{\rm ave} = \frac{N_0 f_{\rm B} d_{\rm tgt}}{T}\,\tau\,(1 - e^{-(T-t_{\rm oh})/\tau}), \tag{3.1}$$

where $f_{\rm B}$ is the beam frequency, $d_{\rm tgt}$ is the average target thickness, and N_0 is the average number of particles injected per cycle. Here, the number of particles in the beam is assumed to decrease exponentially with a lifetime τ. The optimal cycle time T is found by maximizing this expression. The overhead time $t_{\rm oh}$ is usually fixed for a particular maximum current and beam energy, so that making T very small becomes inefficient, while making it too long may sample an excessive amount of the long, exponential decay tail. Similarly, increasing the target thickness too much may greatly reduce the lifetime τ, resulting in a lower $L_{\rm ave}$, high background rates, or poor beam quality. For the CE-06 experiment, the cycle times ranged from roughly 30 to 45 seconds, with $t_{\rm oh} \approx 15$ sec, and the beam lifetimes were directly controlled via motion of the target fiber, as detailed below.

3.2 Targets

The multi-pass nature of the recirculating ions in a cooled-beam storage ring often makes the choice of target crucial to the design of the experiment. Targets in storage

[3] The flux of protons leaving the ring is larger at this point than any at other time in the cycle; wire chambers that are sensitive to this background are operated at reduced bias during injection.

rings are typically much thinner than those in single-pass accelerator experiments, since a "thick" target ($d_{\rm tgt} \approx 10$ μg/cm^2, for example) can heat the stored beam too rapidly for the cooling mechanism to compensate. Under these circumstances, the recirculated phase space volume may increase enough that all the advantages of cooling, including beam localization and good energy resolution, are lost. In addition, the high currents often available in storage rings (I $\approx$ 1 mA) would yield a very sharply peaked luminosity with such a target, resulting in high background and detector dead time problems. The cooling power of the ring effectively limits the internal target thickness to roughly 10^{16} atoms/cm^2, equivalent to about 200 ng/cm^2 of ^{12}C.

The heating of the beam via the target results in a finite lifetime of the stored current even when the target is thin enough that the cooling system can maintain a time-independent shape of the phase space distribution. This lifetime can have several components, the most important of which is usually transverse loss due to single and multiple Coulomb scattering of the beam with target nuclei. In this case, a particle scatters at an angle large enough to put it outside the ring acceptance, and it is lost.

For this process, the lifetime of the beam can be written

$$\frac{1}{\tau} \propto Z_{\rm tgt}^2 \cdot f_{\rm B} \cdot d_{\rm tgt}^n, \tag{3.2}$$

where the dependence on the target's atomic number $Z_{\rm tgt}$ comes from the Rutherford cross-section. For a hypothetical zero-emittance beam, the exponent n is unity, but the value increases [Me85] to roughly 1.66 when the equilibrium non-zero emittances ϵ_x and ϵ_y are taken into account. In the latter case, "extra" particles are lost via $\epsilon_{x,y} \neq 0$ according to their proximity to the ring acceptance $A_{x,y}$. The probability of a beam particle leaving the ring after suffering a Coulomb scattering event can be characterized roughly by the ratios $\epsilon_{x,y}/A_{x,y}$.

Another beam loss mechanism occurs through the large changes in longitudinal momentum that can occur when a beam particle suffers a head-on collision with an atomic electron in the target. The beam particle is lost if the change in momentum is greater than the ring acceptance (see Table 3.1). More likely, however, the particle will remain inside the acceptance but will now experience only a very weak cooling force. Calculations have shown [Me85] that the equilibrium momentum distribution with a typical target and cooling force is very sharply peaked (see Fig. 3.4), with a long tail that contains these "slightly cooled" particles. The calculations further show that increasing the target thick-

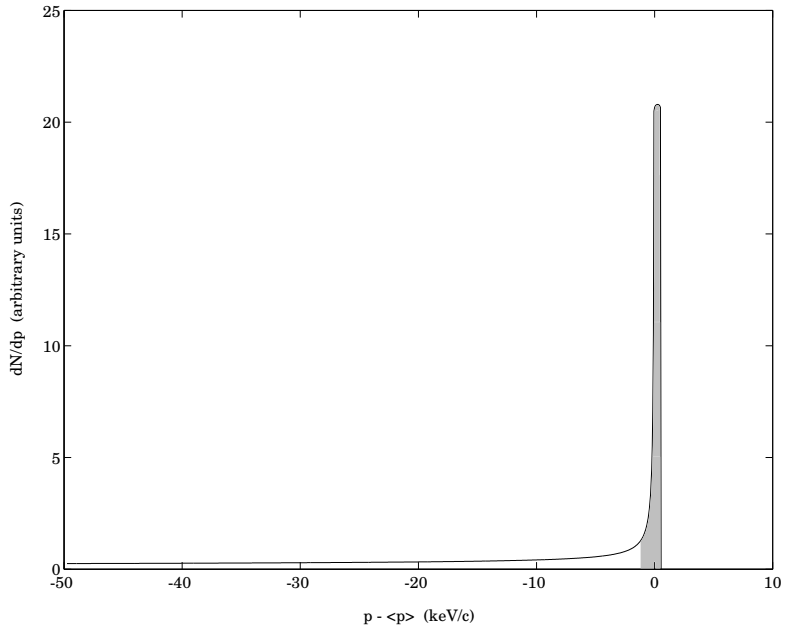

Figure 3.4 Relative momentum distribution of particles in a cooled beam, in equilibrium with a target. The calculation is for $E_{\mathrm{beam}} = 200$ MeV with typical Cooler ring parameters. Beam particles within the shaded region (2 keV in width) primarily experience a cooling force $F_{\mathrm{cool}} = -k(p - \langle p \rangle)$.

ness tends to raise the tail-to-peak ratio without a commensurate increase in the peak width.

Expression (3.2) shows that a thin target (for the Cooler, one with $d_{\mathrm{tgt}} \approx 20$ ng/cm^2) can best take advantage of a cooled, stored, beam. In fact, a primary benefit of these targets for the CE-06 experiment is the dramatic reduction of energy losses of heavy recoils in the target material. Gas jet targets, which have been developed [Sp90] and used extensively at the Cooler, can attain thicknesses of 10^{13}–10^{15} atoms/cm^2 (0.2–20 ng/cm^2 ^{12}C equivalent) for several target species including Ar, H_2 and D_2. The targets work by forcing the gas through a thin (1–2 mm wide) low-temperature nozzle placed within millimeters of the beam. The gas target thickness is fairly well-controlled via adjustment of the flow rate and temperature of the gas jet nozzle.

The extent of the gas target is, however, large compared to a solid target. A typical gas distribution has 80% of the thickness within a few millimeters of the nozzle, with the remainder spread out over ten centimeters, so that an independent determination of the reaction vertex point must be made. Furthermore, in order to maintain the Cooler ring vacuum at the level of 10^{-8} torr, the pumping requirements are quite demanding: isolation of the target chamber from the ring via differential pumping stages is usually necessary.

The above considerations and the experimental target requirements for the CE-06 work led to the use of a solid target material. These requirements were primarily that:

a) The target should be thin enough to minimize ($\Delta E < 0.01 \cdot E$) energy losses of recoil nuclei with $Z \geq 6$. With $dE/dx \approx 5$ keV/μg/cm^2 for particles with energies of 10–50 MeV, this implies a target thickness no larger than about 10 μg/cm^2.

b) The target should be localized in space enough that the reaction point is not a degree of freedom, and can be taken as "known." A point target is important for calculating the recoil rigidity from knowledge of its track through the magnetic field (see Sec. 3.3).

c) The atomic charge distributions of the recoil ions should attain equilibrium in the target material with preferential population of highly stripped states ($Q > Z - 3$). Such stripping is necessary for the production of ions significantly less rigid than the beam so that magnetic separation is possible.

d) The target should be free of heavy contaminants such as ^{16}O.

Requirement (a) is met immediately by the Cooler target thickness restrictions which in fact are much more strict than this. A solid target is well-suited to (b) and allows transverse localization of the reaction point to the size of the beam (typically, less than 2 mm in diameter). The desired equilibrium charge distributions in (c) have been demonstrated in carbon targets down to 5 μg/cm^2 [Yu89] but are unknown for thin gas targets (in which an equilibrium may not be reached). Finally, though both gaseous (CH_4) and solid (graphite) ^{12}C targets are readily available with oxygen and other heavy contaminants at levels of better than one part in 10^6, isotopic purity (i.e., ^{13}C/^{12}C $\ll 1\%$) is generally harder (or impossible) to achieve in the case of methane compared to graphite.[4]

Given the choice of a non-gaseous target, however, one immediately notices that a self-supporting target cannot be used. A 5 μg/cm^2 target (roughly the limit to be self-supporting) has 2×10^{17} atoms/cm^2 and as such is too thick for the Cooler ring by at least an order of magnitude! New techniques were developed to present a time-averaged thickness to the beam which is significantly lower than the actual thickness.

One of these methods involves "wiggling" a thin carbon fiber across the beam, producing an effective thickness which is in the range needed for the Cooler (around 10 ng/cm^2). Typical dimensions of the fibers recently fabricated [Lz93] at IUCF are 3–10 μg/cm^2 thick

[4] The fiber targets used in CE-06 were, however, natural carbon (about 1% ^{13}C).

by 5 μm wide. These are made by carbon evaporation and condensation onto a finely polished glass substrate through a closely spaced wire grid. The "whiskers" are then floated off, annealed (to lower the intrinsic graphite resistivity), and attached to a frame with conductive glue.[5] The frame can then be wiggled mechanically with little stress placed on the fragile target.

For a fiber harmonically oscillating with amplitude x_0 across the beam (where x_0 is much larger than the beam diameter a), the average luminosity for a given sweep is

$$L_{\rm ave} = \mathrm{I}_{\rm beam} \cdot \frac{\xi}{\pi x_0}, \tag{3.3}$$

independent of the fiber frequency ν. Here, ξ is the linear density of the fiber, given by the product of the fiber's thickness and transverse dimension. From (3.3), the effective target thickness is just $\langle d_{\rm tgt} \rangle = \xi/(\pi x_0)$, so that for typical fibers and an oscillation amplitude of 1 cm, $\langle d_{\rm tgt} \rangle \approx 3$ ng/cm^2. Even so, since reasonably attainable fiber frequences for this amplitude are roughly 30 Hz, beam traversal times for the whisker are on the order of one msec. Hence, the target moves very slowly as seen by the beam, which makes about 1000 revolutions in this time. This contradicts the prediction of Eq. (3.3) that the target thickness is characterized by $\langle d_{\rm tgt} \rangle$ rather than $d_{\rm tgt}$, the latter being much too thick!

Experiment and simulations [Pz93] have shown, however, that Eq. (3.3) is indeed correct: the lifetime and energy spread of the stored beam are essentially the same as that for a homogeneous gas target with the equivalent thickness $\langle d_{\rm tgt} \rangle$. The inhomogeneous nature of the fiber target over the extent of the beam allows a particle which has been heated by a target collision to have a negligible interaction probability over the next few msec and thus become cooled again. The lifetimes predicted by simulation agreed with experiment after it was realized that the fiber was charging up and electrostatically deflecting a fair amount of the beam current; conductive glue was used to prevent this effect.

There are, unfortunately, several experimental disadvantages associated with the wiggling fiber target. One of these stems from the fact that the low average thickness depends on the fiber being outside of the beam for 90% of the total "target in" time. The average luminosity in (3.3) consists of 1 msec-long "spikes" in the luminosity, each of which is characterized by a central value $L_{\rm max} \propto N \cdot f_{\rm B} \cdot \xi$, where N is the number of particles in the beam at the time of the sweep. These peaks are separated by 10–15 msec intervals of

[5] The conductivity of the glue turns out to be important to prevent the fiber from charging up.

zero luminosity. The ratio $L_{\rm ave}/L_{\rm max}$ is, in this case, just the amount of time spent in the beam:

$$\frac{L_{\rm ave}}{L_{\rm max}} \approx \frac{a}{2x_0}. \tag{3.4}$$

This "duty factor" for a typical fiber oscillation is $2\,\mathrm{mm}/2\,\mathrm{cm} = 0.1$. Given a (roughly) fixed number of particles N_0 available per cycle, it is best to maximize the duty factor (3.4) so as to minimize the accidental coincidence rate.[6] Note that for a particular target thickness, the maximization of Eq. (3.1) is equivalent to maximizing the duty factor.

Another difficulty involved with the use of the oscillating target is related to the standard IUCF readout/data acquisition system, which requires a dead time period of approximately 1 msec between event triggers. Since each fiber pass through the beam consumes the same amount of time or less, only one trigger is possible per sweep, and two per oscillation period. Assuming that the counts per sweep are distributed according to Poisson statistics, the experimental live time is

$$\varepsilon = \frac{\text{triggered events}}{\text{all events}} = \frac{2\nu}{n}(1 - e^{-n/2\nu}), \tag{3.5}$$

where ν is the fiber frequency and n is the average number of triggers per unit time: $n \propto L \cdot \sigma_{\rm t}$. Here, $\sigma_{\rm t}$ is the total effective cross-section for any reaction events capable of producing event triggers. Even for $n = 2\nu$, i.e., one trigger on the average per fiber sweep, $\varepsilon = 0.63$ and decreases rapidly as n increases.

Consequently, the experimental efficiency is quite low unless either the fiber frequency can be greatly increased (for example, to 1000 Hz) or n can be reduced via fast hardware rejection of background events (included in $\sigma_{\rm t}$). For fiber amplitudes in the range of several millimeters, the only means to achieve such high frequencies may be through oscillating the beam rather than the target. This capability has not yet been fully developed at the T-site of the Cooler ring.

The second tested means of using thick targets in the Cooler, and the method used for this work, involves "skimming" the beam with the target. Here, an open-edged foil or fiber (both with $d_{\rm tgt} \approx 5\ \mu\mathrm{g/cm^2}$) are moved slowly into the beam from the edge, skimming off beam particles that are already in the tails of the beam's transverse phase space. This technique is essentially equivalent to decreasing the ring's transverse acceptance slowly in time. In this way, the cooled properties of the rest of the beam are essentially left

[6] For the CE-06 experiment, this rate was just $R \propto R_{\rm pgac} \cdot R_{\rm pc} \propto L^2$. See Sec. 3.4.

unaffected. No true heating-cooling equilibrium is obtained in this way, however; essentially any particle interacting with the skimmer target is lost via one of the mechanisms described above. If the experimental data rate can be controlled, the duty factor of the skimmed target can be much better than that for the wiggled fiber.

The lower half of Fig. 3.3 shows the beam current and experimental count rate for a typical skimmed-target cycle of the CE-06 experiment. Two graphite fibers of thickness 4.2 μg/cm^2 and widths of 3.3 μm and 8.3 μm were mounted on a target ladder along with a 6.2 μg/cm^2 foil.[7] The horizontal ladder was attached to a rod which could be moved perpendicularly to the beam using externally controlled stepper motors. The external control device [Pp90] was an IBM PC running software allowing specification of all the target motion parameters (e.g., start point, stop point, velocity) and readout of the absolute position of the ladder. The rate from one of the CE-06 detectors (namely, the PGAC, see Sec. 3.4.2) was used as a negative feedback input: if the count rate was too low or high compared to a software rate parameter, the fiber was moved toward or away from the beam center, respectively. The position of the targets with respect to the beam center were measured for each new ring tune, to account for the small transverse shifts in the beam (on the order of 1 mm) from one energy to another.

A successful cycle (as shown in Fig. 3.3) occurred when the experimental count rate was essentially flat over the beam lifetime. The time-averaged luminosity, and the duty factor, was maximized in this case by increasing the control PC's rate goal parameter, while maintaining a reasonable data acquisition live time (at least 80%). In this way, the beam lifetime is decreased, allowing a shorter total cycle time and therefore a larger number of particles used up per unit time.

The primary concerns about this mode of target operation mainly involve background rates, due to the use of a thick target presented at the phase space edge. Most of this background consists of particles scattered at small angles in the target which leave the ring due to their proximity to the surface of the phase space volume. Initial tests of the CE-06 apparatus at the T-site showed that this background did not present any problems for the experiment, especially when the rate feedback mechanism was employed.

3.3 The T-Site Magnet

The centerpiece of the T-region of the Cooler ring is a large-gap dipole magnet, capable

[7] The foil was held with one edge open in a "C" frame.

of bending the beam by six degrees (see Figure 3.5). The beam is bent by the magnet into a small exit pipe, allowing either the detection of 0° neutral reaction products or, as in the CE-06 experiment, the magnetic analysis of soft reaction products emitted at small angles to the beam.

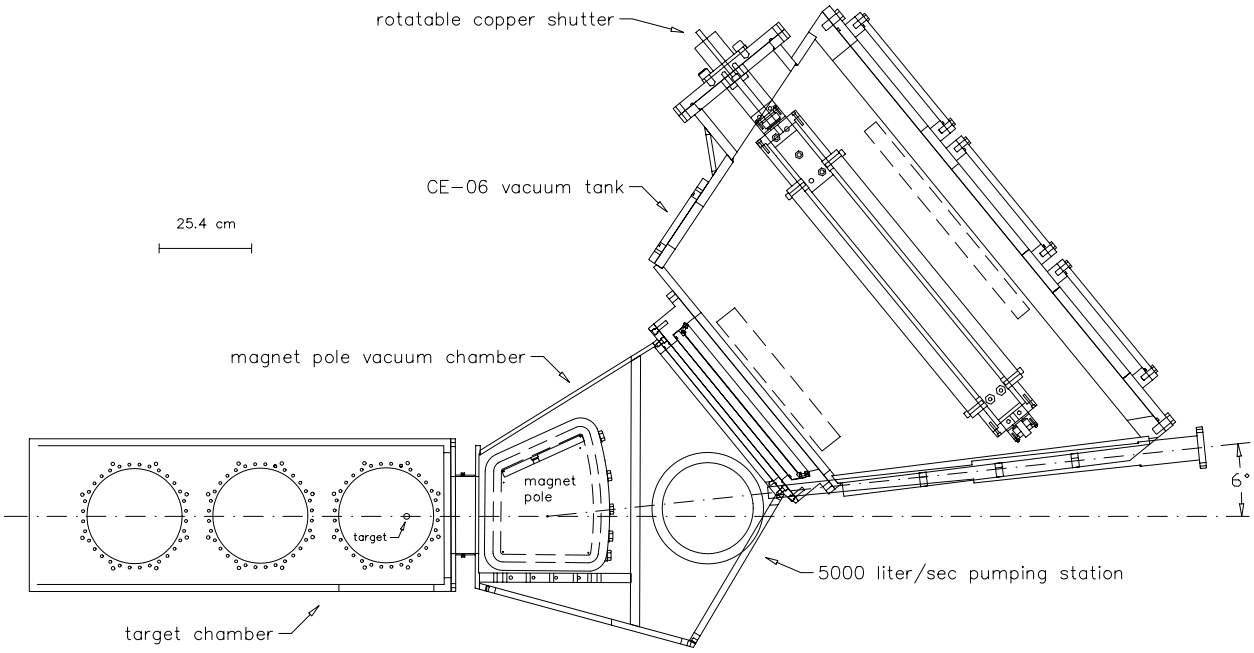

Figure 3.5 Schematic of the accelerator and vacuum apparatus *in situ* at the T-site. The beam circulates from left to right in the figure. Shown for comparison are the locations of the CE-06 detector housings (dashed boxes) and target position.

In order to provide the capability of high solid angle efficiency for proximate detection systems, the physical design of the 6° magnet (shown in Figure 3.6) is quite different from the other ring dipoles. The most experimentally important feature of the magnet for this work is the large vertical gap of 12.7 cm, which allows the passage of emission projectiles with vertical angles between −6° and +6°. The geometric horizontal aperture of the magnet, for positively-charged reaction products, extends roughly between +8° and +20° toward the inside of the ring.

These geometrical parameters are particularly important in experiments such as this work where the reaction projectiles of interest are emitted at small angles with respect to the beam and high acceptance efficiencies are needed. For $^{12}\mathrm{C}(\mathrm{p},\pi^+)^{13}\mathrm{C}$, at E_p = 166 MeV, for example, the recoil ^{13}C ions are emitted in a narrow forward cone of half-angle 3.4°, all of which are accepted through the magnet gap. Use of the more conventional ring

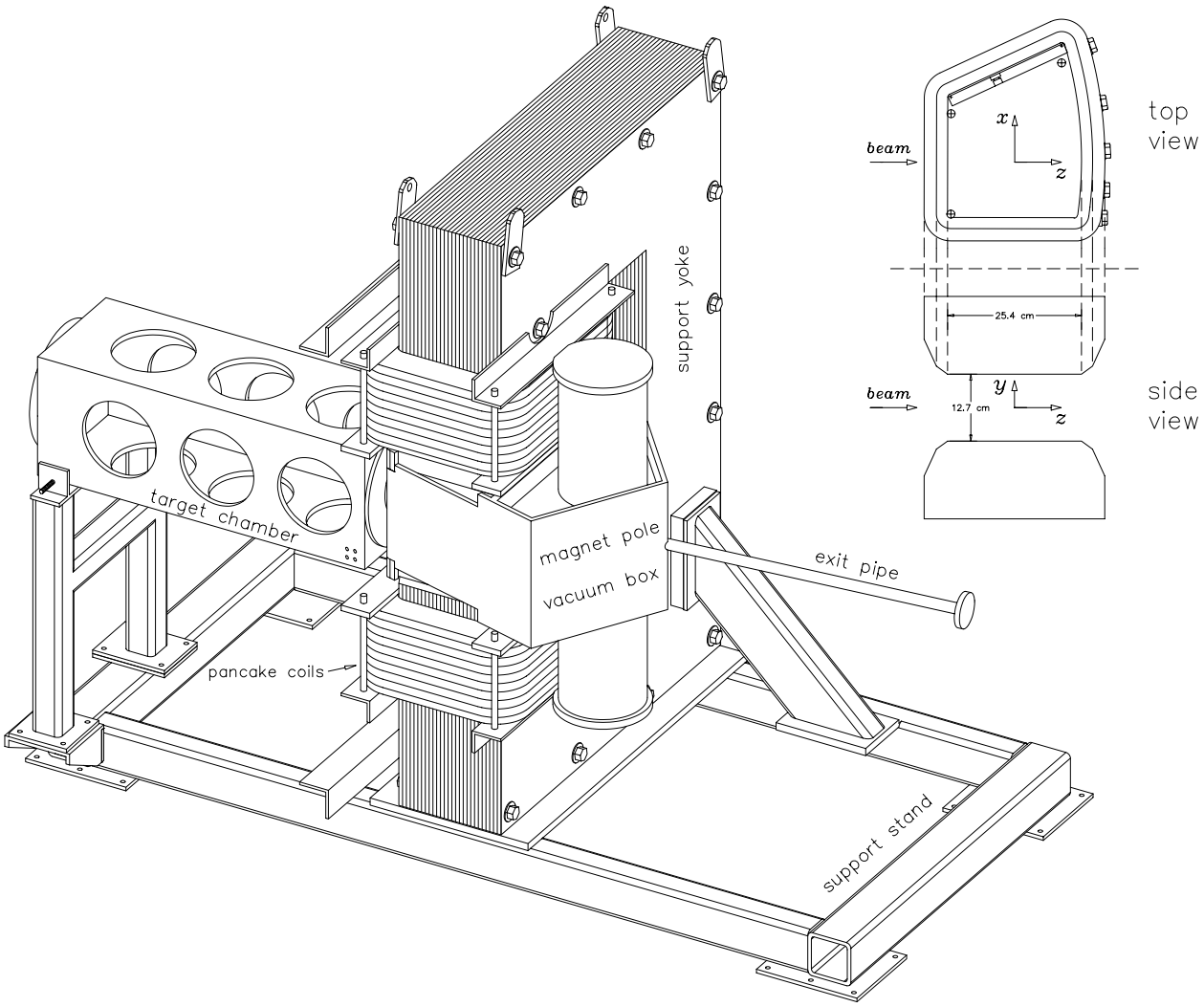

Figure 3.6 The 6° dipole magnet design: entrance box (the large number of ports necessary for pumping support of gas jet targets), support structure, and exit pipe (at 6° with respect to the entrance). Also shown are the top and side views of the magnet poles, along with the magnet coordinate system defined in App. C.

dipoles with typical available gaps of about 5 cm would reduce the geometrical acceptance by at least a factor of three. The large solid angle afforded[8] by the 6° magnet can be especially critical for near-threshold studies of other reactions where the cross-sections are small ($L\sigma \ll 1$ sec^{-1}).

The multi-ton yoke of the magnet serves to contain the field, support the weight of the coils (about 150,000 amp-turns), and resist the attraction of the pole faces (about one ton of force). Figure 3.7 shows the current in the coils needed for a given proton momentum.

[8] This is indeed the single most expensive design parameter, via the vertical gap, of the T-site magnet.

The magnet was built to be operated well below saturation, even at the maximum design strength of 3.76 Telsa-meters. To enhance further the fast ramping ability needed for Cooler operation (see Table 3.1) and to minimize eddy currents, the pole faces were fabricated from laminated iron slices 1.25 cm thick.

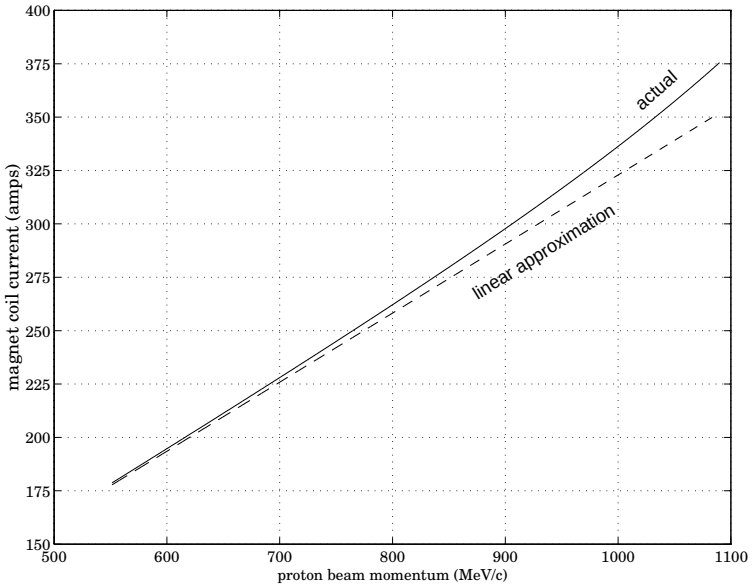

Figure 3.7 Current vs. beam momentum for the six-degree magnet. Shown for comparison is the linear approximation I $\propto p$, matched for $p \to 0$ to the actual relationship. The true current at the top of the Cooler ramp may vary from that shown by 1–2% according to the particular beam tune.

Standard magnet-mapping techniques were used at IUCF to measure the y-component[9] of the field in the x-z plane ($y = 0$) and at several out-of-plane y values. Calculations were then performed (see App. C for details) to construct a uniformly-spaced three-dimensional grid of **B** from this data. Characteristic plots of the magnetic field for I = 300 amps ($E_p \approx 365$ MeV) are shown in Fig. 3.8. The dimensions of the "flat" part of the field ($B > 0.9 \cdot B_{\max}$) are approximately $24 \times 24 \times 8$ cm and the field is large ($B \gtrsim 0.1 \cdot B_{\max}$) and non-uniform over a considerable extent. Particles that deviate by more than a few degrees from the 0° median-plane path heavily sample the B_x and B_z components of Fig. 3.8. The fully three-dimensional raytracing calculations (described in App. C) are therefore necessary for magnetic analysis of charged reaction products via the CE-06 detector stack.

[9] The coordinate system used in this work (referred to as "magnet" coordinates) is defined in Fig. 3.6 and App. C.

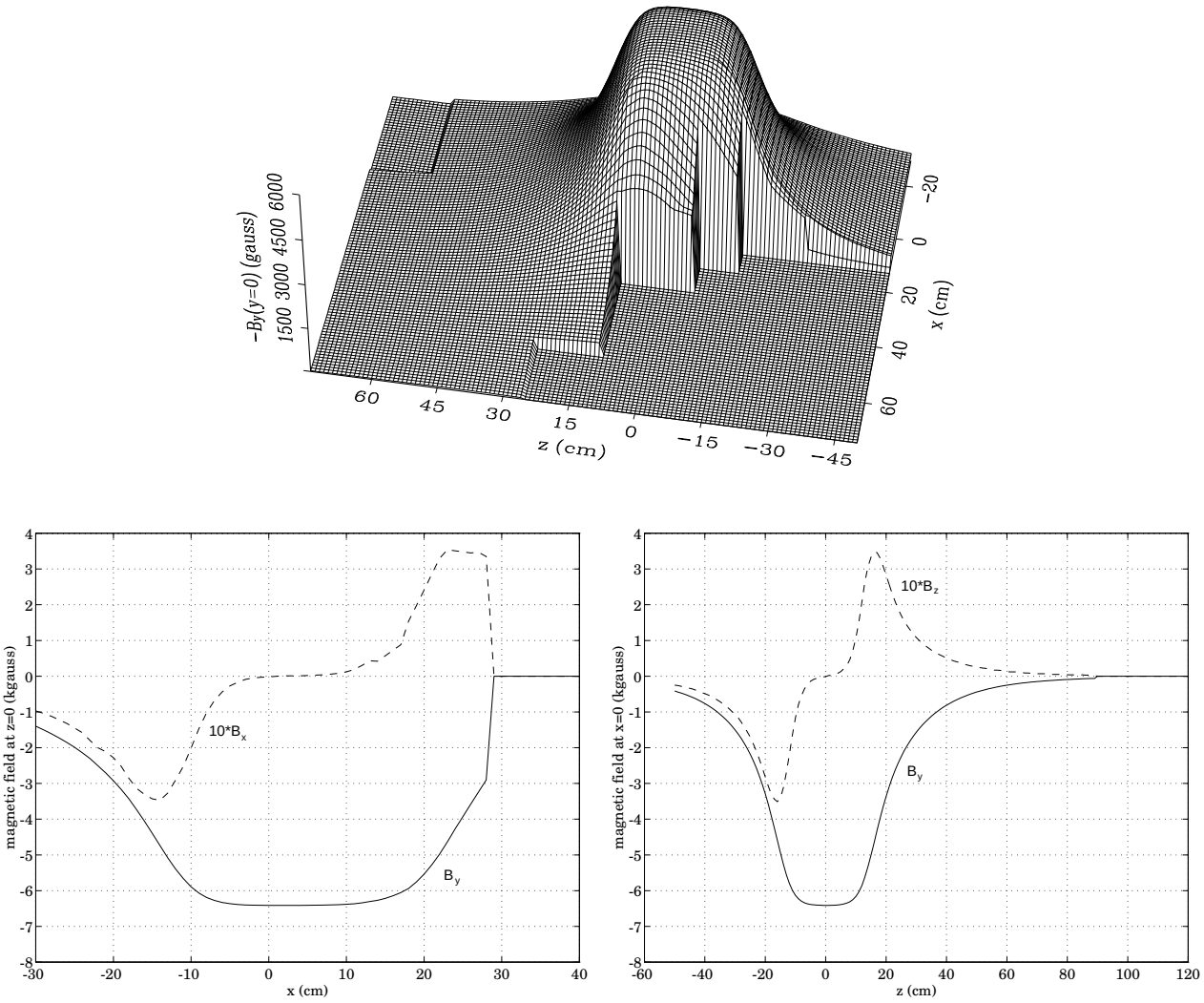

Figure 3.8 The 6° magnet dipole field for I = 300 amps. At this current, $B_{\max} \equiv B_y(0,0,0) \approx 0.6$ Tesla. The median plane ($y = 0$ cm) values of B_y are shown; the plots for B_x and B_z correspond to $y = 1$ cm.

3.4 The Detector Stack

3.4.1 Overall Setup

The detector apparatus used for the CE-06 experiment was primarily designed to detect medium-weight recoils with $Z = 3$–8 in the energy range of 1.5–4.5 MeV/amu with extremely high efficiency. A fundamental concern for a detection system of this type is the reduction of unrecoverable ion energy loss, e.g., losses in pressure foils or in gaseous dead layers. To avoid ion energy losses in air, the CE-06 detector stack was enclosed in a vacuum box attached directly to the exit flange of the 6° magnet box. The complete vacuum enclosure was needed since recoils in the middle of the energy range (3 MeV/amu, $Z = 5$)

experience energy loss at the rate of about 2 MeV per mg/cm^2 of material traversed.[10] Figure 3.9 shows the vacuum box along with the CE-06 detectors in their run positions. A large-area (roughly 1000 cm^2) valve attached between the box and the magnet chamber afforded independent pumping operation or detachment of the CE-06 tank. A thin pressure foil (1 μm of Mylar) covered the flange opening to provide for isolation of the 10^{-8} torr ring vacuum from the 10^{-6} torr tank pressure.

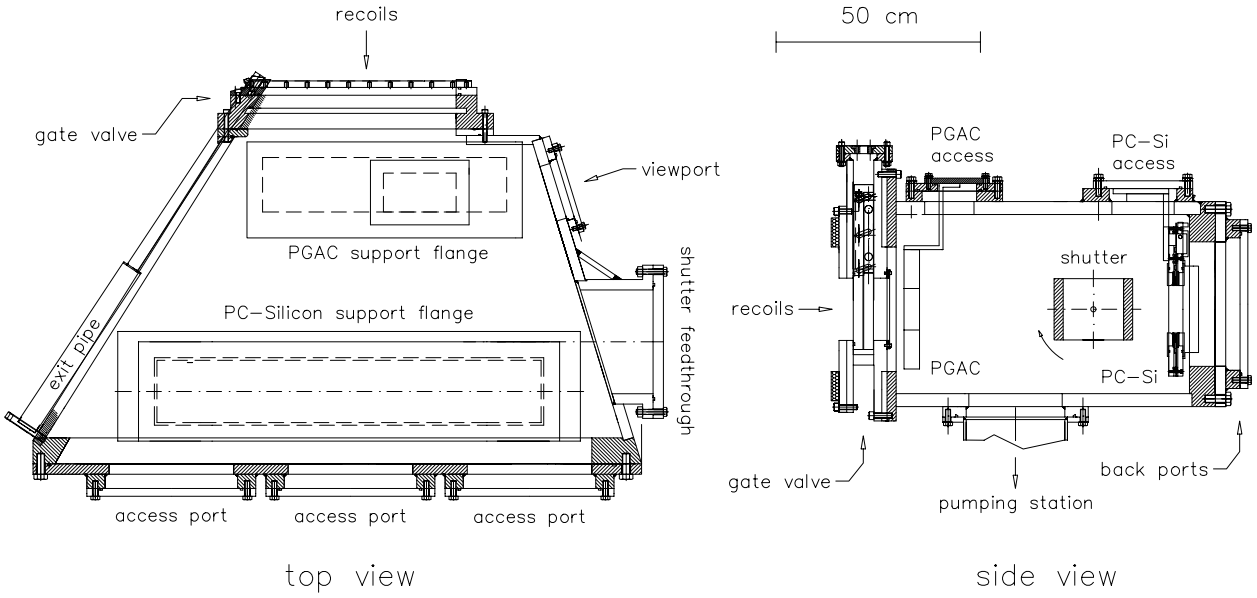

Figure 3.9 Top and side views of the vacuum tank attached to the T-site magnet for the CE-06 experiment. Not shown are the support platform and casters on which the box was mounted to allow it to be rolled back from the attachment flange. The shutter is shown in closed position.

The CE-06 tank provided ports on the top, through which the detectors were mounted into the tank, and whose flanges doubled as support mounts for the detectors. More ports were built into the back (used for cable feedthroughs) and the bottom (for a low-impedance pumping port). Also housed in the tank was a slow-acting "shutter", externally rotatable via a ferrofluidic feedthrough, and consisting of two copper slabs totaling 90 g/cm^2 in thickness. The shutter provided complete protection for the silicon detectors (see Sec. 3.4.4) against 45 MeV injection protons and partial blockage of protons of up to 300 MeV, at times when the experiment was not on-line at the Cooler. Although external motor control coupled to the ring cycle would have made on-line injection background protection possible,

[10] A thickness of 1 mg/cm^2 is equivalent to 4 μm of Al, 7 μm of Mylar, or 8.6 mm of air at STP.

proton count rates on the silicon array were small enough under CE-06 running conditions that this protection was not necessary.

For the reactions of interest in this work, recoil ions with masses comparable to the ^{12}C target nuclei are emitted with roughly the same momentum as the circulating proton beam. The ions are typically highly stripped for the energies of a few MeV per amu and so are bent by $Q \cdot 6°$, where $Q \geq 2$, allowing complete separation of the ions from the beam. Figure 3.10 shows the known charge distributions [Ba81] for the recoils of interest; carbon and nitrogen recoils are typically emitted with $Z - 3 \leq Q \leq Z$.

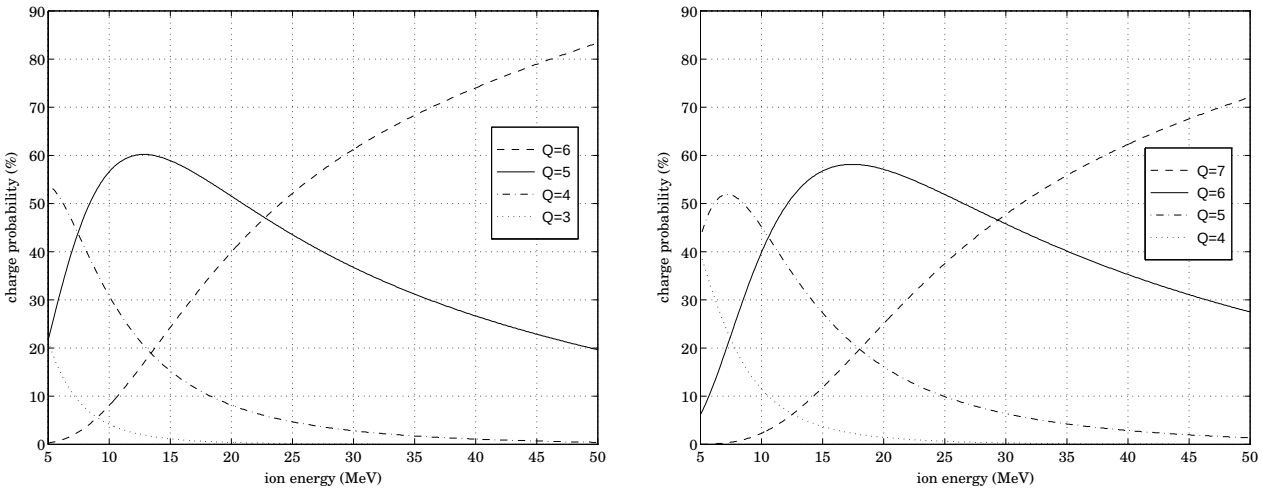

Figure 3.10 Carbon (left) and nitrogen (right) atomic charge distributions. Shown is the probability that an ion with energy E will have charge Q after passage through carbon foils. Other works (e.g., [Yu89] and [Bn68]) have verified the population of highly stripped ions for foils as thin as those used in CE-06.

These distributions are the result of reaction emission ions attaining an equilibrium charge by "pickup" of atomic electrons during passage through the target material. Highly energetic recoils are therefore less likely to experience recombination and tend to remain fully stripped. "Re-shuffling" of the atomic charge can occur whenever the ion passes through matter; however, raytracing (see App. C) showed that, even at the location of the pressure foil, the magnetic field was too weak for this charge change to have a noticeable effect on the direction of the ion track.[11]

A schematic of the detector setup for CE-06 in position at the Cooler T-site is shown in Fig. 3.11, along with calculated median plane projections of flight paths for several important ion species (using single-pion production kinematics at $E_p = 350$ MeV). The

[11] At least, when compared to the effect of multiple scattering, see Chapter 4.

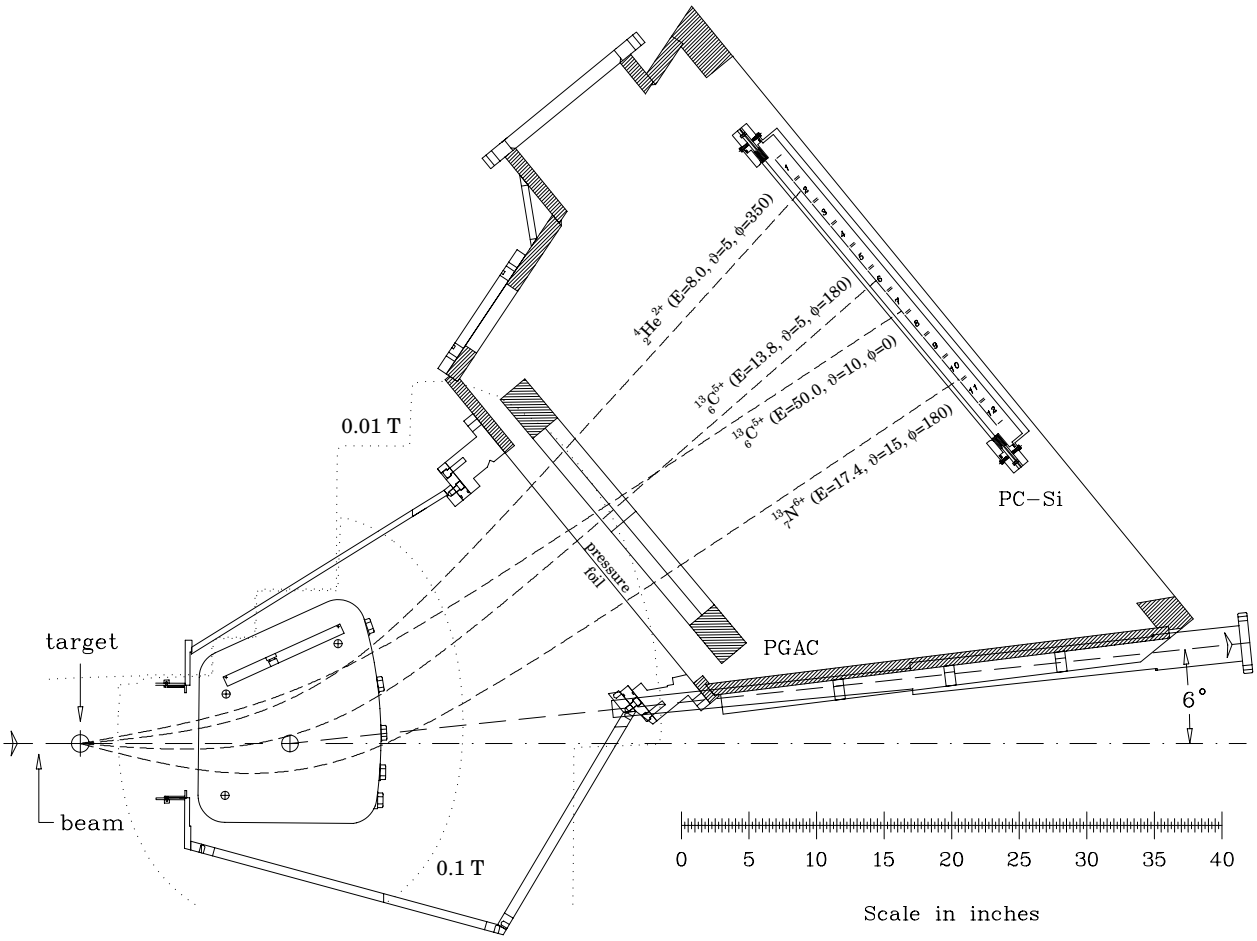

Figure 3.11 The detector apparatus for CE-06 at the T-site, shown with the 100 and 1000 gauss boundaries of B_y for $E_p = 350$ MeV. The target was approximately 38 cm from the field center $\oplus$. Ion tracks, specified by reaction energies (MeV) and angles (deg), are shown projected into the plane $y = 0$.

figure also shows that ${}^4_2\mathrm{He}^{2+}$ ions with energies characteristic of common laboratory sources (several MeV) have the proper rigidity to be transported through the detector stack. This fact was used to advantage in CE-06 as a means of position, energy, and timing calibration of the entire detector stack *in situ* off- and on-line.

With the knowledge of the detector locations and the magnetic field, coupled with the absolute calibration of the raw energy and position signals in particular, the CE-06 detector stack provides the complete identification of recoils along with the determination of the reaction angle θ at the target. The PGAC and Si detectors measure the velocity vector of an ion (all components) by determining its position and time-of-flight. The transmission proportional counter (PC) measures the ion energy loss dE/dx which, coupled with the energy measurement made by the Si array, identifies the ion atomic number. The

knowledge of **B** and the target location completes the picture by determining Q, M, and the reaction angle θ. Since the PGAC and PC are "low-pressure" detectors (cf. App. A), this can be accomplished efficiently for $Z > 3$ with relatively little sensitivity to protons and α particles. A full discussion of the calibration and data analysis for the CE-06 experiment is found in Chapter 4. The remainder of this chapter describes the detector hardware in detail.

3.4.2 The Parallel Grid Avalanche Counter

The Parallel Grid Avalanche Counter, or PGAC, is a low-pressure transmission detector designed to provide two-dimensional position information along with fast timing of highly ionizing particles (see App. A for a more complete discussion of general and low-pressure gas detector operation). The PGAC used in the CE-06 experiment was constructed with grids rather than foils (which would produce a PPAC, where the P stands for "Plate" [Rm88]). In this way, only two foils[12] were necessary (as pressure foils), so that the total detector thickness was kept below roughly 250 μg/cm^2.

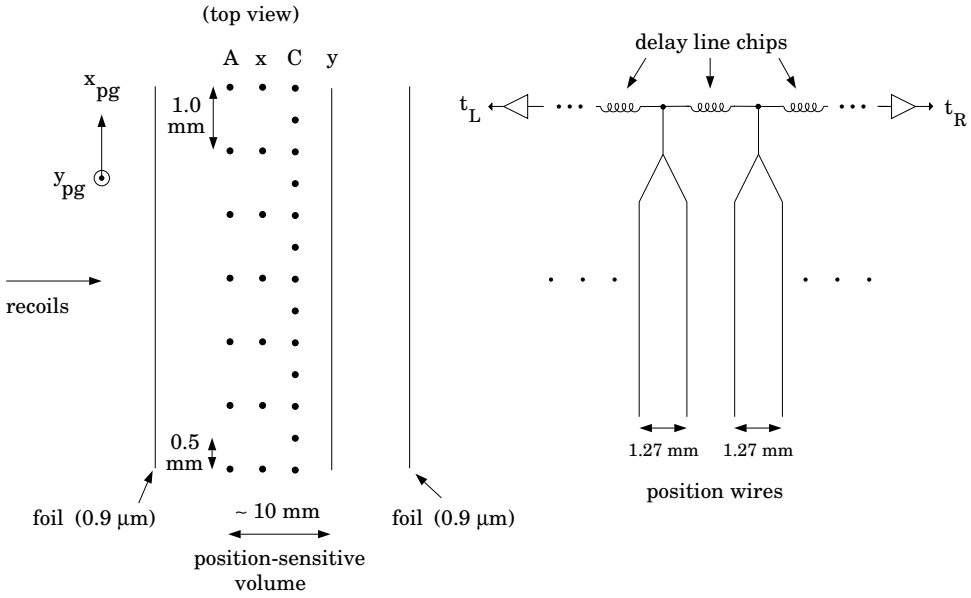

Figure 3.12 Schematic view of the PGAC active volume, with relevant dimensions. All grids are 20 μm Au-plated tungsten except for the cathode (10 μm). Also shown is the equivalent circuit for the internal delay line. Each delay element separates two position wires.

The PGAC is comprised essentially of four wire grids, shown schematically in Fig. 3.12,

[12] All of the foils used in the CE-06 experiment (including the isolation pressure foil) were 0.9 μm thick non-aluminized DuPont Mylar.

which allow a total transmission efficiency of 95%. The two main electrode grids, the cathode (C) and the anode (A), are biased to roughly −310 V and +300 V, respectively. PGAC operation for CE-06 involved bias voltages of up to ±320 V but this was often limited by sparking caused by the relatively large proton background flux during ring injection. With a standard operating gas pressure of 3 torr of isobutane, the PGAC runs in avalanche mode: the 600 volts of potential across the 6 mm gap between the anode and cathode is no further than roughly 10% from the sparking threshold. The negative signal induced on the anode is therefore saturated and fast (typical risetimes are 2–3 nsec). The intrinsic timing resolution of the PGAC using this signal was measured and found to be roughly 400 psec.

The PGAC can also detect the position of an incident ion as it passes through the active volume. Position determination is accomplished by placing electrode grids close to the avalanche grids (C) and (A) in such a way as to minimally disturb the avalanche field configuration. In this case, the x-position grid (measuring displacement along the detector length) is held at ground and located halfway between the cathode and anode. The y-position grid (for displacement out of the plane of Fig. 3.11) is also grounded and is placed behind the anode by half the cathode-anode spacing.

Signals are induced on the position grids in the same way that a pulse is formed on the cathode of a cylindrical proportional counter. As such, they are positive-going and quite small compared to the anode signal. One of the benefits of the avalanche mode of operation is the large multiplication factor, which causes relatively large induced signals on the positions grids. For the PGAC position grid wire spacing of 1.27 mm, an induced signal appears on several wires, even at normal ion incidence, due to the large electron mean free path at these gas pressures.

In order to reduce the amount of electronics that would be necessary to readout all 450 position grid wires in the PGAC, the ends of the wires are connected to a passive delay line, as in Fig. 3.12. The PGAC is separated electrically into two halves along the x-direction so as to minimize attenuation of the induced signal in the delay line.[13] The signals at each end are fed into a TDC's stop inputs with the anode signal for a start. If $x_{\rm pg}$ is the position of an ion path from one end of the delay (total length L) and Δt is the incremental delay between position wires, then

$$t_{\rm left} = (\Delta t)x$$

[13] The bifurcation also improved the detector's event rate capability.

and

$$t_{\text{right}} = (\Delta t)(L - x)$$

so that

$$t_{\text{left}} - t_{\text{right}} = (2\Delta t)x + \text{C}. \tag{3.6}$$

Here, C is a constant depending on the total PGAC delay line length, differences in lengths of the coaxial cable leads, and on offsets in the TDC. The subtraction of the two TDC channels is therefore proportional to the ion position x_{pg} (the method used to determine the ion vertical position y_{pg} is, of course, completely equivalent).

The purely inductive nature of the position signal (there is no actual charge avalanche or multiplication at these wires) implies a non-linear fall-off in its amplitude with distance from the center of the ionization track: $V_{\text{ind}} \propto d^{-n}$, with $n > 1$. Therefore, although the effective wire spacing for the position grids is 2.54 mm, resolutions significantly better than this can be attained. Tests of the PGAC in a spectrograph with an α source showed the position resolutions (scaled to normal incidence ion tracks) to be 1.3 mm and 1.8 mm for x and y, respectively. In general, the resolutions improve for more highly ionizing particles and larger cathode-anode differential voltages, both of which increase the size and risetime of the induced position signals.

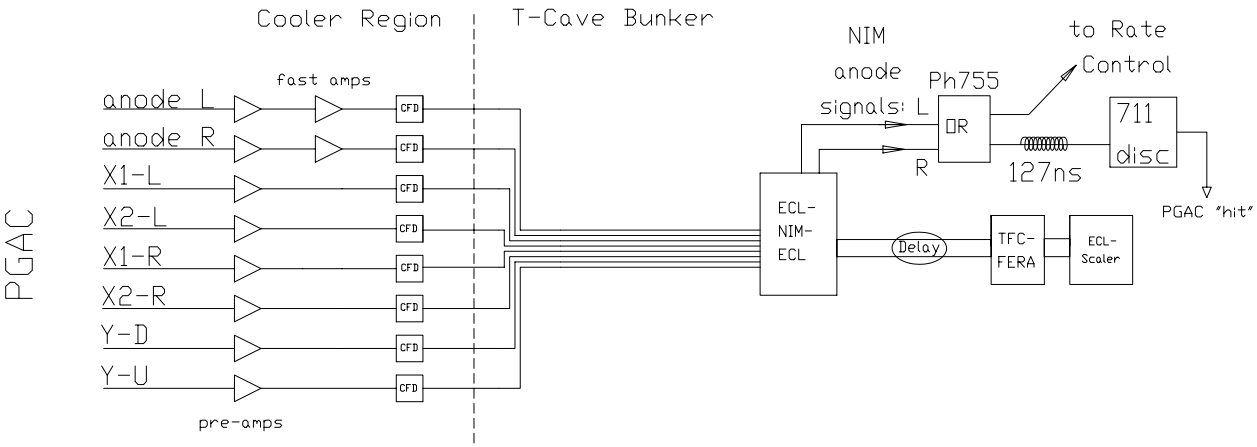

Figure 3.13 The PGAC electronics. All components shown to the left of the dashed line were mounted directly on top of the CE-06 vacuum tank, and connected via vacuum feedthroughs in the PGAC support flange shown in Fig. 3.9. Further details of the T-Cave electronics are given in Sec. 3.5.

The readout electronics used in CE-06 for the PGAC were quite simple due to the delay-line configuration (see Fig. 3.13). The split anode and x-position grid results in two

anode signals and four x-position signals, along with a small dead area between the two anode grids of roughly 3 mm. The near-normal incidence of recoils in the CE-06 experiment (see Fig. 3.11) typically implies a one-to-one correspondence between anode and x-position grid halves.

3.4.3 The Proportional Counter

The Proportional Counter, or PC, was the next major component of the CE-06 detector stack, proceeding outward from the magnet. Like the PGAC, the counter is a low-pressure detector, but it is designed to be operated at high-enough pressures ($P \gtrsim 10$ torr) to be in the proportional mode. In this mode, the PC measures $(\Delta E/\Delta x)_{\rm ion}$, the ion's energy loss per unit thickness of the detector's active volume. Coupled with a measurement of the ion velocity v, the counter determines $Z_{\rm ion}$ from

$$\frac{\Delta E}{\Delta x} \propto f(v) \cdot Z^2, \tag{3.7}$$

where f is a known function. If the ion's incident energy E is known, the mass M and nuclear charge Z are measured via

$$\Delta E \cdot E \propto M \cdot Z^2. \tag{3.8}$$

In principle, it is also possible to measure the ion's atomic charge Q via[14] the transmission energy loss; however, the variation in deposited energy is less than 1% for nitrogen ions with $E \gtrsim 10$ MeV.

There were three main design goals for the PC as developed for the CE-06 experiment. One of these was the maximization of the solid angle subtended to the target. Given reasonable dimensions of the vacuum enclosure on one hand and the benefits of a long time-of-flight (TOF) path on the other (see Fig. 3.11), the active area of the PC needed to be about 10 cm vertically by 65 cm horizontally. With a TOF path length of roughly 60 cm, this would result in a geometrical solid angle of $\Delta\Omega \approx 20$ msr.

Another desired feature of the PC was the ability to measure $\Delta E/\Delta x$ for a wide range of ion types and energies. In particular, good resolution (requiring a thicker active volume) and transmission capability (requiring the reverse) was needed for ions with $5 \leq Z \leq 8$ and 10 MeV $\lesssim E_{\rm ion} \lesssim 50$ MeV. For the operating gas CF_4 (carbon tetrafluoride), calculations using standard energy loss tables for elements [No70], along with interpolations

[14] The specific energy loss of the ion decreases as it captures electrons from gas or foil molecules.

to compounds [Ce75], suggested that a 1 cm thick active volume with pressures in the range of 20–100 torr would be optimal.

The final important capability of the PC was position sensitivity in the y-direction (out of the page in Fig. 3.11). Together with the PGAC y measurement, this information would provide a complete determination of the vertical direction cosine of the reaction ion. At the desired position for the PC, the resolution needed to achieve a vertical angular resolution of 0.1° is $\Delta y \lesssim 5$ mm.

To test the feasibility of attaining these goals, a prototype detector was constructed, using the sense plane parameters (e.g, anode wire spacing) expected for the full-scale device, but with a 5×5 cm active area. Top and side views of the active region are shown in Fig. 3.14. As in the PGAC, wire grids were used as cathode planes instead of foils to minimize energy losses.

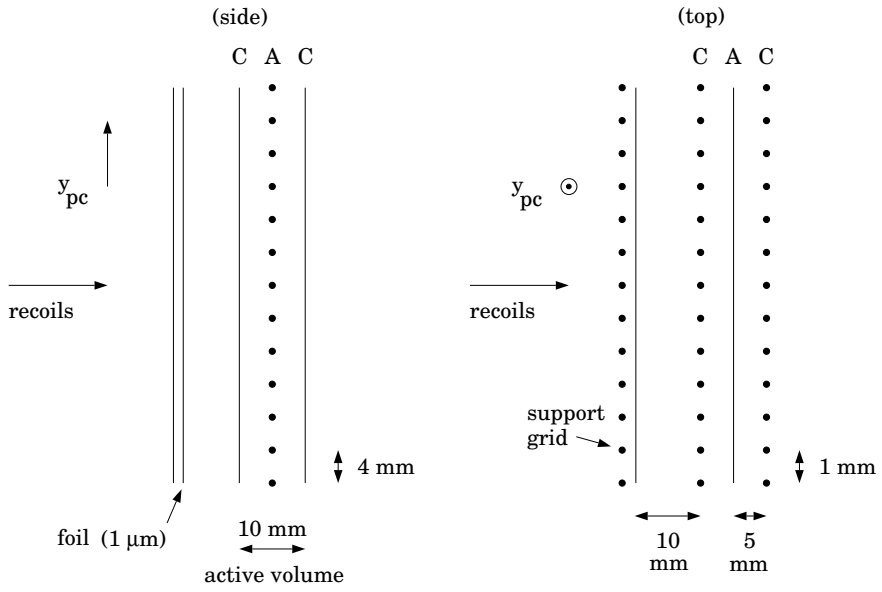

Figure 3.14 Schematic (not to scale) of the operational design of the PC. The prototype detector consisted of only the anode (A) and cathode (C) grids (supported on a small G-10 frame) and was operated in a separate gas enclosure.

To allow the capability of the measurement of y, the PC is actually an MWPC (multi-wire proportional counter): the anode plane consists of electrically independent wires spaced by 4 mm (the prototype wires, however, were OR'd together due to lack of space for separate readout). Assuming that only one wire fires per ion event, the vertical resolution of the PC is simply $\Delta y = 4$ mm. The single-wire behavior in MWPC's was in fact confirmed [Ch68] many years ago; however, whether the PC wires would each act as an

independent detector or not, given the heavy ionization tracks that would occur in CE-06, was not known.

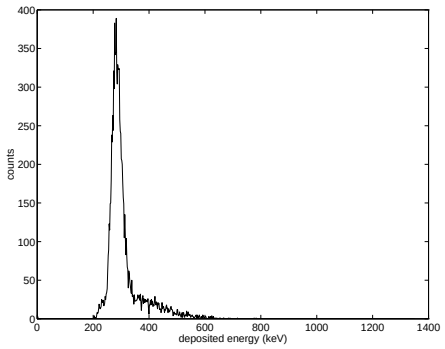

Figure 3.15

The prototype was initially tested with an α source, using a single charge-sensitive pre-amp for the combined anode wires, at a variety of gas pressures and anode biases to check stability and resolution. The figure at left shows the PC energy spectrum obtained at a typical operation point: 100 torr of propane (similar to CF_4 but with less stopping-power) and $V_{\rm bias} = +1000$ volts. The achieved resolution was approximately 5% FWHM, which was better than expected given the relatively small energy loss of the α particles in the active volume (about 200 keV).

To determine the counter performance for more highly ionizing particles, tests with the prototype were carried out at the Princeton University Cyclotron. A 5×5 cm silicon detector[15] was placed directly behind the back cathode grid of the prototype, also immersed in the gas. The main goal of the prototype test was to determine the quality of particle identification possible by measuring ΔE and E.

A 48 MeV α-particle beam from the cyclotron was bombarded on a ^{12}C target to produce a variety of ion species at energies appropriate to CE-06 (up to about 25 MeV). The results of the test, shown in Fig. 3.16, were good: a clear Z separation of the ions was achieved for Z =4, 5, and 6 ($Z = 2$ and $Z = 3$ were also well-separated but off the scale in the figure). The first excited state of ^{12}C at 4.4 MeV is clearly visible in the $Z = 6$ group in the region of silicon energies around 19 MeV, along with the 15.11 MeV state near $E_{\rm si} = 7$ MeV. The ^{12}C ground state (populated weakly at this level of momentum transfer) can also be seen close to $E_{\rm si} = 23$ MeV.

At this stage, the full-scale PC was designed and built. Front and side views of the completed counter are shown in Fig. 3.17. Several important features of the final detector as built do not exist in the prototype. One of these is the support grid for the pressure foil. Tests with the thin (1.0 μm thick and 650 cm^2 in area) Mylar foil showed that it would not hold more than about 10 torr while supported only at the edges. Consisting of

[15] The Si detector was itself a prototype of the CE-06 detection system; see Sec. 3.4.4.

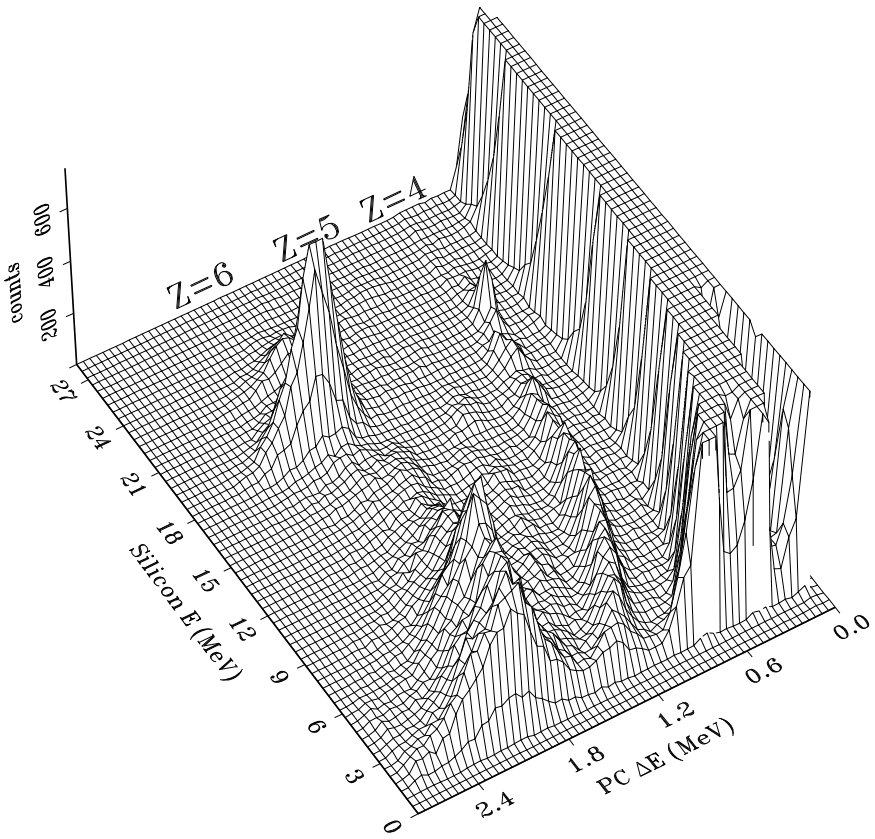

Figure 3.16 Particle identification using the prototype counter and silicon detector, both with active areas of 5×5 cm. The prototype ΔE calibration shown is reliable only for the $Z = 6$ ions.

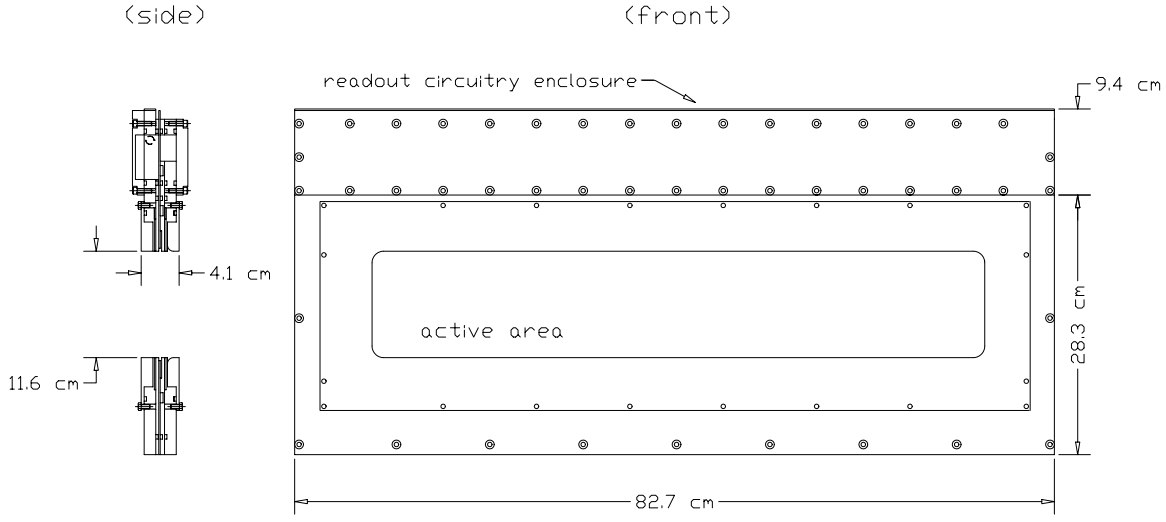

Figure 3.17 The CE-06 Proportional Counter. The pre-amp chips and associated electronics for each wire are contained in the small chamber at the top of the PC proper.

100 μm wires spaced 1 mm apart, the grid serves not only to support the window (which experiences a total force at 100 torr of roughly 200 lbs.) but also to minimize the dead layer between the front cathode and the foil. The grid is aligned with both cathode plane grids so as not to reduce the transmission efficiency of the PC (90%) unnecessarily.

The completed PC also incorporates the initial readout circuitry in the upper part of the PC housing. An integrated charge-sensitive pre-amp chip is AC-coupled to each of the 25 anode wires, which are commonly biased. The circuit board containing these chips is 70 $\times$ 30 cm in area and extends 1 cm past the housing for Lemo connections to the feedthrough cables. The board also serves to support the anode wires and direct gas flow, which proceeds first through the active area, then into the electronics housing in the upper part of the PC. Each pre-amp chip dissipates about 200 mW during operation, so the gas flow through this section is necessary to prevent overheating.

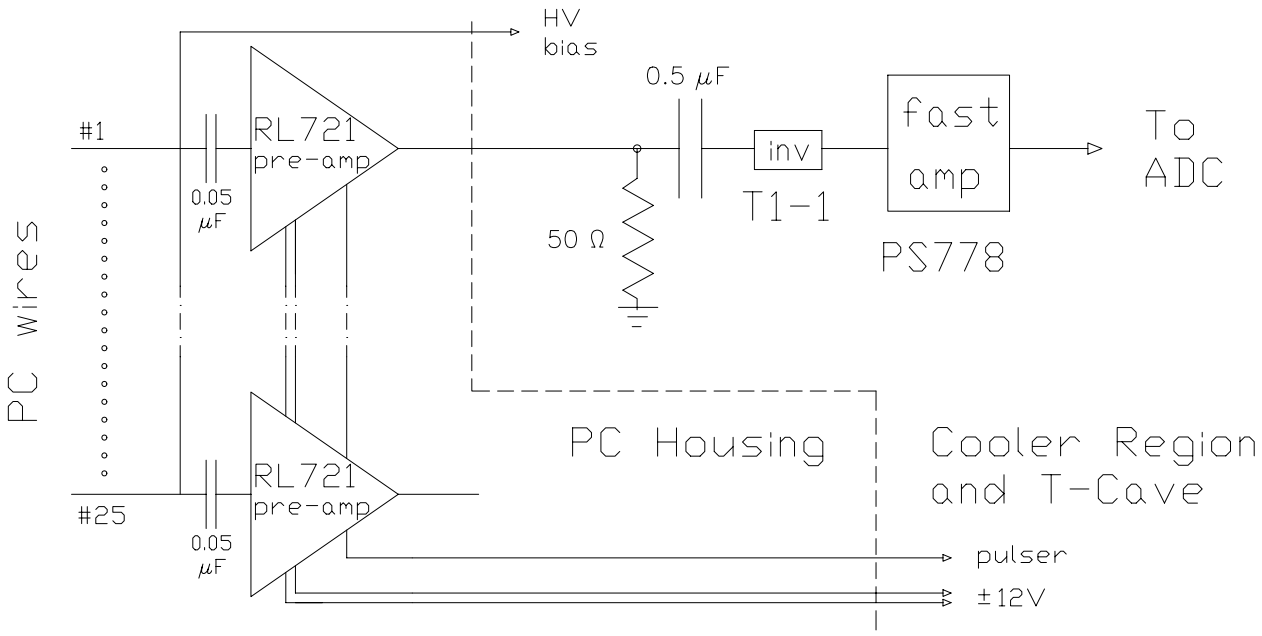

Figure 3.18 The PC electronics, for a single anode wire, as configured for the CE-06 experiment. All components shown to the left of the dashed line were enclosed inside the aluminum PC housing. Further details of the external electronics are given in Sec. 3.5.

A schematic of the readout electronics for a single wire (all wires were identically configured) is shown in Fig. 3.18. A common pulser line is bussed (along with the power) to the pre-amps for all wires, allowing complete calibration and testing of the PC readout electronics. The outputs from the pre-amps are suitable to be shaped in an amplifier or to

be fed directly into a charge-sensitive ADC. The large number of channels involved (one for each of the 25 anode wires) led to the use of the latter readout for the CE-06 experiment (cf. Sec. 3.5).

The PC was tested first at the Yale Nuclear Structure Laboratory's tandem accelerator. Here, a gold target was used to elastically scatter a ^{12}C beam at small angles into a spectrograph. The PC was placed at the focal plane of the device on a vertically moveable platform, so that the scattered ions could be directed anywhere upon the active area of the counter. Fig. 3.19 shows the energy output of two adjacent wires (4 mm apart) when the ions were directed half-way between them. Even under these conditions (high rates of $Z = 6$ ions), the wires acted as independent proportional counters. The rate of correlated events was approximately four orders of magnitude smaller than that for the uncorrelated signals, as shown in the figure, implying that there would be no ambiguity in determining the y-position.

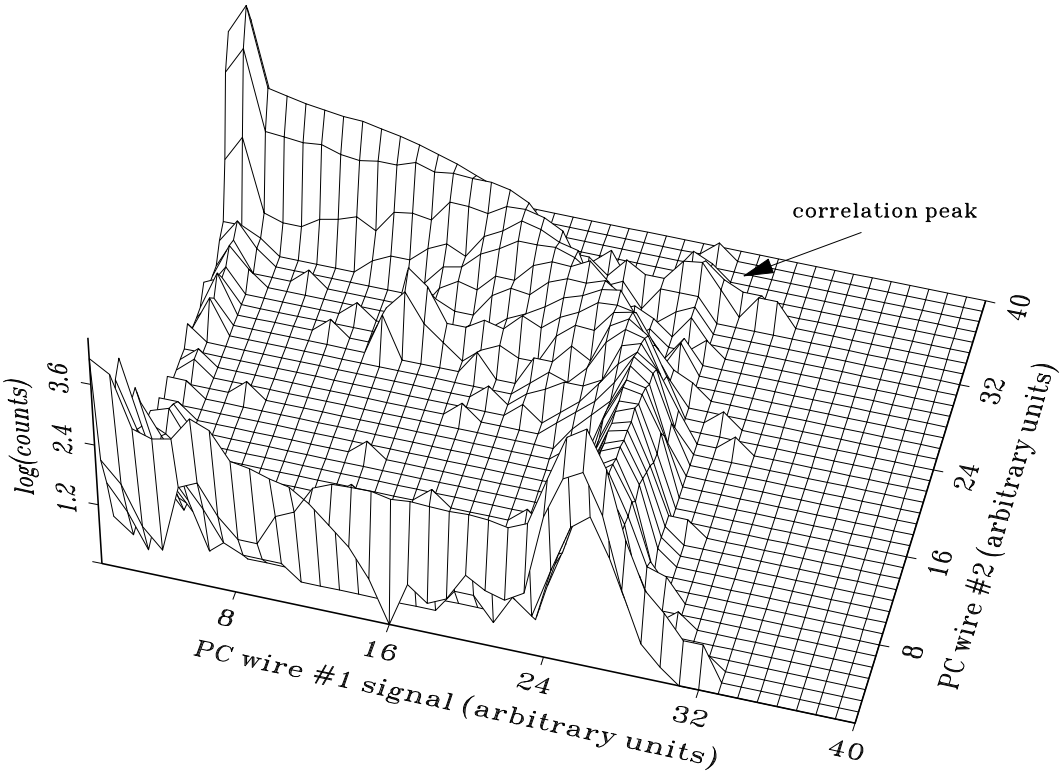

Figure 3.19 Correlation plot for adjacent PC wires with an intense stream of ^{12}C ions incident between them. The arrow points to full-energy correlated events. The vertical scale is logarithmic.

The energy resolution of the PC was determined to be approximately 6% FWHM for ions at the energy used (about 50 MeV), somewhat worse than expected from the

prototype tests. This degradation was due, as determined later (see Ch. 4), to cathode grid wires shifting slightly out-of-plane, because of a lack of tension. These shifts cause a gain variation along the length of each anode wire which, uncorrected, effectively results in poor resolution. The Yale tests also demonstrated the importance of venting the vacuum containment housing slowly, so as not to stress the thin PC foil!

Final tests of the PC were done using the Princeton Cyclotron and QDDD Spectrograph facility. The goal was to determine whether the PC was in proportional mode (and therefore whether it could properly measure Z) even at quite low pressures (below 50 torr). This was accomplished by using a 48 MeV α beam on ^{12}C, ^{13}C, and melamine to produce ^{12}C, ^{13}C, ^{13}N (from (α, t)), and ^{16}O recoils. These were selected magnetically by the spectrograph and detected by the PC at the focal plane. The tests did confirm that the PC ΔE signal for ions of the same energy was linear with Z^2 at 50 and 25 torr, although low count rates made identification difficult, especially for ^{16}O.

3.4.4 The Silicon Array

The silicon micro-strip array was the final detection element in the CE-06 detector stack. The array was used to measure an incident ion's total kinetic energy E, to provide a timing measurement for determination of the ion velocity, and to measure the ion position in the x-z plane (see Fig. 3.11). In order to eliminate the need for another foil, the detectors were to operate directly behind the back cathode grid of the PC, in the gas volume. As with the proportional counter, a large active area of at least 60×10 cm was needed to maximize the solid angle subtended to the target. To achieve this size at reasonable cost, the active area would have to be segmented as an array of smaller Si chips.

The chips used for CE-06 were built by Micron Semiconductor (England), and have an active area of 5×5 cm. The silicon wafers are attached to a custom-designed printed circuit board (PCB) for support and readout capability. A single Si chip is shown in Fig. 3.20, viewed from the front (particles are incident on this face). The particular circuit board mounting allows several chips to be placed side-by-side with minimal dead region between them.

A schematic of the internal details of one of these detectors is shown from a side view in Fig. 3.21. Each detector is a passivated, ion-implanted, n-type silicon wafer, with 50 strips (1 mm pitch) etched on the front face (see App. B for a review of solid-state detector operation). An important feature of these detectors is the thin dead layer (about 1000 Å) of evaporated aluminum on the front face. Although necessary to provide an

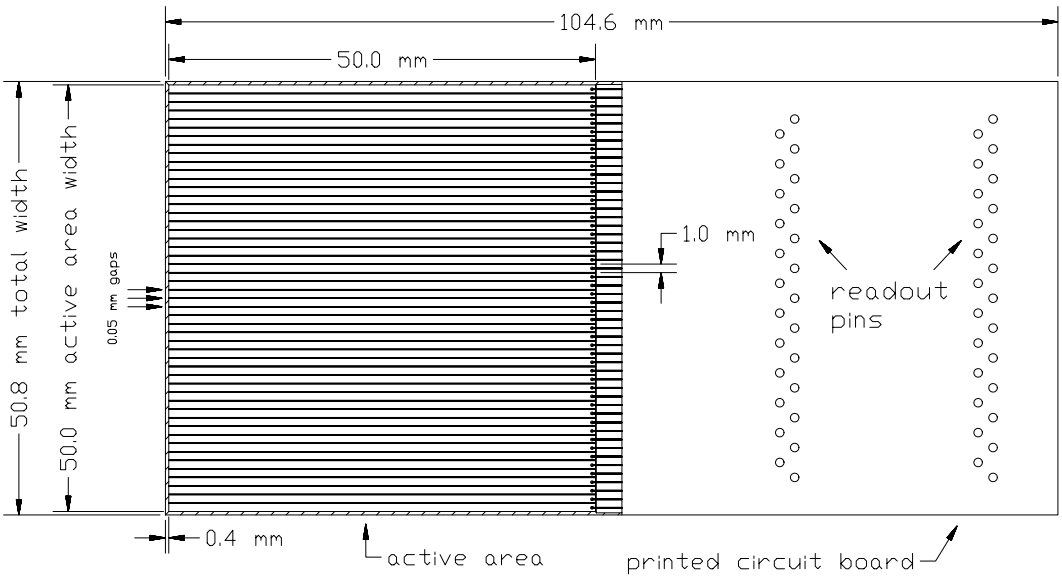

Figure 3.20 A single 5×5 cm Si detector chip. The 50 strips run parallel to the long edge of the detector The printed circuit board containing screw mount holes and pin readouts is attached at the top of the detector, for a total size of 10.5×5.1 cm.

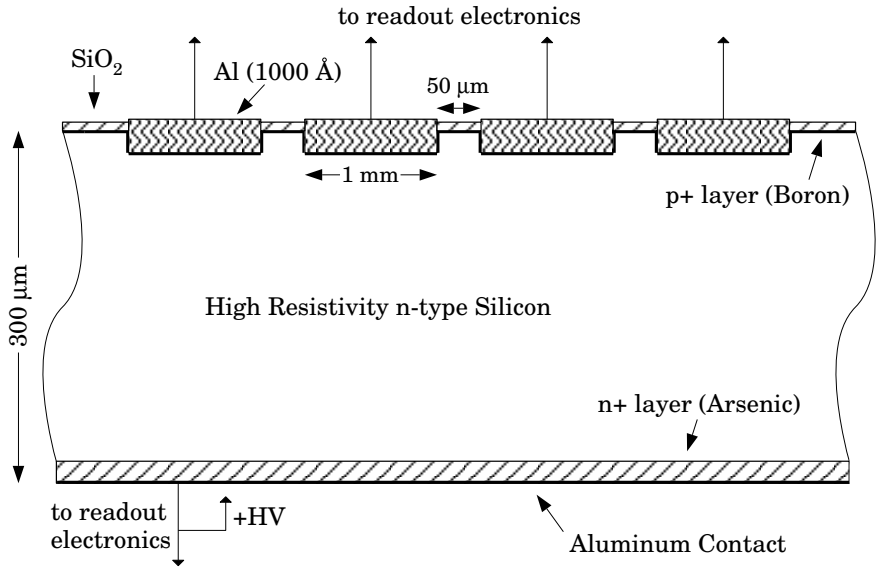

Figure 3.21 Cross-sectional view of the Si wafers used for CE-06. The layers are not drawn to scale for clarity.

electrical contact, the thinness of this layer is vital for minimization of ion energy losses.

As shown in Fig. 3.21, the chip is electrically equivalent to a p-n junction, and is fully depleted when biased by application of $V_{\text{bias}} \approx +15\,\text{V}$ to the back (the n^+ contact). The large depletion depth of 300 μm is possible because of the high-resistivity silicon used

($\rho_n \approx 20,000\,\Omega$-cm). As such, each chip is capable of stopping $Z = 6$ particles with energies up to roughly 130 MeV. The capacitance of each detector when fully depleted is roughly 1 nF.

The mounted PCB allows the readout of each strip (one pin each) and the back (one pin). In this configuration, energy and timing can be obtained from the back along with position information from the front. A significant part of the experimental development work for this project involved the construction of a readout system capable of making these three measurements simultaneously, with the following desired resolutions: $\Delta t \lesssim 1$ nsec, $\Delta E \lesssim 150$ keV, and $\Delta x = 1$ mm.

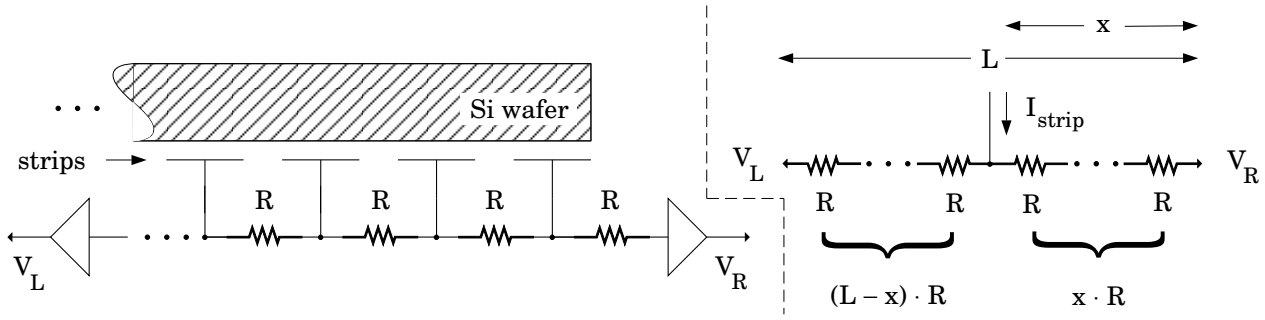

Figure 3.22 Resistive readout method for the Si detectors, shown schematically with the equivalent circuit. Tested resistor values ranged from 100–300 Ω.

Due to the large number of strips expected for the entire array (1200), and the need to have the silicon mounted inside the PC, it was desired that the position readout system would be capable of resolving each strip yet require only two position signals per chip. The first technique developed to achieve this goal employed the method of resistive charge division, shown in Fig. 3.22. A resistor chain was mounted on a chip's PCB, essentially forming a voltage divider for the current sources represented by the strips. For an ion track occurring at a distance x from the left end, the signals $V_{\rm L}$ and $V_{\rm R}$ at each end satisfy

$$x = L \cdot \frac{V_{\rm L}}{V_{\rm L} + V_{\rm R}}, \tag{3.9}$$

where L is the chip length perpendicular to the strips.

Figure 3.23 shows the position spectrum obtained in tests with the prototype PC at the Princeton Cyclotron. Using the energy signal in place of $V_{\rm L} + V_{\rm R}$, a reasonable (though not complete) strip separation was obtained for an inter-strip resistance of 100 Ω. For this type of readout, higher resistor values tend to produce a better strip separation, since $\Delta V_{\rm L} \propto \Delta x \cdot R$, where R is the resistor value.

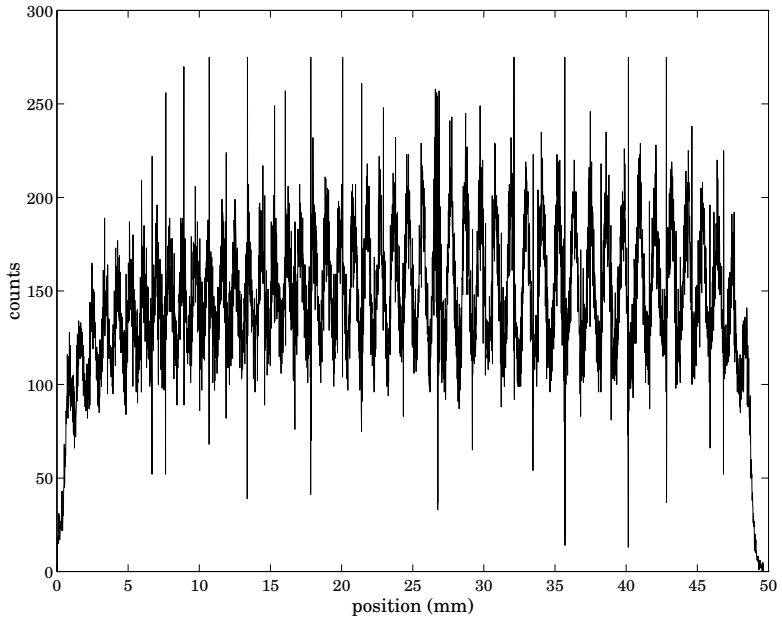

Figure 3.23 Position spectrum from a single chip illuminated by α particles with $E \approx 20$ MeV. The strip resistor value was 100 Ω, and the right end was grounded ($V_{\mathrm{R}} = 0$), so that only 49 out of 50 strips were available from the data.

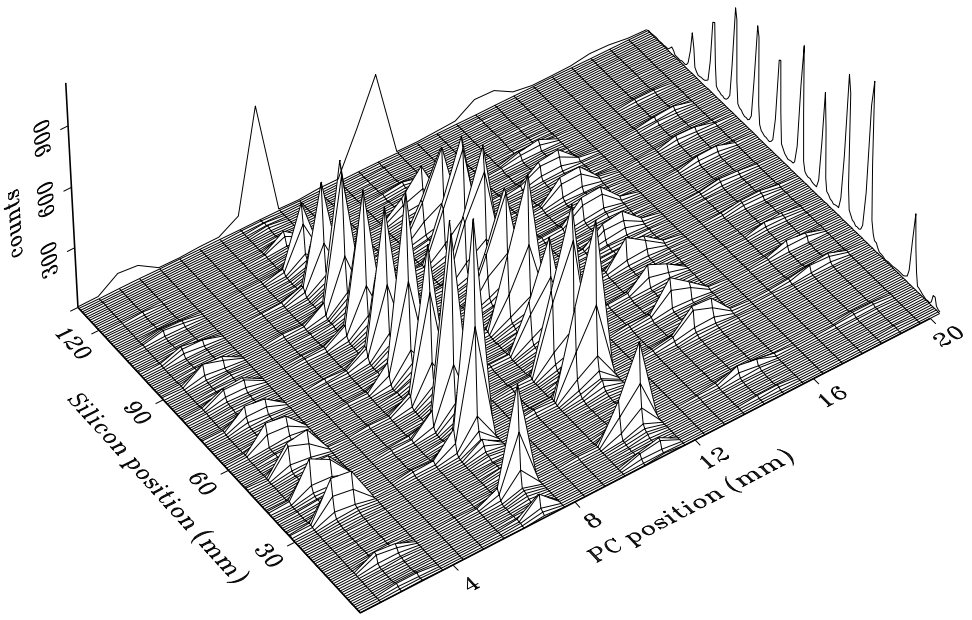

Figure 3.24 Position data for ^{12}C ions from the Yale tandem using the full-scale PC and a single 5×5 cm silicon chip, with (discrete) resolutions of 4 mm and 1 mm, respectively. One Si strip was disconnected during the test.

To test the performance of the readout method with ^{12}C ions, a chip was placed in the back of the full-scale PC for its test run at the Yale facility. Fig. 3.24 shows the two-

dimensional position information obtained by the two detectors, along with a projection of the position spectrum from the silicon. For these highly ionizing particles (50 MeV ^{12}C), each strip was clear and well-resolved from its neighbors. The energy resolution for these particles was better than 1% (about 250 keV FWHM).

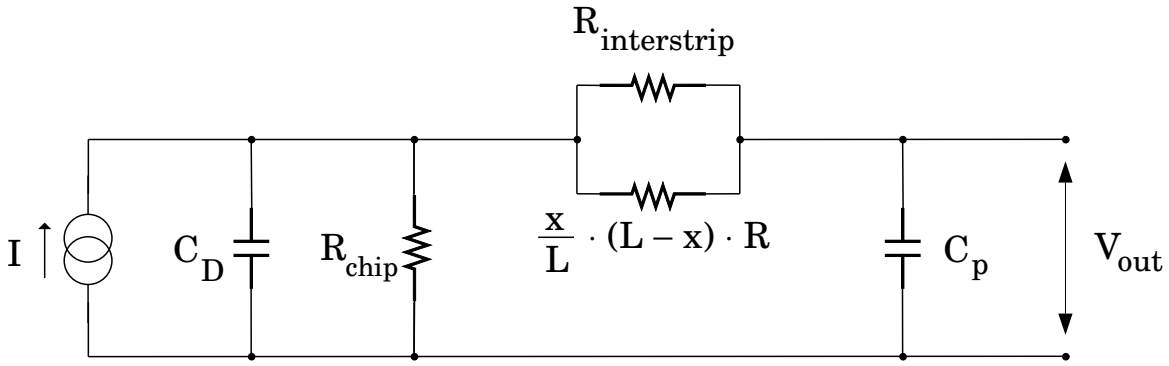

Figure 3.25 Equivalent circuit for the $E_{\rm si}$ and $t_{\rm si}$ measurements using a Si chip with resistive readout; the ionizing event is represented as a current source. $C_{\rm p}$ and $C_{\rm D}$ are the pre-amp and detector input capacitances, respectively.

These results and later data showed, however, that the timing resolution achievable which using a resistive readout was not only unacceptable ($\Delta t > 2\,\mu$sec) but highly position dependent. The equivalent circuit from the viewpoint of the timing pre-amp is given in Fig. 3.25. It can be shown that the effective risetime of the detector so configured is

$$\tau \approx RC_{\rm p}(1 - \frac{x}{L})x, \tag{3.10}$$

using the notation of Fig. 3.22. For $x = 0$ or $x = L$, the risetime is very nearly the intrinsic detector risetime (with a typical matched pre-amp capacitance) of about 25 nsec. However, for $x = L/2$, and using 100 Ω resistors, the risetime is roughly 1 μsec. Reducing the value of the resistors improves this but worsens the position resolution.

A second technique for position readout was pursued in the hope of improving the timing resolution. This method uses a delay-line configuration similar to that employed for the PGAC position readout. Fig. 3.26 shows the electronics schematic; the inductors coupled with the capacitive equivalent of each strip form a delay line with an elemental delay of $\Delta t \approx 1.5$ nsec. The left and right signals are then amplified by physically small (about 3 mm in diameter), integrated, fast pre-amp chips that could be mounted on the PCB attached to the silicon detectors. The time difference of the two position signals is proportional to the ion position (see also Eq. (3.6)), using the signal from the back as the TDC start.

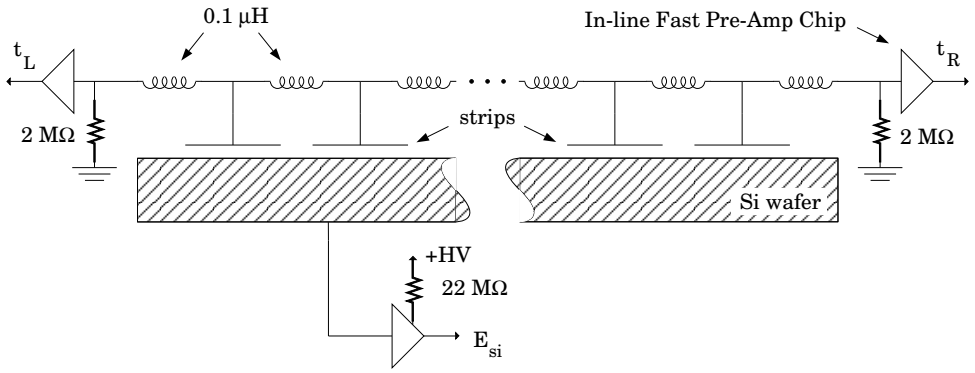

Figure 3.26 Inductive method for position readout of the Si wafers. The 0.1 μH inductors, placed between the strips (each of which is essentially a 20 pF capacitor), constitute a delay line. The small signals from each side (a few mV) are amplified by integrated pre-amp chips and discriminated.

Figure 3.27 shows α source test results of the inductive readout method. The strip separation was quite good; most of the variations in peak height per strip seen here are due to differences in the widths of the peaks. Although there were still small position variations in the timing signal risetime (mainly due to delay-line attenuation), these were quite minor compared to that associated with the resistive readout. Preliminary tests with the PGAC showed that the achievable TOF resolution was equal to or slightly better than 1 nsec.

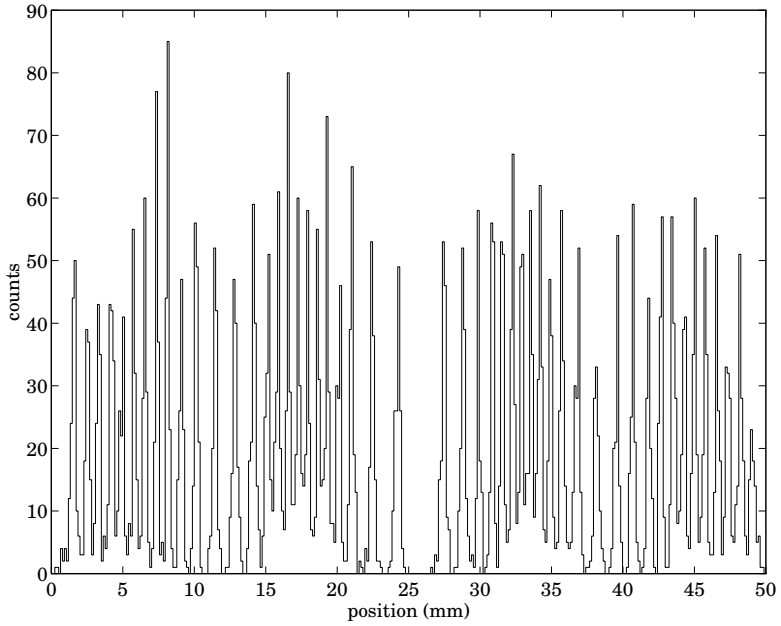

Figure 3.27 Inductive readout position spectrum for a strip detector illuminated by 8 MeV α particles. The grouping of strips (and resulting non-linearity of the strip positions) is due to the particular inductor layout on the PCB.

Unfortunately, difficulties with this readout method became apparent when the system was used with the many chips that comprised the silicon array. The problem was traced to the high-gain nature of the fast pre-amp chips designed to amplify the position signals and shape them for timing. Enough noise was generated by the chips (either radiatively or conductively through the circuit board ground plane) to be picked up by neighboring pre-amp chips via their attached silicon "antennae." The pickup would produce a self-sustaining clipping-level oscillation in the chips that would dominate any real signals. The only solution was to remove enough Si chips until the oscillation stopped, but this was untenable, since, in an actual experiment, access to the detectors would be limited due to the overhead involved in venting the vacuum enclosure.

The third technique developed for position readout, and the one actually used for the CE-06 experiment, was a return to a resistive readout with two important modifications. The first of these was a capacitive shunt to ground placed between each strip and the resistor chain (see Fig. 3.28). The effective resistance of the chain is bypassed for high frequencies by this capacitor, allowing energy/timing signal risetimes to be limited mainly by the chip's intrinsic value

$$\tau \approx \rho\epsilon \approx 25\,\text{nsec}.$$

This capacitive load also eliminates the position dependence of the risetime that was characteristic of the original resistive readout method.

The second modification was necessitated by the first: To reduce the noise contribution of the extra capacitors (totaling about 10 nF via parallel addition) to the position signal, discriminators were added to each strip before the resistor chain. This prevents the firing strip from "seeing" any of the other strips and associated capacitances. The discriminators (actually, just comparator op-amps with a stabilized threshold voltage on one input) trigger current sources located at the node points of the resistor chain, providing position dependent signals V_{L} and V_{R} as with the direct resistive readout.

Figure 3.29 shows a position spectrum for a single Si chip employing the discriminator/resistor readout method, for α particles emitted from a ^{228}Th source (see also Fig. 4.5). Complete separation (zero counts between peaks) of almost all strips is achieved, and even strips in the middle (whose discriminators see the largest series resistance) are clearly defined. Also shown in Fig. 3.29 is the corresponding timing spectrum obtained for a single chip, using the PGAC as the timing start device. The achieved resolution in this setup was $\Delta t \approx 1.3$ nsec, which, although not quite as good as that from the inductive readout, was

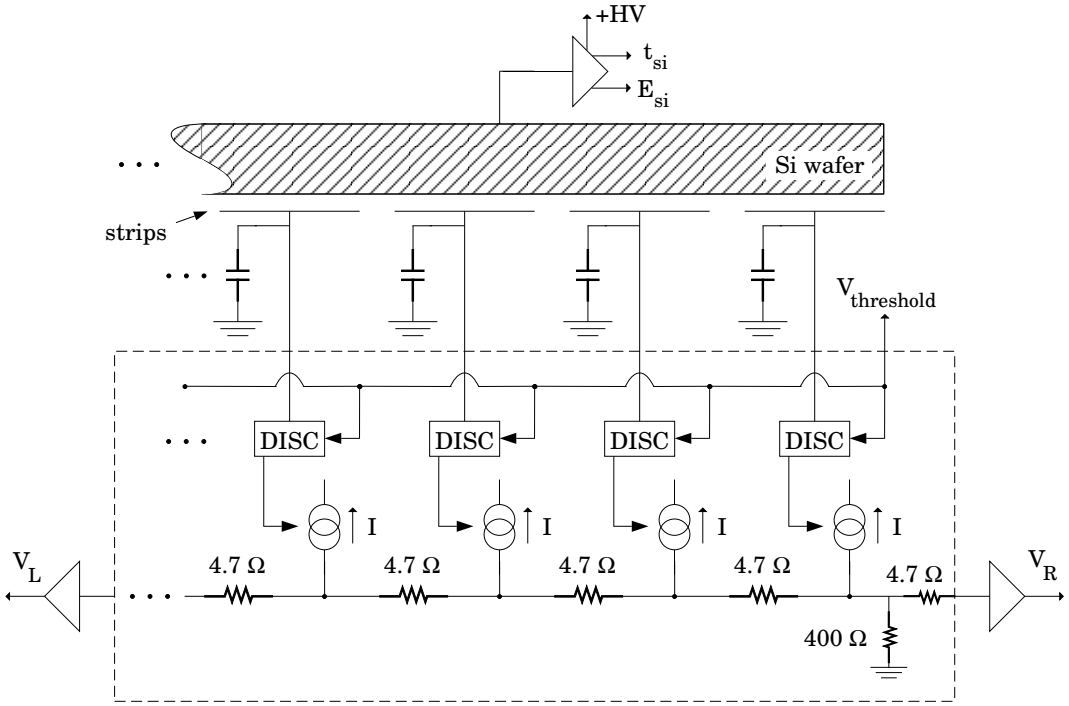

Figure 3.28 Discrimination method for position readout of the Si chips. The capacitor values are roughly 10 times the strip capacity. All the circuitry enclosed in the dotted lines was mounted on small PCBs attached to the Si wafer PCBs via short ribbon cables, for use in the restricted volume of the PC.

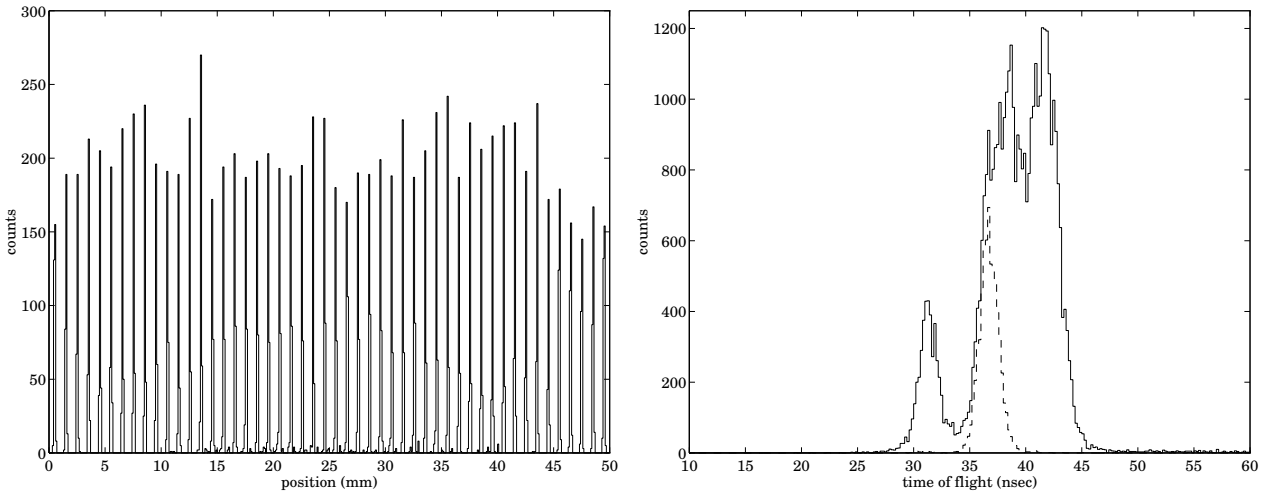

Figure 3.29 A typical position spectrum (left), using the discriminator readout method, for 6.8 MeV α particles. Shown at right is the timing spectrum using the signal from the back of the Si wafer, illuminated by a ^{228}Th source. The dashed line indicates the unresolved 6.8 MeV peak (FWHM $\approx$ 1.3 nsec).

within the range of acceptability. The energy resolution using this method was typically $\Delta E \approx 150$ keV, for 8 MeV α particles.

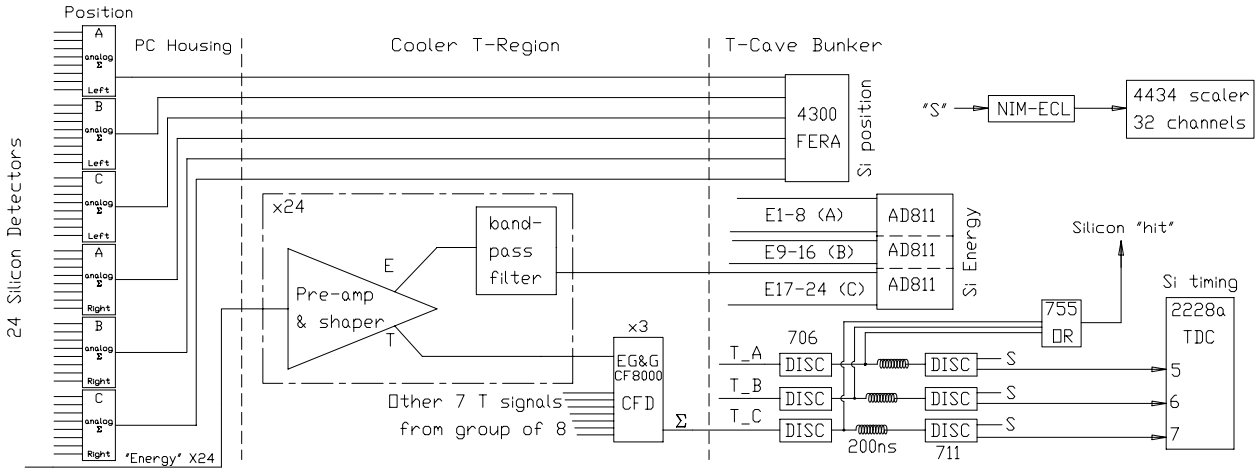

Figure 3.30 The Si electronics used in the CE-06 experiment. Physical locations are delineated by the dashed lines (see Fig. 3.31 below). Sec. 3.5 gives further details of the bunker electronics.

A ramification of such a readout system is the need (for the purpose of this work) to use 1200 discriminators, one for each strip, close to the detectors. To accomplish this, a low-power, small-sized discriminator circuit board was developed [Ho93], enabling the operation of the discriminator electronics for 24 silicon chips in the back of the PC, whether in gas or vacuum. Figure 3.30 shows the CE-06 electronics configuration for readout of the silicon array. To reduce the number of feedthroughs, the position signals were analog-multiplexed into three groups of eight signals each for "left" and "right." Determining the detector that fired could then be handled in software by setting appropriate conditions on the (non-multiplexed) energy signals.

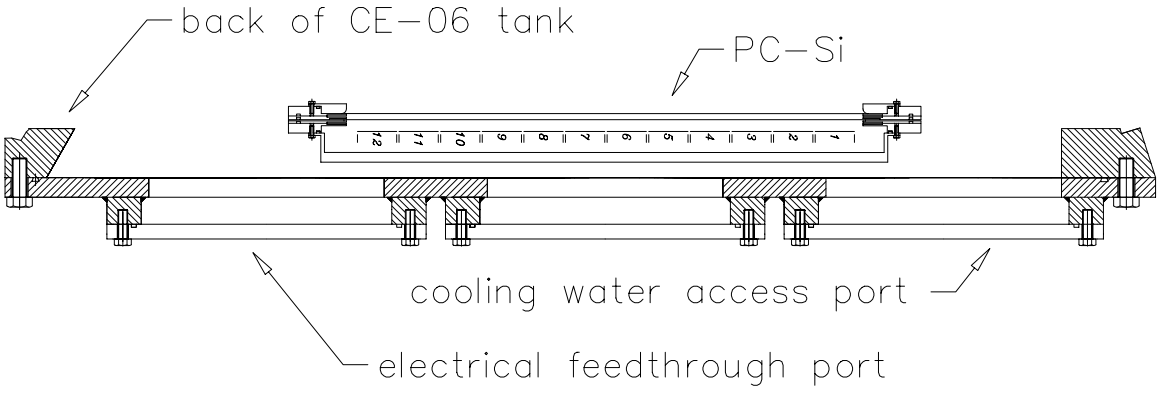

Figure 3.31 The PC and Si detector array assembly, as used in this work. Ions are incident from the top of the figure.

Figure 3.31 shows the physical setup for the PC-Si detector assembly in place as used

for the CE-06 experiment. The unit was mounted near the back of the vacuum tank (see Fig. 3.9), with electrical feedthroughs connected to one the back tank ports. Directly outside the ports were pre-amp/shapers (one for each Si chip) to construct the energy and timing signals, the latter which were then OR'd (by three eight-channel discriminator modules) into three signals corresponding to the position signal groupings. To allow use of the position readout even while in vacuum (no gas in the PC), and to improve the Si detector energy resolution, water at 0 °C was pumped through copper tubing thermally attached to the back of the PC.

3.4.5 The Luminosity Monitor

Although not formally part of the CE-06 detector stack, the luminosity monitor detector system was an important component of the experiment. In a single-pass accelerator experiment, the beam current can be measured fairly accurately using a Faraday Cup beam dump or by other direct means. Clearly, however, any method to measure I_{beam} that disturbs the beam in a significant manner is not suitable to the Cooler ring.

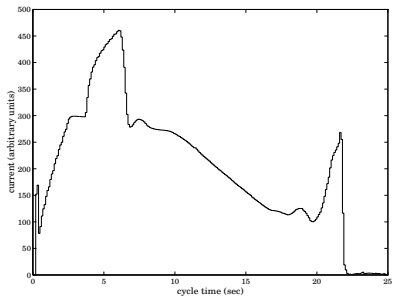

Figure 3.32 I_{ring} vs. t (sec).

Inductive measuring devices have been developed but are not completely reliable for measuring current at the desired level (accurate to a few percent for currents of less than 1 mA). The figure at left shows a typical on-line spectrum of one of these devices, installed on the Cooler ring, for a CE-06 cycle (current in arbitrary units). Problems are especially apparent at the low beam currents (typically, 50–100 μA) near the end of the cycle where the device (falsely) shows an increase in current (for comparison, see Fig. 3.3).

Another factor in the luminosity determination is the target thickness, which can often be determined fairly precisely for a self-supporting target. For the very thin targets used in the Cooler, however, a direct thickness measurement can be very difficult or nearly impossible (as in the case of a gas jet target or a target such as a fiber that doesn't cover the entire beam). In this situation, the most accurate way to measure the luminosity is to determine the event rate for a known (and large) cross-section for a process that is concurrent with the reaction under study.

Figure 3.33 shows the luminosity monitor setup used for the CE-06 experiment. The monitor was comprised of two main parts. The first of these was a Si detector (a 5×5

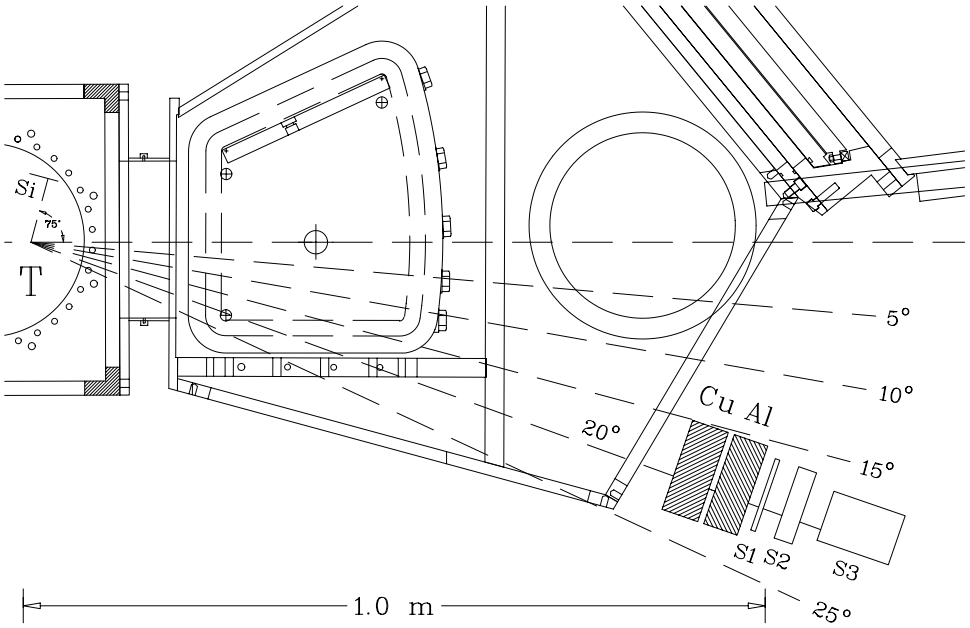

Figure 3.33 Luminosity monitor system for the CE-06 experiment. Shown is the configuration of the monitor for $E_p = 330$ MeV as used in the February, 1993 production run.

cm chip identical to those in the main array) mounted at the beam height less than 10 cm from the target-beam interaction point, located at 75° to the beam direction. The second component was a set of three scintillators, directly preceded by absorbers, mounted just outside the magnet box and centered at 19° degrees with respect to the beam. For $E_p = 330$ MeV, the absorbers consisted of copper and aluminum slabs, 2.0 and 1.88 inches thick, respectively. The scintillator thicknesses for S1, S2 and S3 (see Fig. 3.33) at this beam energy were 0.25, 1.0, and 4.0 inches, respectively.

With this system, the luminosity is measured by determining the number of events from $^{12}\mathrm{C}(\mathrm{p},\mathrm{p}')^{12}\mathrm{C}^*$, where the ^{12}C ground state and first excited state are primarily populated. Since the cross-section for this process is fairly well-known (see [Js86] and [Me83], e.g.), the time-averaged luminosity can be found by inverting

$$N = L_{\mathrm{ave}} \cdot \left[\int_{\Delta\Omega} \frac{d\sigma}{d\Omega}\, d\Omega \right] \cdot \Delta t, \tag{3.11}$$

where N is the total number of monitor events. For this setup, the scintillator defines the acceptance and therefore the limits of integration. The recoil ^{12}C ions can be detected in the Si monitor, in coincidence with a proton event in the scintillators, for the most precise determination of N.

In practice, this coincidence rate is difficult to measure due to the low energy (a few MeV) of the recoils and the relatively high noise-level associated with operating a high-capacitance detector mounted close to the beam. By careful adjustment of the absorber thicknesses, however, a reliable identification of the elastic and inelastic protons scattered from the target can be made by measuring dE/dx and E. The absorbers allow the final scintillator to stop the proton, and ensure a reasonable signal size in the transmission scintillators. The angle of the scintillators with respect to the beam, $\theta \approx 20^\circ$ as run in CE-06, was made large enough to avoid any small-angle multiple scatterings in the target, while maintaining a reasonable event rate (the cross-section for proton scattering drops off steeply for the beam energies used in CE-06).

3.5 Electronics

The complete electronics used for the CE-06 final production runs of December, 1992, and February, 1993, are shown in Figs. 3.13, 3.18, 3.30, and 3.34. Central to the logic scheme shown in the latter figure was the Bira 2206 CAMAC module. This component allowed simultaneous acquisition of several event streams, each involving different CAMAC readout schemes, of various readout priorities. Scalar events (Bira #4) occurred throughout the runs every 0.1 sec (artificially produced by a clock), and consisted of readouts of several detector rate counters (denoted by "S" in the figure). The data was stored in a single-width 32-channel LeCroy 4434 scaler module, for efficient block readout.

A detector stack event (Bira #6) consisted of a coincidence between the PGAC and any one of the silicon detectors. The twenty-four silicon detectors were multiplexed into three groups of eight detectors each, for the position and timing signals. Even so, event #6 required the readout of 55 linear signals (twenty-five for the PC ΔE signals, twenty-four for the silicon detector E signals, and six for silicon position) and 11 timing channels (three for the silicon and eight for PGAC position and timing). Although this total number could have been greatly reduced with a hardware logic trigger and fast clear, the fairly significant gain corrections needed for gain matching of the PC wires and Si chips were possible to carry out only at the software level and so it was necessary to readout all possible channels.

To accomplish the readout, LeCroy 4300B FERA modules were used for fast conversion (in less than 10 μsec) of the linear and timing signals (the latter in conjunction with 4303 TFC modules). These were readout in zero-suppression block mode, leaving the relatively slow AD811 ADC modules (80 μsec conversion) for the E signals last in the

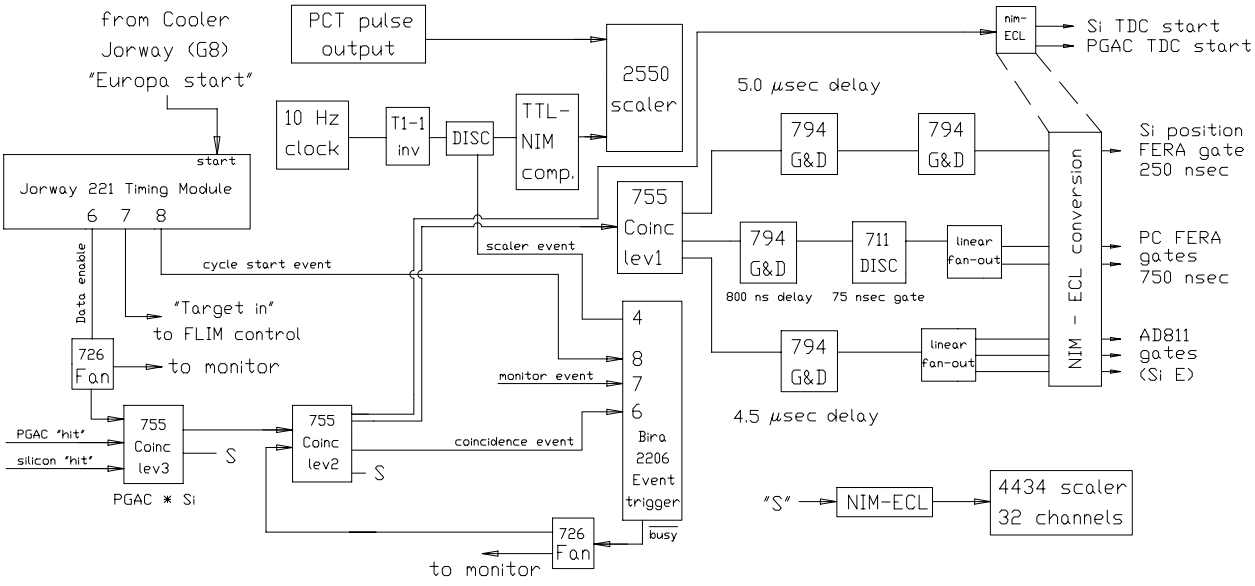

Figure 3.34 Electronics logic configuration for the final CE-06 run. The PGAC and Si "hit" signals were generated via the electronics of Figs. 3.13 and 3.30, respectively. The luminosity monitor electronics are not shown.

readout process. In this way, hardware readout rates for the event #6 stream of roughly 1 kHz were easily attained for direct writing to tape (with no computer processing).

As a separate Bira event stream (#7), the monitor detectors were readout upon receipt of a coincidence trigger from two of the proton arm scintillators. The silicon monitor was readout in slow coincidence with this trigger, since the expected slow rate of true luminosity ^{12}C-p coincidence events (on the order of 1 Hz) suggested that a software coincidence measurement would be a reasonable choice. However, the sensitivity to protons made this event stream the most active one during the CE-06 production runs.

Event stream #8 was an artificial event corresponding to the beginning of each Cooler cycle (the trigger was obtained from the ring's ramping computer). At an appropriate time later (soon after the receipt of another signal, "Cooler Ready"), the target would be moved into the beam. All such times in the cycle period pertinent to the experiment were stored in the Jorway 221 module (near the upper left of Fig. 3.34), which provided a logical "true" when that time was reached. In this way data was taken only when the beam was properly cooled and the target was in position. This "data-on" time ranged from roughly 10 to 25 sec depending on the beam current and lifetime with the particular target.

The only major readout difficulty concerned the PC. Since the internal PC pre-amps invert their (negative) input signals, the signals must once again be inverted and attenuated to be used with the FERA modules, which are sensitive to negative input charge.

Integrated, passive transformer chips were used as inverters, preceded by high-pass filters (characterized by $(RC)^{-1/2} \approx 200$ Hz) for AC coupling and reduction of 60 Hz noise induced by the long ground cable leads from the T-Cave area to the T-Site. An extra resistor was used in each wire's circuit as part of a resistive divider in order to provide an attenuation by a factor of two. This kept the charge integration of the slow PC pre-amp output signals (with fall times of approximately 10 μsec into 50 Ω) below the FERA saturation limit of $Q_{\max} \approx 480$ pC.

A fast amplifier for each channel was necessary since the PC had to be run at a relatively low voltage ($V \approx +565$ volts compared to the prototype voltages of 800–1000 volts). This reduction served not only to reduce the output signal size so as not to produce FERA overflows, but also to minimize gain variations due to the non-rigid cathode grids. Without the amplifier stage, the signal-to-noise ratio was unacceptably small (about 4:1) under these conditions, so twenty-five channels of fast amplifiers, at or near the lowest gain settings, were used for most of the production runs.

4

Data Analysis and Results

Online testing for the CE-06 experiment began in March, 1992, and continued through August of that year, at which point the detector setup and readout design methods were finalized. Production data were taken in December, 1992, and February, 1993, at proton energies of 166, 200, 250, 295, 330, and 350 MeV, using both fiber and foil carbon targets. This chapter discusses the analysis of this data along with the resulting cross-sections obtained near the single-pion reaction thresholds and in the region of possible double-pion production.

4.1 The Analysis Method: An Overview

The experiment described herein is primarily a study of two-body reactions in which the momentum of one emission product is much larger than that of the other. Positive pions produced via $^{12}\mathrm{C}(\mathrm{p},\pi^+)^{13}\mathrm{C}$, for example, have $\vec{p}_{\pi,\mathrm{lab}} \approx \vec{p}_{\pi,\mathrm{cms}}$ whereas the recoil ^{13}C ions' momenta satisfy $\vec{p}_{\mathrm{ion,lab}} \approx \vec{p}_{\mathrm{ion,cms}} + \vec{P}_{\mathrm{cms}}$. For $E_p = 166$ MeV, in particular, the ^{13}C ions have laboratory momenta comparable to the proton beam ($p \approx p_{\mathrm{beam}} \approx 580$ MeV/c) while the pions' momenta are smaller by an order of magnitude ($p_\pi \approx 60$ MeV/c). As seen in Fig. 2.7, this momentum mismatch results (in the laboratory frame) in a quasi-elliptical kinematic locus in the p-θ plane, with a well-defined maximum angle θ_{max} and two possible momenta values for each emission angle. The low- and high-momenta "branches" of the (p,θ) locus correspond to the forward ($0^\circ \leq \theta \leq 90^\circ$) and backward ($\theta > 90^\circ$) scattering of the light particle in the center-of-mass system (CMS), respectively (see Fig. 4.1). For

CMS pion distributions which are strongly forward-peaked, the projection of the p-θ ellipse onto the momentum axis results in a well-defined group in the momentum (and kinetic energy) distribution of the recoils. A localization of recoils in a high-energy group similarly corresponds to a backward-peaked pion distribution.

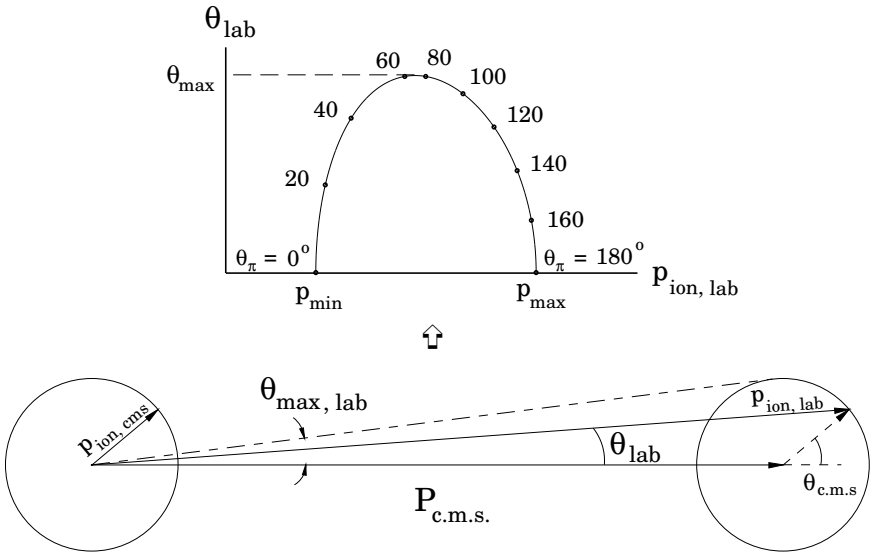

Figure 4.1 Center-of-mass and laboratory kinematics for two-body reactions such as $^{12}\mathrm{C}(\mathrm{p},\pi^+)^{13}\mathrm{C}$. For a given beam energy, there is only one degree-of-freedom in the system: $\theta_{\mathrm{cms}} = \theta_{\mathrm{cms}}(p,\theta)$. See also Fig. 2.7.

For a kinematically complete recoil measurement of reactions of this type, the data at each energy should provide: a) identification of the reaction particles, and b) the recoil momentum and emission angle in the laboratory system. Requirement (a) can be met, if the process is a two-body reaction, by determining the mass M and atomic number Z of the ion.[1] The measurement of (b) then allows the determination of the system's single degree of freedom, the center-of-mass angle θ_{cms}, and the cross-section follows.

Figure 4.2 graphically shows the raw data variables that are measured by the CE-06 detector apparatus, along with the desired intermediate[2] and final[3] calculated quantities that are necessary to determine in order to satisfy conditions (a) and (b). The raw data includes two-dimensional measurements of the intercepts of the ion track at the PGAC and PC-Si active areas which, given the physical location of each detector in magnet

[1] For three-body final states with a p + ^{12}C entrance channel, this is true only for certain limiting cases, for example, $M = 13$ amu.

[2] Half-baked.

[3] Cooked.

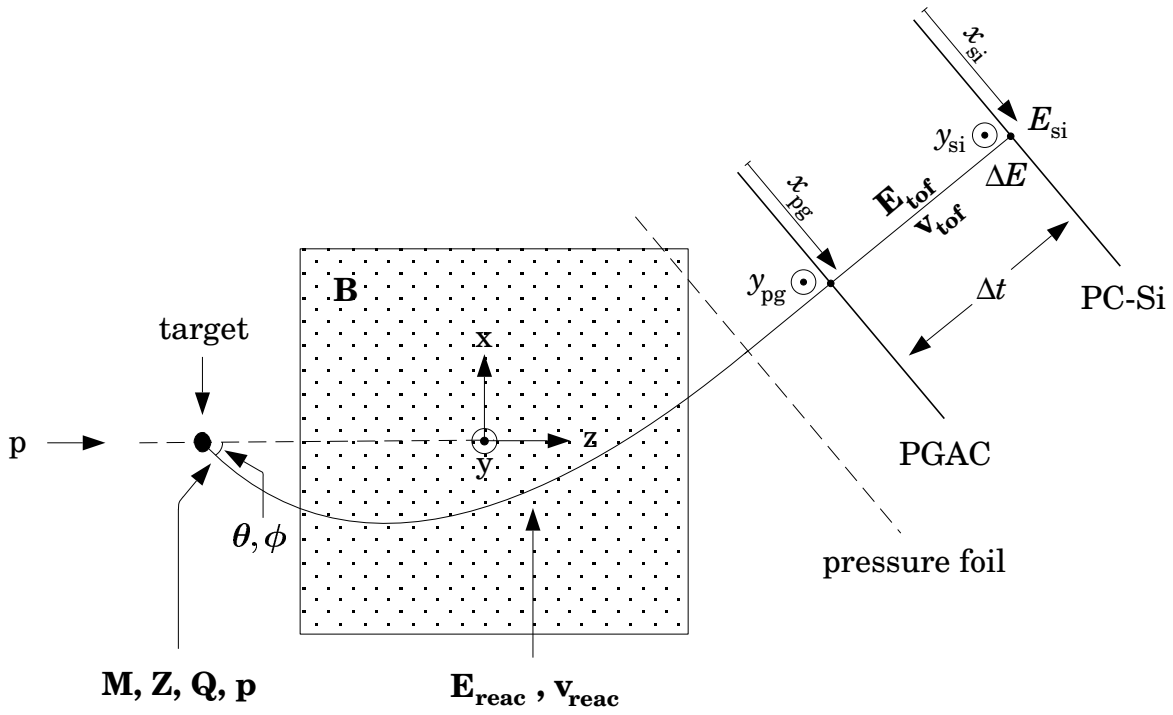

Figure 4.2 The raw and calculated data involved in the CE-06 data analysis, for a single recoil ion flight path. Raw (directly measured) data are shown in italic, and calculated quantities are shown in bold. Figure is not drawn to scale.

coordinates (cf. App. C), yield the (x, y, z) location of the ion at two times in its flight path. With this information, the velocity of the ion while between the PGAC and PC can be calculated using the raw timing signals from the PGAC and Si detectors: $\Delta t = t_p - t_s$. The transmission energy loss ΔE in the PC active volume and the ion energy at the silicon array plane $E_{\rm si}$ complete the raw data obtained for each event.

Further analysis can take one of two paths, depending in effect on whether a complete ion identification can be made by the detector stack or not. In principle (i.e., without regard to detector resolutions), the analysis can proceed as follows. First, the ion nuclear charge is identified via the PC and silicon array detector measurements of ΔE and $E_{\rm si}$ along with Eq. (3.8). Next, the ion mass identification is made using the approximation

$$E_{\rm tof} = E_{\rm si} + k\,\Delta E \tag{4.1}$$

along with

$$M = 2 \cdot E_{\rm tof} \cdot \left(\frac{\Delta t}{l}\right)^2, \tag{4.2}$$

where k is a constant and l is the measured time-of-flight distance.[4]

[4] All of the ion identification calculations done here are non-relativistic: typically, $v_{\rm ion} \approx 0.05 \cdot c$.

Raytracing simulations, as described in App. C, can be used to determine the appropriateness of Eq. (4.1). Fig. 4.3 describes the predicted "true" relationship between $E_{\rm tof}$ and $E_{\rm si}$ as indicated by the solid curve, which can be well reconstructed by Eq. (4.1) with $k = 4.5$, independent of M and Z (since ΔE already contains the dependence on these variables). This value of k (the best fit of the simulated data to the solid curve of Fig. 4.3) is essentially the expected ratio of the total energy loss of the ion in the PC gas and foils to that lost in the active volume alone (ΔE). The mass determination tends to be least accurate for low ion energies (see Sec. 4.3.2).

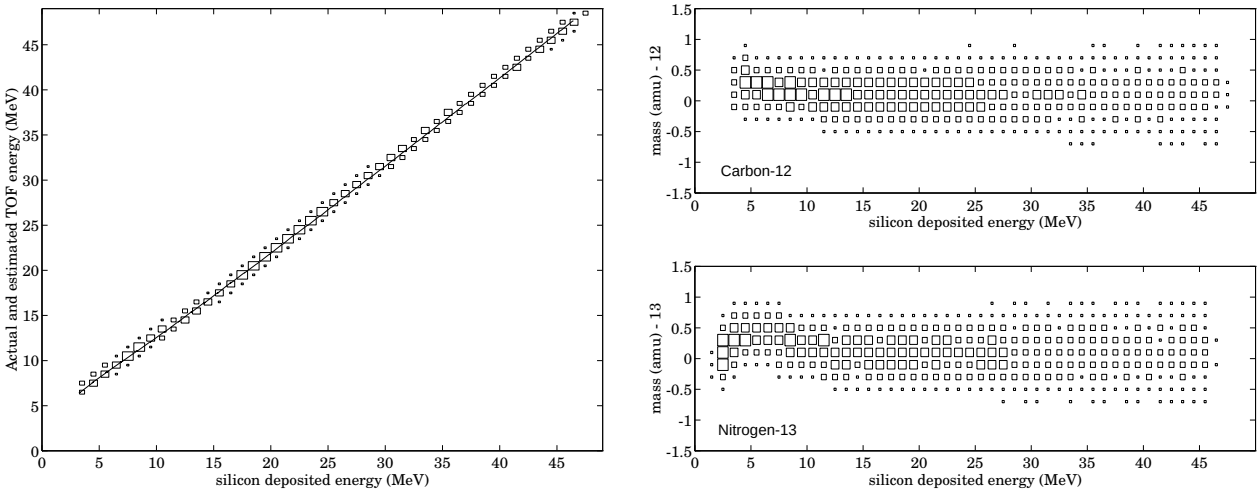

Figure 4.3 Simulated data using forward raytracing and the operating parameters (PC gas pressure, e.g.) from the production runs. At left is a comparison for ^{12}C between the "actual" (solid curve) and simulated $E_{\rm tof}$ values, the latter from Eq. (4.1) with $k = 4.5$. At right are the resulting reconstructed mass values M from Eq. (4.2) for ^{12}C and ^{13}N.

With the mass identification, the ion's flight path from the target can be determined by reconstruction of the ion's energy within the magnet ($E_{\rm reac}$, as in Fig. 4.2) using a method similar to Eq. (4.1) and then by raytracing backwards through the (known) magnetic field. Although the atomic charge Q is undetermined at this stage, the well-defined target location easily eliminates the incorrect charge state since each successively higher level of ionization is bent additionally by approximately six degrees. Given the proper charge Q, then, the ion is traced back to the target location, and the reaction parameters (p, θ, ϕ) are determined.

The uncertainties in Δt and $E_{\rm tof}$, primarily through the timing and PC resolutions, make the calculation of M via Eq. (4.2) inconclusive, however. In order to distinguish

between $M = 12$ and $M = 13$ ions[5], for example, a mass resolution of $\Delta M/M < 8\%$ (or 4% FWHM) is needed. With a timing resolution of 1.3 nsec FWHM, and Si and PC resolutions of approximately 150 keV and 60 keV, respectively, the mass resolution is roughly 5% FWHM, and so the masses are not fully resolved. The methods used to overcome this problem are detailed in Sec. 4.3. The general technique is as follows: first, a second calculation of $E_{\rm tof}$ is obtained using

$$E_{\rm tof} = b \cdot E_{\rm si} + a, \tag{4.3}$$

for constants a and b, which corresponds to fitting the solid curve of Fig. 4.3 to a straight line. This method has the advantage over Eq. (4.1) in that only the comparatively high-resolution Si energy measurement is used instead of the PC measurement. The constants a and b are dependent on the nuclear charge Z of the ion, however.

In analogy to Fig. 4.3, a simulation of the mass calculation via Eq. (4.3) is shown in Fig. 4.4, for ^{12}C and ^{13}N ions. The $E_{\rm tof}$ curves can be fit to straight lines with a maximum absolute error in $E_{\rm tof}$ of 400 keV for any value of $E_{\rm si}$. Restricting the range of silicon deposited energy values to $E_{\rm si} > 15$ MeV reduces the error to less than 175 keV; hence, the curves deviate from straight lines primarily for low ion energies. This deviation is reflected in the corresponding calculated mass values, shown in the figure for ^{12}C and ^{13}N, in which the variation from a "flat" mass locus occurs mainly for low-energy nitrogen ions. Although the mass loci obtained via Eq. (4.1) tend to be more well-behaved for very low ion energies[6], the benefit in the use of Eq. (4.3) lies in the small width of the low-energy mass contours of Fig. 4.4 compared to Fig. 4.3.

Using the measured ion track positions, the backward raytracing methods of App. C are then applied to yield the rigidity and projected angle of the ion at the target. Coupled with the velocity measurement, the ratio M/Q can be determined. A reasonable determination of both M and Q can be made by studying the M (from (4.2) and (4.3)) vs. M/Q correlation. With the rigidity and angle data, the calculation of the ion's reaction parameters is complete. Before any part of this procedure can be applied to the raw data obtained in the experiment, however, it is necessary to calibrate accurately all of the CE-06 detectors; this is the subject of the next section.

---

[5] Masses will be specified implicitly in atomic mass units for the remainder of this work.

[6] The mass calculation method using Eq. (4.1) does not require the $E_{\rm tof}$ curves to be linear in $E_{\rm si}$.

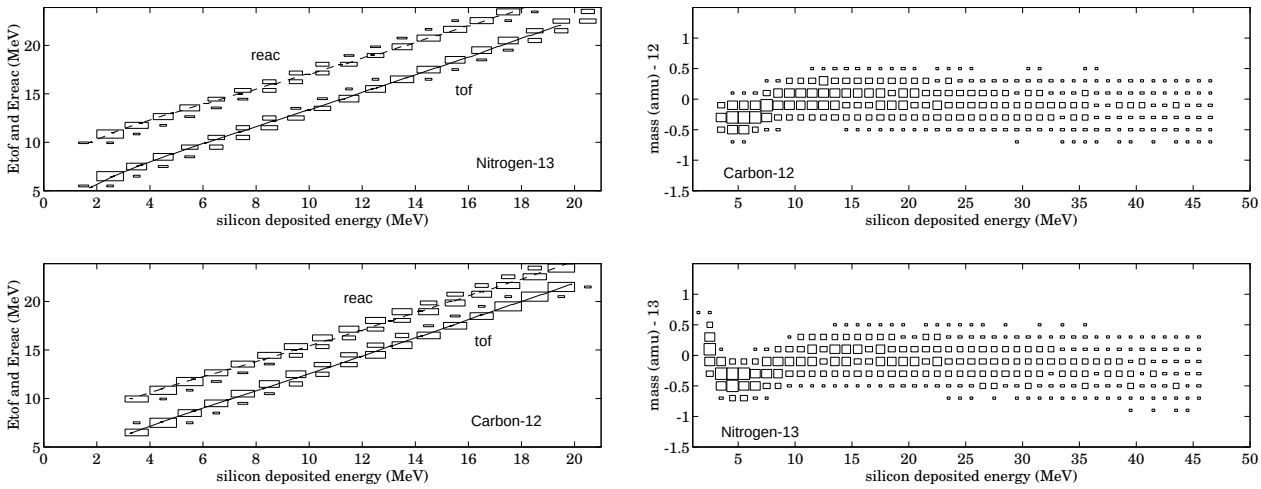

Figure 4.4 Simulated mass reconstructions (right) using only the Si energy measurement. The solid curves at left are the "actual" $E_{\rm tof}$ values for ^{12}C and ^{13}N, superimposed over simulated $E_{\rm tof}$ data using reasonable detector resolutions and Eq. (4.3). Also shown are the corresponding $E_{\rm reac}$ curves (dashed lines) and reconstructions from Eq. (4.6).

4.2 Calibration of the Detector Stack

The calibration of the detectors for CE-06 is a non-trivial but necessary prelude to the data analysis. The procedure is made complicated mainly by two factors: a) the multi-element array nature of the detectors (specifically, the Si and PC components) necessitates the gain (and offset) alignment of many channels; b) the relative insensitivity of some components (e.g., the PGAC) to standard radioactive sources (of γ rays or α particles) implies that some of the calibrations must be done internally, i.e., using the online data. There are four primary aspects of the calibration procedure, involving the silicon energy $E_{\rm si}$, the PC transmission energy loss ΔE, the Si and PGAC $\vec{x}$ measurements, and the PGAC-Si timing.

4.2.1 Silicon Energy Measurement

The matching of the twenty-four Si energy signal channels is the most straightforward element in the calibration process. The desired goal is to match the gains and offsets of all the energy signal channels; these two parameters are matched roughly in the hardware and then fine-tuned in the analysis software. A proper calibration is achieved when the summed resolution is comparable to that of an average single detector.

The multi-line α sources ^{228}Th and ^{226}Ra each provide at least four strong, well-defined energy calibration lines between roughly 4 and 8 MeV. For the CE-06 production runs, a collimated source was placed on an externally adjustable rod located directly in

front of the PC pressure foil. This source could illuminate each of the twelve columns of detector pairs (cf. Fig. 3.31) separately, with minimal interference of intervening material. As such, the proper correspondence of hardware and software channels was checked and the intrinsic resolutions of individual detectors were measured. For 8 MeV α particles, energy resolutions across the array ranged from 130 to 170 keV.

For efficient and time-effective gain matching of all the detectors, however, it was necessary to illuminate many or all of the detectors at once. A slightly collimated source (about 2 mm in width) was placed directly on the target ladder for this purpose, with an aluminum plate mounted to the side of the beam to block α particles from entering the detector stack while a target was in use. This arrangement had several advantages: a) the entire array of 24 silicon detectors could be illuminated by the source, with an appropriate choice of the 6° magnet current; b) the source could be inserted or retracted remotely via the external target ladder controls, independent of ring access, during production runs; and c) the rough operation of the remaining detectors (PC and PGAC) could be checked.

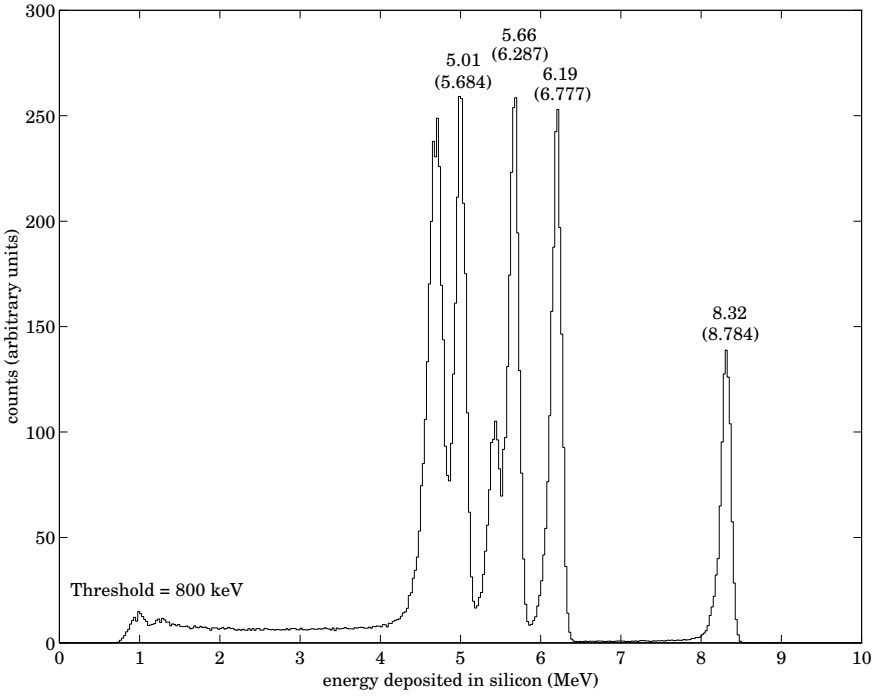

Figure 4.5 Summed energy spectrum of the silicon array illuminated with a ^{228}Th α source. Shown are the deposited energies in MeV corresponding to the source energies in parentheses. The other lines were not used in the calibration. Energy straggling is negligible here compared to the detector resolutions.

Figure 4.5 shows the calibrated Si energy signal, summed (logically) over the array,

with a ^{228}Th target source. The calibration source line centroids in the individual Si chip spectra were fitted to straight lines, whose gains and offsets were then adjusted via software corrections to convenient values. A drawback of the use of the target-mounted source for Si energy calibration is the energy losses of the α particles in the intervening foils. The losses range from approximately 500 to 700 keV, or roughly 10% of the emission energies. Forward raytracing was therefore implemented to provide the abscissas for the straight line fits, which improved the fit quality (maximum deviations from a straight line were roughly 20 keV) compared to fits using the source energies. The centroid locations of the rod source α lines agreed with this calculation within the overall Si energy resolution of about 150 keV.

4.2.2 The PC Calibration

The PC is comprised of twenty-five independent sense wires, each with separate readout electronics. The next step in the calibration process is the gain matching of these signals, which in principle is essentially identical to the procedure outlined in Sec. 4.2.1: a multi-line α source can be used to illuminate the wires, and with this data the overall gain variations among the wires can be determined. This calibration of the PC wires was, however, made significantly more difficult due to the small signals produced by the α source and to variations in single-wire gains along the length of the active area.

The small signals are a by-product of the thin active volume of the PC (see Fig. 3.14) and the relatively low ionization power of the α particles from the source. At typical operating gas pressures ($P \approx 25$ torr) for the production runs, the four α lines used for the Si energy calibration result in deposited energies in the PC active volume from 50 keV ($E_\alpha = 8.8$ MeV) to 75 keV ($E_\alpha = 5.7$ MeV). The difference of 25 keV across the source spectrum is comparable to the PC energy resolution, and so centroid measurements are difficult. The need to apply this calibration to PC signals representing deposited energies larger than this by a factor of 10 to 20 (see Fig. 4.3) further makes the α source of limited use.

Also complicating the calibration procedure was the variation in gain along the length of each sense wire. As detailed in Ch. 3, the cathode planes of the PC were constructed from wire grids to avoid the use of aluminized mylar foils. With approximately 700 wires per cathode plane, it was necessary to use tension of roughly 15 grams (a minimal amount) for each wire so as not to stress the (thin) aluminum frame. The electrostatic attraction of the cathode grid toward the anode along with the mechanical stresses in the frame

applied during the PC assembly procedure produced enough force to displace some of the cathode wires out of the plane, resulting in a position-dependent gain. For this PC design ($C_{\text{wire}} \approx 7$ pF/m), a variation in the cathode-to-anode distance of 0.3 mm is enough to produce a 25% variation in gain for an event occurring in that region (see App. A). Figure 4.6 shows typical results for several representative wires: the gain variation is maximal (at roughly 25%) for wires near the physical center of the active area (located in magnet coordinates at $y \approx 0.4$ cm). Here, the cathode wire deflection is greatest, since the grids are attached to the PC frame at the top and bottom of the active area.

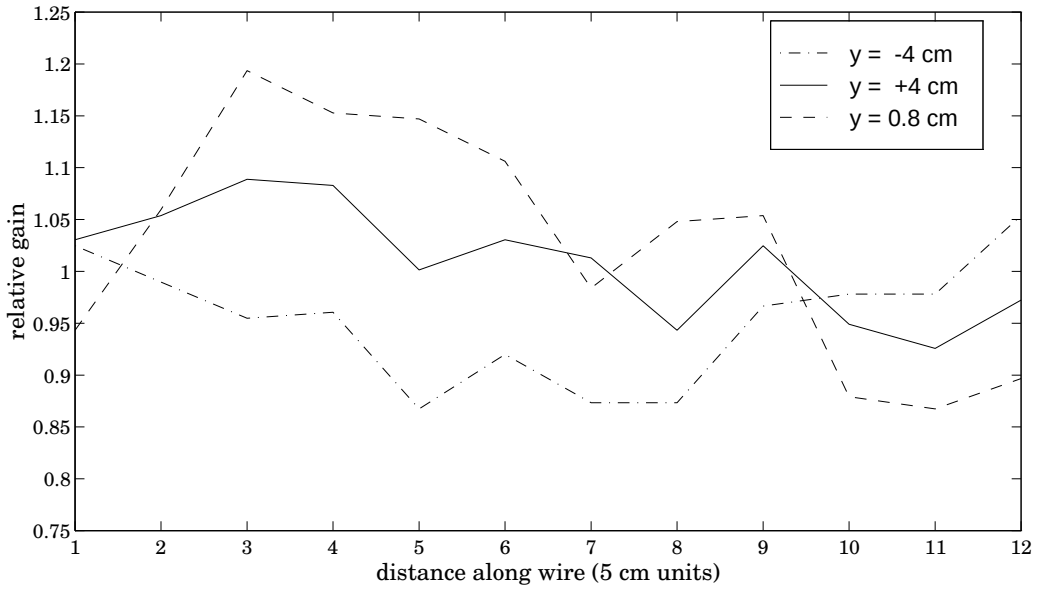

Figure 4.6 Characteristic gain variations in the PC wires, measured using the online α spallation recoils at $E_\alpha \approx 2.5$ MeV. Shown are gains (averaged over 5 cm lengths of wire) relative to the overall average.

These two main problems, the inapplicability of the target-mounted α source, and the x_{si}-dependent PC wire gain variations, were solved to a fair degree of success. Essentially, the calibration was carried out by using the internal ($3 \leq Z \leq 6$) data for gain matching with signal sizes in the region of interest, coupled with the Si energy and position measurements. The method is as follows: first, a narrow region of particle energies is chosen via a window on the Si linear signals. The window is made as narrow as possible, typically about 1 MeV in width, without sacrificing reliable PC centroid measurements. The PC signals that satisfy this gate are then plotted, for each wire, as a function of Si position, and centroid measurements are taken for a reasonable[7] x_{si} gate width. From this data, a

[7] As with the silicon energy, "reasonable" means as small as possible given the total number of counts.

table of multiplicative correction constants is generated, which allows the gain matching to be performed in the analysis software. For the production runs, a gate width of 4 mm was used, resulting in more than 3800 PC calibration constants.

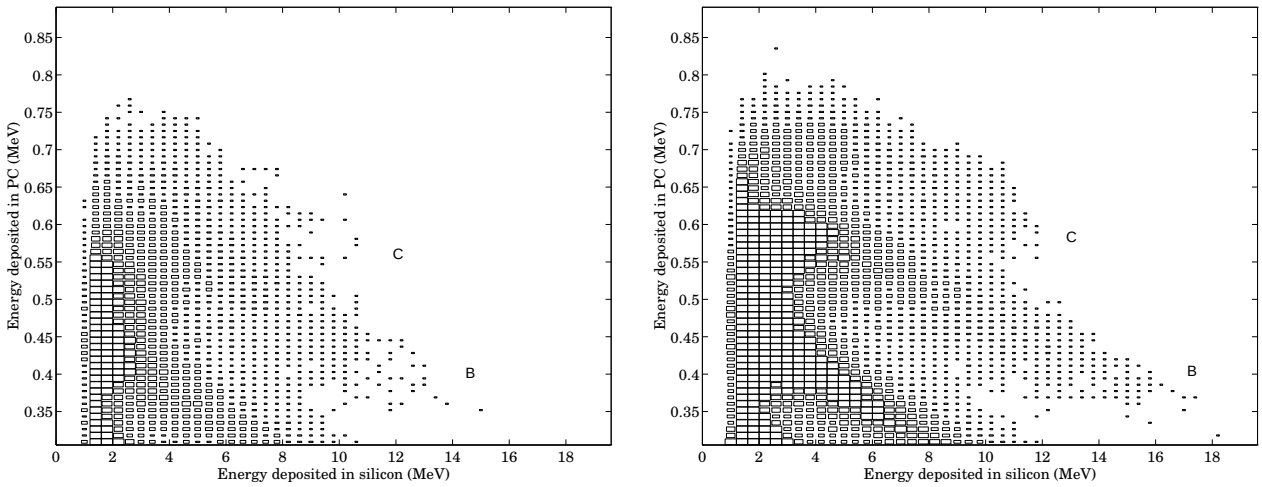

Figure 4.7 The boron and carbon region of the particle ID spectrum (ΔE vs $E_{\rm si}$) with (right) and without (left) the correction for gain variation along the wires. See also Fig. 4.11. The count density scales are the same for both figures.

A representative comparison of data with and without the calibration is shown in Fig. 4.7, where the improvement in the particle ID Z-separation is seen to be quite significant (cf. Sec. 4.3.1). Most of the overall gain fluctuation from wire to wire is due to the mechanical problems mentioned above, with less than 10% of the total variation from differences in pre-amp and ADC channel gains. As mentioned in Ch. 3, the PC was operated during the production runs at a reduced bias voltage to decrease the gain factor m, since the relative change in gain $\Delta m/m$, due to mechanical variations, depends approximately linearly on the applied voltage (cf. App. A).

4.2.3 The PGAC and Si Position Calibration

The next part of the process, the position calibration, is necessary to provide the connection between the raw position data and the corresponding magnet coordinates of the ion track's interception with the PGAC and Si detectors. In particular, the goal of the position calibration is the determination of (using the notation of Fig. 4.2) the transformations

$$\begin{aligned} (x_{\rm pg}, y_{\rm pg}) &\longmapsto (x, y, z)_{\substack{\rm PGAC, \\ \rm magnet}}, \\ (x_{\rm si}, y_{\rm si}) &\longmapsto (x, y, z)_{\substack{\rm Si, \\ \rm magnet}}. \end{aligned} \tag{4.4}$$

Since the T-Site magnet is primarily a dipole with $\mathbf{B} \approx -B\hat{y}$, and the detector active areas are oriented parallel to the y-axis, (4.4) is comprised of two decoupled transformations: one for the (x, z) coordinates and the other for the out-of-plane y positions. With these functions, the methods of App. C can be applied to determine the rigidity (R) and angles (θ and ϕ) of the ion at the reaction point.

In order to develop the coordinate transformation for the CE-06 data, it was necessary to know: a) the location of the active areas of the detectors with respect to an external reference mark on their housings, and b) the position of these marks in magnet coordinates. To determine the latter, the detectors were placed in position before the first production run (and left unmoved until the end of the second run), and direct measurements of the reference mark positions were made relative to the magnet fiducial pins (see Fig. C.2).[8] Two reference marks per detector were necessary for a complete, three-dimensional position measurement. The desired (and achieved) precision for these measurements was 1–2 mm; the knowledge of the absolute position of the ion at this level is necessary to achieve a 1–2% measurement of the ion rigidity.

Direct measurements on the detector housings were then made in order to accomplish (a). For the PC-Si detector, this was relatively straightforward; for the PGAC dimensions, however, only estimates could be made, particularly for the size of the gap between the two electrically distinct halves of the active area. The inductive position readout of the PGAC, as opposed to the discrete nature of the PC and Si detectors (and consequent correspondence of position to physical elements such as wires or strips), requires indirect measurements of its active area to be made using source data.

The procedure for these measurements is as follows: first, data is taken with a target-mounted α source (which is in a known position). Next, the direct measurements are incorporated as external parameter constants in the forward raytracing, along with the best estimates of the parameters that could not be determined directly, such as the PGAC gap. Simulated α particle data is produced with the raytracing (using the location of the α source) and compared to the real data, from which appropriate adjustments are made to the data-analysis position parameters[9], the raytracing constants, or both.

Adjustment of the parameters is accomplished by studying the relationship of the

---

[8] In reality, for reasons of physical accessibility, the relative positions (to the fiducial pins) of three monuments were first determined, and *these* were used as reference points.

[9] These constants are gain and offset parameters which convert the raw position data to the magnet coordinate system.

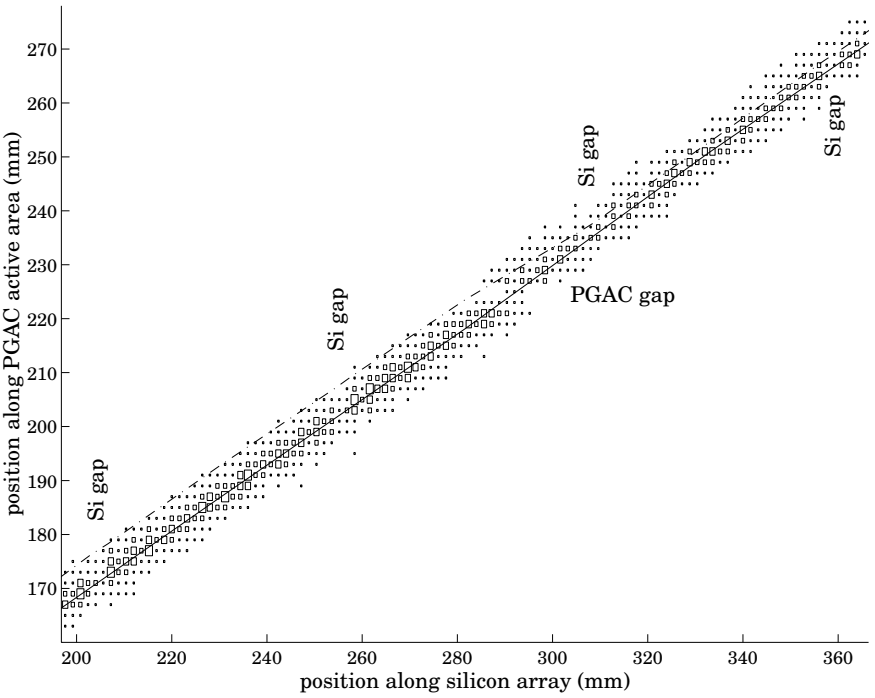

Figure 4.8 The measured position data $x_{\rm pg}$ vs. $x_{\rm si}$, using 6.777 MeV α particles and the final position parameter values, near the middle of the active area of the PGAC. The solid line is the expected relationship from forward raytracing. The dashed line is a fit to the original ("uncorrected") data. The 1.3 mm gaps between silicon detectors (at roughly every 50 mm) and the 3 mm pgac gap (near $x_{\rm pg} = 225$ mm) are also visible.

PGAC position measurement $x_{\rm pg}$ to the Si measurement $x_{\rm si}$, which is predicted to be a straight line by the simulations. The slope of the line is primarily sensitive to the angle of the detectors' active areas (in the x-z plane), whereas the offset depends mainly on the location of the beam-side edges of these areas. Although the true slope is determined fairly accurately using the direct position measurement data, the offset value cannot be determined in this way due to the uncertainties in the location of the PGAC $x_{\rm pg}$-plane edges. The needed adjustments in the position parameters should therefore involve significant corrections only to the offset value.

Figure 4.8 shows representative data (real and simulated) from which these adjustments were made. As expected, the slopes of the fitted data line and simulation line matched within the error of the simulation (this error stems primarily from uncertainties in the direct measurements), and only minor changes to the offsets, due mostly to the gap between halves of the PGAC, were necessary. As seen in the figure, the apparent width[10]

[10] This width is, in large part, due to the fact that the α source was not finely collimated.

of the measured data locus is comparable to the needed offset adjustments of roughly 3 mm. The data and simulated lines were therefore considered to be in agreement when the rigidity value for the α particle (obtained via the methods of App. C) was independent of $x_{\rm pg}$, within the rigidity resolution. This comparison further allowed an second check of the absolute rigidity value calculation; in the case of Fig. 4.8, the measured α rigidity value of $112.8 \pm .4$ MeV/c agrees well with the tabulated value of $p/Q = 112.5$ MeV/c.

A similar linear relationship exists between the out-of-plane position measurements $y_{\rm pg}$ and $y_{\rm si}$ from the PGAC and PC, respectively (the vertical position measured at the PC is virtually identical to the (unmeasured) y position at the silicon). In this case, however, the direct measurements were sufficiently accurate that no adjustments in the vertical position parameters were necessary. In part, this was due to the fact that $y_{\rm pg}$ plane of the PGAC is a single unit, unlike the $x_{\rm pg}$ plane, and the vertical locations of the detector housings were easily measured with a precision of 0.5 mm or better.

At this point, the transformation of raw position data to magnet coordinates is implicitly defined in the forward raytracing (and similarly in the backward code) and the position calibration is complete. The absolute uncertainties in the position measurements resulting from this calibration (including detector resolutions) are on the order of 3 mm, corresponding to absolute errors in rigidity and bend-plane angle of 1–2% and 0.1°, respectively. These values represent the combined intrinsic resolution of the magnet and detector stack (with this particular analysis method) as a "spectrograph." The effective vertical position resolution of 4 mm (dominated by the position resolution of the PC) corresponds to an intrinsic, vertical angular resolution of roughly 0.4°.

4.2.4 The Absolute Timing Calibration

The final step in the calibration procedure is the gain and offset matching of the twenty-four timing channels (one for each silicon detector), in order that the time-of-flight between the PGAC and Si for any event can be determined. Although an *absolute* calibration is not necessary in this case, since the velocity is mainly useful in the construction of a scaled (and discrete) quantity such as the ion's mass M, the complete determination of Δt is a natural consequence of the calibration method detailed below.

The timing calibration is similar in method to that used for the Si energy, although the disadvantages of the low ionization power of the α source as described in Sec. 4.2.2 apply here also. In this case, the PGAC, which provides the timing start signal, is relatively insensitive to the α particles, so that the anode signal is small and fails to provide optimum

timing (the resolution figure quoted in Sec. 3.4.2 was obtained using sulfur ions). The data for the timing calibration were therefore taken using the $Z = 4$ spallation products (^{7}Be and ^{9}Be, mainly) as a compromise between available counts and reliable performance of the PGAC.

The timing data for $Z = 4$ were measured in five narrow slices of $E_{\rm si}$, with typical full widths of roughly 0.4 MeV, and ranging in value from 7 to 16 MeV; the corresponding time-of-flight values ranged from 32 to 53 nsec. Using simulation data for the abscissa values, straight line fits were made to the data from each silicon detector. From these, twenty-four gain and offset pairs were constructed to provide the connection $t_{\rm raw} \mapsto t_{\rm tof}$. This procedure matches gains and offsets while providing an absolute calibration.

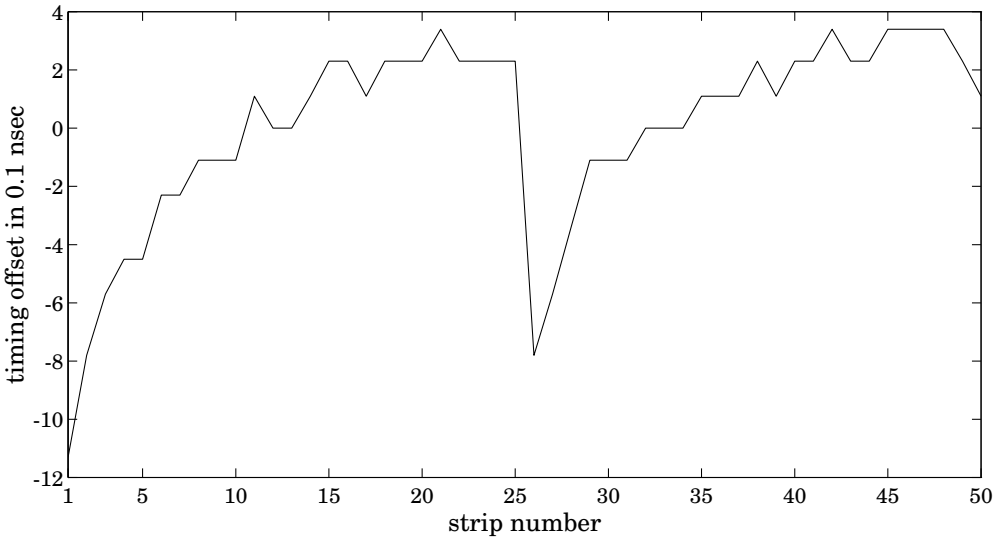

Figure 4.9 Timing offsets, in 0.1 nsec units, for each strip on a CE-06 Si chip, due to the variation in signal-wire lengths on the attached PCB. The maximum deviation from the average is 1.1 nsec.

A complication in the timing procedure arises due to the variations in signal-wire lengths on the circuit boards directly attached to the Si wafers (see Fig. 3.20). This introduces a position-dependence of the timing that cannot be corrected by a single gain/offset pair per chip. Since this is an effect of the Si chip alone, however, it is a straightforward procedure to measure these timing differences from strip to strip using the α source.

Typical data for a single chip is shown in Fig. 4.9. The circuit board is essentially divided into two blocks of 25 signal wires each, producing the large change in offset at the middle of the Si wafer. Since the circuit boards for all of the Si chips are identical, a table of 50 timing offsets suffices to provide the appropriate corrections. In this way, an overall

time-of-flight resolution of 1.3–1.4 nsec was achieved.

4.3 First-Level Analysis: Z, M, Q, p/Q, and θ

E_p (MeV)	ν_p (MHz)	C target	t ("data on")	t (elapsed)
$165.4 \pm .05$	1.81902	foil	3 hr. 18 min.	7 hr. 52 min.
$165.5 \pm .05$	1.81934	fiber	7 hr. 04 min.	18 hr. 12 min.
$199.0 \pm .06$	1.95236	fiber	9 hr. 35 min.	19 hr. 58 min.
$248.9 \pm .08$	2.11660	fiber	8 hr. 41 min.	16 hr. 05 min.
$293.7 \pm .10$	2.23877	foil	9 hr. 45 min.	15 hr. 10 min.
$328.5 \pm .12$	2.32100	foil	6 hr. 12 min.	9 hr. 59 min.
$330.4 \pm .12$	2.32527	both	29 hr. 19 min.	45 hr. 24 min.
$348.3 \pm .13$	2.36368	fiber	11 hr. 51 min.	28 hr. 48 min.

Table 4.1 CE-06 data summary. Beam frequencies refer to $N = 1$ synchotron mode. Events were recorded only during the "data on" time. The foil target was 6.2 μg/cm^2 thick, and the fiber was 4.2 μg/cm^2 thick by 8.3 μm wide. Both fiber (67% of the time) and foil (32%) targets were used at $E_p = 330$ MeV.

A summary of the CE-06 production run data is shown in Table 4.1. The difference between the "data-on" and elapsed times represents the time lost to Cooler ring overhead (filling, ramping, etc.). As discussed in Ch. 3, the listed uncertainties in the unpolarized proton beam energies are primarily systematic.

The essential goal of the first level of analysis of this data is the complete identification of the recoil ions (M, Z, and Q) along with the determination of their reaction parameters (p, θ, and ϕ). Although several different calibrations were used in the analysis (since the data were taken in two runs and three different gain settings for the Si pre-amps were used), the steps in this part of the analysis are the same for all the data. This section describes the identification procedure in detail.

4.3.1 Atomic Number (Z)

The first (and, in principle, the most straightforward) step in the identification process is the determination of the atomic number Z. With the α-particle data as a calibration for $Z = 2$, the PC and Si measurements ΔE and $E_{\rm si}$ can be used, coupled with Eq. (3.8), to separate the different species of ions. The use of the PC measurement ΔE here requires, however, that the (unknown) total ion energy *before* entrance into the PC active volume be

used in the equation, not $E_{\rm si}$. Nonetheless, for most ion types and energies typical to the CE-06 experiment (see Table C.1), this differentiation is minor and does not significantly affect the ability to resolve Z.

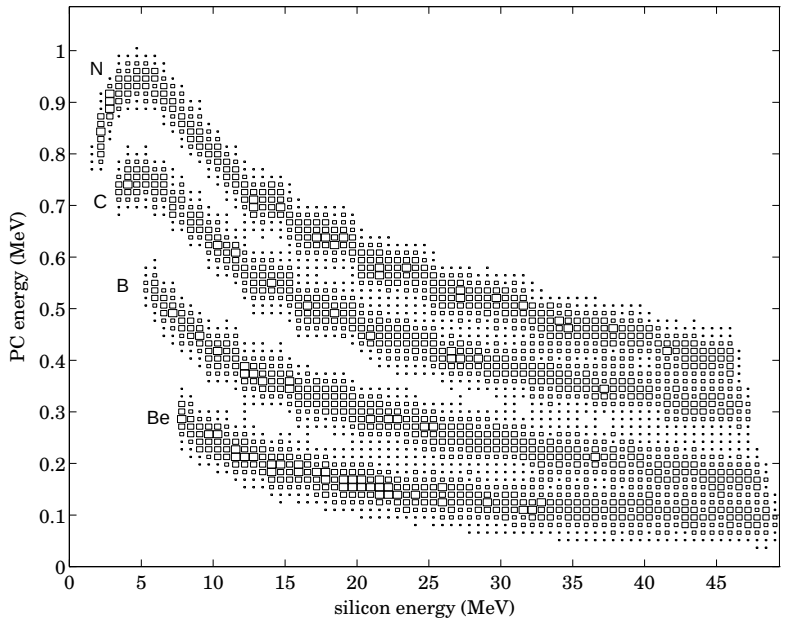

Figure 4.10 A simulation of ΔE (PC) vs. $E_{\rm si}$, using a CF_4 pressure of 22 torr, with characteristic detector resolutions included. The incident ions range in (reaction emission) energy from 10 to 50 MeV.

Figure 4.10 shows simulation data that tends to confirm this hypothesis: For all but very low-energy nitrogen ions ($E_{\rm si} \lesssim 2$ MeV), the product $\Delta E \cdot E_{\rm si}$ easily separates different values of Z (although different masses are *not* resolved). The curves for carbon and nitrogen ions turn over below deposited energies in the silicon of approximately 4 and 5 MeV, respectively. In this region, the specific energy loss of Eq. (3.7) begins to decrease as the ion velocity increases, and Z separation becomes difficult.

Particle identification data taken at $E_p = 166$ MeV is shown in Fig. 4.11. The extremely intense locus[11] for $Z = 2$ has been removed in the figure to clarify the heavier ion groups. The separation between groups is fairly clear except for the low-energy recoils with $Z \geq 5$. In order to properly define a Z-gate (such as that shown for carbon in Fig. 4.12), conditions are placed on the particle ID spectrum to clarify the location of the different groups for low energies. The basic procedure is as follows: first, a rough Z-gate is drawn in the particle ID. Next, using the mass calculation methods of Sec. 4.3.2 (which require

[11] Low-energy spallation α particles were by far the most abundant background in the CE-06 experiment.

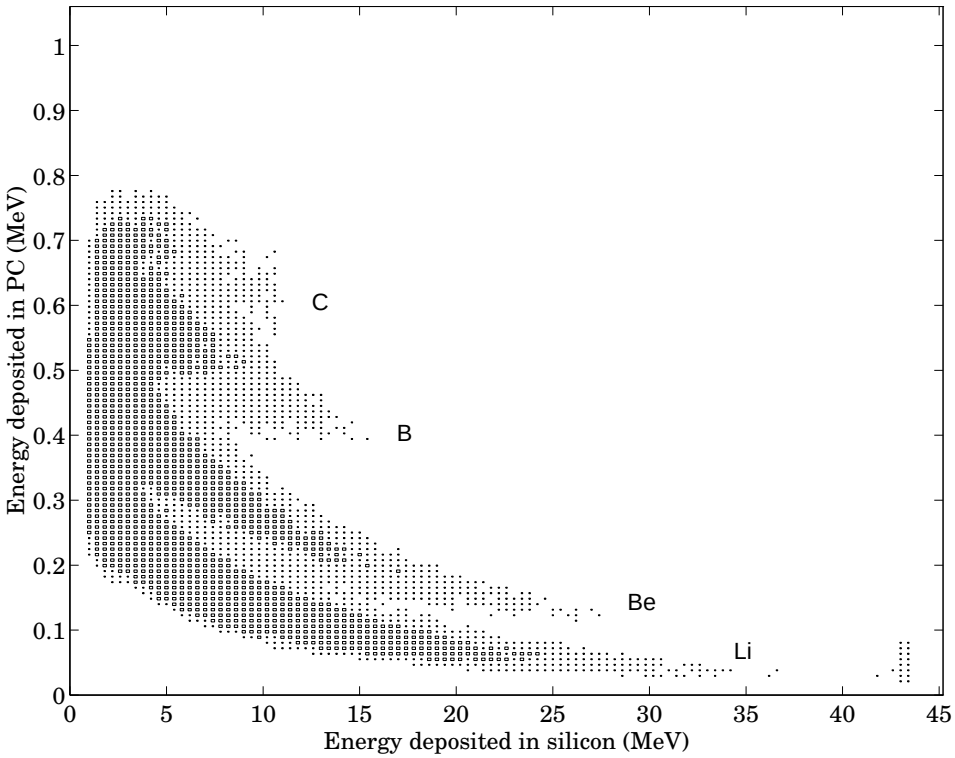

Figure 4.11 The "particle ID" spectrum, ΔE vs. $E_{\rm si}$, for the $E_p = 166$ MeV data. The clipping limits for the PC and Si measurements are roughly 1 MeV and 42 MeV, respectively. The count density scale is logarithmic.

at least a rough knowledge of Z, see below), a characteristic mass condition is specified for the ID, and the Z-gate is redrawn. This procedure is implemented by beginning with $Z = 4$ and working up to the nitrogen group.

A spectrum from this procedure, used for a more precise determination of the $Z = 6$ gate, is shown in Fig. 4.12. Here, an $M = 13$ condition clarifies the upper edge of the $Z = 6$ group, the knowledge of which is important for separation of the $Z = 6$ and $Z = 7$ loci. Similarly, the lower edge of the $Z = 6$ gate is determined previously, by construction of the $Z = 5$ gate, using a characteristic (i.e., commonly produced) mass for boron, such as $M = 10$. Mass values $M = 7$ and $M = 9$ are strongly produced in beryllium spallation products (there are, however, no expected characteristic nitrogen isotopes).

4.3.2 Nuclear Mass (M) and Atomic Charge (Q)

The next step in the analysis is the determination of the ion mass M and atomic charge Q. Although the pair (Z, M) uniquely identifies the recoil, it is further necessary to measure Q to allow calculation of the momentum p using the rigidity (see Sec. 4.3.3). The primary goal of this part of the analysis is to identify charge states from $Q = 3$ to

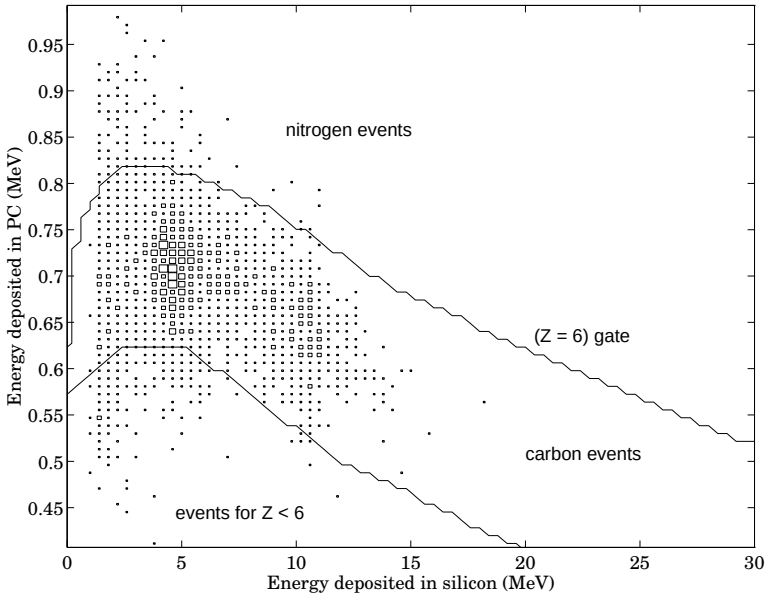

Figure 4.12 Upper portion of the particle ID spectrum, for events satisfying the PC mass condition $M = 13$ (cf. Sec. 4.3.2). The two groups inside the gate at $E_{\rm si}$ values of roughly 5 and 10 MeV are events corresponding to $^{12}\mathrm{C}(\mathrm{p},\pi^+)^{13}\mathrm{C}$. Also shown is the final gate for $Z = 6$.

$Q = 7$ and to distinguish between $M = 12$ and $M = 13$ ions, since the latter are indicative of events corresponding to reactions of interest in this work, and the former are a common background.

There are three primary techniques to calculate ion masses from the CE-06 data. The first and most intuitive of these incorporates the PC measurement ΔE along with relations (4.1) and (4.2). The application of this method to data for $E_p = 166$ MeV is shown in Fig. 4.13. In general, the value of k is adjusted until the mass contours are independent of the silicon energy $E_{\rm si}$, i.e., "flat" as in the figure. This is necessary in order to minimize the width of the projected mass locus and to separate the loci at low energies ($E_{\rm si} \lesssim 5$ MeV).

The resolution of the PC data is, however, not sufficient for complete separation of the $M = 12$ and $M = 13$ ions. The identification is acceptable for desired mass separation at the 22% level (as in the case of beryllium) but not as low as 8% (as needed for carbon). Nonetheless, once the value of k is determined for any value of Z (such as for Be ions), Eq. (4.1) is valid for all ion species, and this mass determination is useful for fine adjustment of other gates (as seen previously in Sec. 4.3.1). The parameter value used in the analysis ($k = 4.7$) compares favorably to the raytracing value ($k = 4.5$) given the expected 15% uncertainty of the energy-loss tables. For the analysis of the CE-06 data, the PC mass

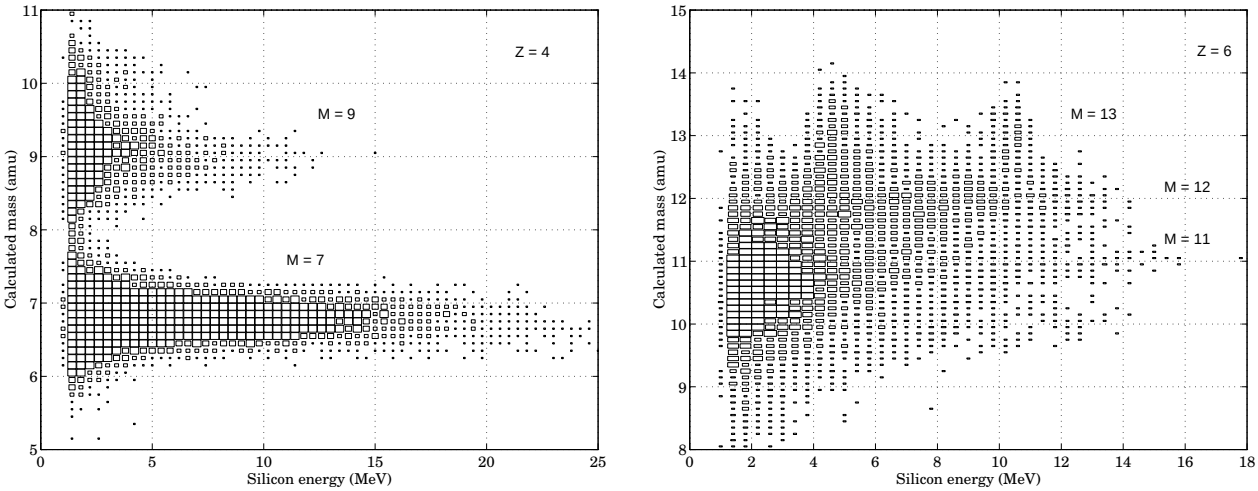

Figure 4.13 Mass determination using the PC for $Z = 4$ (left) and $Z = 6$ (right). The strong groups shown consist of ^{7,9}Be and ^{11,12,13}C. The well-known strong production of the Be isotopes allows the overall scaling of this "PC mass" quantity, along with the determination of the (Z-independent) value of k.

calculation was primarily used to ensure the proper gating and scaling of the more precise but Z-dependent means of mass determination detailed below.

The second method of mass calculation uses only the silicon measurement $E_{\rm si}$, coupled with Eqs. (4.3) and (4.2), in order to avoid the use of the comparatively low-resolution ΔE measurement. As was seen in Fig. 4.4, the applicability of approximation (4.3) is reasonable down to silicon energy values near the maximum of the Bragg curve[12] at $E_{\rm si} \approx 4$ MeV. The parameters a and b are different for each ion species, however, as seen in Table 4.2, so that the analysis requires the determination of new values for each Z value.

Ion	$E_{\rm tof}$				$E_{\rm reac}$			
	b (MeV/MeV)		a (keV)		c (MeV/MeV)		d (keV)	
	data	sim	data	simulation	data	sim	data	simulation
Be	0.96	0.97	2150	1300 ± 50	0.93	0.94	3500	2800 ± 100
B	0.90	0.95	3000	2400 ± 100	0.87	0.90	5500	4800 ± 150
C	0.88	0.93	3800	3300 ± 100	0.85	0.86	7200	6900 ± 150
N	0.85	0.92	4400	4100 ± 150	0.83	0.84	8500	8700 ± 200

Table 4.2 Energy calculation parameters for the mass determination using Eqs. (4.3) and (4.6). Shown are the final data parameters used in the analysis and those expected from simulations.

[12] The curves in Fig. 4.10 are *not* Bragg curves, but the maxima are similar.

Using the raytracing simulations to generate first-order estimates, a method similar to that for the first mass calculation is employed to determine a and b: the parameters are varied until the mass contours M vs. $E_{\rm si}$ are independent of $E_{\rm si}$. The PC mass gate is used as a condition for the contour spectrum to simplify the two-dimensional search.[13] Except for the most heavily ionizing particles (such as nitrogen ions, for the CE-06 experiment), the "true" parameters do not differ greatly from those expected from simulations (see Table 4.2 and Fig. 4.4). In general, the linear fit (4.3) tends to underpredict M at low energies and overpredict at high values of $E_{\rm si}$. To compensate for this in the analysis, the final slope and offset parameters are somewhat lower and higher than the simulation parameters, respectively. This compensation tends to improve the mass calculation for $E_{\rm si} \lesssim 10$ MeV at the expense of minor underprediction for $E_{\rm si} \gtrsim 25$ MeV.

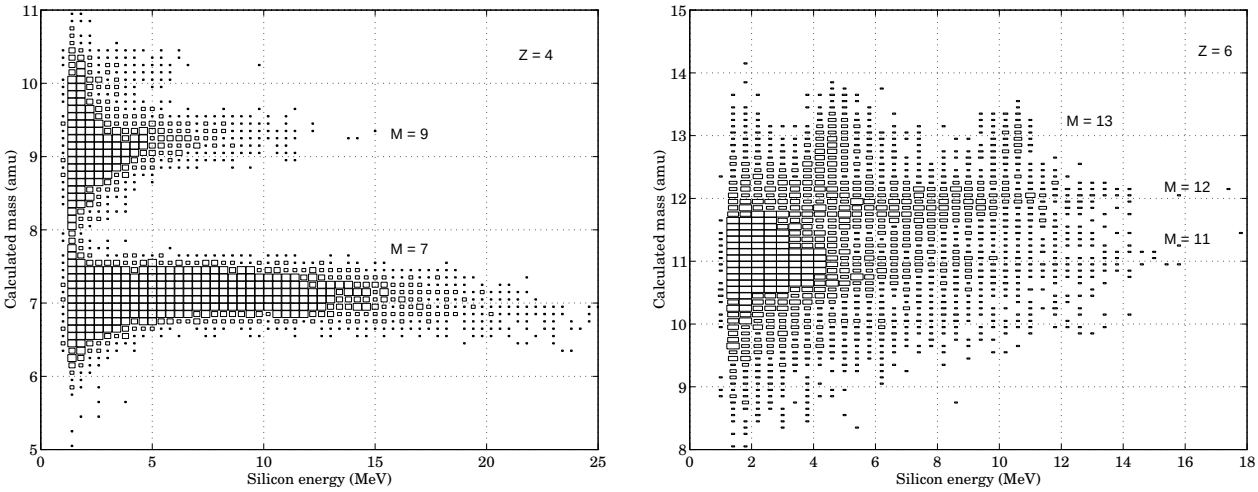

Figure 4.14 Mass determination using $E_{\rm si}$ (the "Si mass" method). Data shown is for $Z = 4$ and $Z = 6$ at $E_p = 166$ MeV (compare Fig. 4.13). The two groups at $M = 13$ correspond to $^{12}\mathrm{C}(\mathrm{p},\pi^+)^{13}\mathrm{C}$ (see also Fig. 4.12).

The application of this method to the carbon group for the $E_p = 166$ MeV data is shown in Fig. 4.14, where the improvement in resolution compared to the PC mass calculation is apparent (note especially the width of the locus for $M = 12$). The $M = 12$ and $M = 13$ groups at low energies are still not fully resolved, however. The mass separation is important in this regime ($E_{\rm si} \lesssim 5$ MeV): For the single-pion production reactions, the low-momentum branches of the kinematic loci (see Fig. 2.7) produce deposited energies in the silicon of a few MeV. The low-energy groups formed by the momentum projection

[13] Unlike k, parameters a and b implicitly define the mass scaling via (4.3) and (4.2); this scaling of the Si mass calculation is greatly simplified by pre-determination of M via the PC mass gate.

of these branches occur even for beam energies well above the thresholds of the reactions, since the low-momentum part of the loci do not "move" considerably over the energy range 166 MeV $< E_p <$ 350 MeV.

A third independent method of mass calculation is necessary to overcome the inability of either the first or second method to resolve $M = 13$ from $M = 12$. With the measurement of the ion's rigidity $R \equiv p/Q$, the mass can also be obtained via

$$M = \frac{RQ}{v_{\mathrm{reac}}}, \tag{4.5}$$

where v_{reac} is the ion velocity while inside the T-Site magnet chamber. The atomic charge Q can be determined in the following way: first, the energy of the ion during traversal of the magnet chamber, E_{reac}, is approximated (see Fig. 4.4) by

$$E_{\mathrm{reac}} = c \cdot E_{\mathrm{si}} + d, \tag{4.6}$$

where c and d are constants determined from raytracing simulations and the related parameters[14] in Eq. (4.3). Then, the atomic charge can be written as

$$Q \propto \frac{\sqrt{E_{\mathrm{tof}} E_{\mathrm{reac}}}}{v_{\mathrm{tof}} \cdot R}. \tag{4.7}$$

The characteristic charge-state populations measured via (4.7) for carbon at $E_p =$ 166 MeV are shown in Figure 4.15. Similarly to the silicon method of mass calculation, the Q contours are adjusted using c and d to be independent of the silicon energy, although the different charge states are well resolved even in the low-energy regime. Furthermore, since Q is quantized, an exact value can be used in Eq. (4.5) with no error contribution. The widths of the projections of the Q-contours are therefore irrelevant, assuming that a two-dimensional separation in the Q-E_{si} plane is possible.

The ion's velocity inside the magnet, v_{reac}, is calculated by applying a "velocity correction" to v_{tof}, which accounts for the energy loss suffered by the ion in the PGAC and in the magnet pressure foil. Since E_{reac} has already been estimated using Eq. (4.6), the correction is facilitated via

$$E'_{\mathrm{reac}} = c' \cdot (\frac{1}{2} m_0 v_{\mathrm{tof}}^2) + d', \tag{4.8}$$

[14] The "true" parameters for E_{tof} provide a guide for variations of the values from that expected from simulations.

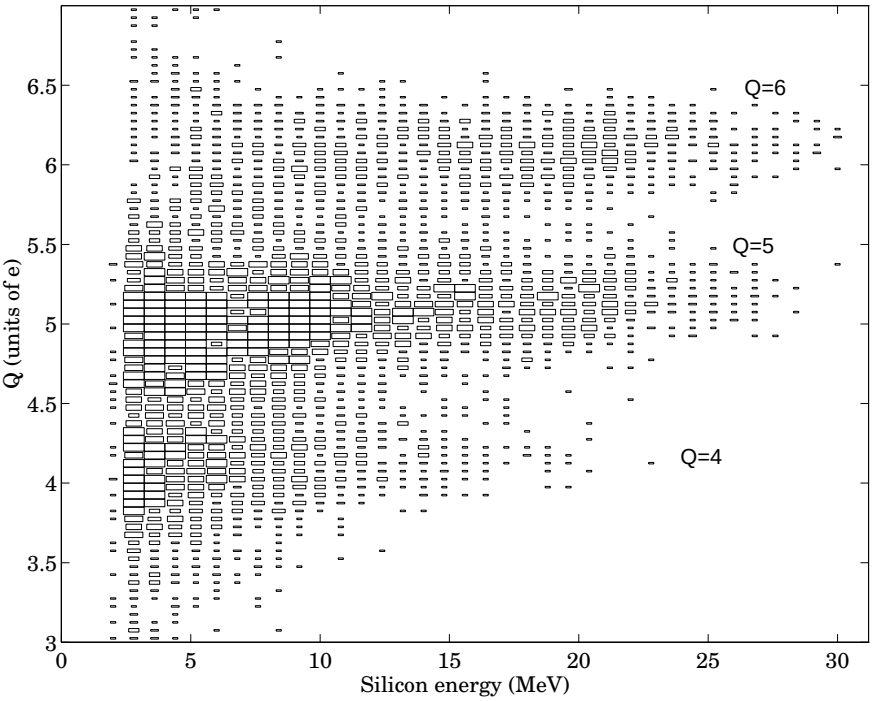

Figure 4.15 Atomic charge calculation, using (4.7) and the parameters of Table 4.2, applied to $Z = 6$ data at $E_p = 166$ MeV. Shown are the $Q = 4, 5, 6$ states of carbon.

and

$$v_{\text{reac}} = \sqrt{\frac{2E'_{\text{reac}}}{m_0}}, \tag{4.9}$$

where c' and d' are similar to but not the same as the parameters in (4.6). Here, m_0 is a provisional (exact) mass chosen to be close in value to the desired mass groups. As usual, c' and d' can be chosen by requiring the independence of the resulting mass (4.5) with respect to E_{si}.

Calculation of the mass via Eq. (4.5) is advantageous in that the relatively low-resolution timing measurement enters linearly through Eq. (4.9) rather than quadratically as in Eq. (4.2). However, the uncertainty in estimating the reaction energy[15] along with the use of another calculated quantity, R, yields a mass measurement comparable in quality to that obtained via the second method of calculation. Hence, neither of these mass calculations is alone able to provide a means of separating $M = 12$ and $M = 13$ ions. Final determination of the mass in the CE-06 data analysis was made by considering the *correlation* of the two results.

Figure 4.16 represents the combination of the second and third mass calculations via

[15] E_{reac} can be quite different from E_{si}, as shown in Table C.1.

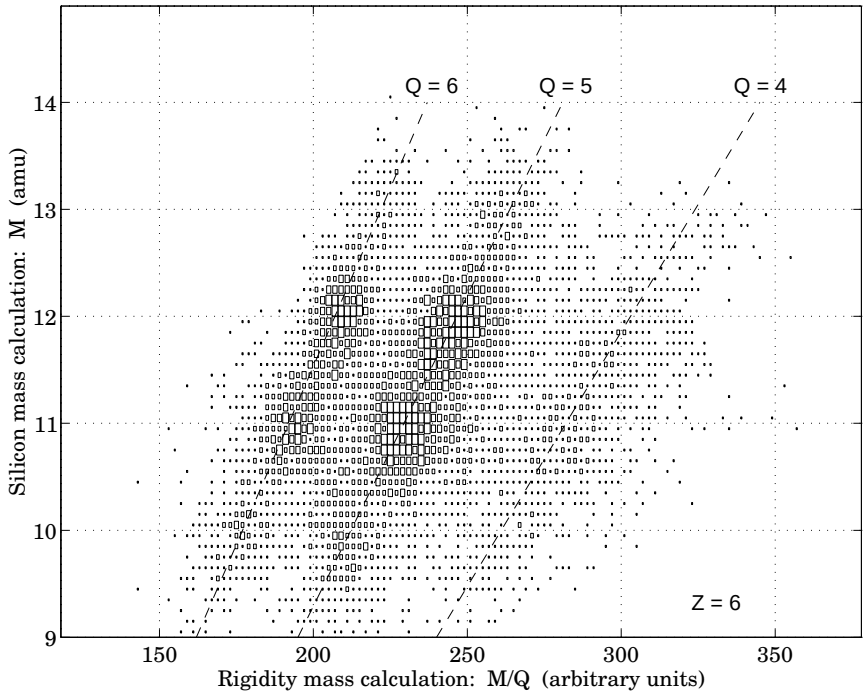

Figure 4.16 The mass and charge identification spectrum, for $Z = 6$ data at $E_p = 166$ MeV. Plotted are $M/Q = R/v_{\mathrm{reac}}$ horizontally and M (from (4.3) and (4.2)) vertically. Lines of constant mass and charge are horizontal and diagonal, respectively.

Eqs. (4.3) and (4.5), respectively. A mass and charge combination is selected using an appropriate two-dimensional gate on the spectrum. In this way, both measurements of the mass, each of which is not of sufficient resolution for separation of $M = 12$ and $M = 13$, are effectively combined to produce a satisfactory identification. Although the projections of these two mass groups onto either of the axes are not separable, the loci can be resolved sufficiently in the two-dimensional plane. The determination of Q is only necessary here to ensure proper charge calibration of the resulting M-Q gate. With knowledge of Z, the quantized mass value M completes the identification of the recoil ion.

4.3.3 Reaction Parameters: Momentum (p) and Angle (θ, ϕ)

The first level of analysis concludes with the determination of the recoils' reaction parameters (p, θ, ϕ) at the target. The rigidity R is obtained directly from the backward raytracing methods of App. C (and in fact this quantity was already used in the mass determination). Using the quantized value of the atomic charge Q, the ion emission momentum is obtained trivially via

$$p = RQ. \tag{4.10}$$

The backward raytracing also yields the ion's projected reaction angles in the x-z plane. Fig. 4.17 shows the geometrical relationship of the directly measured angular quantities θ_p and ϕ_s to the desired spherical angles θ and ϕ. The angle ϕ_s, defined in terms of the ion velocity components by $\tan\phi_s = v_y/\sqrt{v^2 - v_y^2}$, remains constant over the flight path[16], hence it is naturally measured by the detector stack using

$$\tan\phi_s = \frac{\Delta y}{\sqrt{(\Delta x)^2 + (\Delta z)^2}}, \tag{4.11}$$

where $\Delta(x, y, z)$ is the change in magnet coordinates of the ion track from the PGAC to the PC-Si intercepts.

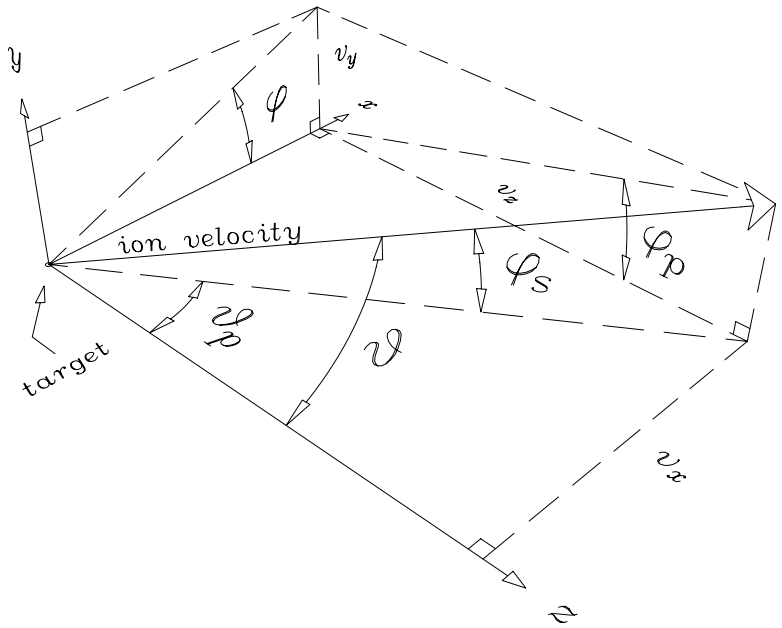

Figure 4.17 Definition of the measured and calculated angular quantities for the ion at the reaction point.

Assuming that $-90° < \theta_p < 90°$ (the T-Site horizontal plane acceptance is roughly $|\theta_p| < 25°$), the direction angle in the y-z plane is given by

$$\tan\phi_p = \frac{\tan\phi_s}{\cos\theta_p}, \tag{4.12}$$

which leads to determination of the spherical angle θ using

$$\tan^2\theta = \tan^2\phi_p + \tan^2\theta_p. \tag{4.13}$$

[16] This is actually a 1st-order approximation, due to the 6° magnet fringe field, but the 2nd-order corrections are much smaller than the detector stack's y resolution.

As a by-product, the azimuthal angle ϕ is then

$$\tan\phi = \frac{\tan\phi_p}{\tan\theta_p}, \tag{4.14}$$

the knowledge of which completes the determination of the recoil ions' kinematic parameters in the laboratory frame.

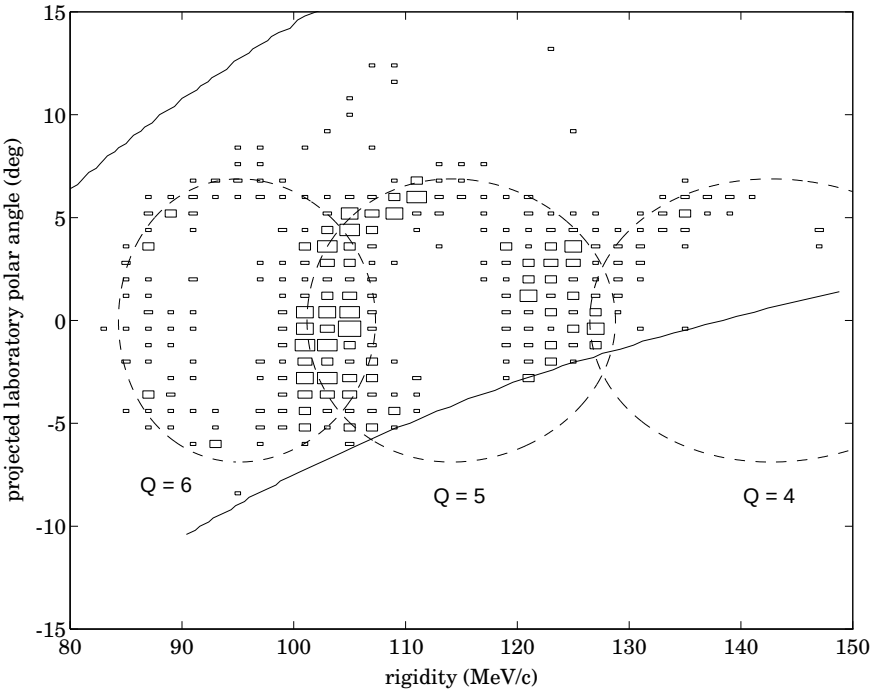

Figure 4.18 The R-θ_p relationship for ^{13}C events at $E_p = 166$ MeV. Also shown are the kinematics for $^{12}\mathrm{C}(\mathrm{p},\pi^+)^{13}\mathrm{C}_{\mathrm{g.s.}}$ (dashed lines) and the calculated acceptance (solid lines), both for $\phi_p = 0$).

The R-θ_p correlations for ^{13}C ions detected during the production runs at $E_p = 166$ MeV and $E_p = 294$ MeV are shown in Figures 4.18 and 4.19, respectively. The identification of ^{13}C implies that these events correspond uniquely to π^+ production from $^{12}\mathrm{C}(\mathrm{p},\pi^+)^{13}\mathrm{C}$, via conservation of baryon number and charge. At 166 MeV, the recoils are sufficiently confined in angle that the acceptance for $^{13}\mathrm{C}^{6+}$ ions is 4π steradians. In general, the projected kinematic ellipses may overlap for different charge states; however, these are separable since the atomic charge is known from the analysis of Sec. 4.3.2. The kinematics of $^{12}\mathrm{C}(\mathrm{p},\pi^+)^{13}\mathrm{C}_{\mathrm{g.s.}}$ are also shown in the figures, along with the calculated acceptances from the forward raytracing simulations. Many of the events occur on the inside edge of the expected ground-state ellipse; this suggests that there is a strong population of the bound

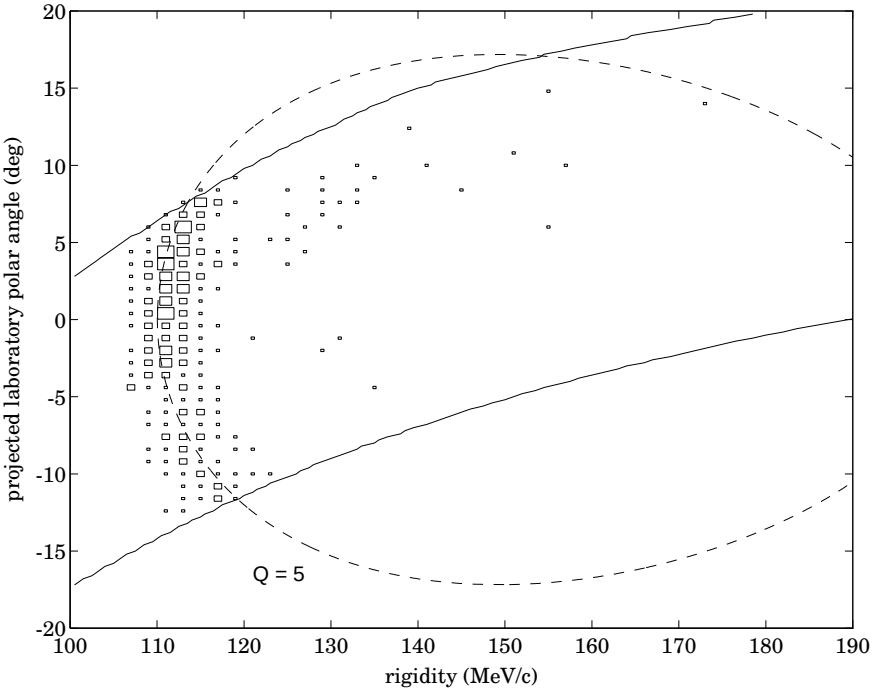

Figure 4.19 The R-θ_p relationship for $^{13}C^{5+}$ events at $E_p = 294$ MeV, with kinematics and acceptances shown for $\phi_p = 0°$ as in Fig. 4.18.

^{13}C excited states at 3.09, 3.68, and 3.85 MeV (this effect is not apparent in Fig. 4.19 due to the scale of the kinematic ellipse at $E_p = 294$ MeV).

Expressions (4.10), (4.13), and (4.14) lead to the end results—the kinematic ellipse of the recoils in the p-θ plane—of the first-level analysis. The events corresponding to (p, π^+) at $E_p = 166$ MeV are shown in Fig. 4.20, in which ions are observed along the entire locus of possible p-θ pairs. The projection in θ of this data is shown in Fig. 4.21, which tends to confirm the weakness of the ^{13}C ground-state contribution to the (p, π^+) reaction, since the maximum angle is sensitive[17] to the available kinematic energy. In principle, the beam energy E_p could be determined from $\theta_{\max}$ to a precision of roughly 500 keV; however, multiple scattering (see Sec. 4.4) artificially degrades the angular resolution and precludes this measurement. Also shown in the figure for completeness is the corresponding ϕ distribution, although this information is not needed in the analysis of the CE-06 data. The localization of counts near $\phi = 0°$, 180°, and 360° reflects the fact that the physical laboratory acceptance is primarily in the x-z plane.

The width of the kinematic overlay in Fig. 4.20 is zero since there is only one degree of freedom for the two-body reaction $^{12}\mathrm{C}(\mathrm{p}, \pi^+)^{13}\mathrm{C}$. A finite width in the data is expected

[17] At $E_p = 166$ MeV, $\theta_{\max}$ increases by 0.2° for every 1 MeV increase in E_p.

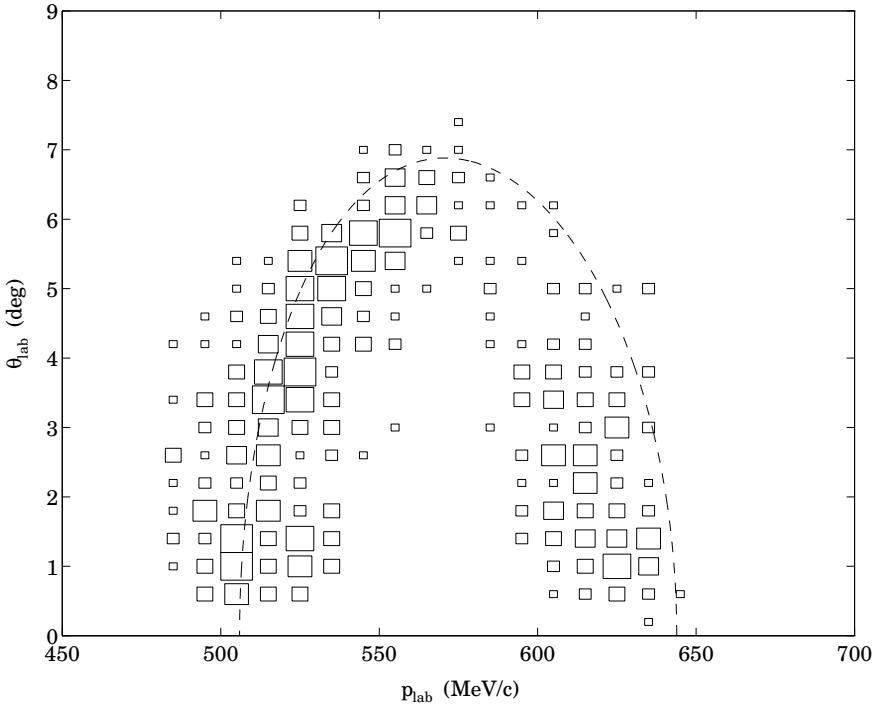

Figure 4.20 Kinematic locus for ^{13}C recoils at $E_p = 166$ MeV, using all detected charge states ($Q = 4, 5, 6$). The expected p-θ relationship for $^{13}\mathrm{C}_{\mathrm{g.s.}}$ ions from (p, π^+) is also shown (dashed line).

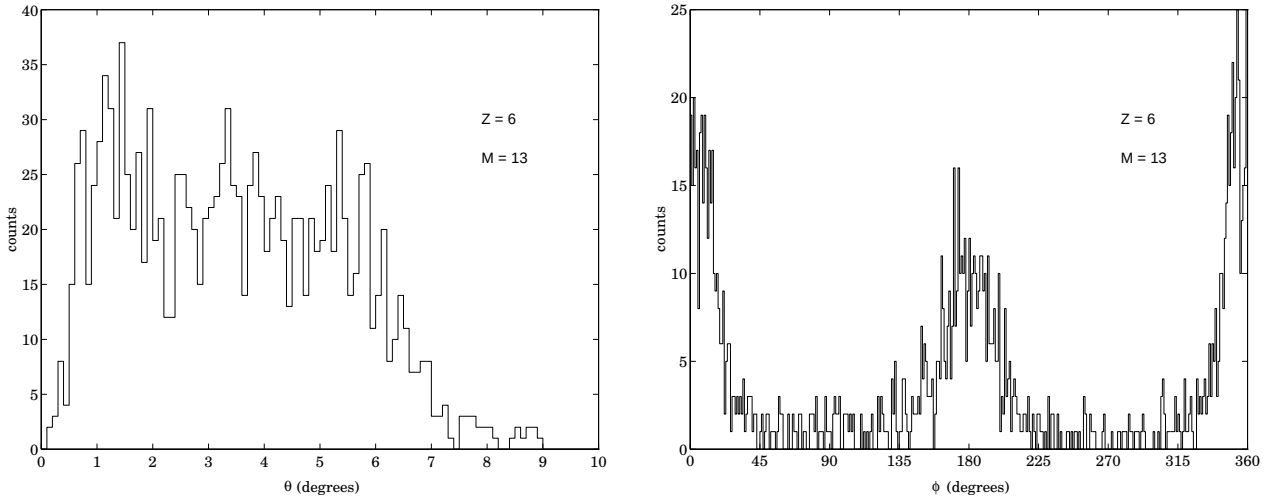

Figure 4.21 The θ (left) and ϕ (right) distributions for the ^{13}C events of Fig. 4.20. The expected maximum polar angles for the ground state and the 3.85 MeV excited state at $E_p = 166$ MeV are 6.75° and 5.82°, respectively.

due to the non-zero resolutions of the detector measurements; however, the width of the data locus in the figure is unexplained from the magnitude of the measured resolutions by roughly a factor of 2. Furthermore, the count distributions along the R-θ_p loci (see $Q = 5$

and $Q = 6$ at 166 MeV in Fig. 4.18, for example) are not symmetric about $\theta_p = 0$. The perceived asymmetry is unrealistic since the unpolarized beam and spinless target define no preferred direction in space. A misalignment of the beam direction from the magnet coordinate system z axis (see App. C) could produce such an asymmetry; however, the effect would simply be to shift the entire locus in a direction parallel to the θ_p axis of Fig. 4.18. This count distribution puzzle is a consideration for the next level of data analysis.

4.4 Second-Level Analysis: L_{int} and $d\sigma/d\Omega$

Given the unambiguous identification of the reaction process, and the laboratory p-θ distribution of the recoil ions (as in Fig. 4.20, for example), the corresponding differential cross-sections in the CMS can be obtained. In principle, this second stage of analysis can be accomplished analytically, as long as the charge-state populations (see Fig. 3.10), detector stack acceptances as a function of recoil rigidity and angle, and luminosities are known. For this work, however, variations in the measured p-θ ellipses due to multiple scattering of the ions, and difficulties in determining the true average luminosities, necessitated the use of numerical methods for calculation of $d\sigma/d\Omega$. This section considers these methods and their application to the CE-06 data at proton energies of 166, 294, and 330 MeV.

4.4.1 Multiple Scattering Effects

As discussed in App. C, multiple scattering of the recoil ions occurs mainly in the four mylar pressure foils of the CE-06 detector stack. At each foil interface, an ion of nuclear charge Z and energy E effectively scatters into a cone centered about the incident direction, and characterized in angular half-width by $\theta_{\text{rms}} \propto Z/E$. For "typical" ions encountered in this work ($E = 25$ MeV, $Z = 7$), $\theta_{\text{rms}} \approx 0.24°$, so that a scattering of such an ion at the initial pressure foil (see Fig. 3.11) produces an average deflection of 3 mm at the silicon plane.

The primary manifestation of multiple scattering effects in the CE-06 data is a range of ion positions at the silicon array for a particular ion rigidity and PGAC position (the latter measurement is essentially unaffected due the proximity of the foils to the PGAC sense planes). Although, for a given R-x_{pg} pair, a similar effect is produced by motion of the target[18] through the beam, the small spot size ($d_{\text{beam}} < 2$ mm) achieved in the Cooler ring implies a maximum deflection at the silicon of less than 1 mm (i.e., within the

[18] The size of the α calibration source, in fact, produces the finite line width of Fig. 4.8.

detector resolution). For ions with "true" reaction parameters (R, θ_p), the corresponding measurement of this pair by the detector stack yields a range of values in the R-θ_p plane, since the rigidity and projected angle are correlated by the fitting procedures of Sec. C.3.

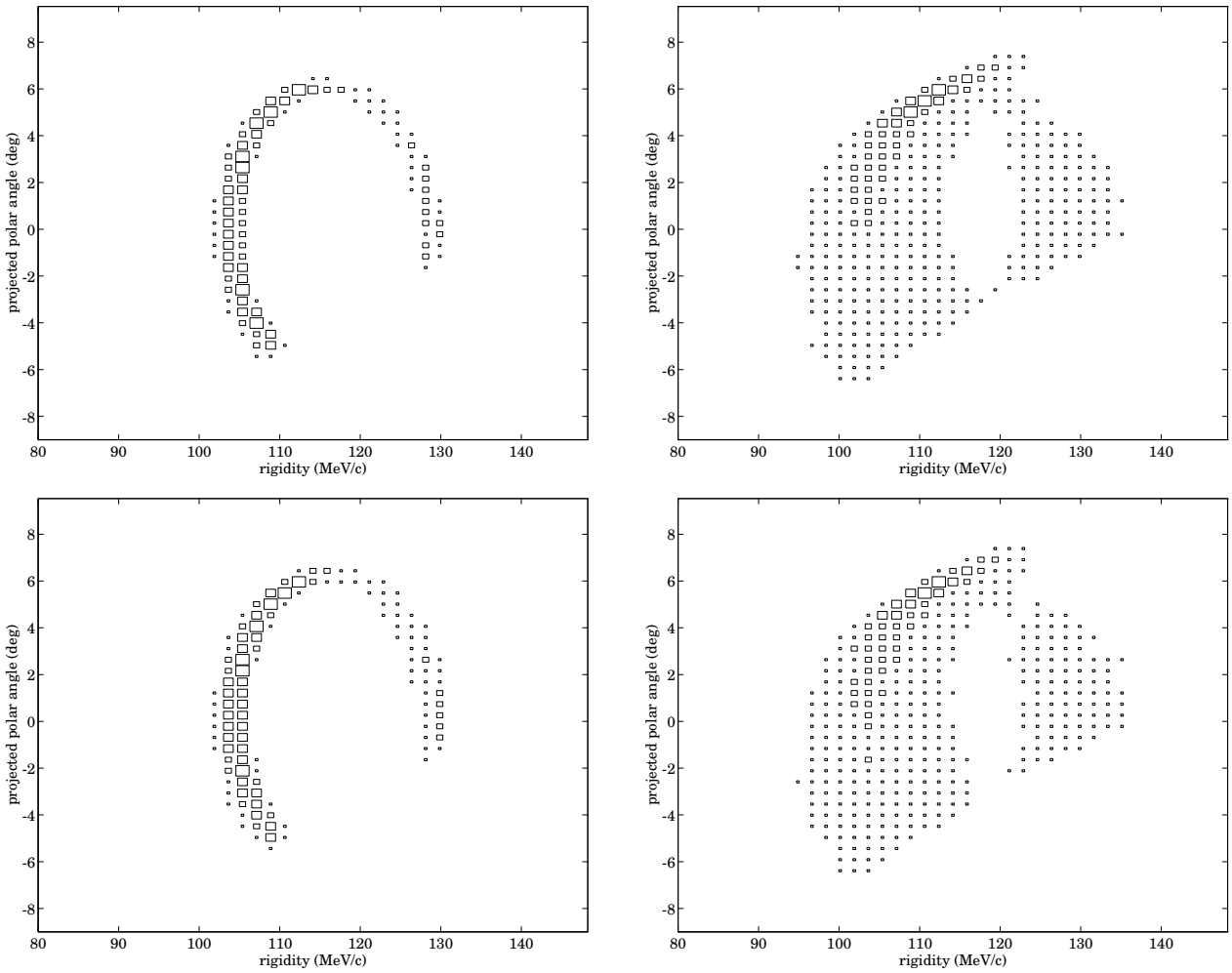

Figure 4.22 Simulation of the measured R-θ_p locus for recoil events corresponding to $^{12}\mathrm{C}(\mathrm{p},\pi^+)^{13}\mathrm{C}^{5+}$ at $E_p = 166$ MeV, using a previously measured [Ho92] pion angular distribution. The bottom (top) row does (does not) include the effects of finite detector resolution, whereas the right (left) column does (does not) include multiple scattering.

Analytical calculations of this effect on the R-θ_p locus are very difficult, if possible at all: the determination of R and θ_p is reasonably complicated (see Eq. (C.2)), and sequential multiple scattering in three foils must be considered (the PC foil is too close to the silicon plane to contribute significantly). Monte Carlo methods based on the forward raytracing of App. C must therefore be used to determine the effects of multiple scattering on the measured angular distributions. Fig. 4.22 shows a simulation of the measurement of the

R-θ_p locus for recoil ions from $^{12}\mathrm{C}(\mathrm{p},\pi^+)^{13}\mathrm{C}^{5+}$ at $E_p = 166$ MeV (compare Fig. 4.18). Not only does the scattering dominate the effects of finite detector resolutions, but also the physical reflection symmetry of the locus about $\theta_p = 0$ is removed.

The concentration of counts near $(R, \theta_p) = (110\ \mathrm{MeV/c}, 5°)$ and dilution of counts close to $(R, \theta_p) = (110\ \mathrm{MeV/c}, -5°)$ suggests that the multiple scattering tends to vary a "true" (R, θ_p) value along a vector with a positive slope of roughly 45° in the figure. In regions where the slope of this error vector and that of the ellipse are similar, the resulting locus is narrow, while a 90° mismatch in slopes causes a maximal broadening of counts. The overall result is that the perceived (measured) distributions can be significantly different from the actual cross-sections. To determine the latter, then, numerical methods directly incorporating the best estimates of multiple scattering effects must be applied.

4.4.2 The Calculation of $d\sigma/d\Omega$

The determination of the differential cross-section in the center-of-mass system, given the true count distribution of events in the lab system, is a fairly straightforward procedure of integration. If $\Delta N_Q(p, \theta, \phi)$ is the number of recoils detected per unit solid angle with charge Q and reaction parameters (p, θ, ϕ), then

$$\Delta N_Q(p, \theta, \phi) = L \cdot T \cdot \left(\frac{d\sigma}{d\Omega}\right)_{\mathrm{lab}} (p, \theta) \cdot P_Q(p) \cdot f_Q(p, \theta, \phi), \tag{4.15}$$

where

$L \equiv$ luminosity averaged over all cycles,

$T \equiv$ total run time (see Table 4.1),

$P_Q(p) \equiv$ probability of charge state Q at ion momentum p, and

$f_Q(p, \theta, \phi) \equiv$ acceptance at (p, θ, ϕ).

The cross-section in the CMS frame, $(d\sigma/d\Omega)_{\mathrm{cms}}$, is then obtained by numerical integration of f_Q in the azimuthal angle ϕ, and application of the Jacobian factor $J(\beta_{\mathrm{cms}}, \theta_{\mathrm{cms}}, \beta)$:

$$\left(\frac{d\sigma}{d\Omega}\right)_{\mathrm{cms}} (\theta_{\mathrm{cms}}) = \frac{\Delta N_Q(p, \theta)}{L \cdot T \cdot J \cdot P_Q(p)} \Big/ \int_0^{\pi} f_Q \, d\phi, \tag{4.16}$$

where β is the ion velocity, and β_{cms} is the CMS velocity in the lab frame. Since the acceptance functions are numerically well-known (see Fig. 4.18), and the other quantities have been previously [Ba81] measured ($P_Q(p)$) or are analytically calculable (J), expressions (4.15) and (4.16) yield the final result of the analysis.[19]

[19] The determination of σ requires knowledge of P_Q, or vice-versa. Using $\sigma(\pi^+)$ from [So81] at 166 MeV, P_Q here agrees within a few percent of previous measurements [Ba81] for typical ion energies.

The results of Sec. 4.4.1, however, demonstrate that the perceived distributions (represented at $E_p = 166$ MeV by Fig. 4.20, for example) can be quite different from $\Delta N_Q(p,\theta)$, the true laboratory angular distribution function, in a manner that is very difficult to calculate analytically. Nonetheless, with the caveat that the simulations of App. C are more heavily relied upon than via Eq. (4.16), the quantity $(d\sigma/d\Omega)_{\rm cms}$ can be calculated numerically, as follows. First, for the reaction process of interest, the measured p-θ spectrum can be generated assuming a "flat" cross-section, $(d\sigma/d\Omega)_{\rm cms} = \sigma_{\rm tot}/4\pi$, resulting in a simulated distribution $n_{\rm sim}(p,\theta)$. The simulated θ vs. p spectrum incorporates the integrated acceptance, detector resolutions, and multiple scattering effects. A comparison of $n_{\rm sim}$ and the measured spectrum for $^{12}{\rm C}({\rm p},\pi^+)^{13}{\rm C}$ at $E_p = 166$ MeV is shown in Fig. 4.23. The lack of counts near $(p,\theta) = (600\ {\rm MeV/c}, 4.5^\circ)$, for example, indicates a significantly smaller CMS cross-section at $\theta_\pi \approx 100^\circ$ (cf. Fig. 4.1) compared to that expected from a flat distribution.

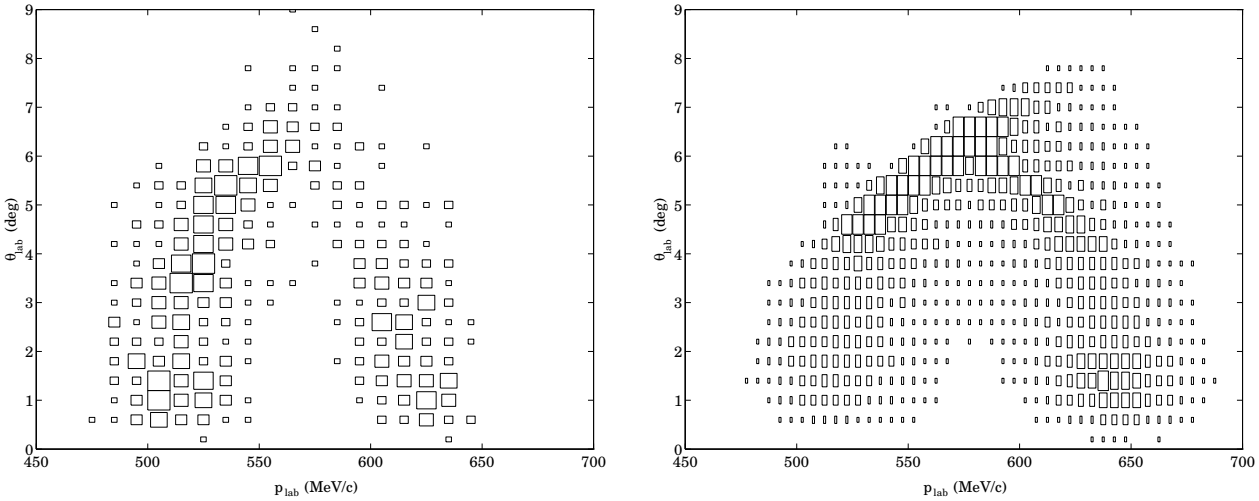

Figure 4.23 Simulated laboratory kinematic spectrum (right) of recoil events corresponding to $^{12}{\rm C}({\rm p},\pi^+)^{13}{\rm C}$ at $E_p = 166$ MeV, for a flat pion distribution in the center-of-mass system. Figure 4.20 is repeated at left for comparison.

Next, weighting factors $w(p,\theta)$ are constructed, as defined by

$$w(p,\theta) \equiv \frac{n_{\rm det}(p,\theta)}{(4\pi/N)\cdot n_{\rm sim}(p,\theta)}, \tag{4.17}$$

where $n_{\rm det}(p,\theta)$ is the number of events in the measured spectrum bin centered at (p,θ), and N is the total number of simulation events thrown. In practice, the simulation counts are more finely binned than the measured p-θ distributions, so that

$$n_{\rm sim}(p,\theta) = \sum_{p_i,\theta_i} n_{\rm sim}(p_i,\theta_i), \tag{4.18}$$

for all simulation bins (p_i, θ_i) contained in the experimental bin centered at (p, θ).

Finally, the differential cross-section in the CMS follows from

$$L \cdot T \cdot \left(\frac{d\sigma}{d\Omega} \right)_{\rm cms} (\theta_{\rm cms}) = w(\theta_{\rm cms}), \tag{4.19}$$

where $\theta_{\rm cms} = \theta_{\rm cms}(p, \theta)$ is given by a Lorentz boost from the laboratory to the CMS system. Statistical uncertainties in the weighting factors are primarily determined by the number of experimental counts per bin (i.e., $n_{\rm det}(p, \theta)$) since, in principle, the total number of simulation events thrown N can be made very large. For this work, N was typically made large enough so that $n_{\rm sim}/n_{\rm det} \gtrsim 100$ for any given region in the p-θ spectrum.[20]

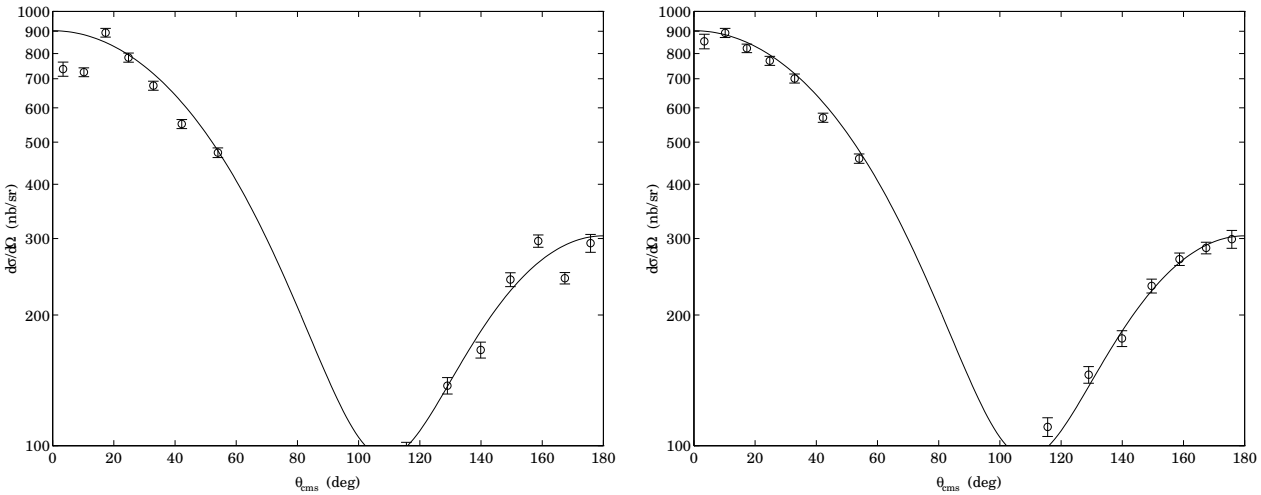

Figure 4.24 Test results of the analysis techniques using (4.17) and (4.19). Both curves are a legendre polynomial fit to ^{12}C(p, π^+)^{13}C data from [Ho92]). Shown is the calculated cross-section assuming no multiple scattering (left), and with multiple scattering (right).

A demonstration of this technique is shown in Fig. 4.24. Here, the expected [Ho92] shape of the summed-state ^{12}C(p, π^+)^{13}C cross-section (for strongly-bound ^{13}C ions) has been used as input to the Monte Carlo simulation programs to create "data," and from this the CMS cross-section has been calculated (or really, regenerated) through Eq. (4.19). The figure shows the results of the cross-section calculation using two simulated count distributions $n_{\rm sim}(p, \theta)$: with and without the inclusion of multiple scattering effects. Although Fig. 4.24 is not a test of the systematic errors involved in this use of the simulations, the distortions produced by the multiple scattering are evidently non-negligible but reasonably well-accounted for by Eq. (4.17). In both graphs of Fig. 4.24, the effects of multiple

[20] This ratio corresponds to a 2% increase in the relative uncertainty of w (compared to $N \to \infty$).

scattering limit the measurement of the cross-section primarily to forward and backward CMS pion angles even at 166 MeV: For $60^\circ \lesssim \theta_\pi \lesssim 110^\circ$, the two branches of the p-θ locus become unresolved. Indeed, the only apparent systematic error occurs at $\theta_\pi \approx 115^\circ$, where the separation of the high-momentum and low-momentum branches is unclear (for example, see the $\theta \approx 5^\circ$ region of Fig. 4.20).

4.4.3 Determination of the Luminosity

The calculation of the integrated luminosity, $L_{\rm int} \equiv L \cdot T$, is an important step in the determination of the absolute cross-sections via Eq. (4.19). Even for the measurement of the π^+/π^0 production ratio R of Eq. (2.1), $L_{\rm int}$ must be fully determined since the CE-06 experiment cannot distinguish ground-state ^{13}C recoils from those in strongly bound excited states. It is conceivable to calculate the $^{12}\mathrm{C}(\mathrm{p},\pi^+)^{13}\mathrm{C}_{\mathrm{g.s.}}$ cross-section from the (summed-state) data by estimation of excited-state population fractions in $^{12}\mathrm{C}(\mathrm{p},\pi^+)^{13}\mathrm{C}$ (using previously measured data [So81]). However, this method to extract the ground-state cross-section is difficult and results in relatively large uncertainties in R (compared to the methods discussed below).

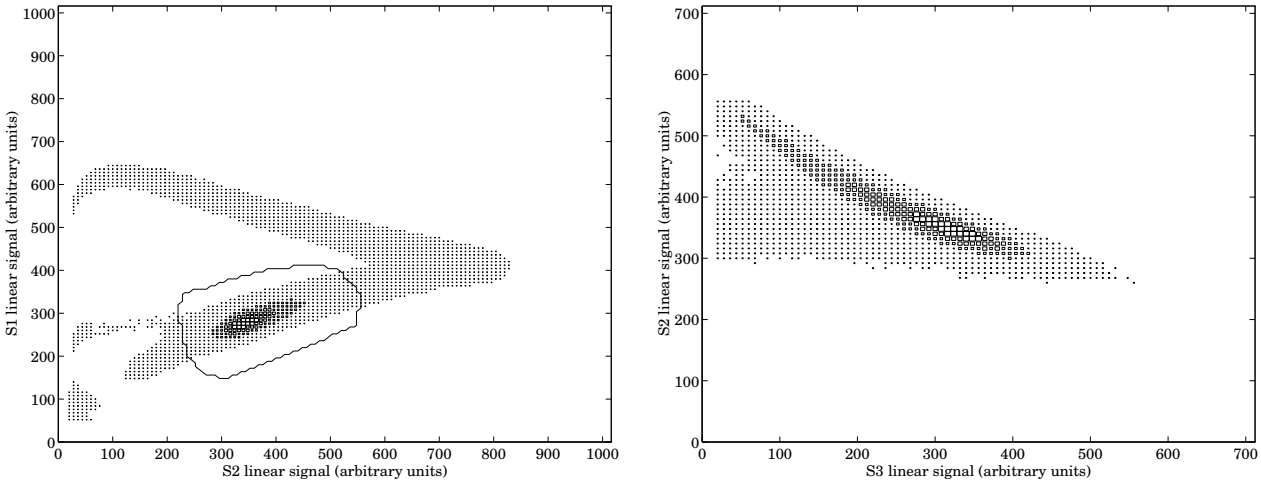

Figure 4.25 Energy loss spectra, taken at $E_p = 330$ MeV, from the monitor scintillators S1, S2, and S3 (see Fig. 3.33). The elastic and inelastic protons are identified as "punch-through" events in S1 vs S2 (left) which are stopped in S3, and which therefore form an $\Delta E \propto 1/E$ locus in S2 vs S3 (right).

As discussed in Sec. 3.4.5, the exclusive concurrent measurement of $^{12}\mathrm{C}(\mathrm{p},\mathrm{p}')^{12}\mathrm{C}^*$ yields in principle an accurate, independent determination of $L_{\rm int}$; however, in practice the detection of low-energy ^{12}C recoils was difficult to achieve. Nonetheless, an attempt was made to use the scintillator portion of the monitor apparatus (see Fig. 3.33) to count

elastically and inelastically scattered protons from the target. Fig. 4.25 shows scintillator data for $E_p = 330$ MeV, where the desired proton counts appear as a strong group in the lower branch of the S1 vs. S2 energy-loss locus. Although the number of protons can reliably be determined, the luminosity calculated [Pp94] from Eq. (3.11) is (at $E_p = 166$ MeV) a factor of roughly 8 greater than that expected from any other rough or careful estimates (see below). The reason for this apparent over-counting, whether due to the difficulty of evaluating the integral of Eq. (3.11) for a rapidly varying cross-section, or because of unexpected and unmeasured small-angle proton background in the ring, remains unclear.

Without a reliable, independent measurement of $L_{\rm int}$, the use of internal data must be resorted to for the determination of absolute cross-sections. Since the CE-06 detector stack is sensitive to all ($Z \geq 4$) ions emitted from the target, there are several possibilities to consider. Perhaps most obvious is the use of ^{12}C ions as a normalization of the luminosity, in analogy to the monitor method described above. Data at $E_p = 166$ MeV clearly indicate (see Fig. 4.14, e.g.) a reasonably strong production of ^{12}C at low energies ($E \lesssim 20$ MeV).

The appearance of these low-energy carbon ions is something of a mystery, however. The kinematics of $^{12}\mathrm{C(p,p')}^{12}\mathrm{C}$ leading to bound ^{12}C states are such that only recoils corresponding to backward proton angles in the CMS ($\theta_p \gtrsim 130^\circ$) are accepted in the lab by the detector stack. Thus, ^{12}C ions corresponding to elastic and inelastic proton scattering from the target enter the silicon array only for $\theta_{\rm lab} \lesssim 25^\circ$, i.e., $E \gtrsim 40$ MeV! Essentially the same kinematics apply[21] to $^{13}\mathrm{C(p,d)}^{12}\mathrm{C}$, for which only ^{12}C ions with $E \gtrsim 50$ MeV are accepted. The large population of low-energy ^{12}C in Fig. 4.14 may be indicative of the possibility that the number of *true* elastic protons in the monitor scintillators have been overcounted; in any case, the internal ^{12}C data cannot be used as a normalization.

Other ions lighter than $M = 12$ appear even more strongly in the CE-06 online data, as in Fig. 4.11. For example, ^{10}B is strongly produced, and the total excitation function of $\mathrm{p} + {}^{12}\mathrm{C} \rightarrow {}^{10}\mathrm{B} + X$ has been measured [Re84], with $\sigma(E) \approx 25$ mb, for $E_p \gtrsim 100$ MeV. The boron angular distributions have not been measured, however, and at least two different reactions can contribute. Furthermore, the unexplained production of ^{12}C may similarly correspond to an anomalous number of ^{10}B events here.

With these considerations, the normalization of the data using ^{13}C recoils from positive

[21] ^{13}C atoms comprise approximately 1% of a natural carbon target.

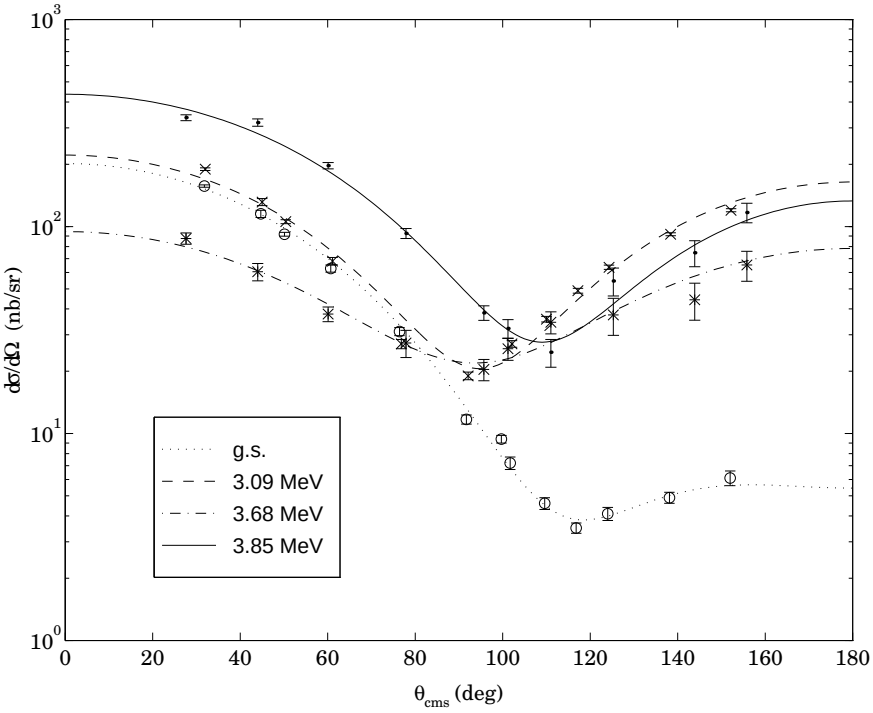

Figure 4.26 Differential cross-sections in the CMS system for $^{12}\mathrm{C}(\mathrm{p},\pi^+)^{13}\mathrm{C}$ leading to the ground state and first three excited states of $^{13}\mathrm{C}$. Data are from [So81]; the solid curves are the result of legendre polynomial fits made here.

pion production is the one remaining feasible candidate in terms of the internal data. Although the total cross-sections are small ($\sigma_{\pi^+} \approx 1\,\mu$b), these recoils are fairly cleanly separated and are produced uniquely via positive pion production. Furthermore, angular distributions for (p,π^+) data have been measured at proton energies nearby to those of interest here. For example, Fig. 4.26 shows data [So81] taken at $E_p = 170$ MeV for $^{12}\mathrm{C}(\mathrm{p},\pi^+)^{13}\mathrm{C}$ leading to the strongly bound states of $^{13}\mathrm{C}$. In order to determine the integrated luminosity, the simulations are used to calculate the acceptance fractions f_i for each of the cross-sections (i = g.s., 3.09 MeV, 3.68 MeV, and 3.85 MeV). Next, an effective cross-section σ_{eff} is constructed: $\sigma_{\mathrm{eff}} = \sum_i f_i\sigma_i$. If N_{exp} is the total number of experimental counts[22] corresponding to $^{12}\mathrm{C}(\mathrm{p},\pi^+)^{13}\mathrm{C}$, then the integrated luminosity is just

$$L_{\mathrm{int}} = \frac{N_{\mathrm{exp}}}{\sigma_{\mathrm{eff}}}. \tag{4.20}$$

The normalization procedure used at 294 MeV and 330 MeV is similar, although angular distributions and total cross-sections are available [Hu87] only at 250 MeV and

[22] Adjusted for the transmission factor (80%) of the detector stack.

354 MeV. To apply the method described by Eq. (4.20), the assumption that the shape of the distribution does not change significantly from proton energies of 354 MeV to 290 MeV was made to determine the acceptance fractions. The value of the total cross-section at $E_p = 294$ MeV was also determined by a smooth interpolation between existing data at 250 MeV, 330 MeV, and 354 MeV.

E_p (MeV)	Runs	$L_{\rm int}$ ($\rm cm^{-2}$)	$L_{\rm data}$ ($\rm cm^{-2}\,sec^{-1}$)	$L_{\rm ave}$ ($\rm cm^{-2}\,sec^{-1}$)
165.4	115–116	$(1.3 \pm 0.2) \times 10^{33}$	$(1.1 \pm 0.1) \times 10^{29}$	$(4.6 \pm 0.5) \times 10^{28}$
293.7	85–104	$(1.5 \pm 0.2) \times 10^{34}$	$(4.2 \pm 0.3) \times 10^{29}$	$(2.7 \pm 0.2) \times 10^{29}$
328.5	106–113	$(1.4 \pm 0.2) \times 10^{34}$	$(6.4 \pm 0.4) \times 10^{29}$	$(4.0 \pm 0.3) \times 10^{29}$

Table 4.3 Results of the luminosity calculations using the internal ^{13}C data corresponding to $^{12}\mathrm{C}(\mathrm{p},\pi^+)^{13}\mathrm{C}$. The $L_{\rm data}$ and $L_{\rm ave}$ columns correspond to $L_{\rm int}$ divided by the last two columns of Table 4.1, respectively.

The final results of this procedure, applied to the February, 1993, CE-06 data at proton energies of 166 MeV, 294 MeV, and 330 MeV are shown in Table 4.3. The luminosities for both the "data-on" and total elapsed times, as calculated using the last two columns of Table 4.1, are also given in the table. The errors given include statistical uncertainties in the CE-06 data and estimated errors in the cross-section normalizations at 294 MeV and 330 MeV.

4.5 Results: 166 MeV, 294 MeV, and 330 MeV

4.5.1 Single-Pion Production at E_p = 166 MeV

Differential cross-section results for positive and neutral pion production at $E_p = 166$ MeV are shown in Figures 4.27 and 4.28, respectively. In both cases, the recoil events have been summed into bins of full-width $\Delta\theta_{\rm lab} = 1.2^\circ$. This size, although much larger than necessitated by the detector stack's intrinsic angular resolution, allows for reasonable statistical uncertainties in the calculated cross-sections. In the case of (p,π^+), the finite width of the low- and high-momentum branches of the recoil locus (as in Fig. 4.20) precludes calculation of the cross-section for $60^\circ \lesssim \theta_\pi \lesssim 110^\circ$ (CMS). For the (p,π^0) measurement, counts were available only for laboratory angles corresponding to forward-scattered pions in the center-of-mass frame.

In general, the agreement of the summed-state $^{12}\mathrm{C}(\mathrm{p},\pi^+)^{13}\mathrm{C}$ measurement here with previous measurements ([Ho92] and [So81]) is good, although the results of this work tend

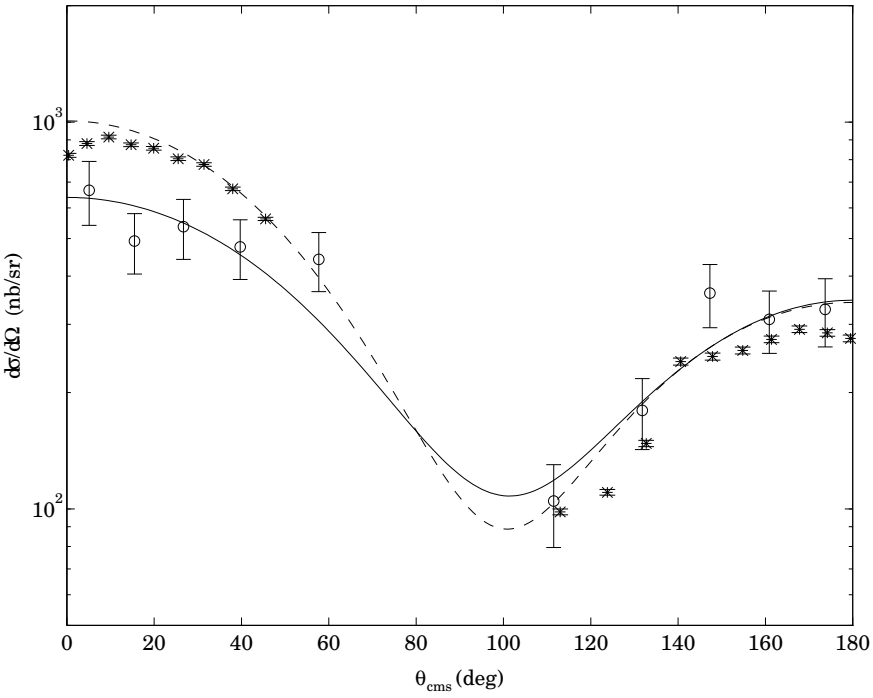

Figure 4.27 Differential cross-section for $^{12}\mathrm{C}(\mathrm{p},\pi^+)^{13}\mathrm{C}$ at $E_p = 166$ MeV, as a function of the pion angle in the CMS. Data from this work are shown by open circles; stars refer to previous recoil data [Ho92]. The dashed line is a sum of (p,π^+) spectrograph data [So81] to separate states in $^{13}\mathrm{C}$. The solid line is a Legendre polynomial fit to the data here.

to underpredict the cross-section at forward angles. Since the small-angle portion of the distribution accounts, in this case, for most of the integrated cross-section, this part of the measurement may be indicative of the systematic error in the calculation using the simulated distributions. For example, when determining the flat simulated distribution at the right of Fig. 4.23, only one kinematical final state could be used without a further assumption upon the relative populations of $^{13}\mathrm{C}$ in the ground state and the three strongly-bound excited states. In particular, the measurement is in best agreement with previous measurements at backward angles, where only the kinematically similar excited states (3.09 MeV $\lesssim E_{\mathrm{ex}} \lesssim$ 3.85 MeV) tend to contribute (as seen in Fig. 4.26).

Only the ground state of $^{13}\mathrm{N}$ is strongly bound, however, and therefore the detection of $^{13}\mathrm{N}$ recoils uniquely corresponds to $^{12}\mathrm{C}(\mathrm{p},\pi^0)^{13}\mathrm{N}_{\mathrm{g.s.}}$. For this measurement, although the effective acceptance was nearly 4π sr, reliable signal events above the background were obtained only for $\theta_\pi \lesssim 45°$. As such, the determination of the total cross-section $\sigma(\pi^0)$ is not possible without making additional assumptions. One possibility is to assume the shape of the cross-section as measured previously [Ho92] and make a fit for the best value

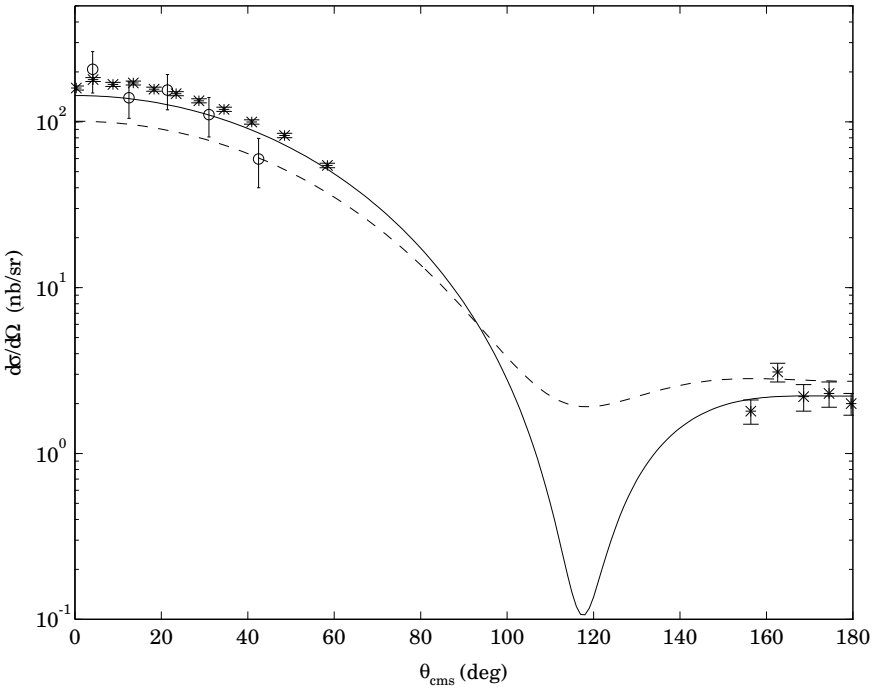

Figure 4.28 Differential cross-section for $^{12}\mathrm{C}(\mathrm{p},\pi^0)^{13}\mathrm{N}_{\mathrm{g.s.}}$ at $E_p = 166$ MeV. Data symbols are the same as in Fig. 4.27. The dashed line is the cross-section [So81] for $^{12}\mathrm{C}(\mathrm{p},\pi^+)^{13}\mathrm{C}_{\mathrm{g.s.}}$, divided by 2. The solid line is a Legendre polynomial fit to the combined (p,π^0) data from [Ho92] and this work.

of the total cross-section. Using the data from this work in Fig. 4.28 and a Legendre polynomial fit to the data of [Ho92], the value $\sigma = 361 \pm 169$ nb is obtained. The relatively large uncertainty in the π^0 data of this work results in a large (50%) error in σ due to the forward-peaked nature of the expected π^0 distribution.

Another method to extract the total cross-section relies on a combination of measured data to allow a reasonable fit to be made. Since the total cross-section is primarily defined by the small-angle portion of the distribution in the (p,π^0) case, the use of external data to constrain the large-angle part of the fit allows a reliable determination of the distribution with a tractable error in the cross-section. Figure 4.28 shows such a fit, using the data of this work ($\theta_\pi < 45°$), and of a previous study [Ho92] for large angles ($\theta_\pi > 150°$), with the final result $\sigma = 374 \pm 46$ nb. This fit is still not constrained enough: the minimum of the distribution close to $\theta_\pi = 120°$ is clearly exaggerated. However, the contribution to the total cross-section from this region ($100° < \theta_\pi < 140°$) is on the order of a few percent (using the expected shape of the distribution from (p,π^+)), i.e., negligible compared to the statistical uncertainty.

Figure 4.28 also shows that the forward-angle portion of the distribution measured

here is in good agreement with that measured before [Ho92], as is the value of the total cross-section ([Ho92] gives $\sigma(\pi^0) = 434 \pm 45$ nb). From the fit to the $^{12}\mathrm{C}(\mathrm{p},\pi^+)^{13}\mathrm{C}_{\mathrm{g.s.}}$ distribution of Fig. 4.26 and the measured $^{12}\mathrm{C}(\mathrm{p},\pi^0)^{13}\mathrm{N}_{\mathrm{g.s.}}$ cross-section here, the ratio of Eq. (2.1) is $R = 1.5 \pm 0.2$. A recent reanalysis [Pi93] of the (p,π^+) data of [So81] and [Gr83] yields a somewhat larger total cross-section for positive pion production, resulting in a ratio here of $R = 1.7 \pm 0.3$. This reanalysis also attempts to calculate Coulomb effects, which tend further to increase the estimate of the strong interaction cross-section, yielding $R = 2.0 \pm 0.3$ using the π^0 result here. It should be noted, however, that this Coulomb calculation results in an anomalous ratio $R = 2.8 \pm 0.4$ when applied to π^+ data at $E_p = 186$ MeV. Whether this discrepancy arises from systematic uncertainty in the π^0 measurement [Ho92] at that energy or from the Coulomb correction of the π^+ cross-section is not clear.

θ_π (deg)	$d\sigma/d\Omega\,(\theta_\pi)$ (nb)
4.1 ± 1.9	207 ± 58
12.5 ± 1.9	139 ± 35
21.4 ± 2.1	155 ± 37
31.0 ± 2.3	111 ± 30
42.5 ± 2.9	60 ± 20

$\sigma(\pi^+)$ (nb)	$\sigma(\pi^0)$ (nb)	R
555 ± 5 [Gr83]	374 ± 46	$1.5 \pm .2$
635 ± 76 [Pi93]	374 ± 46	$1.7 \pm .3$
750 ± 90 [Pi93]	374 ± 46	$2.0 \pm .3$

Table 4.4 Results of the analysis at 166 MeV. Differential cross-sections for $^{12}\mathrm{C}(\mathrm{p},\pi^0)^{13}\mathrm{N}_{\mathrm{g.s.}}$ (left) are given in the center-of-mass frame. The uncertainties listed in the first row of the ratio table (right) are statistical only.

The (p,π^+) cross-section results and ratio calculations are summarized in Table 4.4. Although the absolute measurement of $\sigma(\pi^0)$ here in fact depends on the corresponding value of the $^{12}\mathrm{C}(\mathrm{p},\pi^+)^{13}\mathrm{C}_{\mathrm{g.s.}}$ cross-section, this dependence is very weak (and much smaller than the listed statistical error in $\sigma(\pi^0)$) since the integrated bound-state cross-section is primarily populated by the first three ^{13}C excited states. Furthermore, no Coulomb analysis has yet been made for the excited-state cross-sections, hence Table 4.4 lists only the final result $\sigma(\pi^0) = 374 \pm 46$ nb.

4.5.2 Single-Pion Production at 294 and 330 MeV

Figure 4.29 shows the results of this work for positive-pion production at proton energies of 294 and 330 MeV. The measurements as shown are limited to pion emission angles in the CMS of $\theta_\pi \lesssim 30°$, due to the finite acceptance of the detector stack at

these energies (see Fig. 4.19). For $E_p \approx 300$ MeV, the silicon array admits ^{13}C recoils corresponding to CMS pion angles of $\theta_\pi \lesssim 45°$ and $\theta_\pi \gtrsim 120°$; however, no ^{13}C events in the high-momentum branch (above background) were seen at either 294 or 330 MeV. This result suggests that the differential cross-section for (p, π^+) leading to bound ^{13}C states is less than roughly 10 nb for backward scattered pions ($\theta_\pi \gtrsim 120°$). Furthermore, in contrast to the results at $E_p = 166$ MeV, no backward peak in the distribution is manifested: simulations show that, given a flat CMS distribution, approximately 50% of the total detected ^{13}C events would correspond to $\theta_\pi > 140°$. The results here at proton energies of 294 MeV and 330 MeV limit any backward peak to less than 1% of the differential cross-section at $\theta_\pi = 0°$ (for $E_p = 166$ MeV, $\sigma(0°)/\sigma(180°) \approx 50\%$).

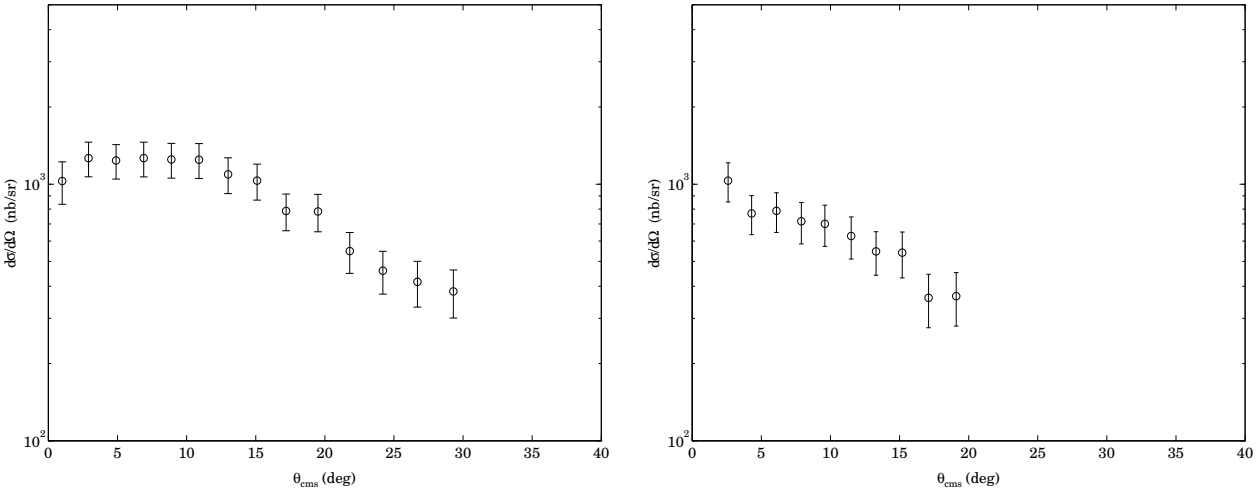

Figure 4.29 Differential cross-section $d\sigma/d\Omega$ for $^{12}\mathrm{C}(\mathrm{p}, \pi^+)^{13}\mathrm{C}^*$ as a function of the pion angle in the center-of-mass frame. Shown are the summed-state results at $E_p = 293.7$ MeV (left) and $E_p = 328.5$ MeV (right).

The cross-sections reported here for production of positive pions, along with previous measurements [Hu87] of $^{12}\mathrm{C}(\mathrm{p}, \pi^+)^{13}\mathrm{C}^*$, are shown in Fig. 4.30, plotted as a function of the Mandelstam variable t, the square of the four-momentum transfer.[23] For the data measured here, the forward-angle cross-section is essentially independent of s (the square of the total four-momentum), holding t constant. This feature has also been seen [Hu87] for $E_p > 350$ MeV and $t = 0.5$ GeV^2/c^2 in the ground state and 9.5 MeV excited state of ^{13}C (the latter is unbound and not detected in this work). However, the small absolute value of the cross-sections measured here, compared to a smooth extrapolation to

[23] The larger values of t in Fig. 4.30 correspond to smaller pion scattering angles.

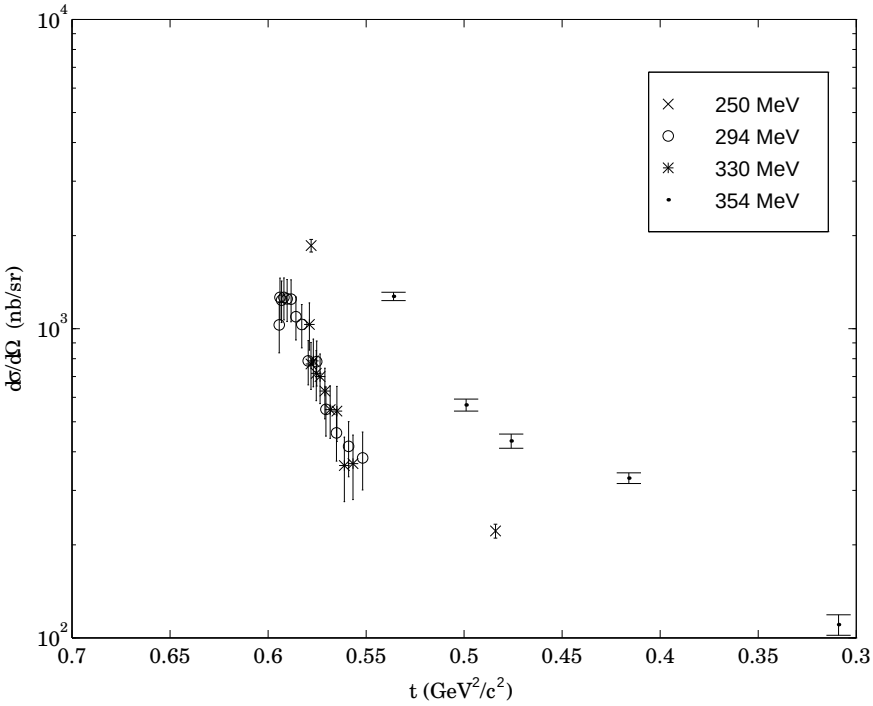

Figure 4.30 Differential cross-sections for positive pion production at intermediate energies, leading to the strongly-bound states of ^{13}C, as a function of the four-momentum transfer. Data at 250 and 354 MeV are from [Hu87].

$t > 0.55$ GeV^2/c^2 of the data at 250 and 354 MeV, is unexpected, and most likely is the result of the systematic errors involved in the calculation of the absolute luminosity at 294 and 330 MeV. In this regard, the absolute scaling of the cross-sections at these energies in Fig. 4.30 should be considered preliminary.

Figure 4.31 shows the results of the analysis for ^{12}C(p, π^0)^{13}N at $E_p = 294$ MeV. Construction of the lower edge of the $Z = 7$ gate applied to the particle ID (see Fig. 4.12) is especially difficult in this situation, given the expected small number of nitrogen events compared to the relatively strong carbon locus. Background ^{12}C events which "leak" into the nitrogen gate tend to appear in the mass-13 and mass-14 region of the calculated mass array. The energy signature of nitrogen events compared to that for carbon recoils is well separated for the low-momentum branch of the (p, π^+) loci (see Table C.1); nonetheless, a clear ^{13}N M-Q locus was not obtainable, as seen in the left graph of Fig. 4.31. The corresponding cross-section results, for a total of approximately 80 ^{13}N events, are preliminary.

For the integrated luminosity given in Table 4.3 at 294 MeV, roughly 2000 ^{13}C events corresponding to ^{12}C(p, π^+)^{13}C were recorded. Although the population of ^{13}N

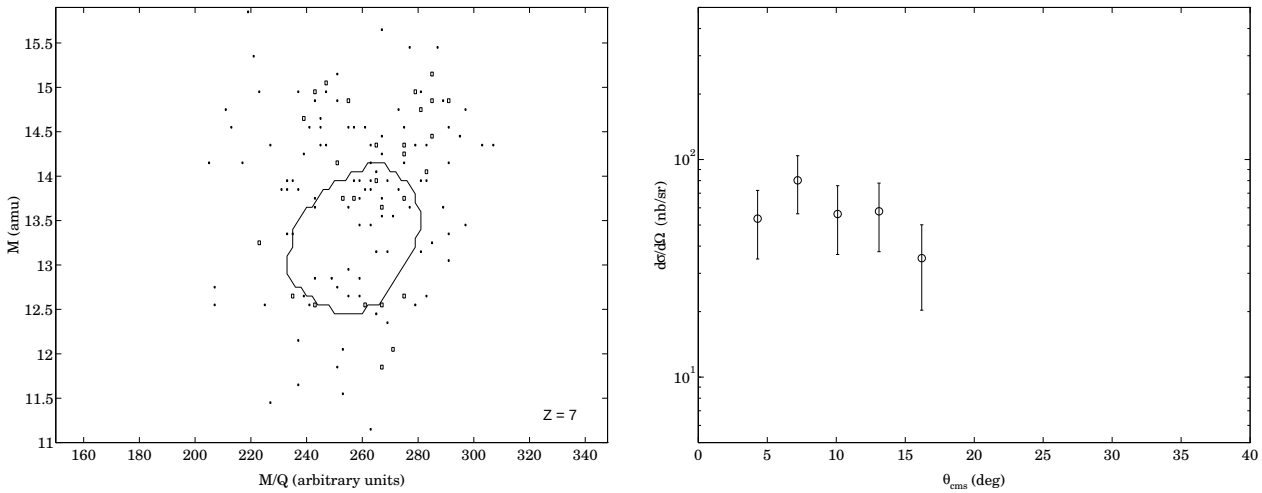

Figure 4.31 Preliminary cross-sections for $^{12}\mathrm{C}(\mathrm{p},\pi^0)^{13}\mathrm{N}$ at 294 MeV. The differential cross-section (right) is derived from events satisfying the M and M/Q gate shown at left (compare Fig. 4.16).

via $^{12}\mathrm{C}(\mathrm{p},\pi^0)^{13}\mathrm{N}_{\mathrm{g.s.}}$ should be only a factor of two smaller than the number of ^{13}C events from $^{12}\mathrm{C}(\mathrm{p},\pi^+)^{13}\mathrm{C}_{\mathrm{g.s.}}$, the strongly-bound excited states of ^{13}C (which together with the ground state produce Fig. 4.29) are strongly populated via (p,π^+). At $E_p = 354$ MeV, the ground state contribution is approximately 15% [Hu87] of the total bound-state ^{13}C production; a similar ratio exists at $E_p = 166$ MeV (see Fig. 4.26). Taking this relative weakness of the ground state into account, a better estimate of the number of ^{13}N events detected is $N_{\pi^0}(294\ \mathrm{MeV}) \approx 100$, assuming a forward-peaked CMS angular distribution.

The total number of ^{13}N events is therefore in reasonable agreement with that expected ($N \approx 100 \pm 15$) from the number of ^{13}C events corresponding to (p,π^+). More precisely, if R is the ratio $\sigma(\pi^+)/\sigma(\pi^0)$ for production of the ground states of ^{13}C and ^{13}N (see Eq. (2.1)) at $E_p = 294$ MeV, then the expected number of ^{13}N events from (p,π^0) is

$$N_{\pi^0}\,(294\,\mathrm{MeV}) \approx \frac{200 \pm 30}{R}. \tag{4.21}$$

Here, the numerator in Eq. (4.21) is derived from the total number of π^+ events obtained, the expected population fraction of $^{13}\mathrm{C}_{\mathrm{g.s.}}$ compared to all bound states, and acceptance fraction of π^0 events compared to π^+ events. This calculation is independent of the absolute luminosity, and shows that the number of π^0 events at 294 MeV (≈ 80) is consistent with a ratio in the range $R \approx 2.2$–2.8. This figure is somewhat higher than that expected from isospin invariance; however, the relatively large error in this measurement of R renders any such conclusions premature.

4.5.3 Double-Pion Production at E_p = 330 MeV

Given the large $Z = 5$ background and limited number of reliable ^{13}N candidates, evidence for $(\mathrm{p}, \pi\pi)$ events is most likely to be found via detection of ^{13}C recoils corresponding to $^{12}\mathrm{C}(\mathrm{p}, \pi^+\pi^0)^{13}\mathrm{C}$. Fig. 4.32 shows data from the 294 MeV and 330 MeV runs for recoils with[24] $Z = 6$, $Q = 5$, and $M = 13$ that satisfy broad conditions in silicon energy and time-of-flight, according to the kinematics of $(\mathrm{p}, \pi\pi)$ shown in Fig. 2.8. In principle, *any* ^{13}C recoil events in the $\pi\pi$ kinematic region of the R-θ_p plane (bounded by the solid lines of Fig. 4.32) uniquely identify $^{12}\mathrm{C}(\mathrm{p}, \pi^+\pi^0)^{13}\mathrm{C}^{5+}$ events.

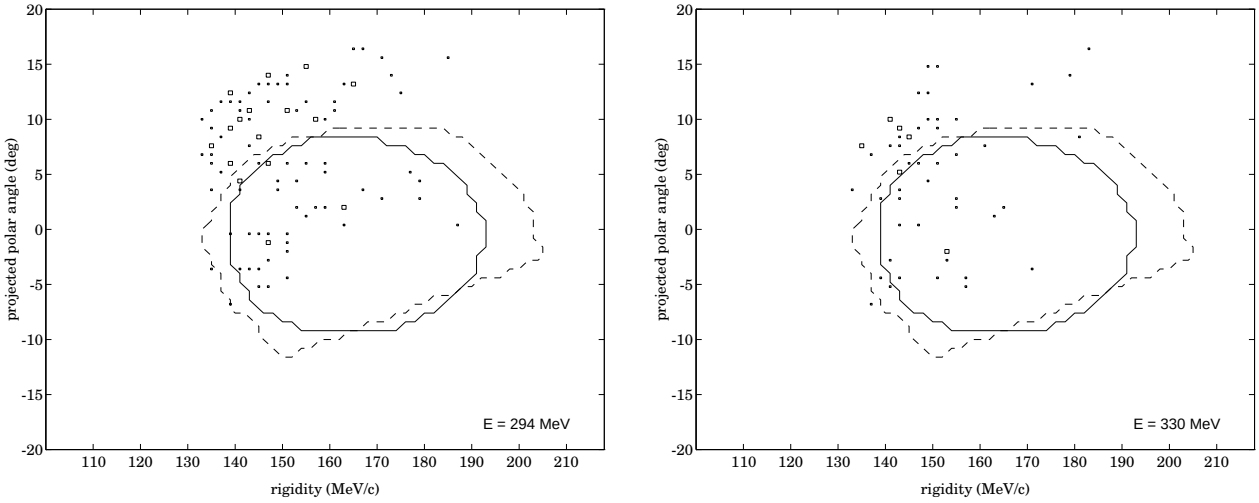

Figure 4.32 Results of the search for ^{13}C events from $(\mathrm{p}, \pi\pi)$ production, for recoils satisfying $Q = 5$, $M = 13$, and $Z = 6$ gates. The solid line denotes the possible kinematic region in the R-θ_p plane for recoils from $^{12}\mathrm{C}(\mathrm{p}, \pi^+\pi^0)^{13}\mathrm{C}$; the dashed line extends this region to account for multiple scattering and finite detector resolutions.

Given a total cross-section for $(\mathrm{p}, \pi^+\pi^0)$ on the order of $\sigma_{\pi\pi} \approx 10$ nb, the expected number of $^{13}\mathrm{C}^{5+}$ recoils detected is on the order of 10, for the 330 MeV runs analyzed here. At $E_p = 294$ MeV, just below the threshold for $^{12}\mathrm{C}(\mathrm{p}, \pi^+\pi^0)^{13}\mathrm{C}_{\mathrm{g.s.}}$ of $E_p = 297$ MeV, the 39 ± 7 counts in the dashed area of Fig. 4.32 (calculated from kinematics and simulations incorporating multiple scattering and detector resolutions) represent the background for this measurement. Assuming that this background strength remains constant from 294 to 330 MeV, an enhanced count rate at 330 MeV would be direct evidence for $(\mathrm{p}, \pi\pi)$ events.

However, after scaling the 330 MeV data by the ratio $L_{\mathrm{int}}(294\ \mathrm{MeV})/L_{\mathrm{int}}(330\ \mathrm{MeV})$, the number of $\pi\pi$ candidate events in the dashed region in the right graph of Fig. 4.32

[24] The background level was smaller for $Q = 5$ than for the other charge states.

is 29 ± 7. Thus, the $\pi\pi$ signal strength is statistically the same as the background level, and no measurement of the cross-section can be made here. Nonetheless, an upper limit on the total cross-section for $^{12}\mathrm{C}(\mathrm{p},\pi^+\pi^0)^{13}\mathrm{C}$ at $E_p = 330$ MeV can be calculated. With $N_{\pi\pi} \approx N_{\mathrm{bkgd}} \approx 39$, the expected mean number of $\pi\pi$ events is $\mu = 0 \pm \sqrt{39} = 0 \pm 6.3$, with a 95% confidence limit of $N_{\pi\pi} < 13$. Using the calculated acceptance for $^{13}\mathrm{C}$ recoils from $^{12}\mathrm{C}(\mathrm{p},\pi^+\pi^0)^{13}\mathrm{C}^{5+}$, and the integrated luminosity $L_{\mathrm{int}}(330\ \mathrm{MeV}) = 14.2\ \mathrm{nb}^{-1}$, the upper limit is $\sigma_{\pi\pi} < 17$ nb, at the 95% confidence level. As a fraction of the total cross-section for (p,π^+) leading to bound $^{13}\mathrm{C}$ states at 330 MeV, this limit corresponds to $\sigma(\pi^+\pi^0)/\sigma(\pi^+) < 0.009$.

5

Conclusion

Meson-nucleon interaction studies are a key component of modern intermediate-energy nuclear physics, in that the current quantitative understanding of the nuclear strong force depends heavily on models incorporating the exchange of mesons between nucleons. The work described here, embodied by the CE-06 experiment, has attempted to improve this understanding through the study of exclusive proton-induced pion production from ^{12}C. Data were taken using proton beams ranging in energy from the near threshold region ($E_p \approx 150$ MeV) up to $\sqrt{s} \approx M_{^{12}\mathrm{C}} + M_\Delta$. In this work, a full analysis was completed for three of these energies (166 MeV, 294 MeV, and 330 MeV) to extract differential ($d\sigma/d\Omega$) and total (σ) cross-sections for single- and double-pion production processes.

At $E_p = 166$ MeV, differential cross-sections[1] for $^{12}\mathrm{C}(\mathrm{p},\pi^+)^{13}\mathrm{C}$ and $^{12}\mathrm{C}(\mathrm{p},\pi^0)^{13}\mathrm{N}$ leading to bound final nuclear states were measured. With an extensive database for $^{12}\mathrm{C}(\mathrm{p},\pi^+)^{13}\mathrm{C}$ in the near-threshold energy region already well-established, the concern here was primarily to investigate an apparent anomaly in the π^0 total cross-section compared to $\sigma(\pi^+)$. Using the (p,π^+) data and previously measured cross-sections as a normalization for the differential (p,π^0) cross-section, the value $\sigma(\pi^0) = 374 \pm 46$ nb was obtained. The shape and magnitude of this cross-section is in good agreement with the only previous measurement [Ho92] of the process, leading to a ratio here of $R \equiv \sigma(\pi^+)/\sigma(\pi^0) = 1.5 \pm 0.2$. Although the ratio is in apparent discord with that predicted by isospin invariance ($R = 2$),

[1] More properly, $d^2\sigma/d\Omega\, dE_p$ (angular distributions) and $d\sigma/dE_p$ (excitation functions) were measured.

other results yielding ratios from $R = 1.27 \pm 0.05$ [Ho92] to $R = 1.73 \pm 0.27$ [Pi93] while using the same $\sigma(\pi^0)$ result suggest that the disagreement may rest primarily in a proper Coulomb analysis of the $\sigma(\pi^+)$ data. Combining the result of a recent such calculation [Pi93], and the $\sigma(\pi^0)$ data from this work, the value $R = 2.0 \pm 0.3$ is obtained.

Pion-production data at 294 MeV and 330 MeV were also analyzed in this work. The first extremely forward-angle (p, π^+) measurements ($\theta_\pi < 20^\circ$) made at intermediate energies were reported, showing a fairly flat small-angle cross-section with little or no large-angle peak, as seen at $E_p \lesssim 200$ MeV. As in the analysis at $E_p = 166$ MeV, the π^+ data at 294 MeV were used to normalize the measurement of $\sigma(\pi^0)$. The lack of previously measured (p, π^+) cross-sections in this energy range, however, made the luminosity calculation difficult and error-prone; the absolute scaling of the π^0 cross-section is therefore preliminary. Nonetheless, the ratio $\sigma(\pi^+)/\sigma(\pi^0)$, the calculation of which here depends only on the knowledge of the relative $^{13}\mathrm{C}_{\mathrm{g.s.}}$ contribution to the total bound-state (p, π^+) cross-section, was found to be in reasonable agreement with that expected from isospin invariance.

As a means of testing underlying symmetries in the diagrams describing pion-nucleon dynamics, a first-ever measurement of $(\mathrm{p}, \pi\pi)$ processes in nuclei was attempted. At $E_p = 330$ MeV, a search for $(\mathrm{p}, \pi\pi)$ events was carried out, using the data at $E_p = 294$ MeV (just below the $(\mathrm{p}, \pi\pi)$ threshold) as a basis of background comparison. The number of valid $(\mathrm{p}, \pi\pi)$ candidates at 330 MeV was determined to be consistent with zero. Using the concurrently measured single-pion production data as a normalization, this result leads to an upper limit (2σ confidence level) of $\sigma_{\pi\pi} < 17$ nb, which corresponds to less than 1% of the (p, π^+) strength at $E_p = 330$ MeV.

This work, as a recoil detection experiment based on an electron-cooled storing ring using very thin internal targets, demonstrates much promise for future studies. Many of the limitations in the data encountered here stem from low integrated luminosities rather than high background levels or other more intrinsically intractable problems. With L_{int} in the 5×10^{35} cm^{-2} range (along with a reliable independent means of measuring this quantity), the CE-06 experimental method is ideally suited to exclusive measurements of other processes which are difficult to measure by standard means.

For example, the study of (p, π^-) reactions such as $^{12}\mathrm{C}(\mathrm{p}, \pi^-)^{13}\mathrm{O}$ (much more weakly populated than (p, π^+), and not seen in CE-06 due to the small value of L_{int}) is well-suited to the recoil method; a PC optimized for heavily-ionizing recoils (it is position sensitive

in two dimensions) has been designed [Sg92] for use in a CE-06 follow-up experiment. Exclusive photo-production, such as the astrophysically important process $^{12}\mathrm{C}(\mathrm{p},\gamma)^{13}\mathrm{N}$, is a good candidate for study via the recoil method, since the complications of detecting high-energy γ rays are avoided (the same reasoning applies to the study of (p,π^0) in this work). Future measurements of $(\vec{\mathrm{p}},\gamma)$ are planned using the CE-06 apparatus and the recently developed high-intensity polarized ion source at IUCF. Further and more conclusive studies of the $(\mathrm{p},\pi\pi)$ reaction near threshold in nuclei are also clearly warranted: the relative populations of different $(\mathrm{p},\pi\pi)$ processes close to threshold are important to know, as is verification of possible resonant $\pi\pi$ states near $E_p = 350$ MeV. Such projects may indeed be very difficult or impossible to accomplish via more standard (non-recoil) methods.

Appendix A: Gas Detector Operation

All detectors which use gas as their working media for the detection of ionizing particles take advantage of the fact that the electromagnetic interaction cross-sections involved in the process are quite large: on the order of megabarns. Gas detectors such as those used in the CE-06 experiment exploit the correspondingly high probability of such interactions to achieve the detection of heavily-ionizing particles with 100% intrinsic efficiency. This appendix describes the operating principles of gas detectors in general (full details are given in [Sa77]) along with specific characteristics of the highly efficient low-pressure detectors.

A.1 General Principles

For energetic, charged particles[1] incident upon a gas volume (or material in any state of matter), the dominant energy loss mechanism is via inelastic collisions with atomic electrons. Here, "inelastic" refers to the fact that in such a process, an atom or molecule may become excited or ionized. Typical ionization energies for commonly used gases are approximately 10 eV, but the *average* energy loss needed to produce one electron-ion pair is about 30 eV, due to the fact that molecular or atomic excitation is much less likely to produce a free electron. Therefore, on the average, a particle losing energy E in the gas volume produces $N_{\text{pair}} \propto E\,[\text{eV}]/30$ electron-ion pairs. A detector such as the PC used in the CE-06 experiment "counts" the number of pairs produced, following which the ionizing particle's energy can be reconstructed. The average ionization potential of 30 eV is the inherent limiting factor in the energy resolution of such a detector.

The transport of electron-ion pairs through the gaseous medium is the active rôle played by the detector, thus the consideration of this mechanism heavily influences the design and operating parameters. Without an externally applied electric field, both the

[1] This discussion is limited to particles and ions with $m \gtrsim m_\mu$ and heavier.

ions and electrons produced by the incident radiation quickly lose their extra energy and attain equilibrium via repeated collisions with other gas molecules. Using classical "billiard ball" arguments, the mean free path for ions or electrons in the gas at pressure P and temperature T can be written

$$\lambda \propto \frac{kT}{P}. \tag{A.1}$$

Typical values for ions in gases at NTP are roughly 0.1 μm, with somewhat larger paths for the negligibly sized electrons. With thermal velocities of $v_{\text{ion}} \approx 500\,\mu\text{m}/\mu\text{sec}$ and $v_{\text{e}^-} \approx 200 \cdot v_{\text{ion}} \approx 100$ mm/μsec (the factor of 200 due to the electron-ion mass difference), thermal equilibrium occurs on the time scale of less than one nanosecond.

At this point, the electrons and ions begin to diffuse and recombine, the latter occurring typically in a few hundred nanoseconds. The ions may recombine with the ionization product electrons, or pick up electrons from other gas molecules, which themselves recombine later. In either case, the signature of the ionization event is soon lost.

A gas detector overcomes the thermal recombination by application of an electric field to the working gas volume, which produces a phenomenon known as *drift*. The thermal motion of the ions and electrons is random and thus favors no particular direction, but an electric field breaks the symmetry and causes the average velocities of the ions and electrons along a particular direction to be non-zero. A drift velocity is attained rather than a "drift acceleration" due to the frequent collisions with gas molecules, which tend to restore the ions and electrons to their (random) thermal motions.

The drift behavior of ions and electrons is quite different, however. For ions, $v_{\text{drift}} \approx 10\ \mu\text{m}/\mu\text{sec}$, which is much smaller than thermal velocities, so that the application of the field doesn't significantly change the velocity magnitude, kinetic energy, diffusion, or recombination of the ions. For electrons, however, the drift velocity can become comparable to thermal velocities. For example, at typical field values of 1 kV/cm, the electron drift velocities can range from 20 to 150 mm/μsec, depending on the particular working gas. As such, it is possible to modify the electron transport significantly, and collection of the electrons, upon which the proper operation of most gas detectors depends, can occur before recombination takes place.

Even with an external field, however, an electron can also be absorbed by electronegative molecules. These are neutral molecules with atoms that have almost-full electron shells and which tend to be more stable as negative ions. After absorbing an electron, they may in turn finally recombine with a positive ion! The presence of these gases (for

example, water vapor) can severely limit detector performance.

The current resulting from the collection of all the electrons generated in the ionization event is still extremely small; most detectors rely on electron "multiplication." This increase in the number of free electrons is accomplished via the strong electric field surrounding a biased, thin wire (the anode): As the average electron energy increases through acceleration toward the anode, inelastic collisions with molecules (producing excitations or ionizations) become more likely. Energetic atomic decay photons can cause secondary ionization and excitation by interaction with the metallic components of the detector. The net effect is an avalanche: the number of electrons increases exponentially as the drift continues toward the anode. Noble gases such as argon produce larger multiplication factors since there are no radiationless molecular excitations to "absorb" electron energies. Furthermore, the relatively large excitation energies in noble gases generate decay photons that can easily produce more electrons from the cathode metal. In contrast, polyatomic gases often have many vibrational and rotational modes and tend to impede multiplication; they are often used mixed with noble gases to provide stability in operation, especially for atmospheric pressure detectors.

Detectors can be classified according to the magnitude of the electron multiplication. Proportional counters are those that maintain a linear relationship between the original number of electrons produced and the electrons that are collected, thus yielding a signal proportional to the energy deposited in the medium. Avalanche counters use such high values of multiplication that space charge distorts the field of the anode and proportionality is limited. The large signals and short total drift times of the electrons allow for good position and timing accuracy, however.

A simple model of the avalanche development in a proportional counter is useful for a first-order analysis of typical signal characteristics. Consider a simple cylindrical geometry (see Fig. A.1), where typically the cathode radius is $b \approx 1$ cm and the anode radius is $a \approx 20$ μm. The field due to the wire for $r > a$ is

$$\mathcal{E} = \frac{CV_0}{2\pi\epsilon_0}\,\frac{1}{r} = -\frac{d\phi}{dr},$$

where the capacitance per unit length is

$$C = \frac{2\pi\epsilon_0}{\ln(b/a)}. \tag{A.2}$$

The electrostatic energy of a cylinder of length l, $E_{\mathrm{cyl}} = (1/2)\,ClV^2$, is a constant during the process of signal formation since the power supply is usually too slow to keep the

cylinder voltage constant on a nanosecond time scale. A charge[2] Q which moves toward the anode from radius r to $r + dr$ ($dr < 0$) gains energy $dE_Q (> 0)$ so that the cylinder loses energy $dE_{\rm cyl} = -dE_Q$.

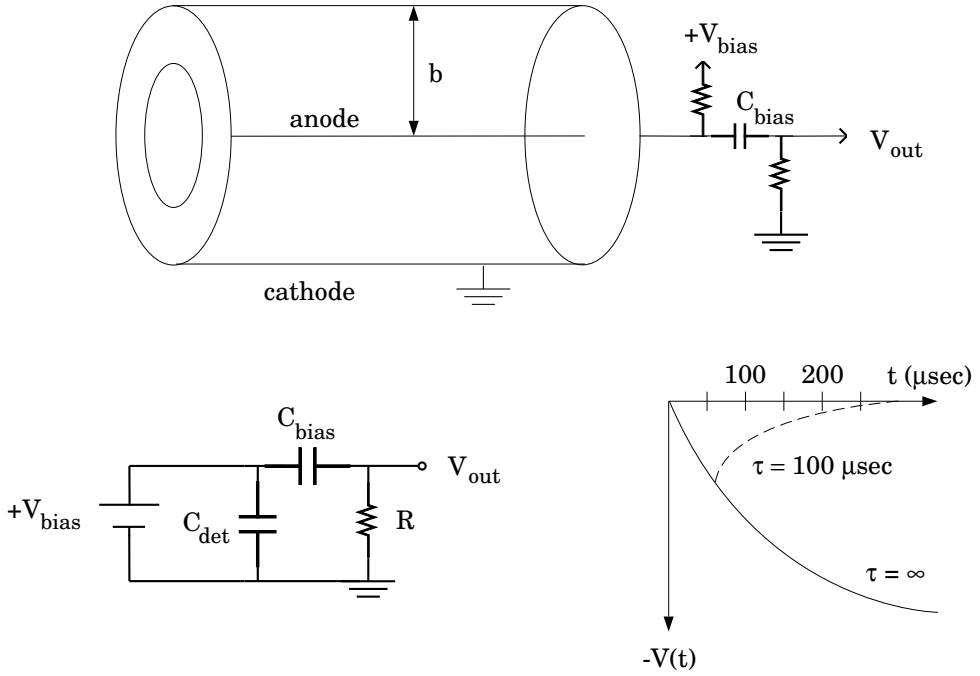

Figure A.1 The simple cylindrical wire chamber. Also shown is the equivalent circuit and the resulting signal development for a proportional mode counter.

An important thing to note is that the signal formation is via induction and not actual charge collection: energy conservation requires that the cylinder energy (and hence voltage) decrease as the electrons' average energy increases. Assuming that the change in cylinder voltage is small compared to the bias voltage V_0, the change in energy of the cylinder is given by

$$dE_{\rm cyl} = ClV_0\, dV$$

and

$$dE_Q = Q\, d\phi = Q\frac{d\phi}{dr}\, dr,$$

so that

$$\frac{dV}{dr} = -\frac{Q}{ClV_0}\,\frac{d\phi}{dr} = \frac{Q}{2\pi\epsilon_0 l}\,\frac{1}{r}. \tag{A.3}$$

Electron multiplication typically occurs within a few μm of the anode surface, i.e., for $(r - a) \lesssim r_0 \equiv 1\ \mu$m. The collection time is thus $t \approx 1\ \mu{\rm m}/v_{e,{\rm drift}} < 1\,{\rm nsec}$, and so the

[2] As used here, Q is the absolute value of negative charge, $Q = |e| \times$ # of electrons.

total contribution to the induced signal by the electrons is small and confined mainly to the initial attack of the signal. The positive ions drift all the way to the cathode in a time scale of 0.5 msec and so produce most of the total integrated signal: with typical values for a, r_0, and b, $V_{e^-}/V_{\rm ion} \approx 0.01$. The induced signal is thus

$$V(t) \approx V_{\rm ion}(t) = \int_{r(0)}^{r(t)} \frac{dV_{\rm ion}}{dr}\, dr = \frac{-Q}{2\pi\epsilon_0 l} \ln \frac{r_{\rm ion}(t)}{a}. \qquad \text{(A.4)}$$

Since the ions' velocities are typically proportional [Sa77] to the field $\mathcal{E}$, $dr_{\rm ion}/dt \propto \mathcal{E} \propto 1/r$ and $r_{\rm ion}(t) = (c_1 + c_2 t)^{1/2}$, where c_1 and c_2 are constants.

Figure A.1 shows the resulting time development of the induced signal in (A.4). Typically, the readout circuit differentiates the tail of the pulse to allow for fast readout of other pulses. The pre-amp circuits used for the CE-06 PC provided an effective differentiation time constant of 20 μsec, for a maximal event rate per wire of about 10 kHz.

The resulting output signal is suitable for further shaping and introduction into a peak-sensing ADC: $\max(V(t)) \propto Q \propto E$, where E is the deposited energy. Alternatively, the signal can be integrated over a selected portion of the development time, since the integral of Eq. (A.4) is also proportional to Q. Assuming that the intrinsic charge pulse risetime of the detector is much smaller[3] than the pre-amp time constant, and that this risetime does not depend appreciably on the total charge deposited, the proportionality is maintained by integration of any portion of the signal. For the CE-06 experiment, the PC pre-amp outputs were integrated in a 750 nsec window near or encompassing the signal peak.

The multiplication factor m, defined as the collected charge divided by the original ionization charge, is given [Sa77] by

$$m \propto e^{CV_0}.$$

Through Eq. (A.2), this implies that m is sensitive to changes in b, the cathode-to-anode distance, according to

$$\frac{\Delta m}{m} \approx \frac{1}{2}\frac{\Delta b}{b} \ln m.$$

For the PC used in the CE-06 experiment, $\Delta m/m \approx 4 \cdot \Delta b/b$, so that a 0.5 mm change in the cathode-to-anode distance produces a 40% variation in the multiplication gain. This sensitivity required the non-trivial PC calibration of Ch. 4: Fig. 4.6 shows that the actual distance variations for the CE-06 experiment were typically 0.2 mm.

---

[3] The PC intrinsic risetime was on the order of 0.1 μsec, while the pre-amp time constant was approximately 20 μsec.

A.2 Low-Pressure Detectors

Both of the detectors used in the CE-06 experiment are low-pressure detectors: the PC operated with 20 to 100 torr of carbon tetrafluoride (CF_4), and the PGAC used 3 torr of isobutane (C_4H_{10}), in contrast to the more common types of wire chambers that operate at or slightly above the ambient atmospheric pressure. For gas detector operation, there are essentially three realms of gas pressures: atmospheric ($P \gtrsim 500$ torr), low-pressure/proportional (20 torr $< P <$ 200 torr), and low-pressure/saturated ($P <$ 10 torr). Each region involves different choices of physical parameters and gases.

For atmospheric detectors, noble gases such as argon are often used to provide for large signal gain. Maximum multiplications are soon reached, however; the ultraviolet photons emitted by de-exciting argon atoms produce enough photo-electrons from the cathode to sustain a permanent discharge. Typically a "quenching" polyatomic gas is added to absorb the ultraviolet radiation without secondary emission. These complex molecules can efficiently transfer charge from ionized noble gas atoms due to their relatively low ionization potentials. A large proportion of quenching gas yields very good stability to sparking, but the signal size is reduced greatly.

In the low-pressure regimes, however, the inverse dependence on P in Eq. (A.1) implies higher mean collision times for electrons (and hence larger average drift velocities), resulting in much higher secondary ionization rates, i.e., bigger multiplication factors. The effect is so pronounced that the use of pure noble gases is precluded and quenching gases such as isobutane, propane (C_3H_8), and CF_4 can be used as the sole working gas. The latter has the advantage of an effectively high-Z molecule and, consequently, a large stopping power relative to most other commonly used gases. The large value of dE/dx is useful in the case of low-pressure proportional counters: the thickness of the active gas volume can remain reasonably small without the need for excessively large pressures. Absolute pressures of more than 100 torr are mechanically difficult to contain with thin entrance windows. Even atmospheric detectors, which are usually not so constrained by the thickness of their entrance windows, are typically operated only a few torr above the ambient pressure. Isobutane has somewhat less stopping power than CF_4 but is well-suited for a low-pressure chamber operating in the limited proportionality or saturated mode, where the amount of deposited energy is not an important factor (this information is discarded in this region of operation).

Down to absolute pressures of about 20 torr, the proportionality between the deposited

charge and collected charge can be maintained. Below roughly 10 torr, however, the variations in output pulse height with changes in applied bias are negligible: the saturation point is reached for any reasonable signal size. In this region of operation, as in the case of the PGAC, position and timing measurements are usually desired, and the bias level is set fairly close to the sparking breakdown voltage to maximize the induced signal size and minimize the signal risetime.

All low-pressure detectors, when used for the detection of highly-ionizing ($Z \gg 1$) particles, afford several experimental advantages:

a) the detectors are virtually 100% efficient for these particles while remaining relatively insensitive to protons and γ-rays;
b) extremely fast timing is possible, especially with avalanche-mode detectors. Typical resolutions for large area detectors such as the PGAC used in CE-06 are roughly 0.5 nsec, and better than 200 psec has been achieved in small detectors [Br82];
c) fairly high counting rates ($\gtrsim$ 10 kHz) can be tolerated with little performance degradation.
d) the achievable position resolutions for these detectors are good: typically, about 1 to 2 mm depending on the particular method of readout.[4]

There are technical challenges that must be met in order the realize these advantages, however. Primary among these is the need to provide a complete vacuum enclosure, since the detector gas pressures are typically 1 to 100 torr. Another difficulty involves the use of extremely thin ($t \approx 100$ μg/cm^2) foils for pressure isolation. While thin enough to minimize undesired ion energy losses, the foils must be strong enough to withstand large differential pressures (for the PC used in CE-06, on the order of 50 torr). The pump-down and venting of the vacuum enclosure which contains the detectors must be done with great care so as to not the break the foils. Most detectors which employ foils of this type use support grids to help balance the pressure. The PGAC and PC detectors incorporated 100 μm tungsten wires spaced at 2.54 cm and 1.0 mm, respectively, as support grids.

[4] High-pressure chambers are usually superior in this respect, though. The large electron drift velocities imply short collection times but tend to worsen the position resolutions via the longer mean free paths.

Appendix B: Semiconductor Detectors

Semiconductor devices have been used as radiation detectors in nuclear and high-energy physics for more than 25 years. In the past decade, however, a new technique has been developed (combining ion implantation and photolithography) for the production of large-area detectors requiring readout configurations for complex position measurement or timing applications. The silicon micro-strip detectors used in the CE-06 experiment are examples of this new technology. This appendix considers the principles of semiconductor detectors in general and these relatively new devices in particular.

B.1 General Principles

The general operating principles of semiconductor detectors are fundamentally similar to that of gas detectors (see Appendix A). In order to detect the minute amounts of free charge produced by the incident ionizing radiation, an electric field is set up in a volume of material (the "active region") in order to "collect" the charge via induction.

There are important differences in the details, however. The stopping power of a semiconductor detector is much greater than any practical gas detector. For example, for 5 MeV α particles, $(d\mathrm{E}/dx)_{\mathrm{Si}}/(d\mathrm{E}/dx)_{\mathrm{CF_4}} \approx 550 : 1$. This implies the capability to detect ionizing radiation using a small active volume detector (often less than 1 mm in thickness), along with the ability to efficiently detect minimally ionizing particles. Another distinguishing feature of these detectors is the relatively small amount of energy required on the average to produce an electron-ion pair; typically, this is about 3.5 eV for silicon, roughly a factor of ten smaller than that of a typical gas [Lw87]. The intrinsic resolution of these devices is consequently much better than that of gas detectors. The most important difference from gas detectors is, of course, the crystal structure of the solid-state medium. This characteristic is the basis for understanding how these detectors work.

A semiconductor is characterized by a gap of order 1 eV between the highest filled

and lowest unfilled electron energy levels. For pure ("intrinsic") silicon, the filled levels (the "valence" band) correspond to electrons attached to ions and the unfilled levels (the "conduction" band) to "free" electrons. Since the valence levels are completely filled, no electron in this band can contribute to a current in the silicon. A valence electron may, however, jump the gap into the conduction band via thermal excitations, which implies that near absolute zero a semiconductor becomes a good insulator. A true insulator is different primarily in the size of the energy gap: a large gap can make thermal excitation very improbable even at high temperatures.

An electron which does reach the conduction band leaves behind a vacancy (or "hole") in one of the valence band energy states. Because of the small separation in energy between the levels in the band, a neighboring electron can easily jump into the available state, itself leaving another empty level. This motion of charge is a current as real as that due to the motion of the electrons in the conduction band, and is called the "hole current." A model for current in a semiconductor must therefore take into account both the electron and hole contributions.

In practice, it is impossible to construct a completely pure sample of crystalline silicon, and impurities even at the level of one atom in 10^9 can significantly alter [As76] the crystal's conduction properties. Typically, impurities produce energy levels deep inside the (previously empty) band gap. These levels can remove or capture charge carriers via recombination or trapping into metastable states.

This charge carrier loss is detrimental to good detector performance: high efficiency, good resolution, and fast signal risetimes depend on the rapid and complete charge collection of the ionization event's charge. Many detectors are produced by purposefully introducing ("doping") impurities into the silicon, replacing atoms at their lattice sites.

Commonly used dopants for silicon are atomically pentavalent and trivalent, for example, arsenic and boron, respectively. Arsenic has an "extra" electron which does not participate in the covalent bonding with the lattice silicon atoms. This electron is only weakly bound to the impurity atom (since the nucleus is shielded by the other valence electrons) and resides in an energy level just below the conduction band. A trivalent impurity has, on the other hand, an "extra" hole and so produces an energy level located just above the valence band. Arsenic and boron, under these conditions, are referred to as "donor" and "acceptor" atoms, respectively.

Doping with donors or acceptors in concentrations of a few parts in 10^9 produces

n-type or p-type silicon, respectively, named for the sign of the extra charge carrier that is donated. For n-type materials, electrons are called the majority carriers and holes the minority carriers, and vice versa for p-type materials. Dopant concentrations as high as a few parts in 10^4 produce n^+ and p^+ silicon, which is highly conductive and often employed to make electrical contact with n- and p-type silicon.

A "p-n junction" is formed when n-type and p-type materials are placed in close contact. These junctions commonly play a major role in silicon detectors. In the absence of an external field, electrons on the n-side tend to diffuse via thermal motion across the junction to the p-side. Normally, a diffusion of electrons in the opposite direction from the p-side would, on the average, cancel this but there are many fewer conduction electrons on that side (they are the minority carriers) and so a net current of electrons results. Exactly the same argument can be made for the p-side majority holes: a net hole current is set up from the p-side to the n-side. The following discussion only considers the (equivalent) electron motion.

The electrons flow across the junction, leaving bare donor atoms (+1 net charge), and recombine with p-side majority holes, producing bare acceptor atoms (-1 net charge). The bare atoms produce an internal electric field which tends to prevent further electron flow. The section of material in which there exists a non-zero electric field is called the "depletion region," since any electron-hole pairs generated there (thermally or by ionizing radiation) are swept out by the field. Here, majority carrier current is suppressed whereas minority carrier current (i.e., conduction electrons flowing from the p-side to the n-side) is not. An equilibrium is reached when the normally small minority carrier current equals the suppressed majority carrier current. In silicon, the "contact potential" corresponding to the internal field thus set up is typically $V_0 \approx 1$ volt. The thickness of the depletion region for an intrinsic n-type detector, such as those used in the CE-06 experiment, is

$$d_{\mathrm{n}} = (2\epsilon\rho_{\mathrm{n}}\mu_e V_0)^{\frac{1}{2}}, \tag{B.1}$$

where ρ_{n} is the n-type resistivity, ϵ is the relative dielectric coefficient, and μ_e is the electron mobility in the silicon. The high resistivity n-type material used in the CE-06 silicon detectors has $\rho_{\mathrm{n}} \approx 2 \times 10^4\,\Omega\,\mathrm{cm}$, thus with a typical value $V_0 \approx 1\,\mathrm{volt}$, $d_{\mathrm{n}} \approx 75\ \mu\mathrm{m}$.

A p-n junction detector is typically reverse-biased: an external field is applied in the same sense as the internal junction field, i.e., a positive electrode is attached to the n-side, and a negative one to the p-side. The calculation of the depletion region width is the same,

with V_0 replaced by the applied voltage $V_{\rm app}$. For the particular type of detector used in CE-06, $V_{\rm app} = 10\,$volts creates a depletion depth of $d \approx 240\ \mu$m. For the experiment, the detectors were "over-biased" to approximately 50 volts. Here, the bias level is more than enough to attain a fully-depleted detector, in which the width of the active volume is comparable to the physical detector thickness. The over-biasing further enhances the timing resolution by 10–15% by increasing the field strength in the depletion region.

The increase in the depletion region and the suppression of the majority current are the main reasons for the reverse-biasing of a p-n junction detector. This region is the sensitive volume of the detector: ionizing radiation produces electron-hole pairs which are accelerated out of the region by the field and collected by the electrodes. Electron-hole pairs produced outside the region (in a "dead layer") are not under the field influence and are free to recombine or become trapped. Fully depleted detectors are those with depletion regions essentially as large as the physical detector depth.

In practice, heavily doped n^+ and p^+ layers are added to the n and p sides respectively, so that metal electrodes can be attached and the induced signals can be read out directly. Without these layers, a depletion zone is formed at the metal-semiconductor interface (a "Schottky barrier"), which would prevent proper charge collection from the actual p-n junction. Such a barrier still forms in the n^+ and p^+ material but the heavy doping causes the width of the depletion region to be essentially zero.

The signal formation in the p-n junction detector is by induction (not actual charge collection) as in Appendix A. In contrast to the gas situation, however, the electron and hole motions contribute roughly equally to the total signal, and no real electron multiplication takes place. The signal on the positive electrode in a standard reverse-biased configuration is negative with a rise-time on the order of $\tau = \epsilon/en_{\rm donor} = \rho_{\rm donor}\epsilon$. The high-resistivity silicon used in the CE-06 Si detectors has an "intrinsic" rise-time on the order of 20 nsec.

In a real detector, a "leakage" current exists which induces a signal of the same sign on the electrodes as the desired signal from the incident radiation. The small current due to the motion of thermally generated minority carriers (electrons moving from the p-side to the n-side) is a contribution to this, although the largest factor in the leakage current is often due to surface effects. This can include current on the surface of the detector edge (via a surface contaminant, perhaps) from one contact to the other or current through an epoxy mount, etc. The leakage current provides a limit on the smallest real signal that can be observed: it is caused by essentially random processes and as such can be indistinguishable

from an ionizing event. The method of oxide passivation can greatly reduce the surface component of the current (to levels comparable to the thermal currents) and thus allow the construction of much larger p-n junction detectors, with areas of 10's of cm^2 compared to 1 cm^2.

B.2 Passivated, Ion-Implanted Silicon Detectors

The micro-strip detectors such as those used in CE-06 combine the technology of oxide passivation, ion implantation, and photolithography. Typically, a planar sample of high-purity silicon (which is often weakly n-type to begin with due to residual donor impurities) is "passified": an insulating oxide layer is formed on it [Kn89]. Photolithography, which is essentially a technique for etching patterns in materials using light, is performed on one face[1] to remove the SiO_2 from specific areas.

At this stage in the construction, the etched silicon wafer is subjected to ion implantation. This is the bombardment of donor atoms on one face and acceptor atoms on the other. For the n-type wafers used in CE-06, acceptors are implanted on the front, etched face to produce a p-n rectifying junction (and a p^+ surface layer), while donors are implanted on the back to produce a non-rectifying n^+ surface.

The sample is then baked to anneal the radiation damage produced by the ion implantation, which could otherwise leave lattice defects producing increased leakage current and slow or incomplete charge collection. Finally, aluminum is evaporated on the faces which can then be etched in the desired entrance and/or exit patterns, again by photolithography.

There are several inherent advantages to the ion-implanted passivated detectors over the devices based on Schottky barriers (also called surface-barrier detectors). The leakage current via surface channels can be greatly reduced since the actual p-n junctions are inside the volume of the sample and do not extend to the physical sample edge. For a fully depleted detector, the dead layer thickness is due to the entrance and exit windows and can be made very small (< 1000 Å) since the largest contribution to the layer is from the evaporated aluminum (barring fingerprints!). Furthermore, complex readout electrodes can be etched on the front or back face to suit a wide variety of applications.

The micro-strip detector is a particular example of a readout configuration where electrode "strips" are etched parallel to one another across the detector face, separated by insulating material (typically, SiO_2). Each electrode can be read out separately and

[1] More complex readouts can require etching of more than one face.

independently of the others since the electric field configuration "traps" the ionization trail to the nearest strips in a way similar to that for the MWPC that was used in the CE-06 experiment. If the strips are wide compared to the extent of the ionization trail and the incidence of radiation is essentially normal to the detector face, the signal is confined to a single strip. From this, a measurement of the position of the incident radiation can be made by determining which strip "fired." The "pitch" of the strips is the distance between the strip centers and can be as small as tens of microns and as large as 1 cm. In the case of the micro-strip detectors used for the CE-06 experiment, the strip pitch was 1 mm, with narrow (50 μm wide) insulating SiO_2 strips between. In the configuration of Fig. 3.31, these dimensions imply a silicon transmission efficiency of 93%.

Since the best position resolution possible is just the strip pitch, small values of this parameter can yield very precise position determination, at the cost of a large number of readouts and complex readout circuitry. If the back face of the detector is unpatterned, a position-independent signal (of the opposite sign) proportional to the deposited energy can also be obtained.

Appendix C: Software

The complete analysis of the data associated with the CE-06 experiment required the development of specialized software for both VMS® and UNIX® platforms. Most of this software is directly related to describing the passage of charged particles through the T-Site 6° magnet and the CE-06 detection apparatus. This appendix discusses the key elements of the software and corresponding use in the analysis of the experimental data.

C.1 The T-Site Magnet Map

Central to the software discussed here is the magnetic field map of the six-degree T-Site dipole. The large-gap design of the magnet, while permitting extremely efficient detection of recoils, results in a fringe field of considerable extent, as seen in Figs. 3.8 and 3.11. As such, a three-dimensional map of **B** is necessary in order to realistically integrate the equations of motion for charged particles traversing the magnetic field.

Analytical calculations of the magnetic field (the results of which are referred to hereafter as the "TOSCA" map) using the expected magnet pole design parameters were completed [Dk91] before the magnet was actually built, to test its suitability to the ring. The fixed coordinate system ("magnet" coordinates) used throughout this work was chosen to match as closely as possible that used in the TOSCA code, for convenience of comparison. The origin of this system is located vertically midway between the magnet pole faces and horizontally in the middle of the B_y field plateau (see Fig. 3.6). Defined to be parallel to the magnet mapper axes, the x and z axes lie in a plane parallel to the pole faces. The y-axis is perpendicular to the poles, with $y = 0$ symmetrically located halfway between. In this manner, the nominal beam direction is along the z-axis, although particular particle trajectories encountered during the ring cycle may yield incident angles on the order of 0.2° to this axis.

The IUCF magnet mapper measured the y-component of the magnetic field in xz-

plane grids at several values of y, including $y = 0$. Since standard ring dipole magnets are typically mapped only in the bend plane, it was necessary to translate the 6° magnet along the y-axis for each desired xz-plane grid. In order to construct the complete map using this data, calculations were performed as follows. First, the data was interpolated to generate a uniformly spaced grid of B_y values in three dimensions. This was necessary since the measured grids were not uniformly spaced over their extents, and the grids of some planes were shifted and rotated with respect to the grid at $y = 0$. The corrections for the latter effects were determined from the measured coordinates of three fiducial marks (essentially, pins in the pole faces) taken during each grid measurement.

Next, the B_x and B_z components of the field were calculated at each (x, y, z) grid vertex, in the following way. From symmetry about the $y = 0$ plane,

$$B_{x,z} \approx y\frac{\partial B_{x,z}}{\partial y} + \frac{y^3}{3!}\frac{\partial^3 B_{x,z}}{\partial y^3}$$

and

$$B_y \approx B_y(y = 0) + \frac{y^2}{2!}\frac{\partial^2 B_y}{\partial y^2} + \frac{y^4}{4!}\frac{\partial^4 B_y}{\partial y^4}.$$

Using

$$\boldsymbol{\nabla} \times \mathbf{B} = 0 = \boldsymbol{\nabla} \cdot \mathbf{B},$$

the partial derivatives of B_x and B_z can be expressed in terms of derivatives of B_y. With

$$B_{x,z}(x, y, z) = -B_{x,z}(x, -y, z)$$

and

$$B_y(x, y, z) = +B_y(x, -y, z),$$

the components can be written

$$\begin{aligned} B_x = {} & \frac{y}{2\Delta}\Big(B_y(x + \Delta, 0, z) - B_y(x - \Delta, 0, z)\Big) \\ & + \frac{y^3}{24\Delta^3}\Big(B_y(x + \Delta, 2\Delta, z) - B_y(x + \Delta, 0, z) \\ & \qquad + B_y(x - \Delta, 0, z) - B_y(x - \Delta, 2\Delta, z)\Big), \end{aligned}$$

$$\begin{aligned} B_z = {} & \frac{y}{2\Delta}\Big(B_y(x, 0, z + \Delta) - B_y(x, 0, z - \Delta)\Big) \\ & + \frac{y^3}{24\Delta^3}\Big(B_y(x, 2\Delta, z + \Delta) - B_y(x, 0, z + \Delta) \\ & \qquad + B_y(x, 0, z - \Delta) - B_y(x, 2\Delta, z - \Delta)\Big), \end{aligned}$$

and

$$B_y = B_y(y=0) + \frac{y^2}{4\Delta^2}\Big(B_y(x,2\Delta,z) - B_y(x,0,z)\Big) + \frac{y^4}{192\Delta^4}\Big(B_y(x,4\Delta,z) - 4B_y(x,2\Delta,z) + 3B_y(x,0,z)\Big).$$

Here, Δ is the grid size, which for the T-Site map is 1 cm. These equations allow the complete calculation of the magnetic field map.

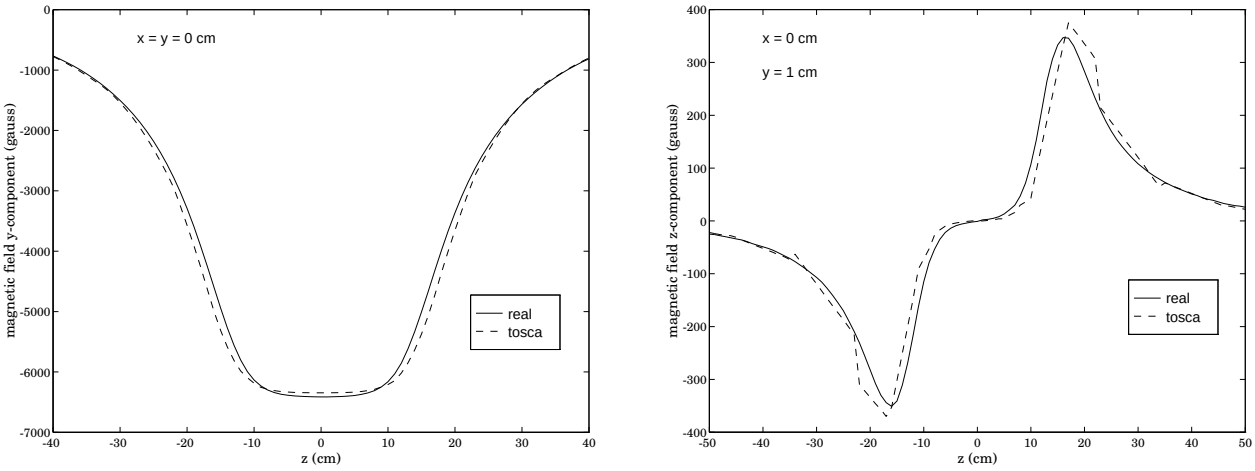

Figure C.1 The B_y (left) and B_z (right) components of the real (solid line) and TOSCA (dashed line) field maps as a function of z. Both fields are for a magnet current of 300 amps.

The strength and shape of this "real" field agree well with that calculated using the TOSCA code. Figure C.1 shows a representative comparison. As a final step in the construction of the map, those regions of space around the magnet for which B_y data could not be obtained (due to physical or temporal constraints) were "filled in" with the TOSCA field. Most particles entering this region (see Fig. C.2) fail to enter the detector stack because either they are too "soft" or they hit the aluminum pole-face spacer. However, raytracing calculations showed that transporting particles through the non-mapped region and assuming $B = 0$ here could result in false simulation of events in the CE-06 detectors. Use of the TOSCA field obviated the need for any time-consuming dipole field approximations in this region.

C.2 Forward Raytracing Simulations

Simulation software was developed for the CE-06 experiment primarily to determine the experimental acceptance as a function of the charge state, momentum, and reaction

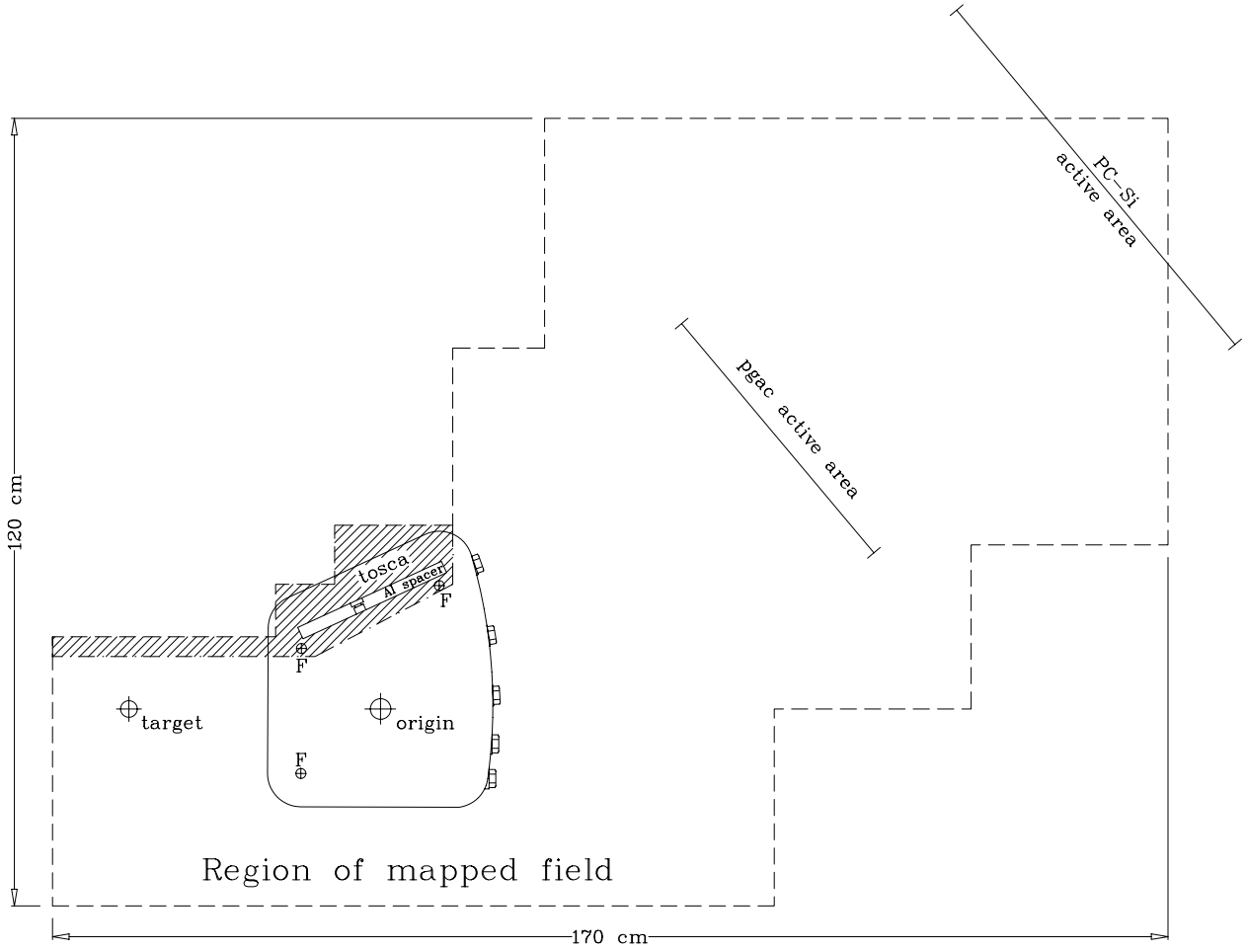

Figure C.2 Extent of the measured (white area) and TOSCA (hatched area) portions of the final map, with the locations of the PGAC and PC-Si for reference. Also shown are the locations of the fiducial pins ("F"), used for the absolute position calibration, and the aluminum spacer placed between the pole faces to assure a constant pole separation.

angle of recoil ions. The software was also used to estimate the effects of energy loss, charge redistribution, and multiple scattering of the ions in the pressure foils. Several specialized programs (e.g., for extraction of acceptance functions or simulation of online histograms) were written to utilize a core program for "forward" raytracing of ions through the magnet map of Sec. C.1. This core program transports ions from the target location, through the magnetic field, and into the detector stack, keeping track of the particle's magnet coordinates, energy losses, and velocity direction changes due to multiple scattering.

The most important element of the program is the magnetic transport of the charged particles. Here, a simple second-order midpoint method is used to integrate the equations of motion. A comparison with a fourth-order Runge-Kutta method [Pr88] showed negligible

track differences, and so the second-order method was chosen to improve execution speed. Far from the detector planes, an integration step size on the order of the grid size Δ is used. Within distance Δ of a detector's active area, however, the step size is reduced typically by a factor of five, for accurate position determination at the plane. This position is determined by an interpolation to the intercept point using the ion track's step coordinates before and after the detector plane. At each step, the magnetic field value is determined via three-dimensional quadratic interpolation of the grid.

Less complicated (but nonetheless important) elements of the forward raytracing include the simulation of energy losses and multiple scattering, both of which are especially relevant for heavily ionizing particles. Energy losses are calculated at each interception of the ion with material. The energy loss is assumed to take place at a point in space for foils, while for extended matter such as gas the losses are averaged over the ion's track in the material. Reasonably accurate (estimated error of 15% or better) energy loss numbers were obtained through the use of data tables [No70] from which $\Delta E(E, Z, M)$ for each type of material could be determined. Table C.1 shows estimates of the data analysis parameters of Ch. 4 for recoils from pion-production reactions at $E_p = 330$ MeV, obtained using the forward raytracing and energy loss tables.

	$^{12}\mathrm{C}(\mathrm{p},\pi^+)^{13}\mathrm{C}_{\mathrm{g.s.}}$			$^{12}\mathrm{C}(\mathrm{p},\pi^0)^{13}\mathrm{N}_{\mathrm{g.s.}}$		
	$p = p_{\min}$	$\theta = \theta_{\max}$	$p = p_{\max}$	$p = p_{\min}$	$\theta = \theta_{\max}$	$p = p_{\max}$
E_{reac} (MeV)	13.17	25.62	49.89	13.15	25.62	49.94
E_{tof} (MeV)	10.0	23.4	48.4	9.0	22.7	48.0
E_{si} (MeV)	7.0	21.5	47.2	5.0	20.1	46.3
ΔE (MeV)	0.7	0.4	0.3	0.9	0.6	0.4
R_{m} (mg/cm^2)	1.9	4.1	10.4	1.5	3.2	8.0

Table C.1 Characteristic energy values and ranges in mylar, calculated using forward raytracing, for ^{13}C and ^{13}N recoils. The reaction energies E_{reac} correspond to $p_{\min}$, $p(\theta_{\max})$, and $p_{\max}$ of the $E_p = 330$ MeV recoil locus.

Multiple scattering is incorporated in the raytracing code via the improved [Hi75] Highland formula: given the momentum p and velocity β of an ion with atomic number Z_{ion}, the r.m.s. scattering angle with respect to the incident direction is

$$\frac{\theta_{\mathrm{rms}}}{\sqrt{2}} = \frac{13.6\ \mathrm{MeV}}{\beta pc} Z_{\mathrm{ion}} \sqrt{\frac{L}{L_{\mathrm{mat}}}} \left[1 + 0.088 \cdot \log_{10} \left(\frac{L}{L_{\mathrm{mat}}} \cdot \frac{Z_{\mathrm{ion}}^2}{\beta^2} \right) \right], \qquad \text{(C.1)}$$

where $L_{\rm mat}$ is the scattering material's radiation length, and L is the scatterer's thickness. The scattering is calculated at each traversal by the ion of a pressure foil in the CE-06 setup[1] by generating a random angle with the proper distribution and r.m.s. value given by Eq. (C.1). Although fairly accurate (10%) for material thicknesses in the range $10^{-3} < L/L_{\rm mat} < 100$, the uncertainty in $\theta_{\rm rms}$ for the CE-06 thin foil thicknesses of $L/L_{\rm mat} \approx 3.5 \times 10^{-6}$ is not known. Nonetheless, it is important and necessary to include the effects of multiple scattering in the analysis of the CE-06 data (see Chapter 4).

A complete simulation of the experiment is possible as a shell using this forward raytracing kernel. A reaction event ion at the target is generated with a given center-of-mass angular distribution, which may be isotropic or an arbitrary combination of Legendre polynomials to simulate a realistic cross-section. With an atomic charge Q, chosen according to the appropriate energy dependence as in Fig. 3.10, the forward raytracing is called and the resulting information (such as time-of-flight, silicon position, etc.) is histogrammed. In this way, the effects of energy loss, multiple scattering, and acceptance on the apparent angular distribution with respect to the center-of-mass cross-section can be separately investigated. Furthermore, the performance of the backward raytracing code as used in the analysis can be examined.

C.3 Backward Raytracing

Given a recoil ion's detector signatures (deposited energies, measured positions, and so forth), it is necessary to completely reconstruct the ion's reaction parameters; this is the thrust of the analysis in Ch. 4. A major part of this reconstruction is the determination of the recoil's momentum and emission angle at the (known) target location, using the position and angle of the ion at the exit of the magnet box. In principle, this could be accomplished by "backward" raytracing, i.e., magnetic transport identical to Sec. C.2 except with $t \mapsto -t$. If the mass and reaction energy of the ion were known, then, by requiring that the recoil come from the target location, the emission angle (and, as a by-product, the atomic charge Q) would be determined.

In the analysis of the CE-06 data, however, uncertainties in the determination of the mass made it impossible to completely identify M without using more information, specifically, the ion's rigidity $R \equiv p/Q$. Furthermore, the calculation of the reaction energy of the ion (using the measured value of energy at the silicon detectors as a starting

[1] The contribution of multiple scattering in the gases is negligible in comparison.

point) was limited to about 10% accuracy. This uncertainty was primarily due to the (unmeasured) energy losses in the intervening foils and gases, and, to a lesser extent, systematic errors in the thicknesses of the materials themselves. True backward raytracing was therefore of limited use, and so a code was developed which could determine rigidity and angle at the target while avoiding the need to estimate these unknown quantities.

This backward raytracing program[2] depends on the fact that a PGAC-Si position pair can be uniquely associated with a R-θ_p pair (where θ_p is the bend-plane angle of the ion, not the spherical angle θ, cf. Fig. 4.17), for a wide range of ion masses, energies, and nuclear charges. For an arbitrary magnetic field, however, the function which connects these pairs cannot be determined analytically. Therefore, the forward raytracing was implemented to generate a set of ion tracks for kinematically possible momenta and angles, using reactions of particular interest[3] to the experiment, for each beam energy desired. In general, due to the small vertical acceptance[4] of the detector stack, it was only necessary here to use ion trajectories in the x-z plane.

Using this data, fits were made in an attempt to determine polynomial functions which could reproduce the initial rigidity and angle pairs with errors no worse than 1% and 0.1°, respectively, with a "reasonable" number of parameters. The best results were obtained with

$$\begin{aligned}\theta_p(x_{\rm pg}, x_{\rm si}) = {} & a_0 + a_1 x_{\rm pg} + a_2 x_{\rm si} \\ & + a_3 x_{\rm pg} x_{\rm si} + a_4 x_{\rm pg}^2 + a_5 x_{\rm si}^2 \\ & + a_6 x_{\rm pg} x_{\rm si}^2 + a_7 x_{\rm pg}^2 x_{\rm si} + a_8 x_{\rm pg}^3 + a_9 x_{\rm si}^3 \,; \\ R(x_{\rm pg}, x_{\rm si}, \theta_p) = {} & b_0 + b_1\theta_p + b_2\theta_p^2 \\ & + (b_3 + b_4\theta_p) x_{\rm pg} + (b_5 + b_6\theta_p) x_{\rm si} \\ & + b_7 x_{\rm si}^2 \theta_p + b_8 x_{\rm pg}^2 \theta_p + (b_9 + b_{10}\theta_p) x_{\rm pg} x_{\rm si} \\ & + (b_{11} + b_{12}\theta_p)/x_{\rm si} + (b_{13} + b_{14}\theta_p)/x_{\rm pg}.\end{aligned} \tag{C.2}$$

Here, $x_{\rm pg}$ and $x_{\rm si}$ are the ion positions along the length of the active areas of the PGAC and Si detectors, respectively (cf. Fig. 4.2). Standard least-squares minimization techniques were used to determine the coefficient vectors **a** and **b**. A set of parameters was calculated for tracks incident upon each half of the PGAC, to constrain the range of fitted values for

[2] Technically, a misnomer, since no real-time raytracing is done.

[3] The traced ions consisted primarily of ^{13}C and ^{13}N.

[4] The vertical angular width presented to the target by the silicon array is roughly 2°.

R and θ_p.

The forward raytracing which provides the input data for these fits includes the physical detector data, specifically, the locations of the PGAC and Si active areas with respect to the magnetic field, as determined in the calibration procedures of Ch. 4. Therefore, it is not necessary to determine the explicit form of the transformation (4.4); this is already incorporated in Eq. (C.2). In the absence of an analytical function, the fit provides an efficient means to combine the raytracing and transformation calculations into a routine suitable for on-line data analysis (i.e., without CPU-intensive code).

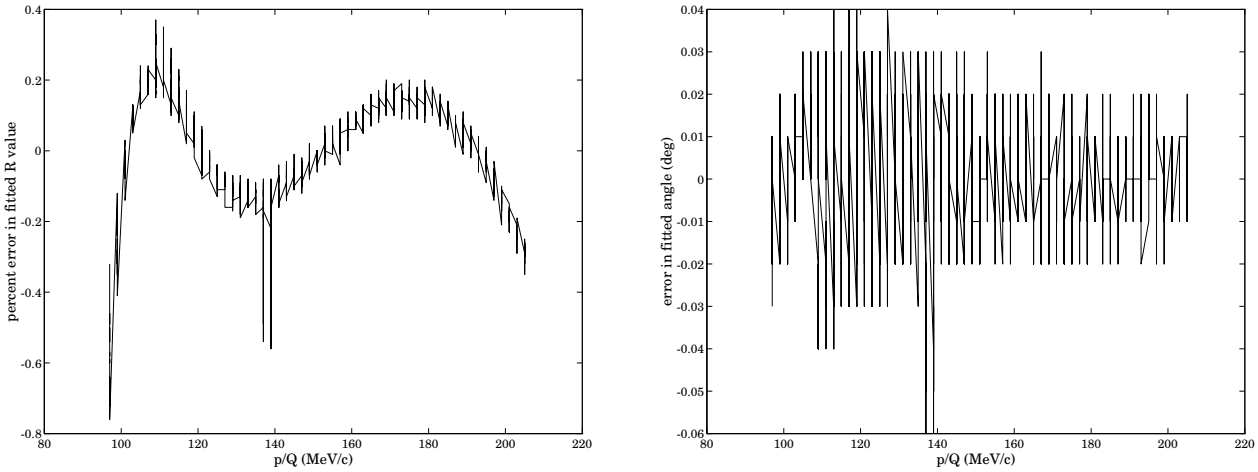

Figure C.3 Errors in a typical fit to forward raytracing data for E_p = 294 MeV, using Eq. (C.2). Shown are $\delta R/R \times 100$ (left) and $\delta\theta_p$ (right), for each point in the input data. The maximum errors in absolute value for this case are 0.8% and 0.06° for the rigidity and angle fits, respectively.

Use of the calculated angle in the rigidity function not only helps to constrain this fit, resulting in a simpler functional form, but also serves to eliminate ambiguities that would surface using independent functions. These ambiguities arise due to the finite resolution of the PGAC and Si position measurements. For example, it is possible for two ions to be emitted with rigidities that differ by more than 1%, but which produce the same $x_{\rm pg}$ and $x_{\rm si}$ values within the respective detector resolutions. In this case, the angle is necessary to distinguish the two values of rigidity.

The quality of the fits that can be achieved is good: particular results for E_p = 294 MeV are shown in Fig. C.3. In general, the average difference errors between the fit and the input data for this functional form were typically 0.2% for rigidity and 0.01° for angle, although errors for very soft ions ($p/Q < 90$ MeV/c) often ranged from 1–2%. In these cases the curvature of the ion track is large and so the momentum is very sensitive

to the detector positions. For the CE-06 experiment, however, most of the ions of interest were not in this range of rigidity.

As an independent test, the backward raytracing was used with α-particle source data (using a target-mounted ^{228}Th source), for which the mass, energy, and atomic charge of the ions were known *a priori*. In this manner, the goodness of the fit in determining R-θ_p pairs for data not explicitly in the forward raytracing input sets could be ascertained. After the calibration corrections of Ch. 4, the rigidities obtained for the four α-particle lines (103 MeV/c $\leq R \leq$ 128 MeV/c) used in Fig. 4.5 matched the tabulated values to within 0.4%. These results suggested that the fits were applicable to all the data of the CE-06 experiment, with characteristic errors given by Fig. C.3.

References

[Aj90] Ajzenberg-Selove, F., "Energy Levels of Light Nuclei $A = 11$–12," *Nucl. Phys. A* **506** (1990) 1.

[Aj91] Ajzenberg-Selove, F., "Energy Levels of Light Nuclei $A = 13$–15," *Nucl. Phys. A* **523** (1991) 1.

[Ak92] Akimov, Y., *et al.*, "Positive-Pion Production on Carbon at Low Pion Energies," *Nucl. Phys. A* **541** (1992) 433.

[Al88] Alons, P., *et al.*, "Microscopic Description of the A(p, π)A+1 Reaction," *Nucl. Phys. A* **480** (1988) 413.

[Al89] Alons, P., *et al.*, "The ^{3}He(p, π^+)^{4}He Reaction Near Threshold," *Nucl. Phys. A* **493** (1989) 509.

[As76] Ashcroft, N. and Mermin, D., *Solid State Physics* (Saunders College), 1976.

[Ba81] Baudinet-Robinet, Y., "Equilibrium Charge-State Distributions of Highly Stripped Ions in Carbon Foils," *Nucl. Instr. and Meth.* **190** (1981) 197.

[Be90] Bent, R., *et al.*, "Energy Dependence of the ^{3}He(p, π^+)^{4}He and ^{3}H(n, π^-)^{4}He Reactions," *Nucl. Phys. A* **511** (1990) 511.

[Be92] Bent, R., *et al.*, "Role of the Δ-Isobar in the A(p, π)A+1 Reaction," *Nucl. Phys. A* **548** (1992) 637.

[Bl90] Blankleider, B., "Pion Production in NN Collisions," in: *Particle Production Near Threshold, Amer. Inst. Phys. Conf. Proc.* **221** (ed. Nann, H. and Stephenson, E.) (1991) 150.

[Bn68] Brown, R., *et al.*, "Equilibrium Charge State Fractions for 11.5 to 37.3 MeV ^{16}O Ions in Carbon," *Nucl. Instr. and Meth.* **58** (1968) 274.

[Br82] Breskin, A., "Progress in Low-Pressure Gaseous Detectors," *Nucl. Instr. and Meth.* **196** (1982) 11.

[Bu76] Budker, G., *et al.*, "Experimental Studies of Electron Cooling," *Particle Accelerators* **7** (1976) 197.

[Ca93] Camerini, P., *et al.*, "Threshold Behaviour of the $\pi^+\pi^-$ Invariant Mass in Nuclei," *Nucl. Phys. A* **552** (1993) 451.

[Ce75] Cesini, G., *et al.*, "Evaluation of Fission Fragment Ranges in Any Medium," *Nucl. Instr. and Meth.* **127** (1975) 579.

[Ch68] Charpak, G., *et al.*, "The Use of Multiwire Proportional Counters to Select and Localize Charged Particles," *Nucl. Instr. and Meth.* **62** (1968) 262.

[Co82] Cooper, E. and Sherif, H., "Distortion Effects in a Relativistic One-Nucleon Model for the (p, π^+) Reaction," *Phys. Rev. C* **25** (1982) 3024.

[Da71] Dahlgren, S., *et al.*, "Positive-Pion Production in Nuclear Reactions Induced by 185 MeV Protons," *Phys. Lett. B* **35** (1971) 219.

[Dh83] Dakhno, L., *et al.*, "Measurement of the Cross-Sections for Production of Pion Pairs in Nucleon-Nucleon Collisions at Energies Below 1 GeV. Isospin Analysis," *Sov. J. Nucl. Phys.* **37** (1983) 540.

[Di82] Dillig, M., *et al.*, "Proton-Induced Pion Production in the Rescattering Model," in: *Pion Production and Absorption in Nuclei – 1981, Amer. Inst. Phys. Conf. Proc.* **79** (ed. Bent, R.) (1982) 275.

[Di89] Dillig, M., private communication (1989).

[Dk91] Daehnick, W., *et al.*, "A Proposal for the Construction of an Experimental Station at the 6 Degree Bend of the Indiana Cooler Ring," *IUCF Internal Report: Equipment Proposal* (1987).

[Dr91] Derenchuk, V. and Friesel, D., "Accelerator Performance," *IUCF Technical and Scientific Report* (1991) 187.

[Du87] Dubach, J., *et al.*, "NN $\rightarrow$ NNπ at Intermediate Energies: Predictions of a Unitary Model," *Nucl. Phys. A* **466** (1987) 573.

[Ei80] Eisenberg, J., "The $(\pi, \pi\pi)$ Process as a Possible Probe of Pion Condensation Precursor Phenomena," *Phys. Lett. B* **93** (1980) 12.

[Fa86] Falk, W., *et al.*, "Pion Production Cross-Sections and Analyzing Powers in the Inclusive ^{12}C(p, π^+)X Reaction at 400 and 450 MeV," *Phys. Rev. C* **33** (1986) 988.

[Fe81] Fearing, H., "Pion Production in Nuclei: Things Known and Unknown," *Progress in Part. and Nucl. Phys.* **7** (1981) 113.

[Fn90] Feng, X., *et al.*, "Cross-Section for the ^{27}Al(p, $\pi^+\pi^+$)^{28}Mg Reaction at 800 MeV," *Phys. Rev. C* **42** (1990) 451.

[Fr93] Friesel, D., "Accelerator Operations," *IUCF Newsletter* **52** (1993) 17.

[Ge54] Gell-Mann, M. and Watson, K., "The Interactions Between π-Mesons and Nucleons," *Ann. Rev. of Nucl. Sci.* **4** (1954) 219.

[Gn87] Grion, N., *et al.*, "Measurement of the ^{16}O($\pi^+, \pi^+\pi^-$) Reaction at $T_{\pi^+} = 280$ MeV," *Phys. Rev. Lett.* **59** (1987) 1080.

[Gr82] Green, M., "Recent Developments and Results in (p, $\pi^\pm$) at IUCF," in: *Pion Production and Absorption in Nuclei – 1981, Amer. Inst. Phys. Conf. Proc.* **79** (ed. Bent, R.) (1982) 131.

[Gr83] Green, M., "The Energy Dependence Near Threshold of Proton-Induced Positive Pion Production in Simple Spin Systems," *Ph.D. Thesis* (Indiana Univ., unpublished) (1983).

[Ha93] Hardie, J., private communication (1993).

[Hd80] Höistad, B., *et al.*, "The (p, $\pi^\pm$) Reaction on ^{12,13}C at 200 MeV," *Phys. Lett. B* **94** (1980) 315.

[He93] Heimberg, P., private communication (1993).

[Hi75] Highland, V., "Some Practical Remarks on Multiple Scattering," *Nucl. Instr. and Meth.* **129** (1975) 497.

[Ho87] Homolka, J., *et al.*, "Measurement of High Momentum Transfer Reactions by Recoil Detection," *Nucl. Instr. and Meth. A* **260** (1987) 418.

[Ho92] Homolka, J., *et al.*, "Measurement of the ^{12}C(p, π^0)^{13}N Reaction by Recoil Detection," *Phys. Rev. C* **45** (1992) 1276.

[Ho93] Homolka, J., *et al.*, "Readout Electronic [sic] for the Silicon Detector Array of the Indiana Experiment," Jahresbericht, Technische Universität München (1992) 160.

[Hu87] Huber, G., *et al.*, "Energy Dependence of the ^{12}C(p, π^+)^{13}C* Reaction in the Region of the Δ_{1232} Resonance," *Phys. Rev. C* **36** (1987) 1058.

[Iq85] Iqbal, M. and Walker, G., "Intermediate Isobar Effects in a Two-Nucleon Mechanism for (p, π)," *Phys. Rev. C* **32** (1985) 556.

[Ja85] Jacobs, W., "High-Spin States with the (p, π) Reaction," in: *Nuclear Structure at High Spin, Excitation, and Momentum Transfer, Amer. Inst. Phys. Conf. Proc.* **142** (ed. Nann, H.) (1985) 181.

[Jk90] Jäkel, O., *et al.*, "Chiral Symmetry and the Near Threshold Pion-Induced 2π Production on the Nucleon (I)," *Nucl. Phys. A* **511** (1990) 733.

[Jo82] Jones, G., "NN $\rightarrow \pi$d and NN $\rightarrow$ NNπ: A Review of Experimental Results," in: *Pion Production and Absorption in Nuclei – 1981, Amer. Inst. Phys. Conf. Proc.* **79** (ed. Bent, R.) (1982) 15.

[Js86] Jones, K., *et al.*, "Energy Dependence of Deformation Parameters in the ^{12}C(p, p$'$)^{12}C Reaction," *Phys. Rev. C* **33** (1986) 17.

[Ju84] Julien, J., *et al.*, "Evidence for a Resonant Structure in Inclusive Cu(p, π^+)X Reactions," *Phys. Lett. B* **142** (1984) 340.

[Kn89] Knoll, G., *Radiation Detection and Measurement, 2^{nd} Edition* (Wiley), 1989.

[Ko89] Korkmaz, E., *et al.*, "^{12,13}C($\vec{\text{p}}, \pi^{\pm}$) Reactions at T_p = 200 MeV," *Phys. Rev. C* **40** (1989) 813.

[Kr82] Krasnov, V., *et al.*, "Analysis of Pion Spectra in Production by 240–500 MeV Protons on Nuclei," *Phys. Lett. B* **108** (1982) 11.

[Ks84] Keister, B. and Kisslinger, L., "Microscopic Two-Baryon Dynamics and the (p, π) Reaction," *Nucl. Phys. A* **412** (1984) 301.

[Ku90] Kurepin, A., "Production and Decay of Δ Isobars in Nuclei," *Nucl. Phys. A* **519** (1990) 395c.

[Le93] Lee, T. and Riska, D., "Short Range Exchange Contributions to the Cross-Section for pp $\rightarrow$ ppπ^0 Near Threshold," *Phys. Rev. Lett.* **70** (1993) 2237.

[Lm70] Lock, W. and Measday, D., *Intermediate Energy Nuclear Physics* (Methuen), 1970.

[Ln87] Londergan, J., and MacFarlane, M., "The Nucleon-Nucleon Interaction: From Mesons to Quarks," *IUCF/NTC Internal Report 87-14* (1987).

[Lo84] Lolos, G., *et al.*, "Polarized-Proton-Induced Exclusive Pion Production in ^{12}C at 200, 216, 225, 237, and 250 MeV Incident Energies," *Phys. Rev. C* **30** (1984) 574.

[Lw87] Leo, W., *Techniques for Nuclear and Particle Physics Experiments* (Springer-Verlag), 1987.

[Lz92] Lozowski, W., private communication (1992).

[Lz93] Lozowski, W. and Hudson, J., "Improved Carbon Micro-Ribbon Targets and Stripper Foils for the IUCF Cooler Ring," *Nucl. Instr. and Meth. A* **334** (1993) 173.

[Ma79] Measday, D. and Miller, G., "Hopes and Realities for the (p,π) Reaction," *Ann. Rev. of Nucl. Sci.* **29** (1979) 121.

[Me83] Meyer, H., *et al.*, "Proton Scattering From ^{12}C Between 100 and 200 MeV and the Optical Potential," *Phys. Rev. C* **27** (1983) 459.

[Me85] Meyer, H., "Beam Properties in Storage Rings with Heating and Cooling," *Nucl. Instr. and Meth. B* **10** (1985) 342.

[Me88] Meyer, H., *Indiana Cooler User Guide, 2^{nd} Edition* (IUCF), 1988.

[Me90] Meyer, H., *et al.*, "Total Cross-Section for $pp \rightarrow pp\pi^0$ Near Threshold Measured with the Indiana Cooler," *Phys. Rev. Lett.* **65** (1990) 2846.

[Me92] Meyer, H., *et al.*, "Total Cross-Section for $pp \rightarrow pp\pi^0$ Close To Threshold, *Nucl. Phys. A* **539** (1992) 633.

[No70] Northcliffe, L. and Schilling, R., "Range and Stopping-Power Tables for Heavy Ions," *Nuclear Data Tables A* **7** (1970) 233.

[Os85] Oset, E. and Vicente-Vacas, M., "A Model for the $\pi^- p \rightarrow \pi^+\pi^- n$ Reaction," *Nucl. Phys. A* **446** (1985) 584.

[Os86] Oset, E. and Vicente-Vacas, M., "Inclusive $(\pi,\pi\pi)$ Reactions in Nuclei," *Nucl. Phys. A* **454** (1986) 637.

[Pa84] Parkhomchuk, V., "Physics of Fast Electron Cooling," in: *Proc. Workshop on Electron Cooling and Related Applications*, ECOOL (1984) 71.

[Pd90] Particle Data Group, "Review of Particle Properties," *Phys. Lett. B* **239** (1990) 1.

[Pi93] Pickar, M., *et al.*, "Near-Threshold Proton-Induced Neutral Pion Production From ^{12}C," *Phys. Rev. C* **48** (1993) 2763.

[Po90] Pollock, R., "The IUCF Cooler After Three Years," in: *Proc. Workshop on Cooler Rings and Their Applications* (ed. Katayama, T.) (1990) 147.

[Pp90] Pancella, P., *et al.*, "Linear Motion Feedthrough for Target Positioning," *IUCF Technical and Scientific Report* (1990) 125.

[Pp94] Pancella, P., private communication (1994).

[Pr88] Press, W., *et al.*, *Numerical Recipes in C, 1st Edition* (Cambridge U. Press), 1988.

[Pz93] v. Przewoski, B., *et al.*, "Interaction of Stored, Cooled Proton Beams with Fiber Targets," *Nucl. Instr. and Meth. A* **328** (1993) 435.

[Re84] Read, S. and Viola, V., "Excitation Functions for $A \geq 6$ Fragments Formed in ^{1}H- and ^{4}He-Induced Reactions on Light Nuclei," *Atomic Data and Nuclear Data Tables* **31** (1984) 359.

[Rm88] Rehm, K. and Wolfs, F., "A Focal Plane Detector for Reactions with Medium Weight Projectiles," *Nucl. Instr. and Meth. A* **273** (1988) 262.

[Sa77] Sauli, F., "Principles of Operation of Multiwire Proportional and Drift Chambers," *CERN Report 77-09* (1977).

[Sc86] Schott, W., *et al.*, "Observation of the ^{12}C(^{3}He, π^{+})^{15}N Reaction Near Threshold Using Recoil Detection," *Phys. Rev. C* **34** (1986) 1406.

[Se87] Segel, R., *et al.*, "Measurements of Nuclear Reactions using Recoil Detection," *IUCF/NTC Internal Report 87-07,* (1987).

[Sg92] Solberg, K., private communication (1992).

[Sk88] Schuck, P., *et al.*, "Bound Two-Pion Cooper Pairs in Nuclei?," *Zeit. für Physik A* **330** (1988) 119.

[So81] Soga, F., *et al.*, "Energy Dependence of the Reaction ^{12}C(p, π^+)^{13}C to Different Final States," *Phys. Rev. C* **24** (1981) 570.

[Sp90] Sperisen, F., *et al.*, "Cooler Target Development: Gas Jet Target," *IUCF Technical and Scientific Report* (1990) 117.

[Vi82] Vigdor, S., *et al.*, "Dominance of High-Spin Two-Particle, One-Hole Transitions in (p, π^-) Reactions," *Phys. Rev. Lett.* **49** (1982) 1314.

[Wa52] Watson, K., "The Effect of Final State Interactions on Reaction Cross-Sections," *Phys. Rev.* **88** (1952) 1163.

[Wi71] Wilson, S., *et al.*, "Isospin Invariance in the Reaction n+p $\rightarrow \pi^0$+d," *Phys. Lett. B* **35** (1971) 83.

[Yk35] Yukawa, H., "On the Interaction of Elementary Particles (I)," *Proceedings of the Physical-Mathematical Society of Japan* (1935) 48.

[Yu89] Yu, Z., *et al.*, "Studies of the ^{12}C(p, n) and ^{13}C(p, n) Reactions Near 180°," *IUCF Technical and Scientific Report* (1989) 43.

Index

!, *31, 32, 51, 98, 113, 126, 141.*
ABCD, *11.*
antennae, *57.*
bags, *2.*
bifurcation, *43.*
billiard ball, *113.*
Bloomington, *24.*
bomb, *12, 19, 47, 123.*
bottle, *1.*
Bragg, *83.*
cave, *95.*
chiral, *13.*
contact potential, *121.*
cooked, *66.*
cup in!, *50.*
cursor, *14, 135.*
dead, *29, 33, 38, 45, 49, 51, 122, 123.*
Doskow, J., *23.*
duty, *33, 34.*
expensive, *36.*
fingerprints, *123.*
flat, *34, 37, 69, 82, 95, 101, 104, 110.*
Götterdämmerung, *27.*
half-baked, *66.*
Jacobian, *94.*
Jones, *1.*
kernel, *130.*
Knuth, D., *ii.*
low-pressure, *42, 45, 112, 117, 118.*
Luxnat, M., *23.*
Mandelstam, *104.*
®, *125.*
methane, *31.*
microscopic, *11, 12, 13.*
Old Lace, *120.*
photolithography, *119, 123.*
pickup, *40, 57.*
punch, *97.*
puzzle, *92.*
quench, *117.*
Rokicki, T., *ii.*
shell, *8, 11, 113, 130.*
shuffling, *40.*
skim, *33, 34.*
soft, *35, 127, 132.*
spikes, *32.*
static, *1, 32, 72, 114.*
thrust, *130.*
ultraviolet, *117.*
whisker, *32.*